A Photoelectrochemical cell for direct conversion of gaseous CO_2 to self-growing graphenic carbon and hydrogenated carbon

A thesis submitted in fulfilment of the requirements for the degree of Doctor of Philosophy

by **Mobin Arab**

Supervisor: Prof. Andrew T. Harris
Co-supervisor: A/Prof. Andrew I. Minett
Co-supervisor: Dr. Tamara L. Church

School of Chemical and Biomolecular Engineering
Faculty of Engineering and IT
The University of Sydney

February 2016

To my best friend: my lovely wife.

Declaration

I declare that the entire contents of this thesis are, to the best of my knowledge and belief, original, unless otherwise acknowledged in the text. This thesis contains no material that has been presented for a degree or diploma at this or any other institute of higher education

Mobin Arab

January 2016

همتم بدرقه راه کن ای طایر قدس که دراز است ره مقصد و من نوسفرم

(حافظ)

Oh Heaven's bird, make persistence my companion
As the journey is long and I'm a new traveler

(Hafiz)

Acknowledgement

After more than three years of working towards achieving this degree I have to express my sincere and heartfelt appreciations to:

My supervisors Prof. Andrew T. Harris, A/Prof. Andrew I. Minett and Dr. Tamara L. Church for their time and support throughout my journey and Prof. Thomas Maschmeyer and Dr. Xiaobo Li for helpful discussions and support;

Members of Laboratory for Sustainable Technology Nikan Noorbehesht, Shaikh Nayeem Faisal, Omar Al-Khayat, Nikki Amos, and Meherzad Variava for their help, discussions, and comments;

Dr. Jiefeng Gao, from Mechanical engineering department of the University of Sydney, and Dr. Javad Foroughi in University of Wollongong for their help on electrospinning of Nafion® and Carol Hua, from School of Chemistry of the University of Sydney, for UV-Vis spectrometry;

The University of Sydney and ANLEC R&D for the financial support for my studies and living.

And Zakieh, my wife, who made this journey a joyful one by her constant encouragements and her eager listening to my lab stories, and my parents, who provided immense support throughout my life and were far from me during this period.

Mobin Arab

Jan. 2016

List of Publications

Journal papers

Arab, M., Minett, A. I., Harris, A. T., & Church, T. L. (2015). Solid particles' recirculation distribution in calcium looping post-combustion carbon capture. *International Journal of Greenhouse Gas Control*, *43*, 161-171.

Arab, M., Church, T. L., Li, X., Noorbehesht, N., Maschmeyer, T., Minett, A. I., (2016). A true artificial leaf: from CO_2 gas to self-growing graphenic carbon, submitted to *Science*.

Patents

Arab, M., Church, T. L., Li, X., Maschmeyer, T., Minett, A. I., (Filed on 11 March 2015). Photoelectrochemical cell. Application numbers: 2015900862.

Arab, M., Noorbehesht, N., Husin, A., Feisal, S. N., Church, T. L., Li, X., Maschmeyer, T., Minett, A. I., Electrocatalysts and electrochemical cells. (Filed on 21 January 2016) Application numbers: 2016900179.

Conference papers

Arab, M., Church, T. L., Li, X., Noorbehesht, N., Maschmeyer, T., Minett, A. I. (2016, February). Fully Integrated Stand-Alone Device for Reduction of Gaseous CO_2 to Self-growing Carbon. International Conference on Nanoscience and Nanotechnology, Canberra, Australia.

Arab, M., Church, T. L., Li, X., Maschmeyer, T., & Minett, A. I. (2015, July). Fully Integrated Stand-Alone Device for Gas-Phase CO_2 Reduction Using Sunlight: Proof of Concept. In Meeting Abstracts (No. 43, pp. 1743-1743). The Electrochemical Society.

Arab, M., Church, T. L., Variava, F. M., Minett, A. I., Harris, A. T. (2013, December). Optimum CaO:Coal Ratio in Enhanced Hydrogen Production. 4th Sino-Australian Symposium on Advanced Coal and Biomass Utilization Technologies.

Abstract

Limiting anthropogenic climate change to below 2 °C is one of the key challenges of the 21st century. Climate models suggest this cannot be achieved without drastically affecting the global economy unless carbon removal technologies, which are able to reduce absolute content of CO_2 in the atmosphere, are deployed. This thesis is aimed at developing a technology to convert CO_2 directly from gas phase to a solid product using non-concentrated sun light, thereby moving beyond mimicking nature's leaf, integrating millions of years of fossilization into a real-time process.

In this thesis a novel electrolyte-less photoelectrochemical cell (PEC) for direct conversion of gaseous CO_2 solid carbon using earth abundant materials is conceptualized, designed, realized, and tested. It was found that the proposed PEC is able to convert CO_2 to a self-growing graphenic material, when placed in an environment where gaseous CO_2, gaseous H_2O, and light at natural intensity coexist. The proposed PEC was extensively experimented under different atmospheres using unassisted and assisted (biased and non-biased) photoelectrochemical and electrochemical techniques. The product of CO_2 conversion reaction was extensively characterized using optical microscopy, Scanning Electron Microscopy (SEM), Energy Dispersive Spectroscopy (EDS), X-ray Photoelectron Spectroscopy (XPS), Infrared spectroscopy, Raman spectroscopy, Atomic Force Microscopy (AFM), Laser profilometry, UV-Vis spectroscopy, and Time of Flight-Secondary Mass Spectroscopy (ToF-SIMS). Extensive evidences were found confirming that CO_2 was converted to a mixture of graphene and hydrogenated amorphous carbon which has self-growing properties through high sp^2 carbon content and semiconducting behavior. Furthermore, using evidences that were found through characterization, a reaction mechanism for such a conversion on the proposed PEC was

suggested. Furthermore, measures to improve performance of the developed PEC were suggested and deployed were possible.

This thesis is the description of the first successful attempt of development of a fully integrated, unassisted, stand-alone PEC for direct conversion of gaseous CO_2 to self-growing solid carbon. Despite some existing limitations of the proposed PEC, such as relatively low levels of generated photocurrent and low photocurrent stability, the results were promising. This warrants further work on improving the design and consequently performance of the proposed PEC.

Table of Content

List of Figures, Schemes, and Images

List of Tables

List of Abbreviations

a	Amorphous	MM2	Molecular Mechanics Force Field Calculations
a-C:H	Amorphous Hydrogenated Carbon	Nafion®-M	Nafion® Nanoribbon Membrane
AFM	Atomic Force Microscopy	NASA	National Aeronautics and Space Administration
AM	Air Mass	NHE	Normal Hydrogen Electrode
AP	Artificial Photosynthesis	NP	Nanoparticle
BOC	Brin's Oxygen Company	NR	Nanorod
BSE	Back Scattered Electron	OC	Open Circuit
CNT	Carbon Nanotube	PAA	Poly(Acrylic Acid)
CuC-O	The Original Copper Cathode	PEC	Photoelectrochemical Cell
Cu-R	The Copper Cathode After Rinsing	PEO	Poly(Ethylene Oxide)
DC	Direct Current	PFSA	Perfluorinated Sulfonic Acid
DFT	Density Functional Theory	PL	Photoluminescence
DI	Deionized Water	PTFE	Polytetrafluoroethylene
DS-O	The Original Deposited Material	PV	Photovoltaic Cell
DS-R	The Deposited Material After Rinsing	SC	Short Circuit
EDS	Energy Dispersive Spectroscopy	SE	Secondary Electron
FWHM	Full Width at Half Maximum	SEM	Scanning Electron Microscopy
GA	Genetic Algorithm	she	Standard Hydrogen Electrode
GDM	Gas Diffuser Membrane	ToF-SIMS	Time of Flight-Secondary Mass Spectroscopy
GLCH	Graphite-Like a-C:H	TON	Turnover Number
HOMO	Higher Occupied Molecular Orbitals	UV	Ultraviolet
IR	Infrared	Vis.	Visible
ITO	Indium Tin Oxide	WOC	Water Oxidation Catalyst
MEA	Membrane Electrode Assemblies	XPS	X-Ray Photoelectron Spectroscopy
MM	Molecular Mechanics	XRD	X-Ray Powder Diffraction

Chapter one

Introduction

About 120 years is passed from the day that Arrhenius suggested there could be a close relationship between concentration of CO_2 in the atmosphere and surface temperature of the earth (*1*). Now after long disputes about the nature of the so-called climate change and considering a variety of causes (e.g. solar cycles (*2*), cosmetic rays (*3*), cloud feedback (*4*) etc.), it is generally accepted that human industrial activity and the consequent emissions of greenhouse gases (GHGs), especially CO_2 as the major greenhouse gas, is the main factor for the rapid change in the global temperature (*5, 6*). Therefore, a global movement has been started to limit the emissions of CO_2 to the atmosphere either by replacing fossil fuels with renewable sources of energy or by capturing and storing CO_2 from industrial point sources of CO_2 or from air (CCS technologies). However, there is a question that needs to be addressed first: how much of CO_2 needs to be mitigated to avoid intense climate change?

According to climatologists, the global peak temperature (the temperature trajectory with a peak at some time in future, followed by a slow decrease) rise (*7*) is a near-linear function of cumulative CO_2 inventory in the atmosphere. Recognition of this correlation provided researchers with a simple method to estimate how implementing different GHG mitigation technologies affects the peak temperature. Stocker (*8*) used a similar correlation to demonstrate the dynamic effect of global emission reduction schemes on the peak temperature (see Figure 1-1). On the other hand, International Energy Agency (IEA) developed a variety of scenarios based on technology maturity level to provide insight toward the contribution of each of the available mitigation technologies on CO_2 emission levels (*9*). Combing the information from the two mentioned sources provides insights into how challenging it is to meet a specific global temperature rise target. The result of such an analysis shows even if all available CO_2 mitigation technologies are deployed as outlaid by IEA (at an average reduction rate of 3.1 percent per year starting by 2025 (*10*), see Figure 1-2) it is barely possible to reach the 2 °C target (i.e. a

maximum of 2 °C increase in global temperature by the end of 21st century relative to pre-industrial levels), which is known to be the maximum safe level of global warming (*11*). In fact, according to the latest estimations the CO_2 emission is rising according to IPCC's A2 scenario (see Figure 1-2), which represents relatively slow demographic transition, convergence in inter-regional gross domestic product (GDP) per capita differences, end-use and supply-side energy efficiency improvements, development of renewable energy, and no barriers to the use of nuclear energy. This CO_2 emission trend leads to about 3.6 °C increase in the global temperature until 2100 (*12*). This trend is in agreement with low enthusiasm toward developing and deploying climate change mitigation technologies, which is being observed throughout the world (*13*). In other words, 1.5 °C target is already missed and 2 °C target will be missed by 2027 (*8*) given that the maximum feasible CO_2 emissions reduction rate without drastically affecting the global economy is 5% per year (*14*). Consequently, to avoid intense climate change in the future (global temperature rise below 4 °C) not only all CO_2 reduction technologies need to be deployed, but also technologies which deal with capturing CO_2 that has already been emitted to the atmosphere, i.e. air capture, needs to be deployed (*15*). These technologies are called carbon removal technologies or carbon negative processes because they provide negative CO_2 emissions (absolute reduction in CO_2 inventory of the atmosphere by reversing direction of CO_2 emissions, i.e. from air to earth). The other alternative is to use geoengineering techniques, to manipulate heat balance of the earth (*16, 17*), which is out of scope of this thesis.

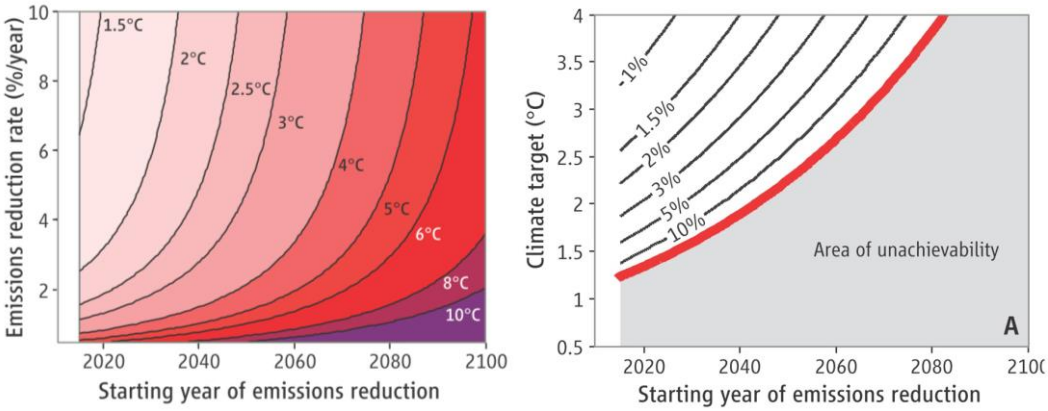

Figure 1-1. Effectiveness limits of emission mitigation policies versurs startting time of implementation (*8*).

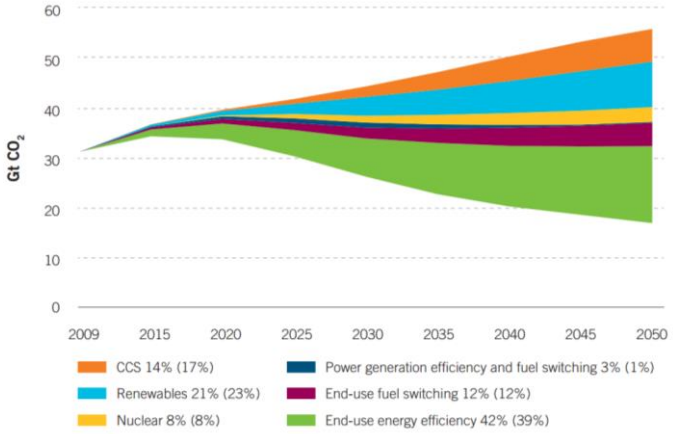

Figure 1-2. Energy–related CO_2 emissions reductions by technology (*10*).

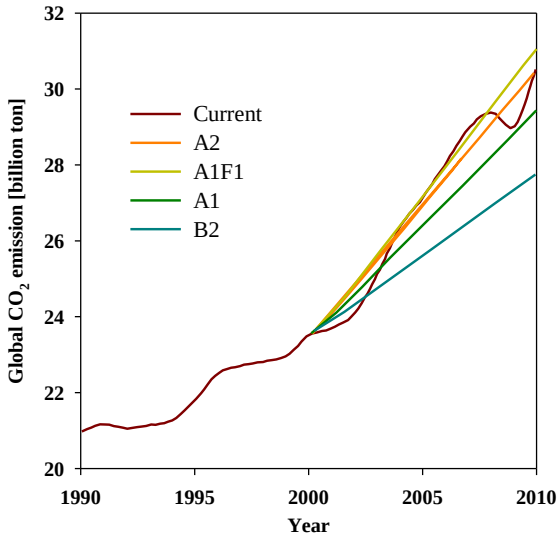

Figure 1-3. CO_2 emissions since 1990 and different IPCC's emission scenarios. Currently the global CO_2 emission is moving according to A2 scenario (*13*). This trend is in agreement with low enthusiasm toward developing and deploying climate change mitigation technologies.

A process/technology which is carbon negative provides permanent removal of greenhouse gases (i.e. CO_2) from the atmosphere. Negative emissions can be achieved through different technologies, e.g. biomass utilization with carbon capture and storage or BECCS (*18, 19*), biochar production (*20*), direct air capture (*15*), enhanced weathering (*21*), and solar sequestration (sequestering CO_2 by only using solar energy). It is of extreme interest to develop technologies for facile sequestration of CO_2 which ideally are, efficient, scalable, fit with already available infrastructure, using abundant and non-conflicting sources of energy and materials for its manufacturing and operation (*22*). In addition, the product must be in demand. Converting CO_2 to chemicals is not suitable to combat the mentioned problems due to drastic difference between demand for producible chemicals from CO_2 and supply of CO_2 (known as market size limitation) (*23*). Therefore, developing a technology to convert the CO_2 to a fuel, which is already compatible with the available transportation and consumption infrastructure, would be a game changer.

Among the available renewable energy resources, solar energy fits well within the requirements. Solar energy is the largest energy resource, providing more energy in one hour than energy consumed by humans in a year (*24*). It is widespread around the globe (*25*) and the harvesting technology is well-developed, therefore it is already deployable in large scales (e.g. in Australia only 4.7 GW of photovoltaics (PVs) are installed by 2015 (*26*)). Therefore, solar energy (i.e. sun light) is one of the best candidates for this application. In addition, nature is being converting CO_2 using sun light for millions of years through photosynthesis. Carrying out the same overall reaction ($CO_2 + H_2O + hv \rightarrow O_2$ + carbohydrate or hydrocarbon, see Scheme 1-1) using a synthetic device is known as artificial photosynthesis (AP). In other words, AP is mimicking natural photosynthesis through synthesizing materials or developing apparatus which can convert carbon dioxide and water to a useful chemical compound using light at ambient condition. AP has been the subject of many studies (*22*, *27*) as it is known as a highly rewarding pathway to achieve a carbon-neutral economy, by recycling CO_2 through production of value added carbonous chemicals and at the same time storing renewable energy in chemical bonds.

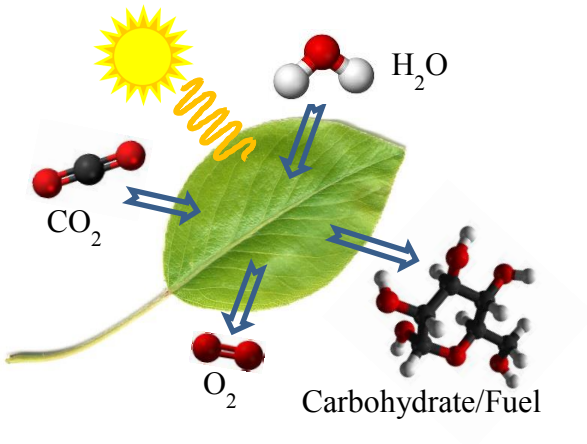

Scheme 1-1 Schematic diagram of natural photosynthesis during which CO_2 is converted to a form of solid hydrocarbon using H_2O as proton and electron donor and sunlight as the source of energy.

Leaves, as the major living organism carrying photosynthesis activity, are photoelectrochemical devices. However, photoelectrochemistry is not the only root toward

conversion of CO_2. CO_2 can be converted through five major categories of technologies, namely thermochemical, bio-conversion, electrochemical, photocatalytic, and photoelectrochemical, as described below (*28-30*):

1. Thermochemical processes are processes through which CO_2 is dissociated and combined with a source of proton (hydrogen or water) to produce a chemical or fuel using thermal energy, which can come from different sources such as concentrated solar thermal plants.
2. Bio-conversion processes are processes through which CO_2 is converted to a chemical or fuel by deploying a form of living organism, e.g. trees or microalgae, using sunlight as the energy source.
3. Electrochemical processes are processes through which the concept of water electrolysis is further expanded to convert CO_2 to a chemical or fuel. Hydrogen or water may be used as proton source. The required electricity can be derived from photovoltaic cells (PVs) using sunlight.
4. Photocatalytic processes are processes through which CO_2 is dissociated and combined with a source of proton (hydrogen or water) to produce a chemical or fuel using photon absorption and excitation mechanisms.
5. Photoelectrochemical (PEC) processes are processes through which the concept of water electrolysis is further expanded to convert CO_2 to a chemical or fuel using sunlight (i.e. AP) using a combination of photocatalytic and electrochemical processes to take advantage of both mechanisms.

Among the mentioned processes not much work is done in photoelectrochemical devices for CO_2 conversion (Figure 1-4) despite promising reported efficiencies (below 0.7% optical efficiency for PECs in comparison to ~0.03% for photocatalytic processes (*22*), and ~0.4% for

thermochemical processes (*31*)) and the fact that the terms “artificial photosynthesis” and “artificial leaf” have been used extensively in the literature, as inferred from bibliometric analysis of the publications shown in Figure 1-4.

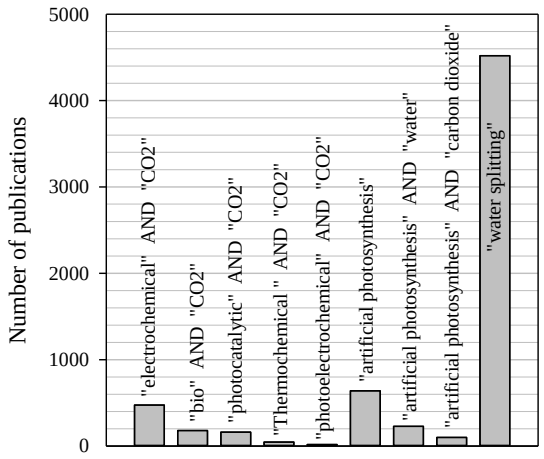

Figure 1-4. Number of publications in each category of CO_2 conversion technologies. Scopus search engine was used to extract publication numbers. To avoid double counting of publications, only “keywords” field were searched using shown keywords in quotation marks for each category of technology. The search results are not intended to be accurate, instead general trend of publications was of interest.

Another important aspect of CO_2 reduction for the purpose of large scale deployment is the reaction media (i.e. reaction phase). The majority of attempts to carry out carbon dioxide conversion were carried out in liquid phase, where CO_2 has first to be dissolved in a liquid electrolyte (*32-34*). However, this approach has some major drawbacks, including low dissolution rate of CO_2 in aqueous phase electrolytes (leading to low concentration of CO_2 on reaction sites) (*32, 35*), decay in catalyst activity (*36, 37*), limit of reaction temperature (up to boiling point of electrolyte), continuous competition between hydrogen generation and CO_2 reduction (*38*), etc. In addition, for large scale deployment a highly concentrated source of CO_2 has to be bubbled through the electrolyte causing agitation and possible detachment of catalysts from electrode surface or forming barrier layers. Furthermore, in liquid phase mainly C1 products are formed (*35*). However, if one could carry out CO_2 conversion directly in gas phase,

using a solid-state device, similar to natural photosynthesis which is being carried out in leaves, most of these problems can be avoided (*35*). Furthermore, one could potentially carry out CO_2 separation and CO_2 conversion in one single step, significantly reducing costs of CO_2 utilization (*39*). Other advantages of operating in gas phase are recovery of reaction products and operating at high temperatures and pressures is simplified, O_2/H_2 diffusion in liquid phase and light scattering through liquid electrolyte is eliminated, stability of electrodes is enhanced (*40*), and reactions take place at higher rates (*41*). However, despite the great potentials of operation in gas phase, only a few studies of gas phase CO_2 reduction have been published in the literature (*42*), starting with the works of D.W. Dewulf (*43*) and C. Ronald (*44*), and followed by recent studies of G. Centi (*45-47*), which were focused on the electrochemical root setting development of an integrated photoelectrochemical device as the ultimate goal (*40*) (see Table 1-1 for the full list of gas phase CO_2 conversion studies). Although pioneering attempts, only cathode sides of the developed electrochemical devices/apparatuses operate in gas phase (anode side was in contact with a counter solution, providing required protons to cathode side using Nafion® membrane). Those devices are known as electrolyte-less (EL) cells, because a bulk liquid electrolyte is absent (*48*).

Table 1-1. List of experimental gas phase CO_2 reduction studies published in literature using different reaction mechanism. The publications are categorized base on reaction mechanism and sorted based on publication year.

Reference	Reaction mechanism	Energy source	Reaction media	CO_2 reduction catalyst	Reaction temperature	Main products
Traynor and Jensen (*49*)	Thermochemical	Concentrated sunlight at 5000 sun	CO_2	None	1900 °C	CO
Loutzenhiser et al. (*50*)		Electric heater	CO_2	ZnO	~ 550 °C	CO
Chueh et al. (*31*)		Concentrated sunlight at 1500 sun	CO_2	CeO_2	~ 1600 °C	CO
Furler et al. (*51*)		Xe arcs at 2865 sun	CO_2 and H_2O vapor	CeO_2 felt	~ 1400 °C	CO, H_2
Thampi et al., (*52*)	Photocatalytic[3]	UV at 310–435 nm	CO_2, H_2 in Ar	Ru/RuO_x sensitized TiO_2	ambient	CH_4
Saladin et al., (*53*)		Xe arcs at 1000 W (< 700 nm)	CO_2 and H_2O vapor	TiO_2 on quartz wool	~70 °C	CO, H_2, CH_4
Anpo et al., (*54*)		UV Hg lamp	CO_2 and H_2O vapor	TiO_2 loaded zeolite	ambient	CH_3OH
Ulagappam and Frei, (*55*)		UV laser at 266 nm	CO_2 and H_2O vapor	Ti-silicalite molecular sieve	ambient	CO, CH_2O, C_2H_4O
Ikeue et al., (*56*)		UV Hg lamp	CO_2 and H_2O vapor	Ti containing SiO_2 film	ambient	CH_4, CH_3OH
Tan et al. (*57*)		NEC Germicidal lamps at 253.7 nm and blue fluorescent lamps at 365 nm	CO_2 and H_2O vapor	TiO_2 pellets, Aerolyst 7708	ambient	CO, CH_4, H_2
Xia et al., (*58*)		UV at 365 nm	CO_2 and H_2O vapor	MW-CNT supported TiO_2	ambient	C_2H_5OH, CH_2O_2
Wu et al., (*59*)		UV at 365 nm	CO_2 and H_2O vapor	Ag/Cu-TiO_2 coated optical fiber	ambient	CH_3OH
Varghese et al., (*60*)		natural sunlight of AM 1.5	CO_2 and H_2O vapor	Cu, Pt co-catalyzed N-doped TiO_2 nanotube arrays	ambient	CH_4, H_2, CO, other alkanes, olefins, Branched paraffins
Wang et al., (*61*)		visible light at 420 nm	CO_2 and H_2O vapor	CdSe/Pt/TiO_2 heterostructure	ambient	CH_4, CH_3OH, CO, H_2
Xie et al. (*62*)		Xe lamp 320–780 nm	CO_2 and H_2O vapor; CO_2 and liquid H_2O	Ag, Rh, Au, Pd, Pt, MgO-Pt all on TiO_2	49.85 °C	CO, CH_4, H_2

Ichikawa[1] (*63*)	Photoelectrochemical or electrochemical	Light and electricity	Possibly CO_2 only	Cu, Cu/ZnO	ambient	CH_4
Dewulf et al., (*43*)	Electrochemical	Electricity by applying 2.00 V bias vs. SCE	Anode immersed in 1 mM H_2SO_4 or 0.5M $KHCO_3$, humidified CO_2 (bubbled through 0.5M $KHCO_3$) in cathode side	Cu/SPE[2]	22 °C	CH_4, C_2H_6
Ronald et al., (*44*)		NS[2]	10% H_2 or aq. inorganic salt solution on anode, CO_2 on cathode	Cu	ambient	CH_4, C_2H_6
Centi et al., (*64*)		Electricity by applying 1.99 V bias	NS[2]	20% Pt/GDM[2]	NS[2]	CH_4, C_2H_6, C_3H_8, C_2H_5OH, CH_3OH
Centi et al., (*47*)		Electricity by pumping 20 mA current	Anode immersed in $KHCO_3$ 0.5M and CO_2 and H_2O vapor on cathode side; H_2 + 4% H_2O on anode side and CO_2 and H_2O vapor on cathode side	Pt/GDM[2]	22 °C	>C6; first observation of long-chain hydrocarbon formation using electrochemical method
Centi et al., (*65*)		Electricity by applying 1.99 V bias	50% CO_2	20% Pt/GDE[2]	ambient	CH_4, C_2H_6, C_2H_5OH, CH_3OH,
Genovense et al., (*42*)		Electricity by pumping 10–20 mA current	Anode side immersed in KCl 0.5M, 50% CO_2 in He on cathode side	Fe, Co, Cu, Pt NPs[2] on CNTs	60 °C	CH_3OH, C_2H_4O, C_2H_5OH, CH_3COOH, C_3H_6O, C_3H_7OH
Ampelli et al., (*45*)		Electricity by pumping 10 mA current	Anode immersed in $KHCO_3$ 0.5M, CO_2 on cathode side	Fe/CNTs[2], Fe/TPE-CMP, Pt/CNTs	60 °C	CH_3OH, C_3H_6O, C_3H_7OH, C_2H_5OH
Genovense et al., (*66*)		Electricity by pumping 10–20 mA current	Anode side immersed in KCl 0.5M, 50% CO_2 in He on cathode side	Cu NPs	NS[2]	CH_3OH, C_2H_4O, C_2H_5OH, CH_3COOH, C_3H_6O, C_3H_7OH

[1] There are many ambiguities in this paper. The experimental condition, products distribution, applied bias, light source if any, cathode and anode condition, etc are not described in the original paper.

[2] SPE = Solid Polymer Electrolyte; GDM = Gas Diffusion Membrane; NP = Nanoparticle; CNT = Carbon Nanotube; NS = Not specified in the paper

[3] An extensive list of photocatalytic conversion of CO_2 refer to ref. (*67*)

To the author's best knowledge, no report exists on mimicking natural photosynthesis in gas phase through photoelectrochemical root, although there have been some efforts to achieve this mainly by G. Centi et al. (*33-35, 42, 46, 47, 65, 66*). In addition, no trace of such a work was found by reviewing the extensive published review papers (*28-30, 68-74*). However, the necessity of development of a fully integrated device to perform CO_2 reduction reaction in gas phase has been already pointed out in a number of concept and vision papers (*40, 45, 48, 75*). In this thesis, a stand-alone unassisted solid-state photoelectrochemical (PEC) device is developed that converts CO_2 to self-growing graphenic solid carbon directly from gas phase using only water vapour (i.e. humidity) as electron and proton donor, and utilizing earth abundant catalysts. The reaction is derived using 1 sun intensity simulated sun light (1000 W/m^2, similar to natural sunlight, AM 1.5, class AAA). The reaction product, self-growing graphenic solid carbon, can be used as a catalyst (electro- and photo-catalytic applications), as a fuel (solar-to-fuel and solar energy storage application), or as a stable material that can be stored away, permanently (CO_2 sequestration applications).

The first step to realize such a device is the conceptual design of the device. This step includes selection of a suitable chain of reactions that is required for converting of CO_2 to solid carbon, determination of required material properties and selection of materials for different components of the conceptually designed PEC, architecture design of the PEC, design of experimental apparatus, experiment design, material synthesis and characterization, and assembly of the device. These are subjects of Chapter 2 of this thesis. In Chapter 3, the manufactured PECs were tested under various conditions to prove the concept through electrochemical methods and measuring generated photocurrent from the PEC in light and dark and under dry and humidified CO_2 and Ar gas. Formation of dark solid deposits on cathode side of the PEC and decline of generated photocurrent with time was observed. In Chapter 4, the possible reasons behind decline of detected photocurrent are discussed in detail, possible causes are investigated and solutions to improve the rate of

decline are suggested. In Chapter 5, the product of CO_2 reduction reaction, the deposited dark material on the PEC, is characterized using various characterization techniques including optical microscopy, Scanning Electron Microscopy (SEM), Energy Dispersive Spectroscopy (EDS), X-ray Photoelectron Spectroscopy (XPS), Infrared spectroscopy, Raman spectroscopy, Atomic Force Microscopy (AFM), Laser profilometry, UV-Vis spectroscopy, and Time of Flight-Secondary Mass Spectroscopy (ToF-SIMS). In Chapter 6, the key findings of this thesis are summarized, emphasizing on the possibility of conducting such a reaction chain to form self-growing solid carbon form gaseous CO_2, directly from gas phase. In addition, possible future works are suggested.

Although not directly related to the core aim of this thesis, which is the development of a PEC for direct gas phase CO_2 utilization and conversion, further contribution to the literature were made through conducting research in other related fields of CO_2 capture, specifically in pre- and post-combustion carbon capture. The purpose of those researches were to understand the concepts behind the most promising pre- and post-combustion carbon capture technologies (namely, enhanced coal gasification through calcium looping and calcium looping post combustion CO_2 capture from coal-fired power plants). To that end, in one study the effect of CaO addition on gasification performance and hydrogen generation rate of Australian brown and black coal were studied using integrated thermogravimetric and mass spectroscopy method for a wide range of CaO:coal ratios. In another study, the effect of CaO-based sorbents quality on performance of a coal-fired power plant was investigated in detail. A new mathematical model for short-cut modelling of CaO-based CO_2 capture plants were proposed, which was particularly relevant for synthetic high performance sorbents. Because these studies were not directly related to the main aim of this thesis, for consistency sake, they are presented in two appendix chapters, Appendix A and Appendix B, respectively.

Chapter two

From conceptual design to assembly of artificial leaf

In this chapter, first, design of a photoelectrochemical cell (PEC) suitable for direct conversion/reduction of CO_2 from gas phase to solid carbon is conceptualized. Then, components of designed PEC were manufactures, synthesized, and characterized. After the required components were successfully synthesized, various PECs with different characterizations were assembled through a specifically designed assembly procedure. Design of a reactor which was used for conducting proof-of-concept tests using the assembled PECs is also discussed in detail.

2.1 Conceptual design of the photoelectrochemical cell (PEC)

A photoelectrochemical cell is a device which converts light energy into chemical energy through electricity production within a two-electrode cell. A PEC takes advantage of a semiconductor material to create electron/hole pairs using photons in light. Electro/hole pairs that are generated upon illumination of semiconductors can create an electric potential difference between the two electrodes (cathode where reduction reactions take place and anode where oxidation reactions take place), which can be used to derive a chemical reaction (*76*). In order for a reaction to take place, electrodes should be placed in contact with an electrolyte (commonly in liquid phase) which is able to transfer ions produced on one electrode to the other electrode (from cathode to anode or vice versa). The electrodes also need to be in electronic contact, using an electrically conductive medium such as Cu wires. In a PEC each of the anode and/or cathode may be a photo-electrode. In theory, three arrangements of photo-electrodes in the assembly of PECs exist (*77*):

1. photo-anode made of a n-type semiconductor and a metal cathode
2. photo-anode made of a n-type semiconductor and a photo-cathode made of a p-type semiconductor
3. photo-cathode made of a p-type semiconductor and a metal anode

PECs may be tailored to derive a set of specific reactions. Depending on the desired set of reactions, any of the three mentioned photo-electrodes arrangements may be chosen. In addition, selection of cathode, anode, semiconductor, and electrolyte materials also significantly impacts operation of a PEC both in terms of performance, products type and distribution. A fully integrated stand-alone PEC device is a device which does not need assistance (operation wise or energy wise) to convert raw reactants to desired products solely using light as the source of energy. If no wiring is used in a PEC, then it may be called wireless.

As explained in Chapter 1 (Introduction), only few attempts to conduct CO_2 reduction in gas phase is reported in literature. Therefore, there is limited experience with designing a PEC suitable for this specific process. Reviewing the literature, only one PEC design was found for gas phase CO_2 reduction which incorporates an integrated concept. This design was first suggested by Dewulf and Bard (*43*) in 1988 (shown in Scheme 2-1a). This design was originally developed for electrochemical CO_2 reduction, and therefore technically is not a device, as authors suggested (the authors presented this design as an electrode for CO_2 reduction rather than a device). However, one may slightly modify the design to incorporate a light harvesting device or material to convert light to electricity, and therefore make it a device suitable for photoelectrochemical applications, as suggest by Ichikawa (*63, 78*) (shown in Scheme 2-1b). In following years, Centi et al. suggested other variations of the device (*47*), although, the design essentially remained the same (shown in Scheme 2-2).

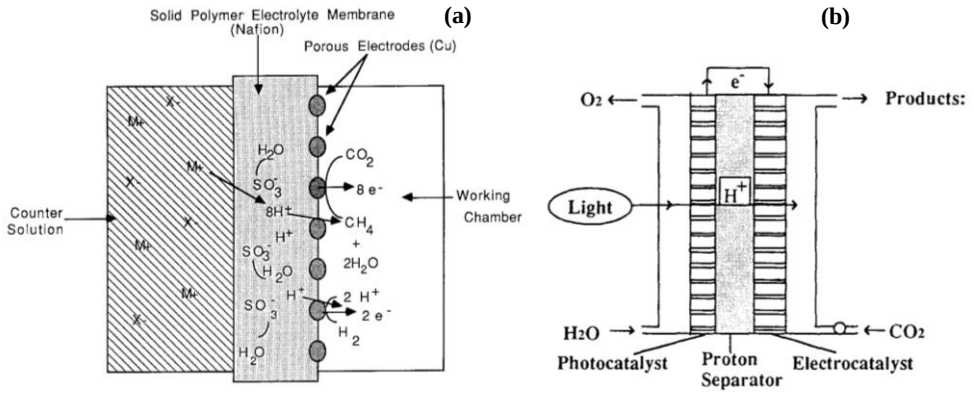

Scheme 2-1 a) Schematic diagram of a porous metal electrode supported on a solid electrolyte membrane for electrochemical reduction of CO_2 in gas phase (adopted from (*43*)). b) Schematic diagram of a photo-electrochemical cell (PEC) for reduction of CO_2 in gas phase (adopted from (*63*)).

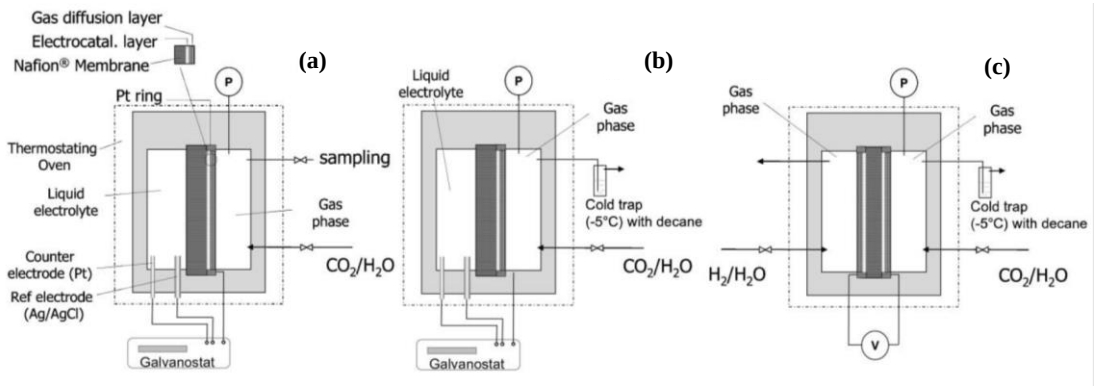

Scheme 2-2 Schematic diagram of variations of PEC design suggested by Centi et al. (*47*). In this scheme light harvesting element is not shown because the devices were used for electrochemical tests rather than photoelectrochemical tests. The major difference between these variations is related to flow pattern of feed and products. a) semi-half discontinuous cell in which reaction takes place in batch mode and purge is allowed in predefined time intervals for cathode side. There is no flow of liquid electrolyte on anode side, b) semi-half continuous cell in which products are allowed to be purged out of the device but liquid electrolyte on anode side does not flow. Product separation were performed by condensing products in outlet stream using a cold trap. c) fully continuous cell in which humidified H_2 were used instead of liquid electrolyte. A continues purge of gases exists for both anode and cathode side.

The main concept behind these designs was laid on already existing fuel cells. Using fuel cells architecture enables the designer or manufacturer to benefit from a great deal of knowledge that already exists in fuel cell industry. More specifically, extensive number of publications exist focusing on optimizing properties and manufacturing techniques of membrane electrode assemblies (MEAs) in fuel cells addressing issues such as water balance, proper catalyst/membrane contact, proton conductivity, gas diffusion layer, etc (*79-82*). Furthermore, fuel cell industry continuously grew after first application of a fully operational fuel cell in NASA's Gemini 5 space program in 1960s (*83*). Therefore, in PEC scale-up stage one may use already available infrastructures that were originally developed

for fuel cell industry, which consequently leads to considerable reduction of manufacturing costs and acceleration of PEC commercialization.

However, there is at least one major challenge with the current fuel-cell like design, related to integration of a semiconducting material, as a light harvesting component, to the electrochemical cell and realizing a fully integrated photoelectrochemical cell. In a fully integrated PEC, ideally, water is used as electron and proton donor through water splitting reaction (i.e. $2\ H_2O \rightarrow O_2(g) + 4\ H^+ + 4\ e^-$). Water splitting reaction should take place on the anode side of the PEC using a semiconducting material, such as TiO_2 or Si, to produce required electrons and protons for reduction of CO_2. Usually, these materials are grown on a mechanically strong and electrically conductive material to serve as mechanical support and current collector. Metal sheets perfectly suit this application and therefore are used extensively for this purpose. Therefore, metal sheets provide a path for conduction of generated electrons from anode side towards cathode side, as shown in Scheme 2-3a.

However, metal sheets are not transparent to light; therefore, metal sheet has to be placed after the semiconducting material and toward the cathode side, to avoid blockage of incoming light, as shown in Scheme 2-3b. At the same time, protons (i.e. H+ cations) generated through water splitting reaction should be transferred to the cathode side through a proton conducing material. If one uses architecture b in Scheme 2-3, then there would be no pathways for protons to move toward cathode side because a proper connection between semiconductor and proton exchange material does not exist, due to solid metal sheet blocking proton transport pathway. If a mesh of any type and shape is used instead of metal sheet and then semiconductor, semiconductor support, and proton conductor material are tightly pressed, then pathways of protons and electron transport would be similar within the semiconductor material, which causes significant reduction of semiconductor efficiency due to increased electron/hole recombination rate within the semiconductor. (Efficiency of semiconductors as light harvesting materials are defined by two major factors: light

absorption and electron/hole separation (*84*)). Furthermore, due to operation in gas phase, a media in which protons can move from point of generation to reach the proton conductive material does not exist, (in liquid phase operation generated proton may travel a specific distance through convection in electrolyte). This is another major resistance for proton transport from anode side to cathode side.

A third approach might be placing anode catalysts directly on top of proton conducting material and using a mesh type metal sheet, as shown in Scheme 2-3c. In this case, although the problem of proton transport would be minimized, still a good portion of incoming light would be blocked by semiconductor support. In addition, penetration of reactants (i.e. H_2O and CO_2) toward anode catalyst side would be drastically reduced unless a high porosity semiconducting material is used. In case of fuel cell or electrochemical CO_2 reduction, problems as such do not exist due to absence of the mentioned strict requirements for positioning of anode side electrode. Therefore, electrocatalysts can be placed directly on proton conducting material (usually though spraying) and then mesh-like current collectors can be placed on top of both anode and cathode catalysts to enable electron conduction between cathode and anode while having proper proton transport pathway in place (see Scheme 2-3d).

Therefore, lack of possibility of an arrangement of semiconductor and proton exchange material in a way to allow simultaneous efficient electron and proton conduction seems to be an intrinsic problem of the proposed architecture in literature and the major cause behind not seeing a fully integrated PEC for gas phase CO_2 reduction in the literature. One way around this problem is to rearrange components of the PEC using a different morphology of proton conductor material, as one of the key components of the PEC which limits achieving wider architecture alternatives. This is described in details in the following section.

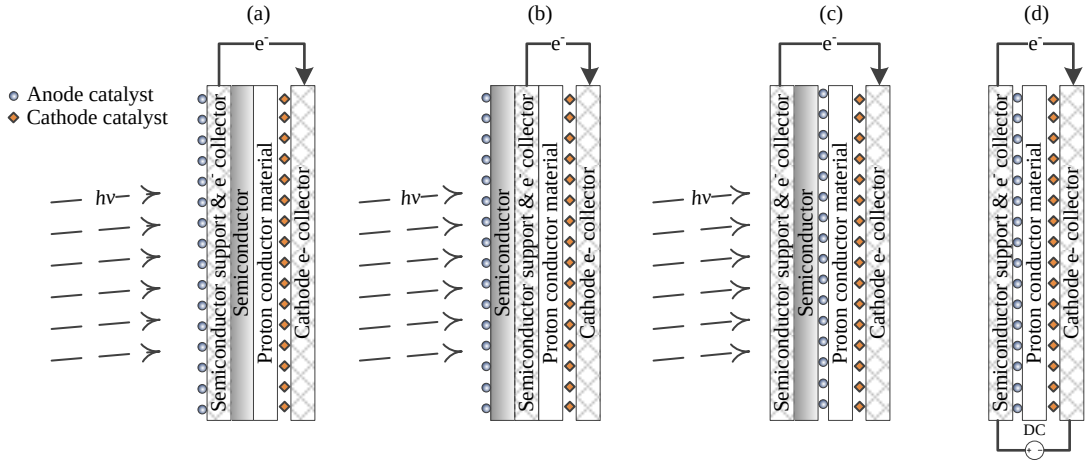

Scheme 2-3 Schematic diagram of possible arrangements of components of a fully integrated PEC imitating common architecture of fuel cells.

2.1.1 Architecture of the proposed PEC

In the previous architectures, the main idea was to use the same design principles that are widely used in fuel cell technology. However, this approach, as explained, has a major short sighting if it is used for designing a PEC. In fuel cell technology there is no requirement for light to reach the reaction sites on cathode or anode. Therefore, although the developed devices were practical enough to confirm that gas phase CO_2 reduction is principally possible using an electric current, but arrangements were inherently limited when a Nafion® sheet is used as the proton conductor. We hypothesis if one uses a porous and transparent Nafion® membrane, in form of fibers or ribbons, one can essentially change the architecture around. In this way, instead of sandwiching Nafion® membrane with catalysts and current collectors, one may coat the whole device using a properly synthesized Nafion® mat. This can be achieved in at least two ways.

One method is to use laser patterning. In this method laser patterning is used to produce porous Nafion® coating, and therefore enable reactants to reach reaction sites. In this process, the substrate, which may be catalysts coated semiconductor layer, cathode, and/or anode electrodes, is coated with a photosensitive resin which is then patterned with a laser, removing photosensitive resin from the desired areas of the substrate. Once the desired

pattern is developed on the photosensitive resin coated substrate, the substrate can be coated with Nafion®. Then, residuals of Nafion® on photosensitive resin can be washed away in a lift off process using isopropyl alcohol, acetone, H_2SO_4 and H_2O_2 leaving behind patterned Nafion® coating. Using this method, material incompatibility issues rises from using isopropyl alcohol and/or strong acids. Isopropyl alcohol dissolves Nafion® and strong acids etch the semiconductor as the substrate. In addition, the process is costly and slow, therefore not suitable in large scale. Therefore, this process in current form is not suitable for developing a Nafion® mat with the required morphology.

Another method is to coat Nafion® nanofibers around the device once all components are assembled. We propose here to use electrospinning for this purpose which is a facile, quick, and scalable technology. Benefiting from a Nafion® nanofiber mat, structure of the PEC can be redesigned as shown in Scheme 2-4.

The schematic diagram of the proposed PEC cell with back-to-back or wireless architecture (no wiring required) is shown in Scheme 2-4a. This PEC has two compartments, the photoanode side (left-side of the cell) and the cathode side (right-side of the cell). The sequence of PEC components from left to right are Nafion® nanofiber mat (annotated by ① in Scheme 2-4a), photoanode catalyst (annotated by ⑥ in Scheme 2-4a), semiconductor layer (annotated by ① in Scheme 2-4a), anode support and current collector (annotated by ② in Scheme 2-4a), cathode support and current collector (annotated by ③ in Scheme 2-4a), cathode catalyst (annotated by ④ in Scheme 2-4a), and Nafion® nanofiber mat (annotated by ① in Scheme 2-4a). Here photoanode support and cathode support also perform as anodic and cathodic current collectors. On the top of photoanode support, various types of catalysts materials may be loaded. These configurations are further explained in Section 2.3.1. The catalysts (④ and ⑥ in Scheme 2-4a) may be loaded on the anode and cathode surface (① and ③ in Scheme 2-4) by spin coating or drop casting before coating the PEC with Nafion® nanofiber mat.

The side-by-side architecture is schematically shown in Scheme 2-4b. This is the wired architecture because some sort of conductive wiring should be in place to transfer electrons from anode side to cathode side (conductive copper tape was used in this thesis). Side-by-side architecture is superior to back-to-back architecture due to three main reasons: shorter proton conducting pathway, easier assembly, and higher control on catalysts selection. Firstly, the proton conducting pathway length is shorter in side-by-side architecture. This is beneficial because proton conduction through Nafion® polymer is orders of magnitude slower than electron conduction in metals (Nafion® proton conductivity is in range of 0.01–0.5 S/cm (*85*) and copper electron conductivity is 5.96 x 10^5 S/cm (*86*)). Theoretically, proton conducting pathway can be easily made as small as microns by making ribbons of photoanode and cathode and placing them side-by-side. In this way, effective proton resistances as small as 20 μΩ is achievable, comparing to a minimum of 20 mΩ for back-to-back configuration (in back-to-back configuration the highest achievable proton conductivity is limited by thickness of anode catalyst/semiconductor/anode support/cathode support/cathode catalyst assembly). Secondly, knitting Nafion® fibers around the PEC, as in back-to-back architecture, requires development of special electrospinning units to rotate the PEC around cross-plane direction while currently available electrospinning units are perfectly suitable for knitting Nafion® fibers simultaneously on multiple PECs when side-by-side architecture is assembled. Lastly, in side-by-side architecture, multiple types of catalysts for both anode and cathode side can be developed, synthesized, and assembled because catalysts can be integrated to the PEC in later stages, while in back-to-back architecture connection of cathode support to anode support is difficult to achieve for some types of catalyst including Cu_2O/CuO hybrid nanorods.

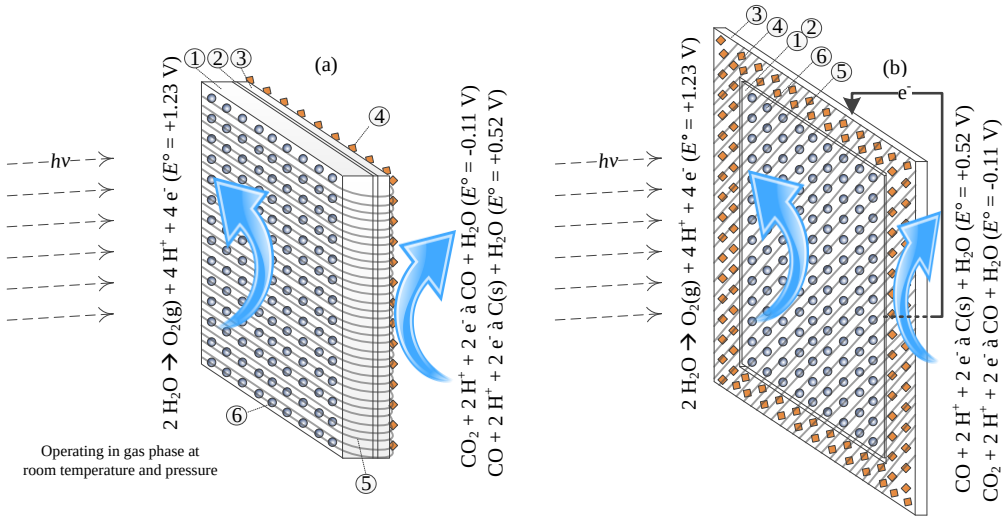

Scheme 2-4 Schematic diagram of the proposed PEC in a) back-to-back (wireless) configuration and b) side-by-side configuration; ① is photoanode, ② is photoanode support and current collector, ③ is cathode support and current collector, ④ is cathode catalysts, ⑤ is Nafion® nanofibers proton conductor, and ⑥ is anode catalyst.

Due to the above mentioned reasons in this thesis we explored side-by-side architecture. In the next subsections of section 2.1 we explore role of different components of the proposed PEC and discuss material selection issues for each specific component.

2.1.2 Light harvesting component

Light harvesting component is the component at which convert photons energy in light to electrical potential occurs. This is the component which acts like a pump to provide required driving force for flow of electrons from anode side to cathode side. Therefore, it plays a critical role and performance of this component has direct impact on performance of the PEC device. In electrochemical devices, power sources providing direct current (DC) are used instead of this component. In general, single semiconducting materials or combination of various semiconducting materials with proper band gaps are required for this purpose. This semiconductor might be a single chemical, such as Cu_2O, or a hybrid of multiple layers of doped elements, such as multi junction amorphous silicon, or a hybrid of multiple layers of different chemicals, such as inverted metamorphic concentrator deceives, or a hybrid of organic-inorganic material, such as perovskite solar cell. Many semiconductor materials

were tested for CO_2 reduction through photocatalytic root (see Table 1-1) however the majority of them are made of rare materials (i.e. $BaLa_4Ti_4O_{15}$ (*87*) or GaP (*88*)) or material which have low visible light conversion (i.e. TiO_2). In this thesis, we aim to assemble a PEC which uses only earth abundant materials. To that end, Si is an attractive light harvesting material and semiconductor due to its extreme abundance on earth and well-developed industrial processing technologies. If assembled in multi-junction architecture (*p*-doped/inert/*n*-doped a-Si), it is able to provide high enough open circuit voltages (V_{OC} > 2 V) due to formation of an electric field at the interface of the junctions with different Fermi levels. This electric field makes a barrier for electrons to move toward the wrong direction (*89*). This is high enough potential to derive simultaneous H_2O splitting and CO_2 reduction reaction. Its application in stand-alone H_2O splitting PEC, in form of 3 junction a-Si photovoltaic (PV), is also already been demonstrated (*90-92*) by Reece et al. and proved to be able to break down water to produce H^+ required for CO_2 reduction with relatively high efficiency. 3-junction a-Si PV is able to provide open circuit voltage of ~ 2.3 volts although not at the highest possible light to electricity efficiency of ~ 7% (*90*). We used the a-Si PV which is commercially manufactured by Xunlight Co. The a-Si is coated on the stainless steel support to give the PV enough mechanical strength (annotated by ② in Scheme 2-4). The stainless steel sheet also performs as current collector.

Internal structure of 3-Jn a-Si PV is shown in Scheme 2-5. The *pin* architecture is particularly the reason behind ability of the PV to provide such high V_{OC}. The inherent electrical field may be further enhanced if a *p*-type semiconductor is used as cathode catalyst and kept in electronic contact with the stainless steel support. Another way to increase generated V_{OC} is to use an *n*-type semiconductor as anode catalyst which is coated on transparent ITO layer.

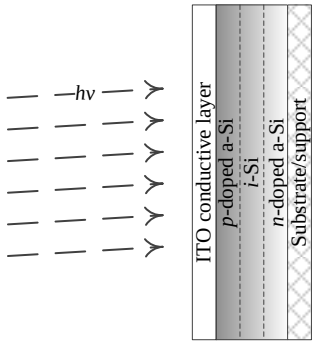

Scheme 2-5 Internal architecture of 3-jn a-Si PV manufactured by Xunlight Co. and used in this thesis as the light harvesting component of the proposed and developed PECs.

2.1.3 Cathode catalyst component

The cathode side has two sections: cathode support and catalysts particles. Cathode support acts as electron distributor, support for catalysts, and may be a catalyst by itself. Three different catalyst morphologies have been considered for the cathode side here: sheets, nanoparticles, and nanorods. For all of them a 0.5 mm thick copper sheet is considered as support because it provides enough mechanical strength. In cases were nanoparticles are used as cathode catalyst, Cu cathode support also plays catalytic role due to partial exposer to CO_2 environment.

2.1.3.1 Experimental studies

Transition metals and metal oxides were subject of many studies as catalysts for CO_2 reduction (*93*). List of catalysts used for this purpose is extensive. Among all the catalysts, Cu seems to be the most widely studied heterogeneous catalyst for conversion of CO_2 (*94*). Cu was also used in combination with many other materials including Ni (*95*) and Zn (*96*) and it was found that Cu rich catalysts on alumina support were most active for CO_2 conversion in thermochemical processes (*96*). Cu was also used in many electrochemical CO_2 reduction studies and is being known as one of the best catalysts for this application with high selectivity and low overpotential (*42, 63, 97-99*). In addition, metallic Cu sheet is abundant and relatively cheap. Furthermore, formation of solid carbon from CO_2 is already reported in the literature on Cu foil (*100-104*). Cu is being widely used for graphene and

carbon nanotube synthesis using precursors other than CO_2 though thermochemical pathways (*105-109*). Therefore, we chose metallic Cu as one of the main cathode catalysts to test. Based on the same selection methodology, we selected metallic Ni and Fe as well because these earth abundant transition metals were also reported to have high electrochemical CO_2 reduction activity (*38, 93, 110-114*).

Apart from metallic catalysts, we also searched for earth abundant, easily synthesizable semiconductor materials to use as cathode catalyst in our PECs. For electrochemical CO_2 reduction root, Cu_2O/CuO hybrid nanorods seemed to be especially active offering good selectivity and low overpotential toward CO_2 reduction (*115-117*). In addition, it provides very high surface area due to nanorod morphology. Furthermore, Cu_2O/CuO hybrid nanorods is a *p*-type semiconductor with band gaps of ~ 2 eV (i.e. 2.0–2.2 eV for Cu_2O and 1.3–1.6 eV for CuO (*116*)). This band gap is suitable for activation of CO_2 molecule to undergo reduction reactions (conversion of CO_2 to $^{\bullet}CO_2^-$ takes place at -1.9 V vs. NHE (*118*). This is known to be the highest energy state of CO_2 molecule during several steps of reduction reactions. (*119*)). As shown in Scheme 2-6, Cu_2O/CuO hybrid is the only earth abundant semiconductor with proper band gap size and band gap position for conversion of CO_2 to solid carbon and most of other hydrocarbons including CHCOOH, CH_3OH, etc. (the criteria for proper band position is that band edges must encapsulate the dashed area in Scheme 2-6). In addition, as explained in section 2.1.2, incorporating a p-type semiconductor on cathode side and illuminating cathode side as well as anode side may further enhance inherent electric field of a-Si PV and therefore increase available electrical potential for driving CO_2 reduction reaction. Therefore, we selected Cu_2O/CuO nanorod as a semiconductor cathode catalyst to be tested in our PECs.

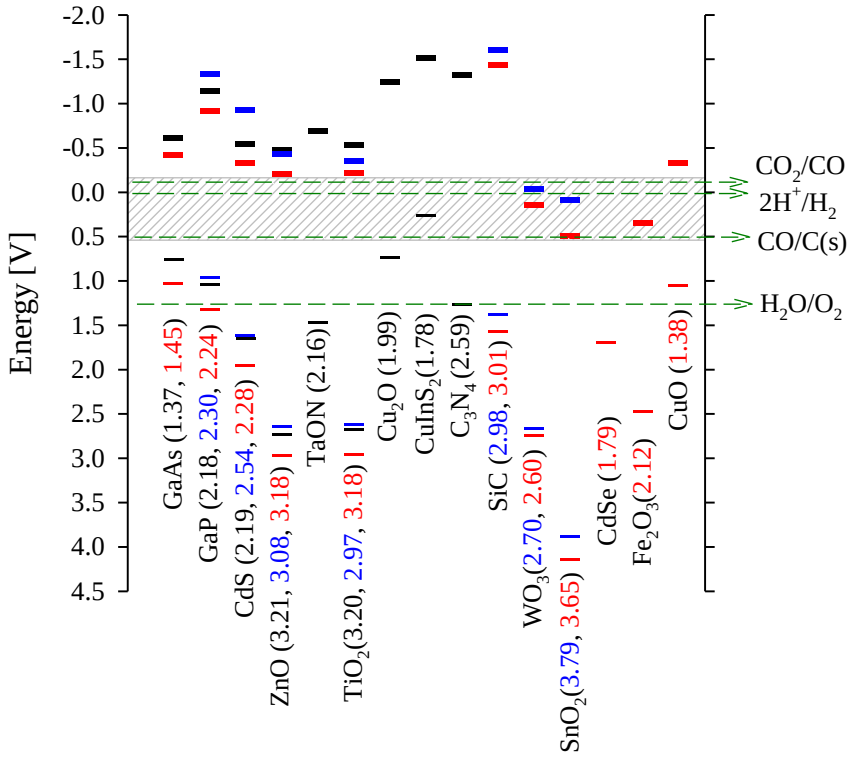

Scheme 2-6 Band gap and band edge location of potential semiconductors useable for CO_2 reduction in PECs. Thin dashes are upper edge of valence bands and thick dashes are lower edge of conduction bands. On the right side redox couples relevant to conversion of CO_2 to solid carbon, which is the aim of this thesis, are presented against *she* (PH = 7). Different colors correspond to different PH levels. Band edge and band gap data at PH = 7 (black dashes) were extracted from ref. (*120*), at PH = 5 (blue dashes) were extracted from ref. (*121*), at PH = 1 (red dashes) were extracted from ref. (*76*). For CuO band gap data at vacuum condition were extracted from ref. (*76*) and band gap data at PH = 1 were calculated. Band gaps are stated in parenthesis in eV. Colors correspond to PH values. Gray dashed area shows the required band gap position for conversion of CO_2 to solid carbon and most other hydrocarbons.

2.1.3.2 Molecular simulation studies

In addition to reviewing published experimental works, a preliminary molecular modeling study was carried out to gain a deeper understanding of interactions between different possible catalysts and CO_2 in vacuum condition. For this purpose, Chem3D Pro software package was used. The materials that were tried for this analysis were molecular Cu, Fe, Ni, Pt, Cu_2O, Fe_2O_3, NiO, crystalline CNT, and crystalline Cu. The equilibrium geometric distance between a CO_2 molecule and any of the above molecules or crystals was calculated through minimization of Steric energy using molecular mechanics (MM2) force field calculations and used as a reflection of interaction strength between CO_2 and the

possible catalyst. MM2 was developed in 1977 by N. L. Allinger (*122*) for conformational analysis of hydrocarbons as well as small organic molecules. It is designed to reproduce the equilibrium covalent geometry of molecules and reported to be an accurate method for estimation of properties of hydrocarbons (*122*). This method is simpler and computationally less expensive than quantum mechanics methods especially where bond breaking and formation is not of interest (*123*) (molecular mechanics techniques cannot be used for bond formation and breaking because MM uses atomic nucleus properties instead of electronic properties (*124*)). The results of calculations are presented in Figure 2-1 and Image 2-1 below.

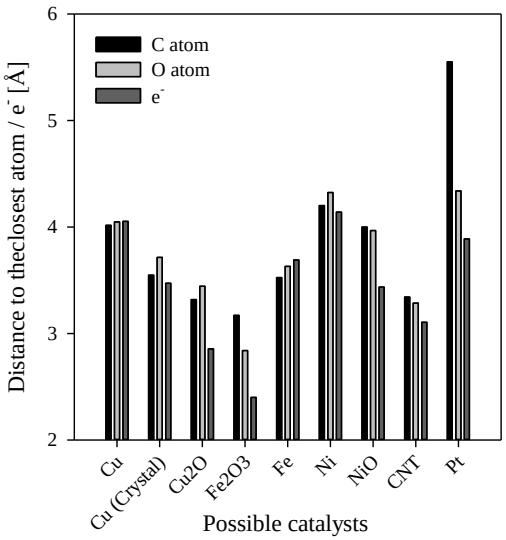

Figure 2-1 The closest equilibrium distance between any of CO_2 molecule components (electrons or atoms) with potential catalyst molecule component (electrons or atoms). The closer the equilibrium distance, the higher the tendency of the potential catalyst to adsorb CO_2 molecule and weaken its bonds.

Figure 2-1 shows the closest equilibrium distance between atoms of the potential catalysts and each of C, O, and e^- of a CO_2 molecule. The closer the equilibrium distance, the higher the tendency of the potential catalyst to adsorb CO_2 molecule and weaken its bonds (adsorption of a molecule on a catalyst is the first step of catalyzing process (*125*)). It was observed that oxide form of the tested transition metals (i.e. Cu, Fe, Ni) have higher tendency to adsorb CO_2 in comparison to metallic form. In addition, oxide form caused more

significant effect on CO_2 bond angles. This was observed in 3D models but can also be inferred from the difference between distances of CO_2 components from the potential catalysts in Figure 2-1. Among the studied potential catalyst CNT, Fe_2O_3, and Cu_2O stand out. For these three potential catalysts, molecular driving force was strong enough to cause higher Occupied Molecular Orbitals (HOMO) to amalgamate, as shown in Image 2-1. In addition, electron densities in HOMO of CO_2 was significantly changed, causing distinguishable positive and negative charge separation and accumulation on CO_2 molecule, shown with red and blue colors in Image 2-1. The strongest charge separation was observed for Cu_2O. These results further affirmed the selected catalysts in section 2.1.3.1 are appropriate catalysts for CO_2 reduction to be tested in our PECs.

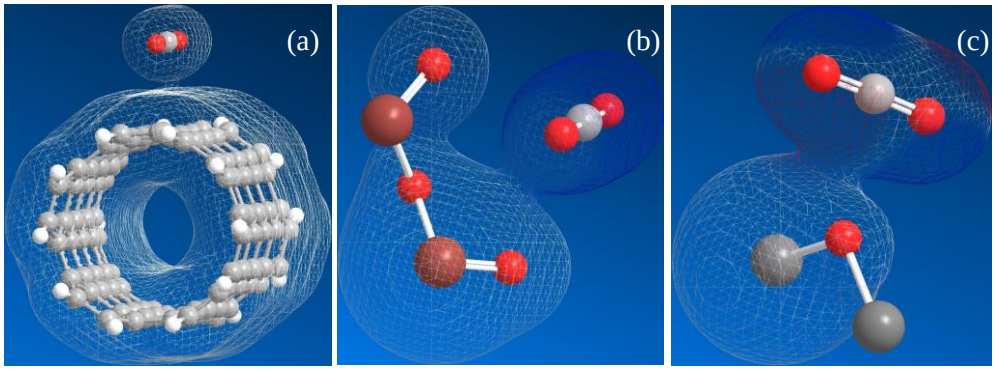

Image 2-1 Instances of HOMO amalgamation as obsereved for a) crystaline CNT, b) Fe_2O_3, and c) Cu_2O. Steric energy was minized through MM2 force field calculations using Chem3D Pro software to calculate equilibrium distance between CO_2 and either of the three molecules .

2.1.4 Anode catalyst component

Likewise other components of the PEC, we searched for earth-abundant materials to use as catalyst on the anode side of the PECs. Anode catalyst is used to decrease energy barrier for water splitting reaction to produce required electrons and protons for CO_2 reduction reaction. Among three earth abundant metals, Ni, Fe, and Co, Co is the oldest and most widely studies element for synthesizing water oxidation reaction catalyst (*126*). In addition, very high oxygen evolution turnover numbers (TON's) were reported for Co-based ligand catalysts (TON ~ 1000) (*127*). Reece et al. successfully synthesized a Co_2^+ self-assembly catalyst for high efficiency water splitting in a standalone PEC (*90*). This cobalt-based water

oxidation catalyst (Co-WOC) is a functional model of the oxygen-evolving complex of Photosystem II. Co-WOC shows some interesting properties including but not limited to: (1) a film can be produced using Co-WOC in situ under mild conditions, pH 7.0 and room temperature; (2) a variety of cobalt precursors can be used for Co-WOC synthesis; (3) the Co-WOC exhibits high activity in pH 7.0 water; (4) the catalyst film is ‘‘self-healing’’ in aqueous solution; (5) and most importantly, for the purpose of this thesis, the catalyst is highly stable in the atmosphere (*128-132*). Among all forms of CO-based catalyst Co_3O_4 NPs are of particular interest here because it is relatively cheap, earth-abundant, and efficient water splitting photo (*133, 134*) and electro catalyst (*135, 136*). Furthermore, it can be produced through facile methods (*137*), while more complex synthesis methods are required for ligand based catalysts. In addition, Co_3O_4 is a semiconductor with band gaps of ~ 1.52 and 2.01 eV, depending on photon absorption mechanism (*138, 139*). Thus, using Co_3O_4 NPs on illuminated side of the proposed PEC may facilitate water splitting reaction, when the PEC is under illumination. Therefore, Co_3O_4 NPs are selected as the water oxidation catalyst to be used on the illuminated surface of the proposed PEC.

2.1.5 Solid proton conductor component

Despite catalysts and light harvesting components, options for commercially available proton conductive materials are limited. There are two major types of proton conductive materials available: polymers (*140, 141*) and ceramics (*142, 143*). Ceramic based proton conductive materials are not of interest in this thesis due to lack of control on morphology during synthesis and requirement for high temperatures for synthesis. Polymer based proton conductive materials may be classified to Perfluorinated Sulfonic Acid (PFSA) membranes, Irradiation Grafted membranes, Sulfonated thermostable polymers, polymers obtained by acid complexation, and Hydrocarbon based block copolymers (*144*). Nafion® is a commercially available PFSA based membrane with the molecular structure shown in Scheme 2-7. Nafion® is a form of sulfonated Teflon®, a Polytetrafluoroethylene or PTFE

polymer, developed by DuPont Co. Nafion® has shown a very promising proton conductivity at ~ 0.1 S/cm. However, it has some drawbacks including high cost of perfluorinated ionomer membranes, low swelling and loss of mechanical properties at > 100 °C, loss of ohmic connection due to frequent change in operation temperatures and material throughput, and relative high diffusion of liquids (*144*). These drawbacks are mole relevant to fuel cell applications. In addition, Nafion® is transparent to visible range of electromagnetic waves. Light transparency is a key required property of the proton conductive material in the PEC architecture suggested in this thesis (see Scheme 2-4). Furthermore, Nafion® can be made highly porous through nanofiber fabrication. Nafion® nanofibers have shown very good performance in terms of proton conductivity in gas phase. According to Choi et al. (*145*) proton conductivity of Nafion® nanofibers is a function of relative humidity in the gas phase. Higher the relative humidity (or water activity in vapour phase), higher the proton conductivity (proton conductivity of Nafion® is in range of 0.01 S/cm at RH = 50% and ~ 0.1 S/cm at RH = 100%). Therefore, proton conductivity between anode side and cathode side can be made using Nafion® nanofibers (annotated by ⑤ in Scheme 2-4).

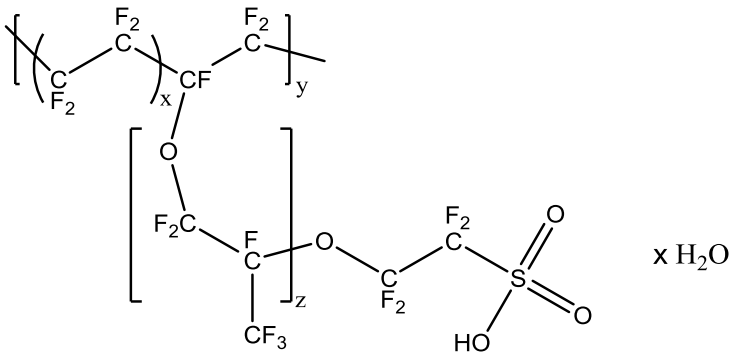

Scheme 2-7 Molecular structure of Nafion®.

Nafion® nanofibers can be produced form Nafion® solution through electrospinning technique. Nafion® is inherently difficult to electrospin due to its very low chain entanglement. Therefore, pure Nafion® can be electrosprayed rather than electrospun. But its properties can be modified for electrospinning if proper amount of a carrier polymer is added

to Nafion®. First trials of Nafion® electrospinning using Poly(acrylic acid) (PAA) succeeded in 2008 but more than 25% of carrier polymer were added to Nafion® solution (*146*). This high amount of carrier polymer can affect the superior proton conductivity properties of Nafion®. Therefore, it is extremely important to keep the concentration of the third polymer as low as possible. In 2010 Dong et al., for the first time, succeeded to produce Nafion® nanofibers with 99.5% purity using high molecular weight poly(ethylene oxide) (PEO) in methanol solution (*147*). At the same time other researchers also succeeded to produce high purity Nafion® nanofibers by mixing very small amount of lower molecular weight PEO in different solvent systems (*85, 148*). As mentioned, for our application Nafion® mat should have three distinguished characteristics: high proton conductivity, high light transparency, and high porosity. Therefore, We modified electrospinning method originally developed by Ballengee et al. (*85, 148*) for nanofiber production to synthesis nanoribbon morphology, which offers higher transparency, lower individual fiber thickness, and higher contact area between individual fibers. The modification details and resulted Nafion® nanoribbon mat are discussed in section 2.3.4.

2.2 Design of experiment rig and experiment procedure

The experimental setup to test the PECs is shown in Scheme 2-8. Photoelectrochemical tests were carried out in this specially designed reactor. Prior to each test, the reactor was purged for 30 min at 1 L/min with Ar gas. Before each test, PECs were left in dark for at least 10 min and kept under continues purge of intended gas (CO_2 at different concentrations, Ar was used as balance) for 10 min. Sequence of tests were dry Ar (grade 4.0, BOC), humidified Ar (RH = 98%), dry CO_2 (food grade, BOC), humidified CO_2 (RH = 98%). Gases were humidified by bubbling through a specially designed bubbler which was filled with Milli-Q ultrapure water at room temperature (c.a. 23 °C). Humidity and temperature of the reactor atmosphere were continuously monitored using a digital hygrometer and thermometer. All electrochemical and photoelectrochemical experiments were performed

using an eDAQ ER466 Potentiostat System integrated with solar simulator (16S-300, Solar Light Co) as light source. The light source was a solar simulator (AM 1.5 G) providing incident intensity of 100 mW/cm^2 as measured by a Pyranometer (Solar Light Co, PMA2144).

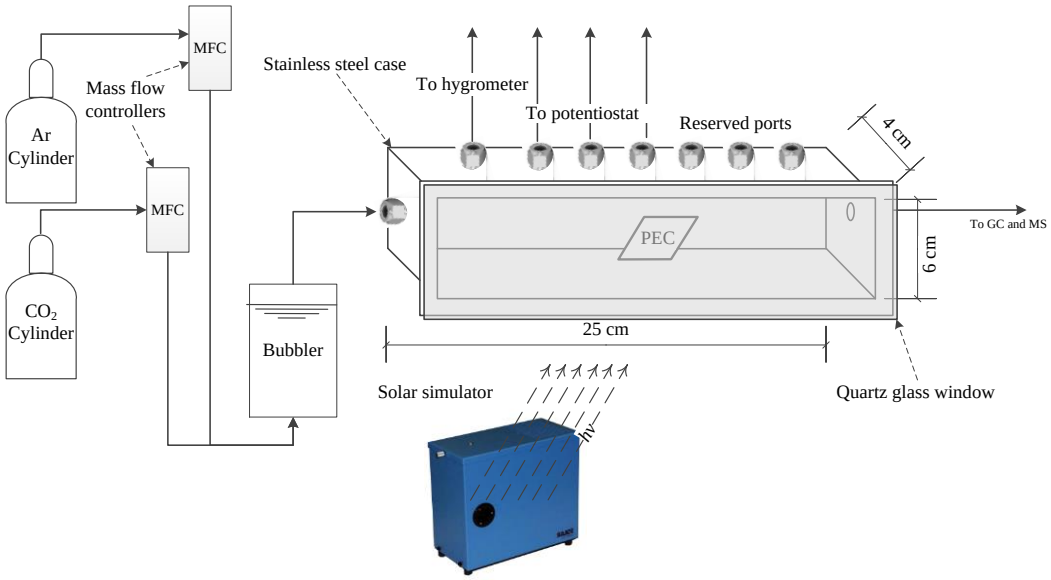

Scheme 2-8 Experimental apparatuses made for gas phase testing of the PECs. Gases input flowrates and composition were controlled using Alicat mass flow meters. Bubbler was filled with Milli-Q ultrapure water. Gas cylinders are used to manipulate reactor atmosphere.

2.3 Material synthesis and characterization

In this section material synthesis procedure and characterization for each component of the PEC are discussed in detail.

2.3.1 Preparation of the light harvesting component

The first step in assembly of the PEC is to prepare the light harvesting component. To that end, 3-junction a-Si photovoltaic cells were purchased from Xunlight Corp (Toledo, OH). PVs were cut to size using scissors (2 x 3 cm). Edges were etched in 1.0 M HCl (made from UNIVAR 36 wt%, reagent grade) for 30 seconds to remove ITO conductive layer, then rinsed with excessive DI water and left to dry under continues flow of instrument air (see Image 2-2).

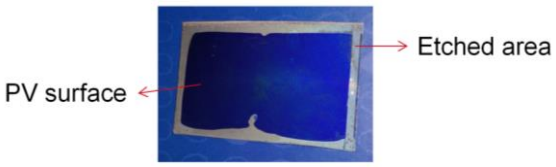

Image 2-2 Digital photograph of cut and chemically etched PV.

Performance of each PV was tested prior to use as follows. Two thin strips of Cu tape (1 x 30 mm) were attached on ITO conductive layer on the middle of surface of the PV as anode current collector and on stainless steel support at cathode current collector. Then the PVs were illuminate using 1 sun intensity (AM 1.5) and generated photocurrent was measure while the PVs was under variable potential (using potentiostat) between cathode and anode (from 0 to 2.5 V, scan rate of 0.1 V/s) to obtain current-potential characteristic curve (i.e. I-V curve) for each single PV. PVs with open circuit voltage over 2.0 V and fill factors over 25% were used in PEC assembly. PVs were numbered for identification purpose (e.g. PV121). PEC made from each PV was numbered in the same manner (e.g. PEC121 is made from PV121). Edges of the selected PVs were coated using UV paste (LOCTITE 3106) to avoid possible short circuit when coated with Nafion® nanoribbons. A set of indicative results of performance of the prepared PVs, hereafter referred to as photoanodes, are shown in Figure 2-2.

As shown in Figure 2-2, although the preparation method is the same for all PVs, there was a great variation in performance of the prepared photoanode. Two factors were observed to significantly affect the quality of the prepared photoanode: cutting method and etching time. If cutting is done with dull scissors, microfractures or micro cracks may develop through the PV internal structure. As the result the connection between different parts of the PV is lost or significantly affected which leads to low electron and hole conduction through Si (*149*). This results in formation of inactive cell parts (*150*). This may further lead to recombination of greater portion of generated electron/hole pairs, which can be observed as loss in generated photocurrent. Furthermore, microfractures can cause hot spots which

occurs when the internal resistance of the damaged cell rises, causing an increase in cell temperature and further damage (*150*).

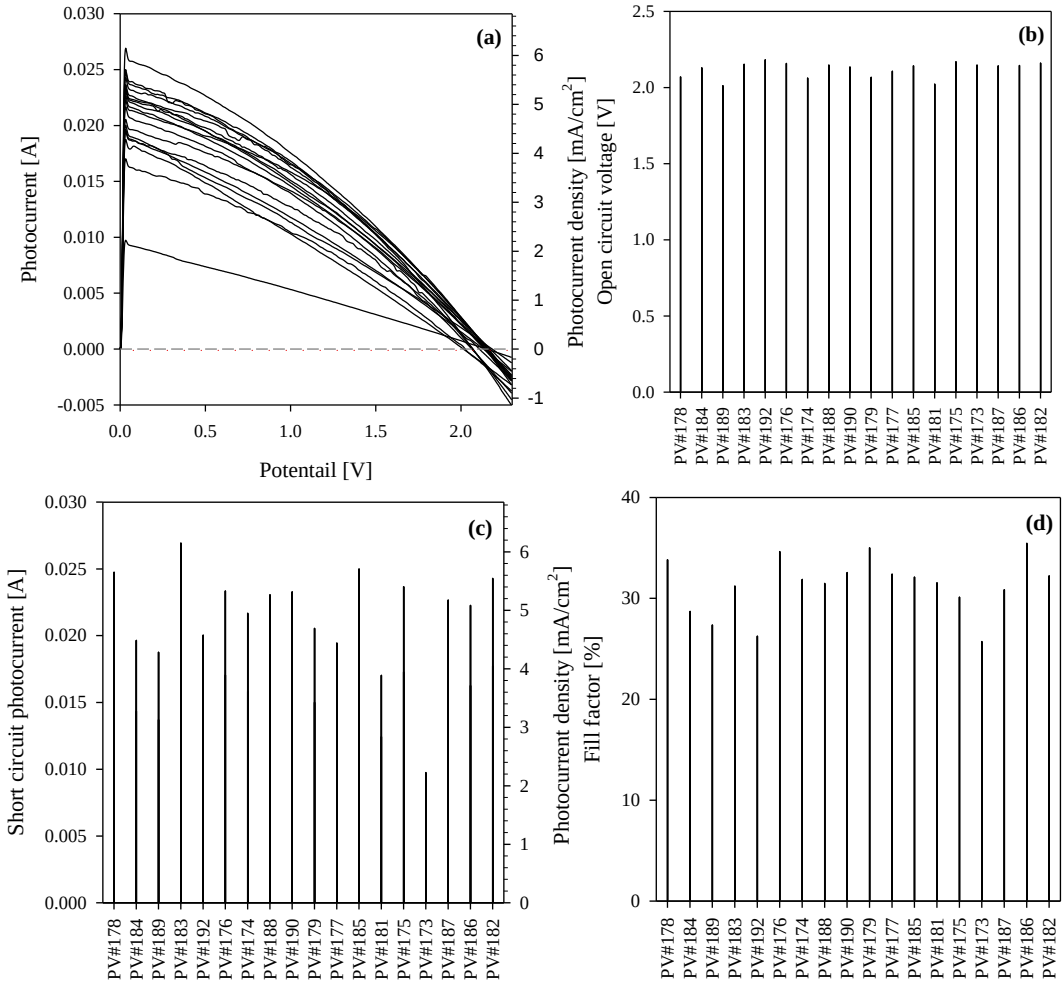

Figure 2-2 Characteristics and performance of a batch of prepared photoanodes from a-Si PV. a) I-V curve. The gray dashed line corresponds to I = 0 A. The intersection between this line and the I-V curve shows the open circuit voltage (V_{OC}). Maximum detected current, which typically happens at lowest applied potential bias, corresponds to short circuit current (I_{SC}); b) V_{OC}; c) I_{SC}; d) fill factor (*f*) which is calculated as $f = \frac{I_{max\ power} \times V_{max\ power}}{I_{SC} \times V_{OC}}$. Fill factor, the ratio of maximum power provided by the PV and theoretical power, is widely considered as an index of PVs quality.

Etching quality on the other hand has a different effect. When scissors is used for cutting, edges of stainless steel support bend toward the ITO layer of the PV, making ohmic contact with ITO layer. Etching is used to remove the ITO layer at edges and therefore remove the ohmic contact. If etching is not done properly, some portions of ohmic contact may remain on edges, which lead to electron/hole recombination due to short circuiting at the edges. This leads to significant loss in produced V_{OC}. The performance results presented

in Figure 2-2b shows a uniform V_{OC} is achievable using the mentioned preparation method. However, we struggled to achieve very high fill factors and I_{SC}. Although high fill factor is required for an efficient PEC for any application, V_{OC} is the parameter which determines if a specific set of reactions occurs. Therefore, as shown in next chapters, such challenges in photoanode preparation do not impose a significant risk to conducted proof-of-concept tests as long as $V_{OC} > 2$ V, which is achievable with the used preparation method.

It is noteworthy that the mentioned preparation problems exist because dimension of as received PVs were different than what we required. These problems do not exist if one changes the tools which are used for preparation of photoanode. However, a-Si found to be very delicate and special care should be taken to avoid damaging the prepared photoanode during PEC assembly and testing steps. The prepared photoanodes were very sensitive to pressure, thus, one should avoid applying pressure during assembly process. One may change the PV type to a more flexible type to avoid these handling and technical yet important challenges.

2.3.2 Cathode catalyst synthesis and characterization

For Cu sheet as cathode catalyst, we used 0.5 mm thick Cu sheet (99.9% purity, Goodfellow). Cu sheets were cut to size and then washed using 1 M HCl in bath sonicator for 30 s and subsequently with Isopropanol, Ethanol, Acetone, and DI in bath sonicator for 5 min each. Next, it was dried under N_2. Dry and chemically cleaned Cu was used as cathode catalyst.

Cu_2O/CuO hybrid nanorods were grown on copper sheet through a procedure adopted from Ghadinkhani et al. (*116, 117*) with some modifications. Cu sheet (99.9% purity, Goodfellow) was washed using 1 M HCl in bath sonicator for 30 s and subsequently with Isopropanol, Ethanol, Acetone, and DI in bath sonicator for 5 min each. Then dried under N_2 and left in the furnace under following air at 500 ml/min. Furnace temperature was then

increased to 400 °C at 10 °C/min and then kept constant for 2, 4, and 6 h for different synthesis trials. Oxide layer that was formed on surface of Cu substrate was characterized using X-ray powder diffraction (XRD) and scanning electron microscopy (SEM), as shown in Figure 2-3 and Image 2-3, respectively. According to XRD patterns the 6 h oxidation fits the Cu_2O/CuO XRD patterns best. As observed under SEM in Image 2-3, Cu_2O/CuO nanorods morphology was successfully achieved only for 6 h oxidation sample.

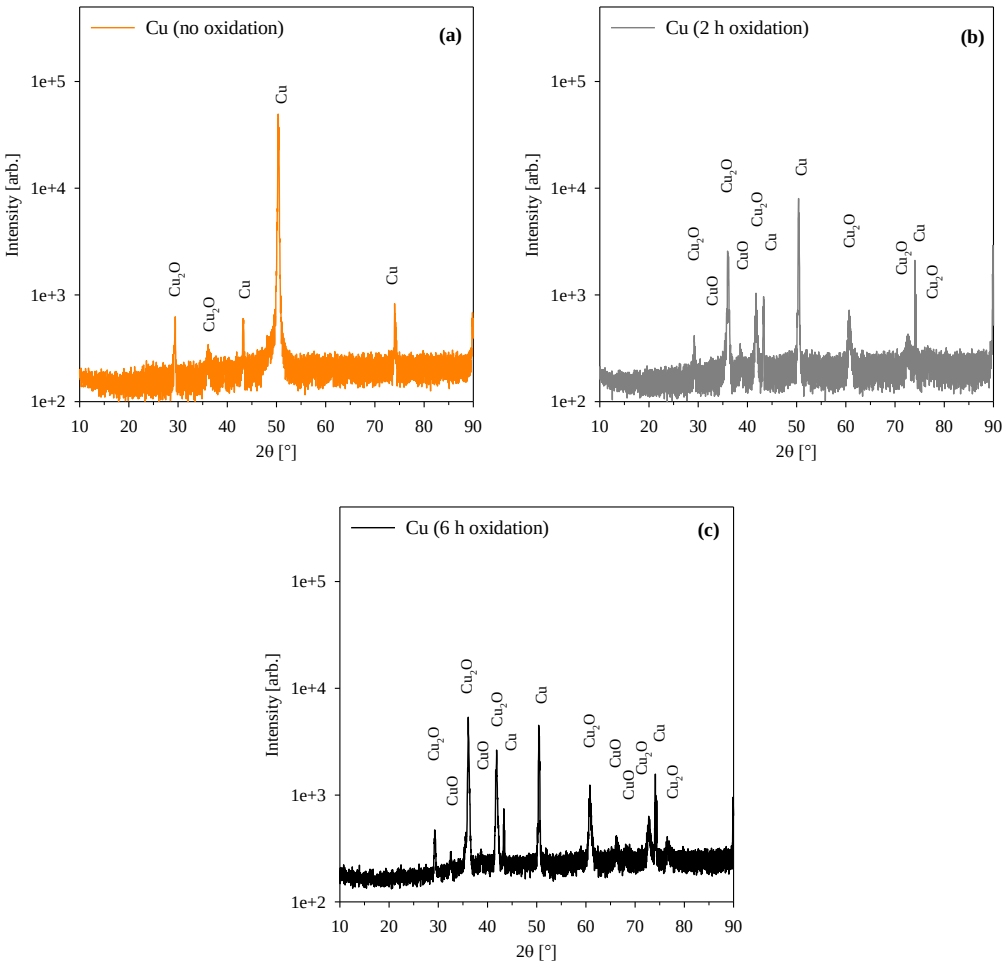

Figure 2-3 XRD pattern of oxidized copper sheet in furnace under air at 400 °C. XRD characterization peaks were extracted from (*116*).

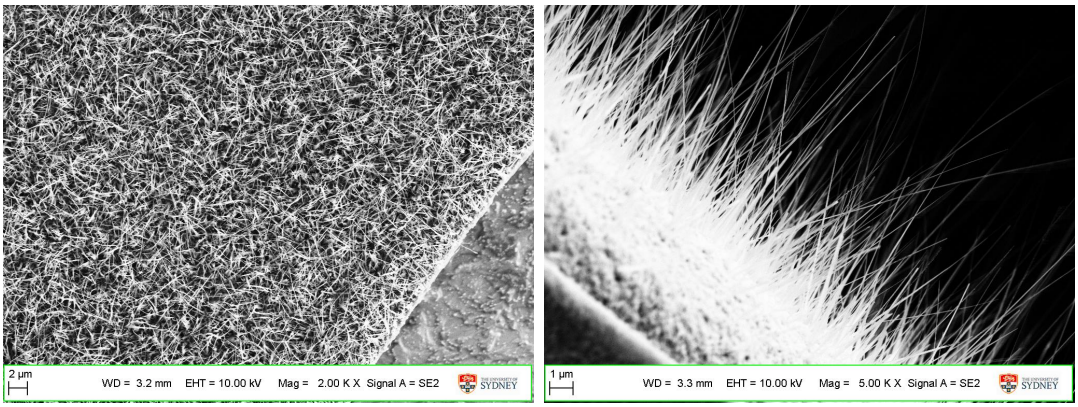

Image 2-3 SEM micrograph of Cu_2O/CuO hybrid nanorods grown on Cu sheet through oxidation at 400 °C for 6 h under continues flow of instrument air. left) top view; right) side view.

For 4 h oxidation sample partial formation of nanorods was observed under SEM when the oxidation was carried out in a tubular furnace, as shown in Image 2-4. For 2 h reaction time no nanorod were observed under SEM as show in Image 2-5.

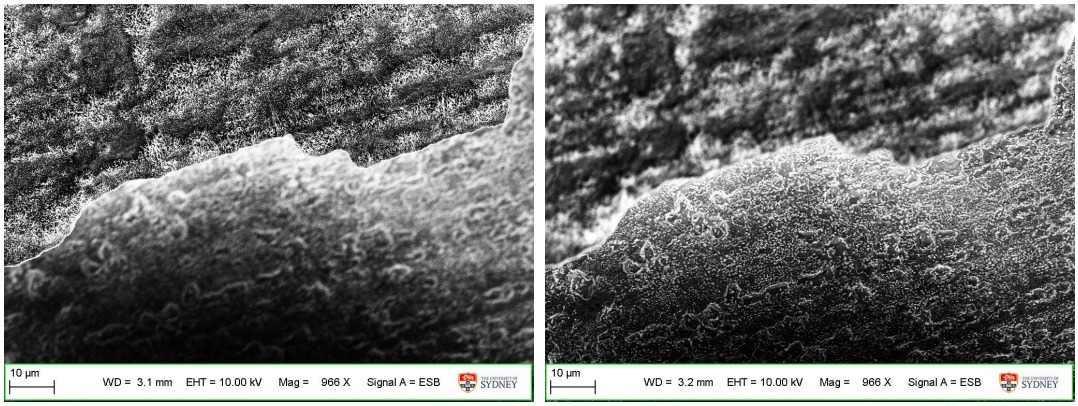

Image 2-4 SEM micrograph of Cu_2O/CuO hybrid nanorods grown on Cu sheet through oxidation at 400 °C for 4 h showing partial growth of nanorods. left) focused on top layer at 3.1 mm working distance showing partail formation of nanorods; right) focused on bottom layer at 3.2 mm working distance showing nanorods were not formed.

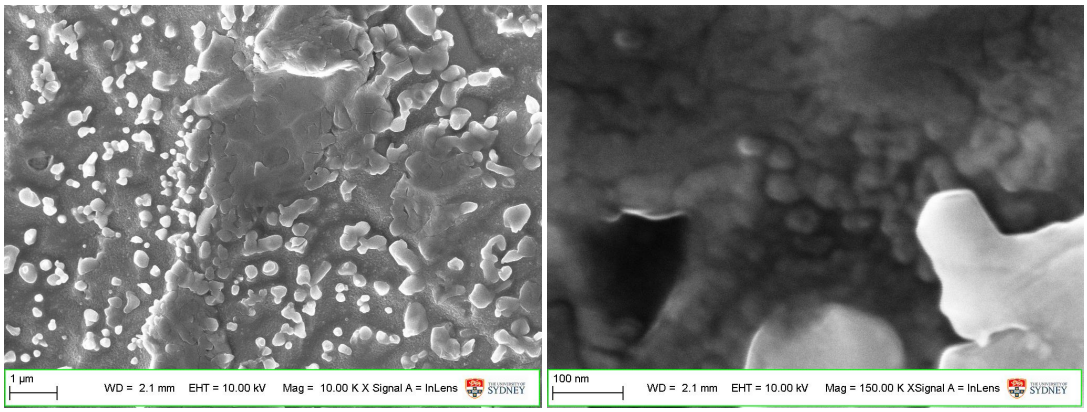

Image 2-5 SEM micrograph of Cu_2O/CuO hybrid nanorods grown on Cu sheet through oxidation at 400 °C for 2 h showing no growth of nanorods. left) image at 10,000 magnification; right) a close-up at 150,000 magnification. The bumpy morphology may be the base of future nanorods.

Cu, Fe, and Ni nanoparticles were also tested as cathode catalyst. These particles were purchased from Sigma Aldrich Co. and used after dispersion in DI water using bath sonication for 30 minutes. No further characterization was performed for these nanoparticles.

2.3.3 Anode catalyst synthesis and characterization

A simple two-step hydrothermal method is used for synthesis of Co_3O_4 nanoparticles, adapted from Liang et al. (*137*) with some modifications. As shown in Scheme 2-9, 3.57 g of $Co(Ac)_2$ ($(CH_3CoO)_2Co{\bullet}4H_2O$, Ajax Finechem Pty. Ltd.) was mixed with 100 ml DI water (> 18.2 MΩ cm resistivity), then 24 ml EtOH (FRONINE) was added, followed by additional 1.2 ml of DI water. Resulted solution was kept at 80 °C for t_1 hours while mixing in a beaker. Then the solution were transferred to sealed PTFE reactors and heated to 150 °C for t_2 hours. The modifications were made on the reaction times (i.e. t_1 and t_2) for nucleation and particles growth phases (steps ④ and ⑤ in Scheme 2-9, respectively) as shown in Table 2-1.Then the reactors was left at room temperature to cool down. The resulted solution was vacuum filtered and left to dry.

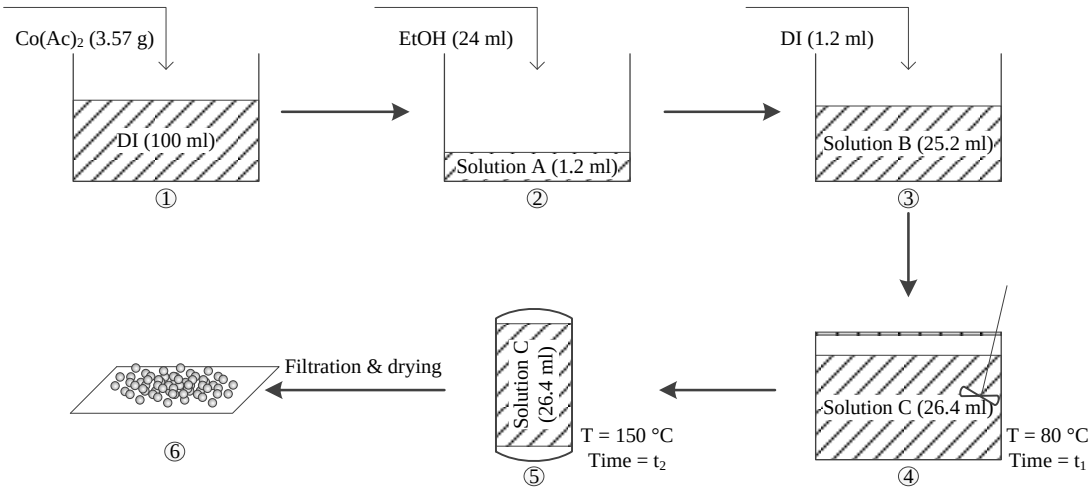

Scheme 2-9 Schematic diagram of Co_3O_4 nanoparticle production using hydrothermal method.

Table 2-1 Different samples with different reaction times for nucleation and particle growth stages.

Sample ID	t_1 [h]	t_2 [h]	NP size [nm]
C_1	24	2	5–40

C_2	24	4	10–40
C_3	14	4	5–50

The synthesized nanoparticles were characterized using XRD and transmission electron microscopy (TEM) as shown in Figure 2-4 and Image 2-6, respectively. Particle sizes in range of 5–40 nm was achieved for sample C_1, corresponding to t_1 = 24 h and t_2 = 2 h. Co_3O_4 nanoparticles were coated on PVs through drop casting of Co_3O_4 nanoparticles which were dispersed in ethanol.

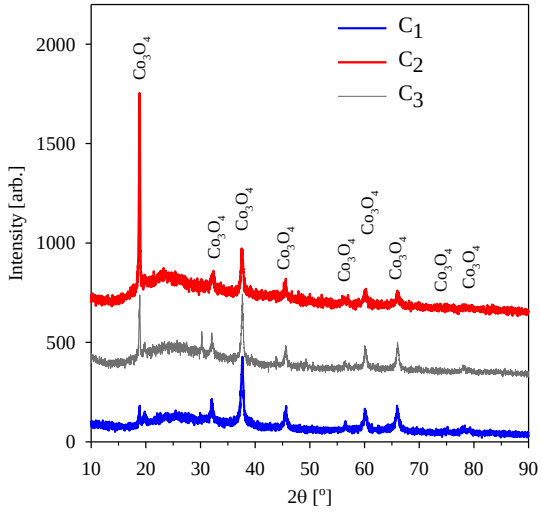

Figure 2-4 XRD pattern for different Co_3O_4 NPs. XRD characterization peaks were extracted from (*137, 151*).

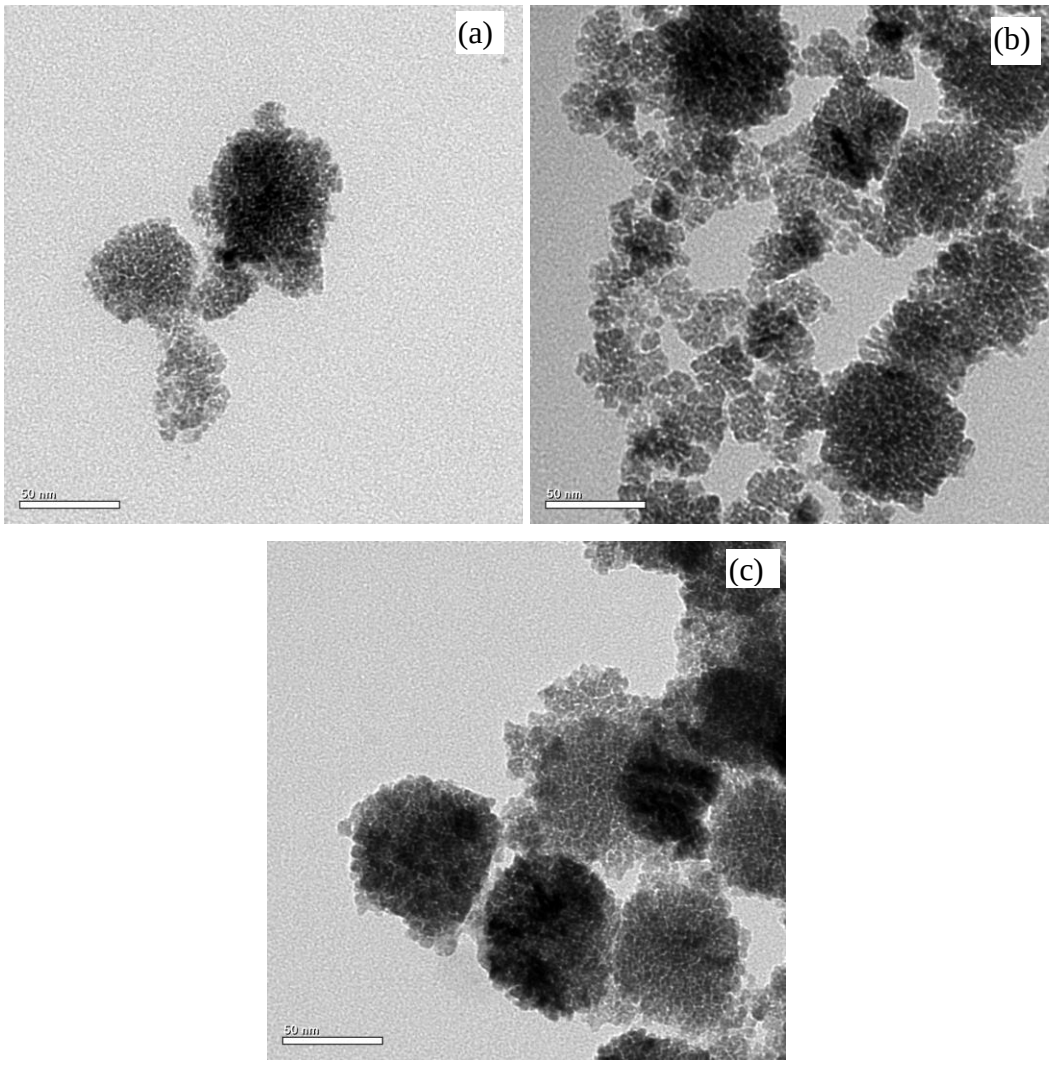

Image 2-6 TEM micrographs of synthesized Co_3O_4 NPs; a) for C_1, b) for C_2, c) for C_3 samples.

Scherrer equation (*152*) was also used to determine the nanocrystal mean size according to Eq. **(2-1)**, where L is crystal particle size in the direction perpendicular to the lattice planes, K is shape factor (here $k = 0.9$, a good approximation (*153*)), β is peak broadening represented by full width at half maximum (FWHM) in radian, θ is the Bragg angle, and λ is wavelength of x-ray source (here we used k-α of Cu, therefore $\lambda = 0.15418$ nm).

$$L\,[nm] = \frac{K \times \lambda\,[\mathrm{nm}]}{\beta \times cos(\theta)} \qquad \textbf{(2-1)}$$

This equation is valid for crystals up to 200 nm in size (*153*). Beyond this size contribution of other peak broadening factors becomes significant and contribution of those factors to peak broadening may not be distinguishable from contribution of crystallite size on

peak broadening (with increasing crystallite size peak broadening decreases). The results of such analysis are presented in Figure 2-5. Only the most intense peaks were used for this analysis, namely peaks at 18.8, 37.5, 45.6, 60, and 66°. Figure 2-5a shows different mean crystal size for each XRD peak position, however in almost all peak position C_1 had smaller crystallite size (except for 60°). Figure 2-5b shows mean crystallite size, which is the average of crystallite sizes of each sample over the five mentioned peak positions. As expected, C_1 had smallest crystallite size. Although using Scherrer equation and XRD data, the calculated average crystallite size seems different than what was derived from TEM micrographs shown in Image 2-6, relative conclusion remains the same. Thus, for the rest of this thesis sample C_1 was used for PEC assembly due to smaller size and therefore higher specific surface area.

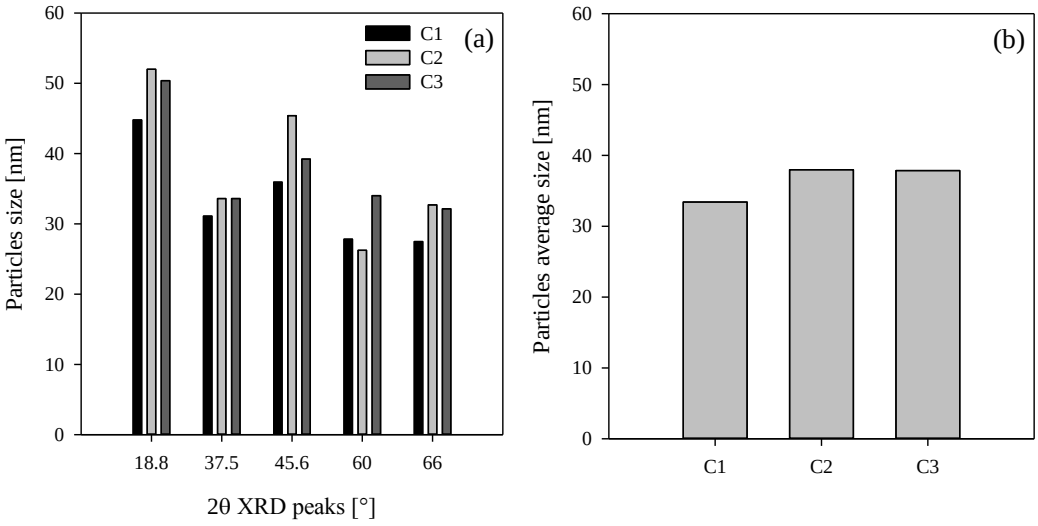

Figure 2-5 Mean crystal size analysis using XRD peaks through Scherrer equation. a) calculated mean crystal size at each peak position; b) mean crystal size for each Co_3O_4 NP sample.

2.3.4 Proton conductor synthesis and characterization

We used a variety of PEO polymers with different molecular weights ranging from 100–8000 kDa in a variety of solvent systems, electrospinning conditions, total polymer concentration, and Nafion® content based on a method developed by Ballengee et al. (*85*, *148*, *154*), as listed in Table 2-2. All of the Nafion® micro/nano fibers synthesis attempts

were characterized using SEM. Successful formation of Nafion® fibers were only observed in solutions with total polymer contents higher than ~ 20 wt%, as shown in Image 2-7.

Table 2-2 Samples ID and electrospinning conditions for different solvent systems and polymer concentrations.

Solution ID	Carrier polymer	Solvent System	Total polymer content (wt%)	Nafion® content (wt%)	Condition	Electrospinning condition
NafSol01	PEO 8000kDa	Isopropanol:DI:Methanol	10.0	99.3	1	RH=33%; T=24 C; V=5-20; Dis:12.3 cm; Syring:21g new; FLow:0.3-1.2 ml/h; rpm=100; Speed=10; Duration:30 m; Cleaning every 1 minutes.
NafSol02	PEO 8000kDa	Lower aliphatic alcohols:Methanol	13.8	99.1	1	RH=33%; T=24 C; V=5-20; Dis:12.3 cm; Syring:21g new; FLow:0.3-1.2 ml/h; rpm=100; Speed=10; Duration:30 m; Cleaning every 1 minutes.
NafSol03	PEO 8000kDa	Methanol	7.9	99.6	1	RH=33%; T=24 C; V=5-20; Dis:12.3 cm; Syring:21g new; FLow:0.3-1.2 ml/h; rpm=100; Speed=10; Duration:30 m; Cleaning every 1 minutes.
NafSol04	PEO 8000kDa	Methanol	6.2	99.4	1	RH=33%; T=24 C; V=5-20; Dis:12.3 cm; Syring:21g new; FLow:0.3-1.2 ml/h; rpm=100; Speed=10; Duration:30 m; Cleaning every 1 minutes.
NafSol05	PEO 8000kDa	Isopropanol:Methanol	6.5	99.3	1	RH=33%; T=24 C; V=5-20; Dis:12.3 cm; Syring:21g new; FLow:0.3-1.2 ml/h; rpm=100; Speed=10; Duration:30 m; Cleaning every 1 minutes.
NafSol06	PEO 8000kDa	Lower aliphatic alcohols:Methanol	4.2	99.4	1	RH=33%; T=24 C; V=5-20; Dis:12.3 cm; Syring:21g new; FLow:0.3-1.2 ml/h; rpm=100; Speed=10; Duration:30 m; Cleaning every 1 minutes.
NafSol07	PEO 8000kDa	Lower aliphatic alcohols:Methanol	4.3	98.7	1	RH=33%; T=24 C; V=5-20; Dis:12.3 cm; Syring:21g new; FLow:0.3-1.2 ml/h; rpm=100; Speed=10; Duration:30 m; Cleaning every 1 minutes.
NafSol08	PEO 8000kDa	1-propanol:DI	20.0	99.0	1	RH=31%; T=23 C; V=6; Dis:7 cm; Syring:21g new; FLow:0.5 ml/h; rpm=100; Speed=10; Duration:30 m; Cleaning every 1 minutes.
					2	RH=31%; T=24 C; V=7; Dis:14 cm; Syring:21g new; FLow:0.3 ml/h; rpm=100; Speed=10; Duration:30 m, Cleaning every 30 minutes.
					3	RH=31%; T=24 C; V=7; Dis:14 cm; Syring:21g new; FLow:0.3 ml/h; rpm=200; Speed=10; Duration:30 m, Cleaning every 30 minutes.
NafSol09	PEO 8000kDa	1-propanol:DI	20.2	98.0	1	RH=31%; T=23 C; V=8.5; Dis:12 cm; Syring:21g new; FLow:0.5 ml/h; rpm=100; Speed=10; Duration:46 m; Cleaning every 5 minutes.

					2	RH=31%; T=23 C; V=7; Dis:14 cm; Syring:21g new; FLow:0.3 ml/h; rpm=100; Speed=10; Duration:40 m; Cleaning every 30 minutes.
NafSol10	PEO 8000kDa	1-propanol:DI	20.1	99.5	1	RH=31%; T=24 C; V=6; Dis:12 cm; Syring:21g new; FLow:0.5 ml/h; rpm=100; Speed=10; Duration:30 m; Cleaning every 30 minutes.
					2	RH=31%; T=24 C; V=9; Dis:14 cm; Syring:21g new; FLow:1.2 ml/h; rpm=100; Speed=10; Duration:20 m; Cleaning every 30 minutes.
NafSol11	PEO 600kDa	1-propanol:DI	20.2	98.1	1	RH=31%; T=23 C; V=6; Dis:7 cm; Syring:21g new; FLow:0.5 ml/h; rpm=100; Speed=10; Duration:30 m; Cleaning every 1 minutes.
					2	RH=29%; T=23 C; V=6; Dis:7 cm; Syring:21g new; FLow:0.5 ml/h; rpm=100; Speed=10; Duration:1 h; Cleaning every 1 minutes.
NafSol12	PEO 600kDa	1-propanol:DI:DMF	19.9	98.0	1	RH=29%; T=23 C; V=6; Dis:7 cm; Syring:21g new; FLow:0.5 ml/h; rpm=100; Speed=10; Duration:1 h; Cleaning every 1 minutes.
NafSol13	PEO 8000kDa	1-propanol:DI	20.2	99.0	1	RH=42.8-37.5%; T=24.2 C; V=12; Dis:10 cm; Syring:21g new; FLow:0.04 mm/min; rpm=5.93 m/min; Speed=17.84 cm/min; Duration:20 m; No Cleaning.
					2	RH=43.5-35.0%; T=24.2 C; V=12; Dis:5 cm; Syring:21g new; FLow:0.04 mm/min; rpm=5.93 m/min; Speed=17.84 cm/min; Duration:28 m; No Cleaning
					3	RH=41.0-35.0%; T=24.7 C; V=6; Dis:5 cm; Syring:21g new; FLow:0.04 mm/min; rpm=5.93 m/min; Speed=17.84 cm/min; Duration:30 m; No Cleaning
NafSol14	PEO 100kDa	1-propanol:DI	20.2	98.1	1	RH=31%; T=23 C; V=6; Dis:7 cm; Syring:21g new; FLow:0.5 ml/h; rpm=100; Speed=10; Duration:30 m; Cleaning every 1 minutes.
					2	RH=29%; T=23 C; V=6; Dis:7 cm; Syring:21g new; FLow:0.5 ml/h; rpm=100; Speed=10; Duration:1 h; Cleaning every 1 minutes.

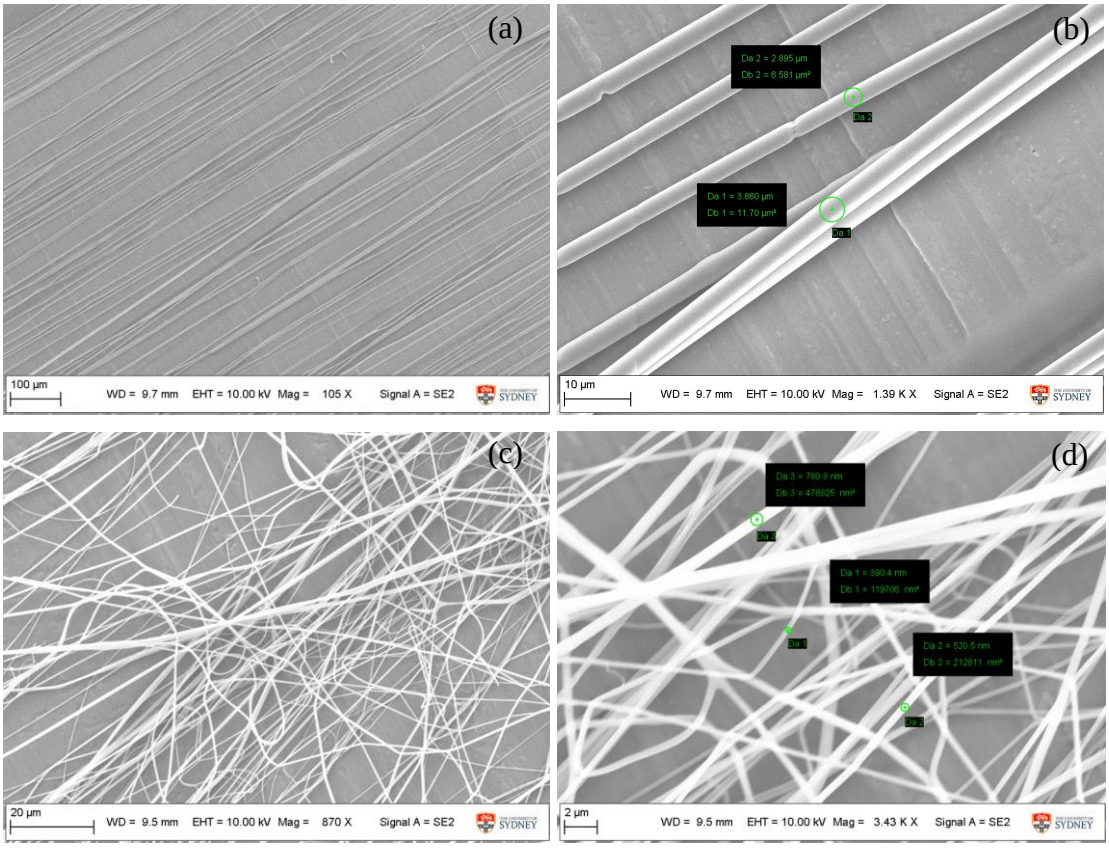

Image 2-7 SEM micrographs of successful Nafion® micro/nanofibers production using electrospinning method; a) NafSol08 condition 3 produced fibers of ~2.5 um diameter with lower light scattering, b) NafSol11 condition 2 produced fibers of ~500 nm diameter with higher light scattering. No sputter coating was used before SEM imaging.

However, we visually observed these fibers have high ratio of light scattering (light scattering for the fibers was not measure). We hypothesized high light scattering is due to cylindrical morphology of the fibers because fibers with higher diameter had lower light scattering than fibers with lower diameters (see Image 2-7). Cylindrical morphology cases the synthesized Nafion® mat to have higher number of edges per mass of Nafion® mat (drop casted Nafion®, which does not have any edges, was a clear sheet). In addition, the solution used for electrospinning was clear. Therefore, it thought to be possible to reach a relatively transparent and yet porous Nafion® mat by changing the morphology of the fibers, from cylindrical to ribbon, and subsequently decrease the number of edges per weight of Nafion® mat. In other words, using ribbon morphology less number of fibers would be required to coat the surface of

the PEC in comparison to cylindrical morphology. Since each fiber has two edges, less number of fibers is equivalent to less edges and subsequently less light scattering. To that end we modified the fabrication method and found a condition at which Nafion® nanoribbons can be produced. This method is detailed below.

Isopropanol (UNIVAR, reagent grade)/DI water solvent systems was made first (2:1 ratio). 0.12 g of PEO (8000 kDa, SigmaAldrich) were dissolved in 12 g of the solvent system (1 wt% solution). In a different beaker 3.32 g of Nafion® pellets (produced by drying as received Ion-Power Nafion® 1100 solution) was dissolved in 6.15 g of solvent system (35 wt% solution). Then appropriate amounts of the two solutions were mixed for 2 hours to product electrospinning solution with 20 wt% polymer content (99.5 wt% Nafion®, 0.5 wt% PEO). Then electrospinning solution was electrospun using the PECs as target at 24.9 °C, 30.8% relative humidity, 5 V, 15 cm needle to target distance, 21g needle, flow rate of 0.85 ml/h, and drum rotating linear speed of 10 m/min. Resulted Nafion® nanoribbon mat were characterized using SEM for morphology (see Image 2-8 for SEM and Image 2-9 for digital photograph).

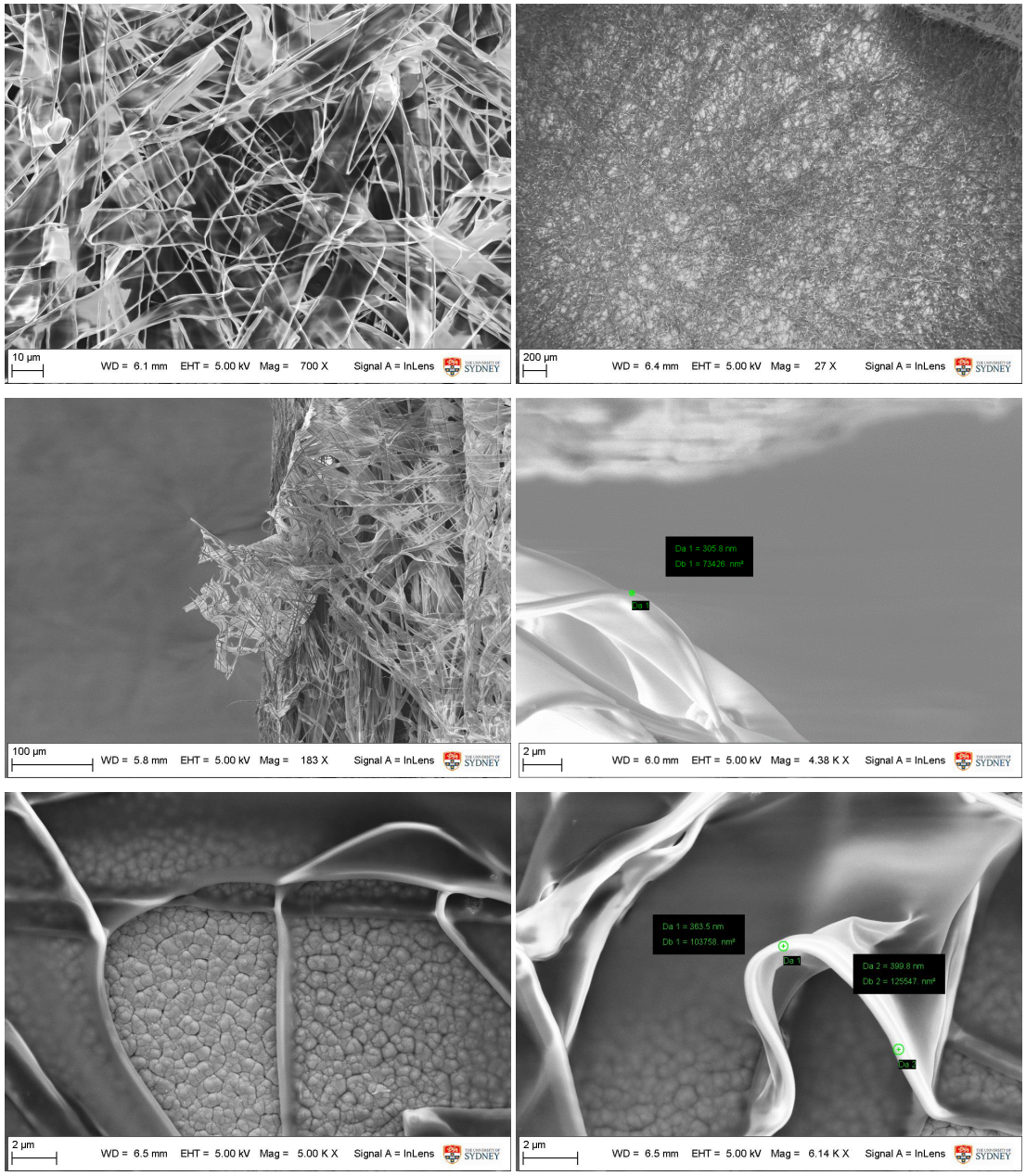

Image 2-8 SEM micrographs of Nafion® nanoribbons synthesized in this study. Using the modified method high purity Nafion® nanoribbon as thin as 300 nm were synthesized using electrospinning method. Prepared photoanode were used as electrospinning target, therefore Nafion® nanoribbon mat was formed directly on fully assembled PECs. The bumpy substrate is a-Si PV. No sputter coating technique was used before SEM imaging.

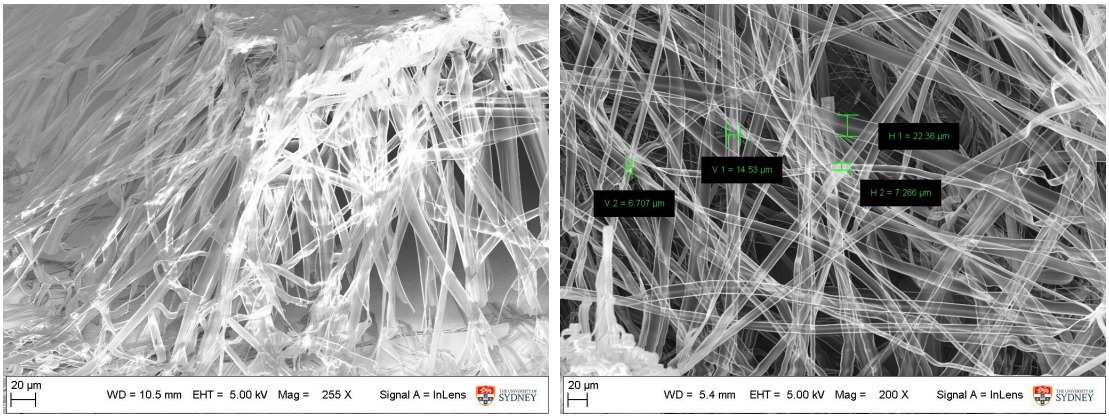

Image 2 8–continue SEM micrographs of Nafion® nanoribbons synthesized in this study.

Image 2-9 Digital photograph of a PV used as electrospinning target. The image shows formation of Nafion® nanoribbon mat on the PV.

As shown in Image 2-8, high purity Nafion® nanoribbons as thin as 300 nm, at the edges, were successfully synthesized using electrospinning method. Thickness of the Nafion® nanoribbons seem to be much thinner than 300 nm because under SEM with low electron gun voltage of 5 kV, they look transparent to electrons (the substrate is easily observable through Nafion® nanoribbons). The thickness of the Nafion® nanoribbon in those spots were not measured. Nanoribbons were in range of ~ 7–22 µm in width. No attempt were made to manipulate nanoribbons width. Mechanical strength of the synthesized Nafion® mats were not analyzed as well.

2-point probe impedancemetry were used for proton conductivity measurements (see Figure 2-6) using a methodology adapted from (*155*). For proton conductivity measurements, Nafion® nanoribbon mats were pretreated using thermal, chemical, and thermochemical pretreatment methods which included mixing Nafion® solution with 5.0 M H_2SO_4, boiling in 5.0 M H_2SO_4 (30 min) and then in DI (30 min), soaking in 1.0 M HCl (21 h), soaking in 5.0 M H_2SO_4 (21 h), and thermal annealing at 80 °C for 48 h under air. All the proton conductivities were compared with that of as spun Nafion® nanoribbon mat. Equation (2-2) were used to calculate proton conductivity from impedancemetry data

$$\sigma\ [S/cm] = \frac{l\ [cm]}{R\ [\Omega] \times S\ [cm^2]} \tag{2-2}$$

where σ, l, R, S denote the proton conductivity of Nafion® mat, distance between the electrodes, the measured frequency independent resistance of the Nafion® mat, and the cross-sectional area of the membrane, respectively.

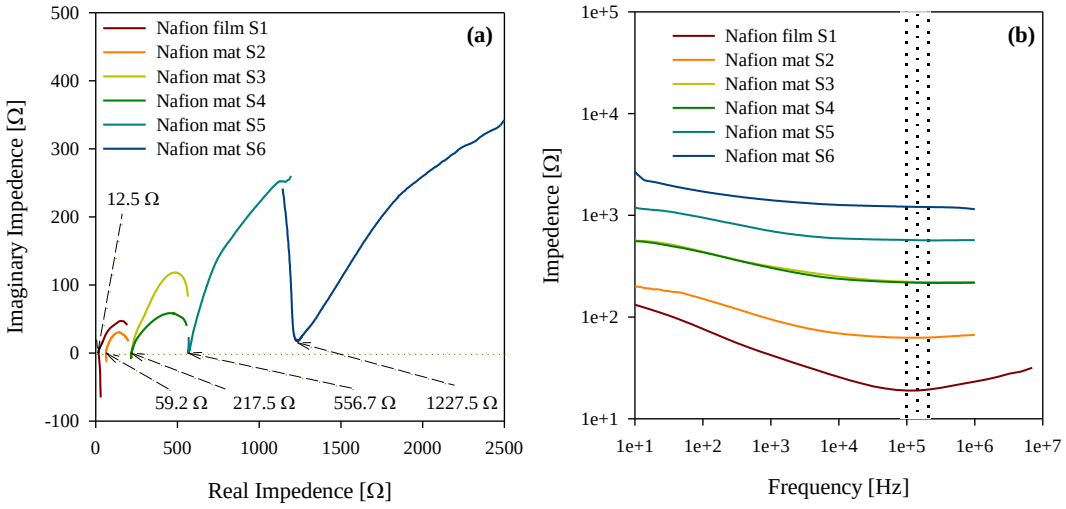

Figure 2-6 Proton resistance measurement of Nafion® nanofiber mat treated with different methods. a) Cole-Cole plot. The noted values are frequency independent real impendence of the samples; b) Bode plot. The dotted area shows frequency impendence impedance range. The samples were immersed in DI water (> 18.2 MΩ cm resistivity) during the test. Electrode length = 8 mm and membrane thickness = 450 µm. The dotted area in (b) shows the frequency range at which measured impedance was independent of applied frequency. S1: Nafion® film made from a mixture of 5.0 M H_2SO_4 and Nafion® solution through drop casting. 7 g of 15 wt% Nafion® solution were mixed with 11.12 g 5.0 M H_2SO_4 using magnetic rotary mixer. Immediately after

addition of H_2SO_4 to Nafion® solution, the mixture became colloidal. The film did not dry completely after 72 h in oven at 80 °C. Thickness of drop casted Nafion® film S1 was 1 mm ($\sigma = 0.32 \frac{S}{cm}$); S2: Electrospun Nafion® boiled in 5.0 M H_2SO_4 for 30 minutes then in DI for another 30 minutes ($\sigma = 0.15 \frac{S}{cm}$); S3: Electrospun Nafion® Soaked in 1.0 M HCl for 21 h ($\sigma = 0.041 \frac{S}{cm}$); S4: As spun Nafion® ($\sigma = 0.041 \frac{S}{cm}$); S5: Electrospun Nafion® soaked in 5.0 M H_2SO_4 for 21 h ($\sigma = 0.016 \frac{S}{cm}$); S6: Electrospun Nafion® thermally annealed at 80 °C for 48 h under air ($\sigma = 0.007 \frac{S}{cm}$).

As shown in Figure 2-6a, as spun Nafion® mat, sample S4, had a proton conductivity of 0.041 $\frac{S}{cm}$. This is in agreement with the values reported by Ballengee et al. (*85, 148*). Proton conductivity of Nafion® is governed through two main mechanisms: hopping (or Grotthuss) mechanism and diffusion (or vehicular) mechanism (*156, 157*). Through hopping, O-H bonds in Nafion® (see Scheme 2-7) are continuously breaking up and forming to pass new arriving protons form one side of the polymer to the other side. To increase proton conductivity of Nafion® one may protonise acidic sites of Nafion® to provide higher concentration of protonic sites, which can be used to conduct protons by Nafion® polymer through hopping mechanism. (The higher the number of protonic sites in Nafion® polymer, the higher the number of hooping sites, and the higher proton conductivity.). Protonization is facile and therefore is widely used for this purpose (*85, 148*). Diffusion of proton, referring to diffusion mechanism, is done through bulk of swallowed water in Nafion® membrane. Formation of water clusters in Nafion® is experimentally validated using AFM-IR spectroscopy (atomic force microscopy couple with infrared microscopy) (*158*). Manipulation of proton diffusion rate is possible through manipulating size of water microchannels and clusters in Nafion® membrane matrix (*159, 160*).

Here we tested effect of protonization using various acids and through various methods. Sample S1, which is Nafion® film made from a mixture of 5.0 M H_2SO_4 and Nafion® solution through drop casting and then dried for 72 h at 80 °C, is the first tested sample. S1 had the highest measured proton conductivity at 0.32 $\frac{S}{cm}$ (in comparison to as spun Nafion® nanoribbon mat, S4, at 0.041 $\frac{S}{cm}$). This proton conductivity is 3 fold higher than proton conductivities

reported in literature for Nafion® 117 (*154*). The reason is after 72 h of drying the film did not completely dry, leaving liquid residues of H_2SO_4 within the Nafion® film matrix (a paste was formed rather than a solid film). Consequently, the synthesized film did not have any standalone properties, limiting its real life application (i.e. the film could not be used by itself as a proton conducting material). The residue of H_2SO_4 causes significant increase in proton concentration in the film, due to high H_2SO_4 molarity, and as a result very high proton conductivity. Therefore, although high proton conductivity was obtained, the synthesized film was not usable due to lack mechanical strength.

Traditionally Nafion® treatment is done after electrospinning step using a strong acid (*154*). Therefore, we treated our electrospun Nafion® mat through boiling and soaking in H_2SO_4 and HCl solutions. The respective samples are S2 (boiled in 5.0 M H_2SO_4 for 30 minutes then in DI for 30 minutes), S3 (Soaked in 1.0 M HCl for 21 h), and S5 (soaked in 5.0 M H_2SO_4 for 21 h). It was found that boiling has much greater impact on proton conductivity of Nafion® than soaking because $\sigma_{S2} = \mathbf{0.15}\,\frac{\boldsymbol{S}}{\boldsymbol{cm}}$ (3.75 times higher than that of as spun Nafion® mat), $\sigma_{S3} = \mathbf{0.041}\,\frac{\boldsymbol{S}}{\boldsymbol{cm}}$ (same as that of as spun Nafion® mat), and surprisingly $\sigma_{S4} = \mathbf{0.016}\,\frac{\boldsymbol{S}}{\boldsymbol{cm}}$ (60% lower than that of as spun Nafion® mat).

Thermal treatment was also reported to increase proton conductivity of Nafion® through sintering of individual fibers to a fully connected 3D network of Nafion® and change in crystalline structure of Nafion®. However, in our experiments thermal annealing lead to decline in proton conductivity (*154*). For S6, thermally annealed Nafion® mat at 80 °C for 48 h under air, proton conductivity declined from 0.041 $\frac{\boldsymbol{S}}{\boldsymbol{cm}}$ for as spun mat to 0.007 $\frac{\boldsymbol{S}}{\boldsymbol{cm}}$. Observation under SEM showed confirmed no sintering took place under such condition. It is hypothesized in Chapter 4 that substrate of Nafion® mat has significant role in successful sintering through

thermal annealing. This is discussed further in section 4.1.2. Possible loss of connection between Nafion® fibers might be the reason behind the observed decline in proton conductivity of S4.

Since conducting chemical pretreatment is not compatible with current design of the PEC, we used as spun Nanoribbon mat for in this thesis unless otherwise stated. Effect of thermal annealing on performance of the PECs is discussed in section 4.1.2.

Effect of Nafion® nanoribbon coating on PV performance were analyzed using I-V curve measurement as explained in section 2.3.1 in laboratory environment and in controlled atmosphere where humidity were monitored. Effect of Nafion® coating on appearance of the PVs for various durations of coatings are shown in Image 2-10. Various durations of coating resembles various thicknesses of Nafion® coating on PVs. Longer the coating time, thicker the Nafion® nanoribbon mat on the PVs. As shown, at 45 minutes of coating, the visual appearance of the PV seems to be significantly affected while there is not big difference in appearance of 15 minutes and 30 minutes coatings.

Image 2-10 Digital photograph of Nafion® nanoribbon coated PV for (left to right) 15 min, 30 min, and 45 min, respectively. Copper color ribbons are Cu tapes which were used as current collectors.

In order to grasp a better understating of Nafion® coating on PV performance, I-V curve measurements were carried out before and after Nafion® coating. As shown in Figure 2-7a, for PV179 and PV184, no significant difference in I-V curves were observed before and after 30 minutes of Nafion® coating, but for PV178, I-V curve was declined after 45 minutes of Nafion®

coating. Therefore, 30 minutes Nafion® coating was used as the benchmark of Nafion® nanoribbon coating time for the rest of this thesis, unless specified.

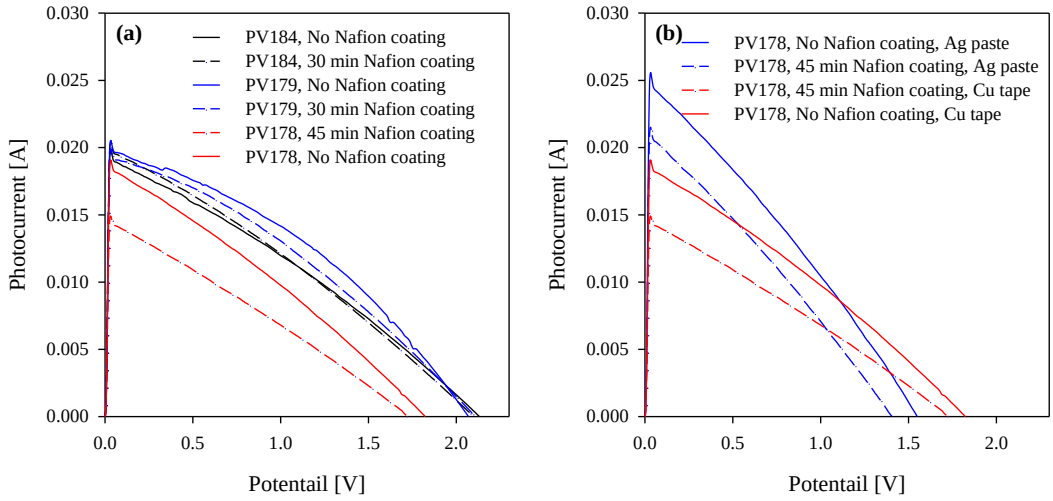

Figure 2-7 Effect of a) Nafion® nanoribbon coating and b) current collector type on performance of prepared PVs. Solid lines correspond to PVs with no coating and dashed lines correspond to PVs with either 30 or 45 minutes coating. 1 sun intensity simulated sun light (AM 1.5) were used for I-V curve measurements.

For comparison, for PV178, two types of current collectors, Cu tape and silver paste, were used to observe effect of current collector type on measured I-V curves and consequently on PV performance assessment. For Cu tape current collector, a 1 mm thick Cu tape was mounted on ITO layer of PV178 by slight pressing. For Ag paste current collector, Ag paste (TED PELLA, Inc.) was used to form a ribbon-like solid current collector by slight brushing (see Image 2-11). Although the results shows different I-V curve for the same PV under the same atmospheric conditions and simulated sunlight intensity, but the effect of Nafion® coating on measured I-V curve were the same irrespective of current collector material and installation method, as shown in Figure 2-7b (using both current collectors both V_{OC} and I_{SC} declined significantly for 45 minutes coating).

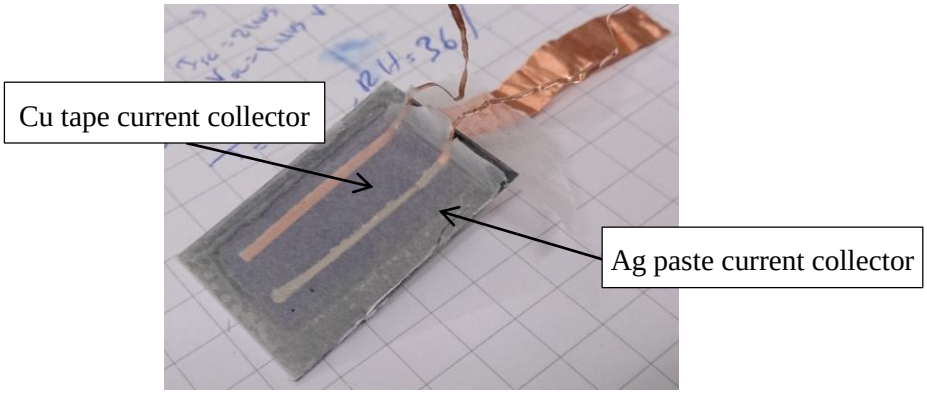

Image 2-11 Digital photograph of PV178 when both Cu tape current collector and silver paste current collector are mounted on the ITO layer of the PV, under the Nafion® nanoribbon coating layer.

2.4 Assembly of the PEC

In this section assembly procedure of PEC is discussed, assembly challenges are covered, and solutions are provided in cases where any solution was found.

2.4.1 Coating of NPs on photoanode surface

The assembly process starts with coating photoanode and cathode with desired catalysts. Two main methods were used for this purpose: spin coating and drop casting. Spin coating provides good uniformity and reproducibility and is suitable for thin film deposition by controlling parameters like spinning speed and duration, solution injection speed, and multistep coating vs. single step coating. However, it is not a suitable technique to reach high catalyst loading on the surface and to reach uniform coating for noncircular surfaces. In addition, material loss is significant and exact loading value is hard to obtain. The reason is due to centrifugal force, a great portion of coating solution escapes from the surface, leading to unknown level of coating. On the other hand, drop casting is easy and exact level of coating is easily reachable although coating uniformity is not guaranteed.

For spin coating method, 0.0361 wt% solution of CO_3O_4 NPs in ethanol were used. Ethanol were selected as the base fluid for all coating solutions due to good wettability of Cu sheets and

PVs. Prepared PVs were coated by adding 200 µl of NP solution to the center of PVs (drop wise) while PVs were rotating at 500 rpm for 60 seconds, and then adding 200 µl of NP solution to the center of PVs (drop wise) while PVs were rotating at 3000 rpm for 60 seconds. After coating Energy Dispersive X-ray Spectroscopy (EDS) were used to examine coating uniformity. As shown in Image 2-12 and Image 2-13, uniform distribution of catalyst is confirmed by EDS mapping and SEM. However, as discussed in Section 2.3.2, it was found that the coating level achieved through this method might not be high enough, as visible in Image 2-13 (left). Therefore, drop casting method was used instead unless otherwise stated.

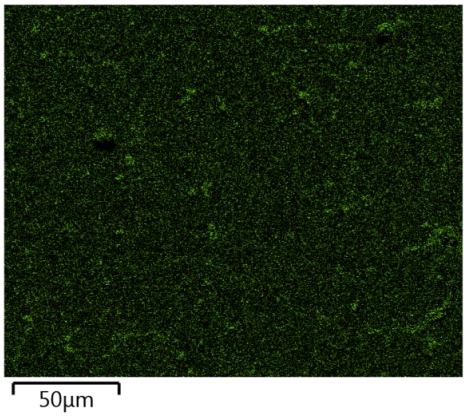

Image 2-12 EDS mapping of spin coated Co_3O_4 NPs on prepared PVs. Only Co map is shown here.

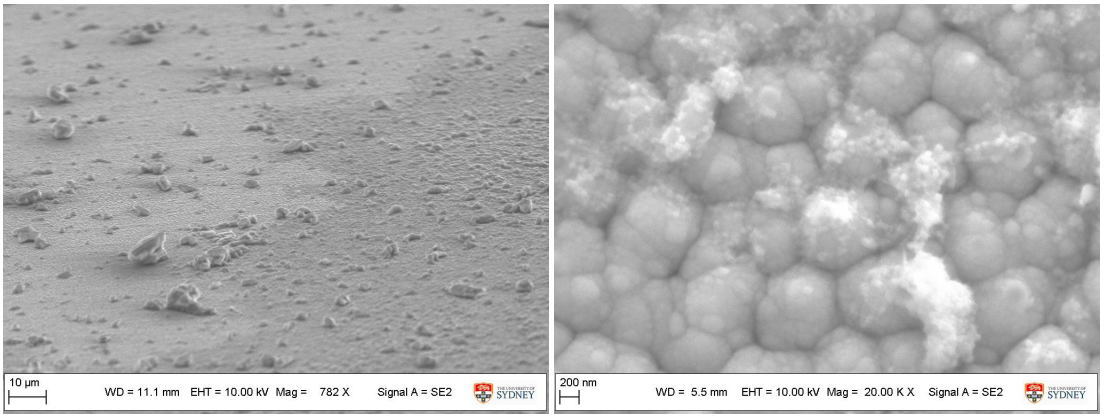

Image 2-13 SEM micrograph of coated Co3O4 NPs on prepared PVs through spin coating method. Left) side view, the stone like residuals are Co NP clusters; right) top view, the tiny particles are Co NPs. The bumpy background is ITO layer of the prepared a-Si PV.

For drop casting method, level of coating was rather justified visually and through I-V curve measurements. Drop casting was repeated to the point that visible change in appearance of coated PVs was obvious and significant change in I-V curve was not detected. This is shown in Image 2-14. Because there is a risk that a thick coating may block the incident light to photoanode, a piece of plain glass was used as a control sample to observe the effect of coating level on light penetration. Then, effect of coating level on PV performance was analyzed through I-V curve measurement.

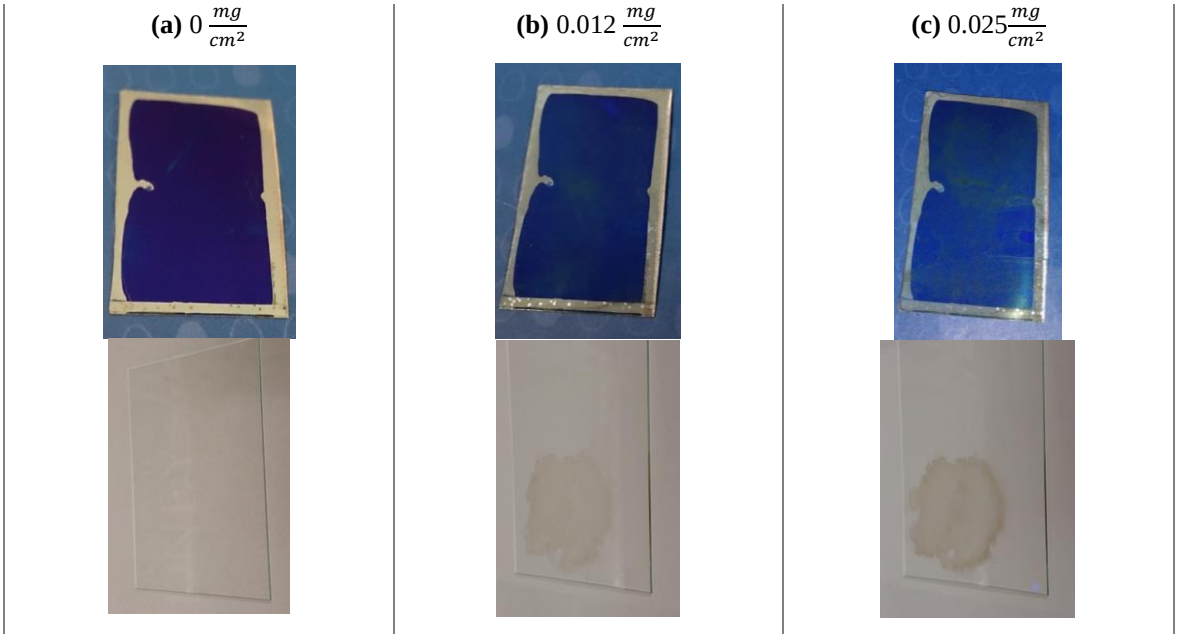

Image 2-14 Effect of Co_3O_4 NP coating level on appearance of prepared PVs through drop casting. Plain glass control samples were used with the same coating level to visually observe the effect of coating level on penetration of light through coating layer. a) before coating; b) 0.012 $\frac{mg}{cm^2}$ (total of 0.055 mg) coating; c) 0.025 $\frac{mg}{cm^2}$ (total of 0.11 mg) coating.

As shown in Image 2-14c, it was found that at 0.025 $\frac{mg}{cm^2}$, coating thickness becomes thick enough to affect light penetration through coating layer. This catalyst loading is at least one order of magnitude smaller than optimal Pt loading (0.2–0.35 $\frac{mg}{cm^2}$) typically used in polymer electrolyte membrane (PEM) fuel cells (*161*). However, although higher catalyst loading is achievable using drop casting method, here no optimization was carried out. Rather, the effort

was directed toward prevention of drastic adverse effect of catalyst loading on performance of the photoanode as the key driving force producer of the PEC. Therefore, effect of catalyst loading on PV performance was used as the decision criteria. This effect in depicted in Figure 2-8.

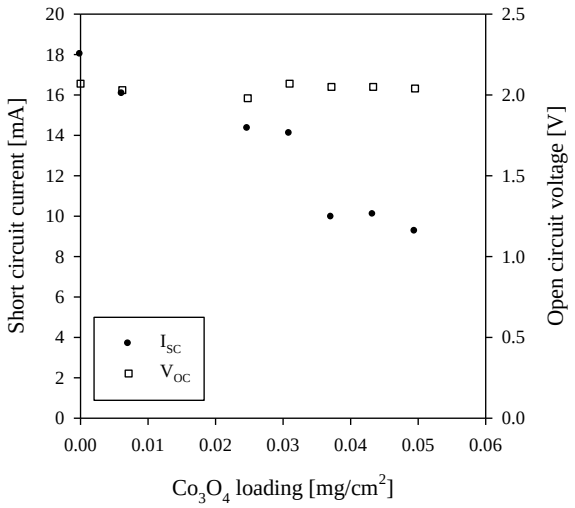

Figure 2-8 Effect of Co_3O_4 catalyst loading on short circuit current (I_{SC}) and open circuit voltage (V_{OC}) of the prepared photoanodes (PV221).

As show in Figure 2-8, despite what was observed in Image 2-14, the effect of catalyst loading on photoanode I_{SC} is not significant up to for catalyst loading < 0.03 $\frac{mg}{cm^2}$ (I_{SC} decreased by 20% at 0.03 $\frac{mg}{cm^2}$ in comparison to not coated photoanode). After this pint, I_{SC} suddenly decreases to 55% of the initial value. Interestingly, the effect of catalyst loading on V_{OC} was minor and negligible up to 0.05 $\frac{\text{mg}}{\text{cm}^2}$. Therefore, it is concluded that catalyst loading of 0.025 $\frac{mg}{cm^2}$ is safe to use because it did not significantly affect the photoanode performance, and consequently will not drastically affect performance of assembled PECs.

2.4.2 Coating of NPs on cathode surface

The same drop casting method was used for cathode side catalyst loading in case of using nanoparticles. Suspension solutions of 0.0066 wt% of desired nanoparticles in ethanol were used

for this purpose. Nanoparticles solutions were sonicated using bath sonicator for 1 h before coating. Catalyst loading of 0.05 $\frac{mg}{cm^2}$ was used for all nanoparticles.

2.4.3 Assembly procedure

Assembly procedure is outlined below:

1. Prepare photoanode as outlined in section 2.3.1.
2. Prepare the desired cathode catalyst as outlined in section 2.3.2.
3. Arrange cathode supports with loaded catalyst in a rectangular shape as shown in Scheme 2-4b. Depending on the desired cathode surface area, one may need to use multiple cathode supports in various shapes or have less or more than four cathode pieces, which are required to make a rectangular form.
4. All the cathode supports must be in proper ohmic contact. We used a combination of Cu tape and Ag paste for this purpose. Cu tape provides enough mechanical support for cathode support to hold a particular shape. Ag paste enables having proper ohmic contact between Cu tape/Cu support and Cu tape/Cu tape pairs. An extra piece of Cu tape is required to connect the cathode area to potentiostat.
5. Prepare photoanode catalyst as outlined in section 2.3.3.
6. Use a non-conductive yet strong support to make a bridge between the assembled cathodes and the back of prepared photoanode (stainless steel side of photoanode in case of using the same a-Si PV as photoanode). This is an important step because if the bridge is not strong enough, handling of the PEC will be very challenging in electrochemical and photoelectrochemical testing steps. In addition, one must ensure no ohmic contact exists between the assembled cathode and the prepared photoanode.

7. Mount a current collector on the back of photoanode using Cu tape and Ag paste. No pressure should be applied to ensure proper ohmic contact. Instead use Ag paste and a brush to diagnose any poorly installed connections.
8. At this stage, the PEC is ready for final step, which is coating with Nafion® nanoribbon mat. Use the assembled PEC as the target during electrospinning process. Use of a rotary drum in electrospinner is unavoidable to ensure a uniform coating of Nafion® mat.
9. At this stage, the PEC is fully assembled and is ready for use.

Digital photograph of the first assembled PEC is shown in Image 2-15. Image 2-16 shows the first set of assembled PECs using different cathode catalysts.

Image 2-15 Digital photograph of the first assembled PEC (PEC115).

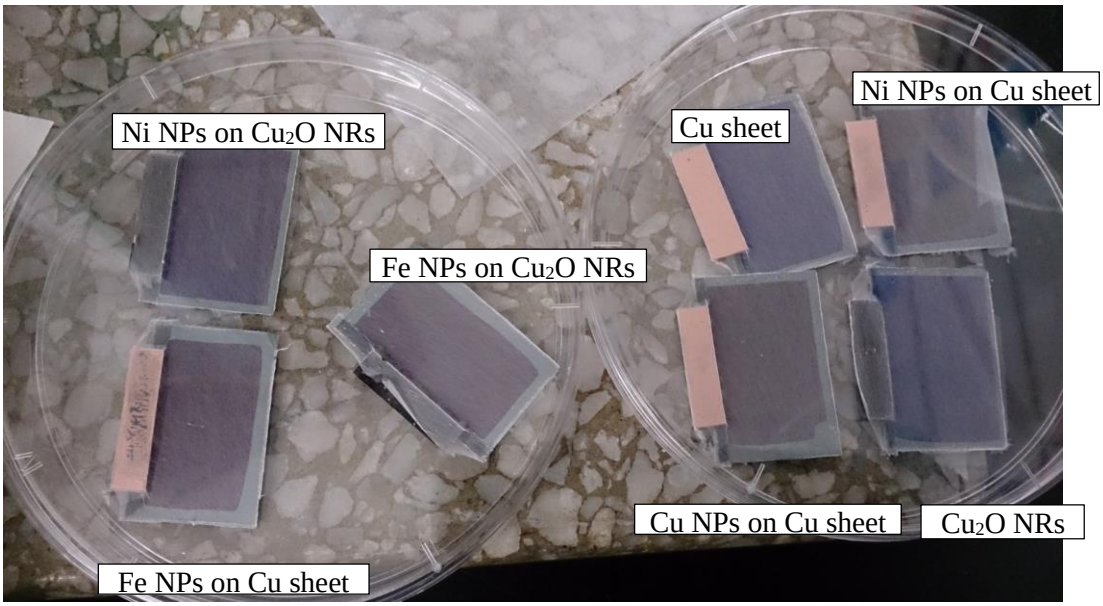

Image 2-16 Digital photograph of the first set of the assembled PECs using a variety of cathode catalsyts.

2.5 Summary

In this chapter we discussed material selection, synthesis, and characterization for each component of the proposed PEC and presented the procedure that was used to assemble the PECs. In the next chapter (Chapter 3), we present and discuss proof-of-concept tests to determine if the proposed PECs are able to reduce CO_2 from gas phase to any product, bearing in mind the ultimate aim which is reduction of CO_2 to solid carbon.

Chapter three

Proof-of-concept

In this chapter proof-of-concept tests were conducted and the results were analyzed in detail using a variety of assembled PECs and at different conditions. The discussed issues include photoelectrochemical and electrochemical testing of PECs, effect of photoanode quality on behavior of PECs, and effect of humidity content and CO_2 concentration in reactor atmosphere on performance of the PECs. The procedure used for proof-of-concept tests are presented in Section 2.2 of Chapter 2. For all the photoelectrochemical tests 1 sun intensity simulated sunlight were used as light source.

3.1 Specification of experimented PECs

A list of PECs experimented in this chapter is provided in Table 3-1. A variety of PVs with a variety of V_{OC} values, fill factors, anode catalyst loading, cathode catalysts, and cathode areas were selected for the proof-of-concept tests.

Table 3-1 Specification of PECs experimented in this chapter.

PEC ID	PA[a] ID	PA V_{OC} [V]	PA Fill factor [%]	PEC V_{OC}[b] [V]	Anode Catalyst loading [mg]	Cathode Area [cm^2]	Nafion® coating duration [min]	Nafion® mat morphology	Cathode Catalyst
115	115	1.94	30.98	NA	0.01	1	30	Nanofiber	Ni NPs on Cu_2O NRs
137	137	2.05	38.43	1.89[c]	0	5	30	Nanofiber	Cu sheet
113	113	1.66	27.03	1.52	0	5	30	Nanofiber	Cu sheet
182[d]	182	2.16	32.23	0.95	0.11	10	30	Nanoribbon	Cu sheet
175[d]	175	2.17	30.11	1.10	0	5	30	Nanoribbon	Cu sheet
165[d]	165	2.07	37.10	1.52[c]	0.11	5	30	Nanoribbon	Cu_2O NRs

[a] PA = Photoanode

[b] V_{OC} of PEC was measured by connecting reference and working electrode wires of potentiostat to cathode support and back of photoanode, respectively, while having Nafion® mat as the connection between cathode and photoanode. No Cu tape or Ag paste was used as current collector for this measurement. Therefore, these values may not be a true representative of V_{OC} of the actual PEC because the humidity at which these voltages are measured affects the results.

[c] PEC V_{OC} was not stable, continuously declined as it was under illumination. This issue is discussed in Chapter 4.

[d] On this PEC, heat sinks were used for stabilization of photocurrent. The reasoning is discussed in Chapter 4.

From the first set of PECs made (Image 2-16 in Chapter 2), only PEC115 survived for proof-of-concept tests. The reason was the cathode support was not bridged strong enough to prevent breakage of Nafion® mat (see Image 3-1) during mounting of the PECs on alligator clips connection of the potentiostat in designed reactor. The synthesized Nafion® mat was flexible enough to expand up to 3 mm under mechanical strain; however, extreme care must be taken to prevent breakage of Nafion® mat. We successfully changed the method we used to attach the cathode support to the PEC and solved the issue for later PECs.

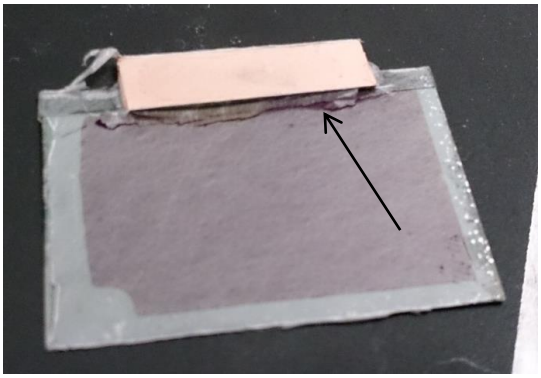

Image 3-1 Nafion® breakage due to mechanical strain during mounting on potentiostat alligator clips.

3.2 Unassisted photoelectrochemical experimentation of assembled PECs

PEC115 were used for the first proof-of-concept tests. For this test, as explained in section 2.2 of Chapter 2, the PEC was under continues purge of dry Ar (grade 4) at 1 L/min for 30 min prior to the photoelectrochemical test, in order to minimize the amount of air-born CO_2 and other gaseous contaminants that might exist in the reactor. After mounting the PEC insides the reactor, quartz glass window was put on the stainless steel reactor and sealed, using a water soluble sealant, and was hold in place using 8 Irwin grip clamps. Then generated photocurrent of the PEC was measured while the PEC was under continues purge of desired gas at desired humidity level for at least 10 min. The results of such a test for PEC115 are shown in Figure 3-1.

At first PEC115 were tested under humidified Ar. As shown in Figure 3-1a, when the cell was under illumination a small photocurrent, in range of 40 nA, were detected. However, when the reactor ambient gas was changed to humidified CO_2, the generated photocurrent drastically increased up to 570 nA. This indicates a 13 fold increase in generated photocurrent. However, generated photocurrent declined rapidly after 10 times of light ON/OFF cycles, each taking 5 seconds, and during each illumination period. When the PEC was left in dark for 100 s, the PEC was able to generate photocurrents up to 200 nA. Further relaxation of the PEC in dark for another 100 s, enabled the PEC to produce the maximum amount of detected photocurrent in this test, at ~ 900 nA. When reactor atmosphere was changed from humidified CO_2 to dry CO_2, no photocurrent was detected. By replacing dry CO_2 with humidified CO_2 generation of photocurrent was restored. When Nafion® mat connection between cathode and anode was disconnected intentionally, no or very small photocurrent was generated under various conditions (see Figure 3-1b). Therefore, it was concluded here that a photo-induced reaction involving CO_2 and water vapour happened on PEC115 simply because no comparable photocurrent was generated when CO_2 was replaced with Ar, and when water vapour was removed from the reactor. Dark photocurrent of the PEC was negligible for all reaction atmospheres. A close-up of the generated photocurrent under humidified Ar and humidified CO_2 is shown in Figure 3-2.

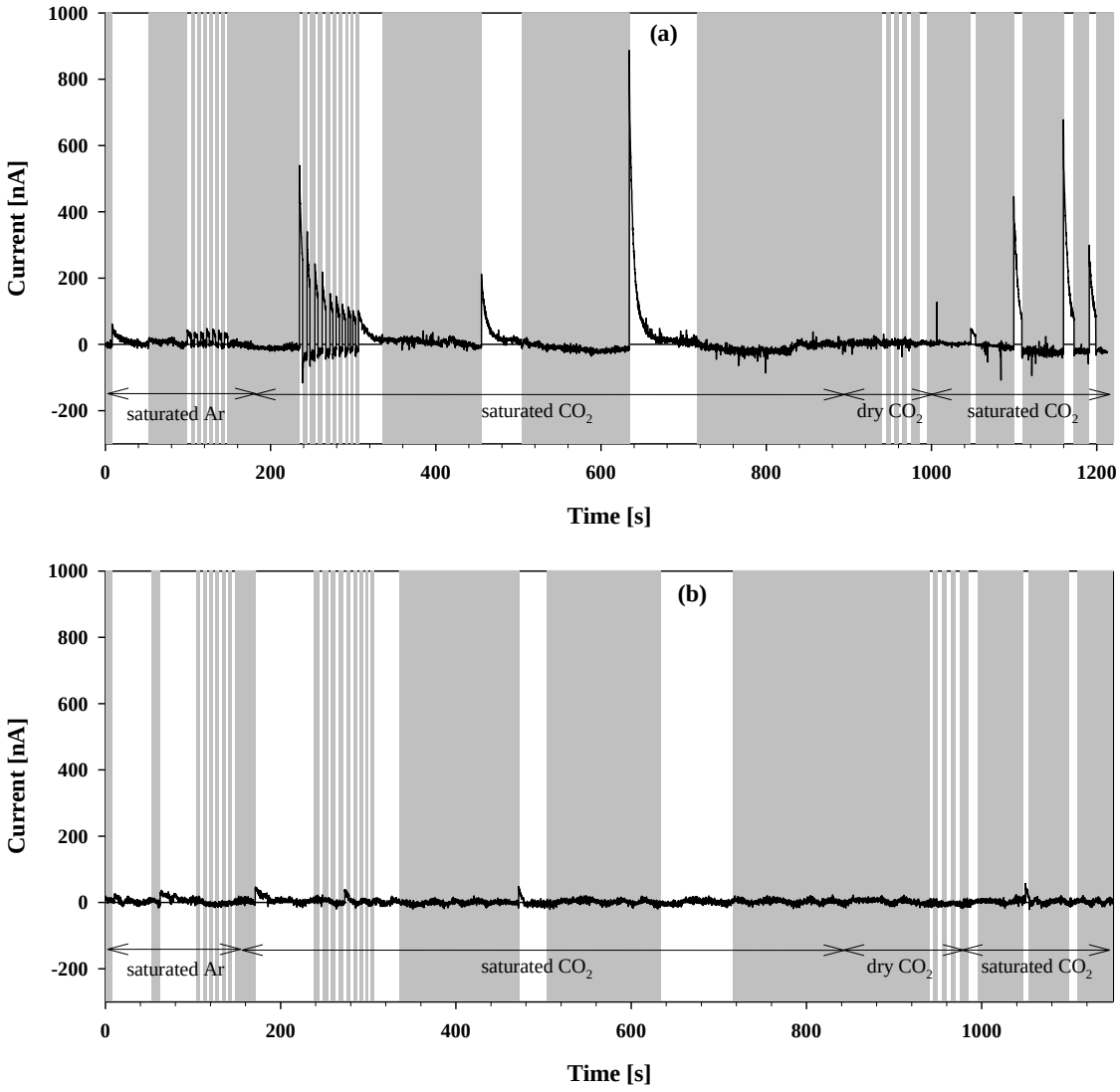

Figure 3-1 proof-of-concept test for PEC115: a) with Nafion® nanoribbon mat connection; b) without Nafion® nanoribbon mat connection. Gray areas indicate durations at which no light is being illuminated on the PEC.

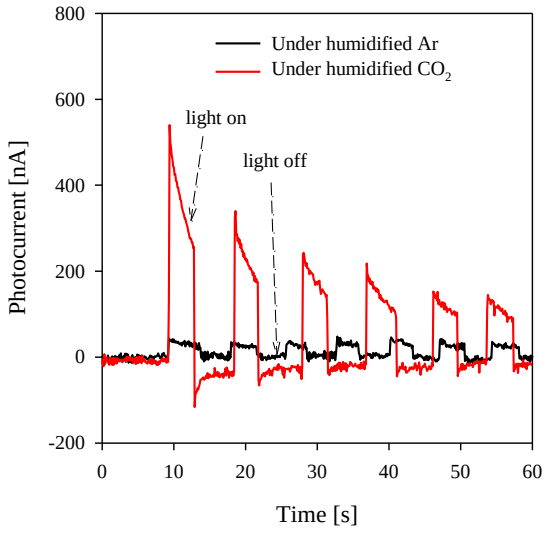

Figure 3-2 Photoelectrochemical test of PEC115 under humidified Ar and humidified CO_2. Drastic increase in generated photocurrent was observed when PEC115 was under humidified CO_2 relative to when PEC115 was under humidified Ar.

The proof-of-concept test was repeated for other PECs made from different catalysts and prepared photoanodes. This time we used a cleaned Cu sheet as the cathode catalyst to make PEC137 and PEC113, as detailed in Table 3-1. The major difference of PEC137 and PEC113 with PEC115 is photoanode of PEC137 and PEC113 was not coated with Co_3O_4 NPs, as water splitting catalyst. The difference between PEC137 and PEC113 is that photoanode of PEC113 has lower V_{OC} and fill factor in comparison to photoanode of PEC137. The hypothesis is because photoanode of PEC113 is able to produce less driving force upon illumination, it may fail to produce high enough voltage to drive simultaneous water splitting reaction and CO_2 reduction reaction. On the other hand, PEC137 is able to produce higher driving force upon illumination; therefore it may succeed to produce high enough voltage to drive simultaneous water splitting reaction and CO_2 reduction reaction. Since no water splitting catalyst exists on PEC137 and PEC113, higher energy barrier and onset potential exits for simultaneous water splitting reaction and CO_2 reduction reaction to occur. Therefore, it is easier to distinct between the two PECs deploying two different photoanodes, in comparison to a case where water spitting catalyst

exists. This test further shows if the observed photocurrent under humid CO_2 atmosphere is related to CO_2 reduction reaction or some other phenomenon because as explained in Section 2.3.1, titled Preparation of the light harvesting component, a minimum electric potential is required for CO_2 reduction reaction to occur. Removal of Co_3O_4 nanoparticles helps to further increase onset potential of CO_2 reaction because CO_2 reduction reaction cannot occur if water, which exists in form of humidity in gas phase, does not dissociate to produce required H^+ cations and e^-. As a result of this higher required electrical potential performance of PEC137 with V_{OC} = 1.89 V should be fundamentally different than that of PEC113 with V_{OC} = 1.52 V.

As shown in Figure 3-2a, significant spikes in photocurrent was observed upon illumination of the PEC. There may a number of reasons associated with this. The first one is recombination of electron/hole is one of the possible explanations for this. In this case, due to inefficient separation of electron/hole pair, the generated pairs recombine and therefore the generated driving force for the CO_2 reaction declines quickly. Another possible explanation may be related to readily available protons for the reaction. In this case, upon illumination of the PEC readily available protons start the CO_2 reduction reaction. However, after a very short time, new protons must be supplied through water splitting reaction, which may not be fast enough to compensate consumption of protons through CO_2 reduction reaction. Therefore, rate of reaction significantly declines. Drying up of the Nafion film may be another explanation for this. In this scenario, upon illumination Nafion losses the water that is already trapped in its pores or absorbed on its surface. Therefore, photocurrent declines due to lack of presence of water for splitting. However, the true cause of such an observation is not known at this stage.

The results for photoelectrochemical tests of PEC113 and PEC137 are shown in Figure 3-3. As shown in Figure 3-3a, when PEC137 was purged with humidified Ar in closed reactor space, a maximum photocurrent of ~ 800 nA was detected when under illumination. However, when

reactor atmosphere was changed to humidified CO_2, generated photocurrent increased to over 1000 nA. When PEC113 was used for the same test, as shown in Figure 3-3b, measured photocurrent under humidified CO_2 was in fact slightly lower than the measured photocurrent under humidified Ar. Therefore, it is concluded that the extra generated photocurrent for PEC137 under humidified CO_2 is related to CO_2 reduction reaction because photoanode of PEC137 was able to produce enough driving force for CO_2 reduction reaction to occur. When PEC113 was under illumination, as shown in Figure 3-4 using I-V curve of PV113 and PV137, corresponding photoanode could not produce enough electrical potential to drive higher energy demanding CO_2 reduction reaction. This logic leads to the conclusion that generated photocurrent under humidified Ar should be related to relatively facile water splitting reaction or recombination of already dissociated water molecules on Nafion® mat.

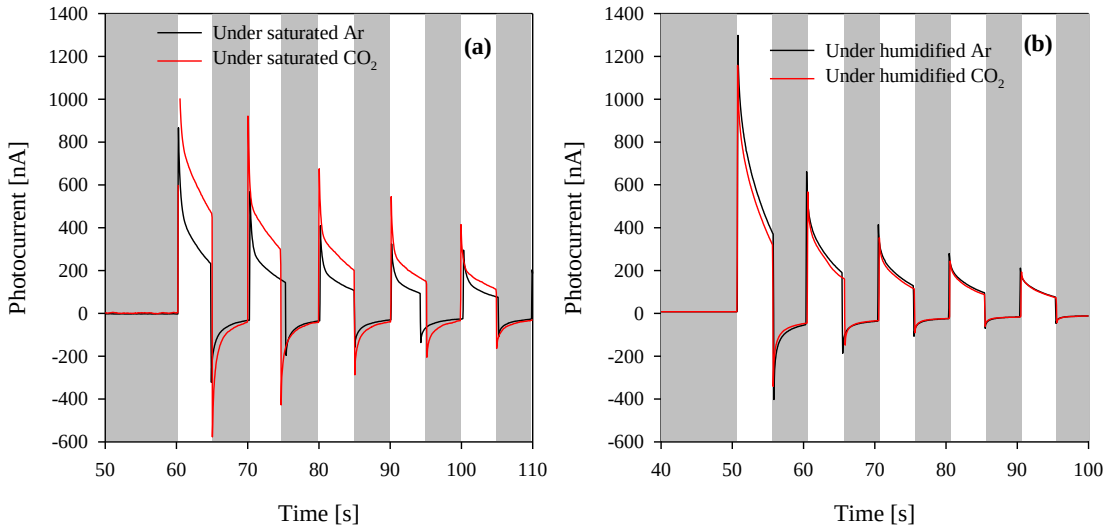

Figure 3-3- proof-of-concept test for a) PEC137 and b) PEC113. Gray areas are related to durations at which no light is being illuminated on the cell.

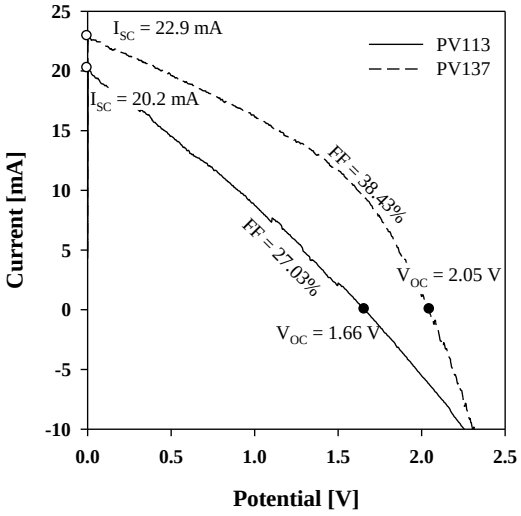

Figure 3-4- IV curves for PV113 and PV137. FF stands for fill factor as defined in caption of Figure 2-2.

A connection between generated photocurrent and water content of reactor atmosphere was observed for PEC113. For PEC113 generated photocurrent under humidified Ar was actually slightly higher than generated photocurrent under humidified CO_2 by 10.1%. This can be explained by considering the fact that Ar, at its water saturation point, can carry more water vapour than CO_2. At 26.6 ℃ (bubbler temperature corresponding to Figure 3-5), specific humidity (SH) of fully water saturated CO_2 gas stream (RH = 100%) is 0.0144 $\frac{g_{H_2O}}{g_{moist\ gas}}$ while specific humidity of fully saturated Ar gas stream (RH = 100%) at the same temperature is 0.0158 $\frac{g_{H_2O}}{g_{moist\ gas}}$. This means at the same temperature, there is 9.7% more water vapour in fully saturated Ar in comparison to fully saturated CO_2. Consequently, it means 9.7% more water vapour was available to PEC113 under saturated Ar in comparison to saturated CO_2 (estimated using Buck equation (*162*)). This value compares favorably with the average ratio of generated photocurrent under humidified Ar and humidified CO_2 at 10.1% (upper value and lower value are 13.9% and 7.5% between illumination intervals, respectively). Although this observation confirms some interconnection exists between concentration of water vapour in reaction

atmosphere and generated photocurrent, it does not provide insight about underlying mechanism of photocurrent generation when PEC is in humid environment. Therefore, using this methodology it is not possible to distinguish between photocurrent generated through full water splitting reaction (electrochemical conversion of H_2O to H^+ on photoanode and H^+ to H_2 on cathode) and photocurrent generated through recombination of H^+ and OH^- ions, which are sourced from dissociation of H_2O on acidic sites of Nafion® mat. We tried to clarify this through electrochemical testing of the assembled PECs in this chapter (section 3.3).

The same photoelectrochemical tests were carried out for PEC182 and PEC175. As shown in Table 3-1, one difference between PEC182 and PEC175 is photoanode of PEC182 was coated with Co_3O_4 NPs at catalyst loading of 0.025 $\frac{mg}{cm^2}$ while photoanode of PEC175 was not coated with any water splitting catalyst. V_{OC} of the PECs were relatively similar at ~ 1 V (0.95 V for PEC182 and 1.10 V for PEC175). The hypothesis is since PEC182 was coated with water splitting catalyst it requires less electrical potential to drive simultaneous H_2O oxidation and CO_2 reduction reactions. Therefore, a meaningful difference between generated photocurrent under humidified CO_2 and humidified Ar should be observed for PEC182. However, PEC175 should produce essentially similar levels of photocurrent under both atmospheres because it cannot produce high enough potential to drive water splitting which in absence of proper catalyst, as observed for PEC113 (V_{OC} of PEC175 is ~0.4 V lower than that of PEC113). Results were as expected, as shown in Figure 3-5. PEC182 produced ~ 5-fold higher photocurrent when tested under humidified CO_2 in comparison to humidified Ar, while PEC175 produced essentially similar photocurrent for humidified CO_2 and humidified Ar. Therefore, although PEC182 and PEC175 had similar photoanodes, existence of water splitting catalyst on PEC182 helped it to lower energy barrier of simultaneous water splitting and CO_2 reduction reactions, and

consequently produce higher photocurrent under humidified CO_2 in comparison to humidified Ar.

The other difference between PEC175 and PEC182 was in cathode area. PEC182 had twice more cathode area available at 10 cm^2 in comparison to 5 cm^2 for PEC175. In theory, if the generated photocurrent corresponds to a set of reactions, higher cathode area should lead to higher rate of reaction and therefore higher generated photocurrent (this may not be true for photocurrent density). Experiments results also support this hypothesis. As shown in Figure 3-5, under humidified CO_2, PEC182 on average produced 1.5 times higher photocurrent than PEC175.

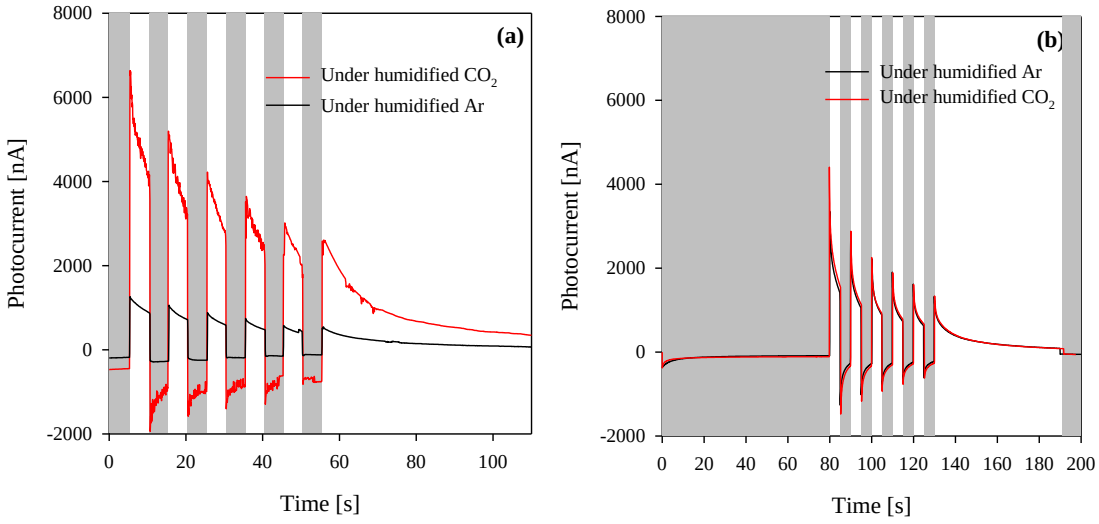

Figure 3-5- proof-of-concept test for: a) PEC182; b) PEC175. Gray areas are related to durations at which no light is being illuminated on the PECs. Test condition for PEC182 under humidified Ar was T = 23.0 °C and RH = 99% (SH = 0.0126 $\frac{g_{H_2O}}{g_{moist\ gas}}$), under humidified CO_2 was T = 23.2 °C and RH = 99% (SH = 0.0116 $\frac{g_{H_2O}}{g_{moist\ gas}}$). Test condition for PEC175 under humidified Ar was T = 24.1 °C and RH = 95% (SH = 0.0129 $\frac{g_{H_2O}}{g_{moist\ gas}}$), under humidified CO_2 was T = 24.8 °C and RH = 92% (SH = 0.0118 $\frac{g_{H_2O}}{g_{moist\ gas}}$).

It was interesting to observe that under humidified Ar, PEC182 produced less photocurrent than PEC175 while both were in relatively similar atmospheres (for PEC182 SH was 0.0126 $\frac{g_{H_2O}}{g_{moist\ gas}}$ and for PEC175 SH was 0.0129 $\frac{g_{H_2O}}{g_{moist\ gas}}$). According to Figure 3-5, PEC182 produced

~ 0.45 less photocurrent than PEC175 under similar humidified Ar atmosphere. This might be related to two factors, which correspond to origin of detected photocurrent when the PECs were under humidified Ar, as explained below.

First, if the origin of the detected photocurrent is related to water splitting reaction (electrochemical conversion of H_2O to H^+ on photoanode and H^+ to H_2 on cathode), then investigation of I-V curves of assembled PECs may provide a clue. As shown in Table 3-1, V_{OC} of the PECs after assembly was different than that of prepared photoanodes. This drop of V_{OC} is related to the installation of heat sinks on the back of the PECs (heat sinks were used to stabilize generated photocurrent. This is throughly discussed in Chapter 4). During installation we had to apply a slight pressure due to the type of heat sinks used. As discussed in Section 2.3.1, applying pressure on a-Si PVs affects their performance. Therefore, I-V response curve of PEC182 and PEC175 was not the same as PV182 and PV175. Consequently, the maximum producible current by PEC182 and PEC175 at water splitting potential is not known at this stage. Thus, there is a chance that PEC182 has essentially less ability to produce current at water splitting potential in comparison to PEC175. This can also be inferred from the fact that PEC182 has lower V_{OC} than PEC175.

Second, if the origin of detected photocurrent is related to recombination of H^+ with OH^- ions, which are sourced from dissociation of H_2O on acidic sites of Nafion® mat, the lower photocurrent of PEC182 may be related to existence of Co_3O_4 coating on photoanode surface of PEC182. For PEC175, path of electrons form cathode to photoanode is Cathode>Nafion®>ITO>a-Si>stainless steel. For PEC182, the path is Cathode>Nafion®>Co_3O_4 NPs>ITO>a-Si>stainless steel. In theory, Co_3O_4 coating on photoanode provides an extra resistance layer for electrons to circulate from cathode to photoanode of PEC182, mainly because Co_3O_4 is relatively non-conductive to electrons (In one study, Co_3O_4 film had a

minimum electrical resistivity of 14.2 Ω cm (*138*). This is ~ 7 orders of magnitude higher than that of Cu sheet). This extra resistance may have caused lower detected photocurrent for PEC182 in comparison to PEC175. The true reason might be a combination of the two above mentioned hypotheses.

Comparing generated photocurrent for PEC182 and PEC137 shows generated photocurrent for PEC182 was roughly 6 times higher than that of PEC137. This difference in photocurrent intensity is most probably related to the structural difference between PEC182 and PEC137. On PEC137 there is no cobalt oxide nanoparticle on the anode surface. Therefore, production of H^+ cations which is required for CO_2 reduction reaction was done by possible catalytic activity of Si or ITO layer of photoanode. Therefore, water oxidation reaction took place at lower kinetic rates. However, for PEC182 the surface of photoanode was coated by cobalt oxide nanoparticles. Since the role Co_3O_4 NPs is to catalyze water splitting reaction and therefore facilitate H^+ cations generation, it is expected that more reaction took place at a given potential difference between cathode and photoanode of PEC182. Therefore, one may conclude higher photocurrent generation when Co_3O_4 NPs exist on the anode surface is simply a reflection of activity of this catalyst for water splitting reaction. Furthermore, this observation may be counted as an evidence of simultaneous occurrence of the two expected water splitting and CO_2 reduction reaction.

In a new test, sensitivity of generated photocurrent with CO_2 concentration in gas phase was experimented. The hypothesis is if the generated photocurrent under humidified CO_2 atmosphere is related to CO_2 reduction reaction, at lower concentration of CO_2 lower photocurrent should be generated. The results of such a test confirmed the underlying hypothesis as shown in Figure 3-6.

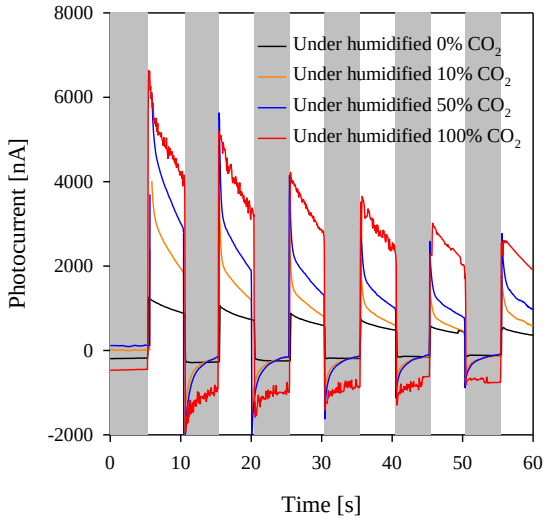

Figure 3-6 Photoelectrochemical test of PEC182 under humidified CO_2 at various CO_2 concentrations. Ar gas was used as balance in all cases. Gray areas indicate durations at which no light is being illuminated on the PEC.

As shown in Figure 3-6, although concentration of CO_2 affected the generated photocurrent, confirming the mentioned hypothesis is true, the correlation between concentration of CO_2 and measured photocurrent does not seem to resemble an Arrhenius like behavior. This suggests at least one physical phenomenon also affects photocurrent generation. This is discussed in detail in Chapter 4 and Chapter 5, where we discuss the reasons behind decline of generated photocurrent with time and CO_2 reduction mechanism on the proposed PECs, respectively.

3.3 Electrochemical experimentation of assembled PECs

To further examine if the detected photocurrent has a reaction root another experiment was designed and conducted. In this experiment, a variable bias was applied to PEC165 from 0 to 5 V while the PEC was not under illumination. This was a two-electrode electrochemical test during which passing electrical current through PEC165 was measured continuously while variable potential was applied. The hypothesis is at some applied potential the applied potential should exceed on-set potential of CO_2 reduction reaction and therefore an increase in measured current should be observed. In this way, we can determine onset potential of water splitting and

CO_2 reduction reactions on PEC165, as an indicative PEC. If the measured current shows continuous uninterrupted increase in the detected current then the detected current is purely due to ionic conductivity of Nafion®, which has been somehow intensified when the PECs were under humidified CO_2. If the current increase continually to a specific potential difference and suddenly step-up to a different level, in a way that an on-set potential can be determined, then that increase in current is related to the minimal activation potential required of a set of reactions. The result of the explained experiment for PEC165 and PEC182 is shown in Figure 3-8 and Figure 3-8, respectively.

For PEC165 bias were applied in two ways, variable continues bias at 0.1 V/s ramp rate from 0 to 5 V (variable continues bias case, see Figure 3-7a) and variable step-wise bias by 0.5 V per step from 0 to 5 V for a minimum of 20 s step time (variable step-wise bias case, see Figure 3-7b). For variable continues bias case (Figure 3-7a), detected current were linear with applied bias up to 1.745 V after which a deviation from expected linear variability and measured current was obvious. For variable step-wise bias test (Figure 3-7b), slope of current with time was considered as the criteria for on-set potential determination. As shown, up to step 4 (2.0 V applied bias) slope of current-time curve was negative (current decreased with time at constant applied bias). At step 5, 2.5 V bias, current-time curve was flat (current did not changed with time at constant applied bias). From step 6 onwards, slope of current-time curve was positive (current increased with time at constant applied bias). This can be viewed from another perspective as well. For step 1 and step 2, the same increase in current was observed per increase in bias potential (~ 500 nA/V). From step 3 onwards, the rate of increase in current accelerated from 732 nA/V at step 3 (1.5 V bias) to 1,550 nA/V at step 9 (4.5 V bias). Therefore, it is concluded for PEC165, first the change in current is non-linear after a specific bias potential,

which confirms the detected current has a reaction origin. Second, a bias of between 1.5–2 V can be considered as the onset potential for a set of reactions involving CO_2 and H_2O.

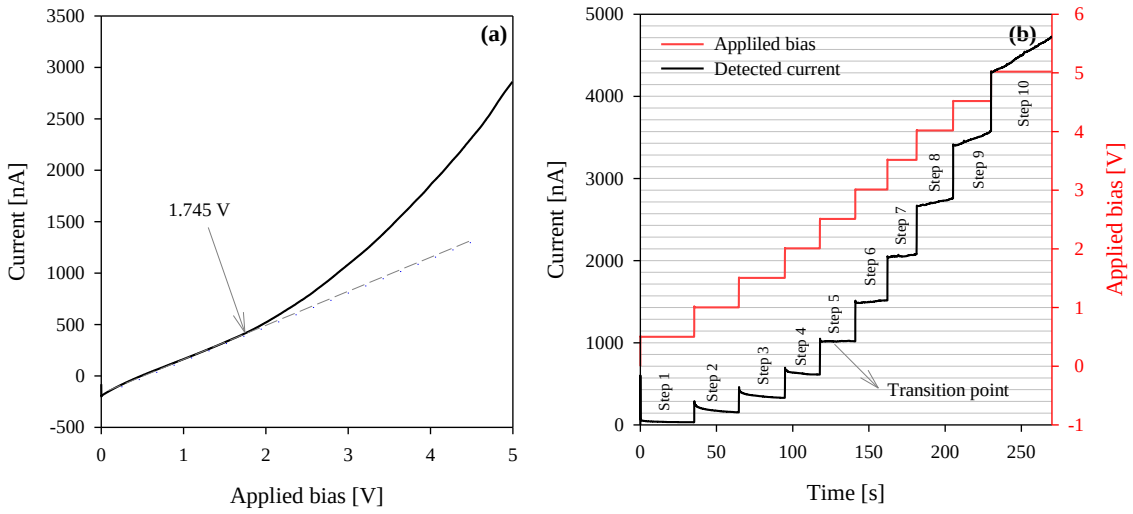

Figure 3-7 Proof-of-concept test for PEC165 when a variable bias is applied to the PEC under no illumination (Co_3O_4 NPs on photoanode, Cu_2O as cathode). The PEC was under continuous purge of water saturated CO_2 at 1 l/min. a) under continues variables bias from 0–5 V; b) under variable step-wise bias from 0–5 V.

Conducting the same experiment for PEC182 provides more insights. As shown in Figure 3-8a, when PEC182 was under humidified CO_2 atmosphere, under variable bias two interruptions to steady increase of current was occurred. The first interruption took place at ~ 10 s after the start of the experiment, corresponding to ~ 0.9 V potential difference between photoanode and cathode (no reference electrode was used in this experiment). The second interruption took place at ~ 15.3 s after the start of the experiment, corresponding to ~ 1.5 V potential difference between photoanode and cathode. When PEC182 was under humidified Ar, only one interruption in current took place at ~ 10 s after the start of the experiment, corresponding to ~ 0.9 V potential difference between photoanode and cathode (see Figure 3-8b). The second interruption at ~ 1.5 V did not occur under humidified Ar atmosphere. This strongly suggests that the first interruption at ~ 0.9 V is related to H_2O vapour because this is the only common component in the atmospheres of the two mentioned experiments. Therefore,

presumably, peak of current at 0.9 V is related to water splitting reaction, during which humidity in gas phase reaction media splits to produce H^+ and e^- which are required for CO_2 reduction reaction. Gaseous O_2 should be formed as reaction by-product. In addition, it was concluded that the second interruption at ~ 1.5 V was related to CO_2 in gas phase because in absence of CO_2 such an interruption did not occur. Therefore, presumably, the second current peak at ~ 1.5 V was related to CO_2 reduction reaction.

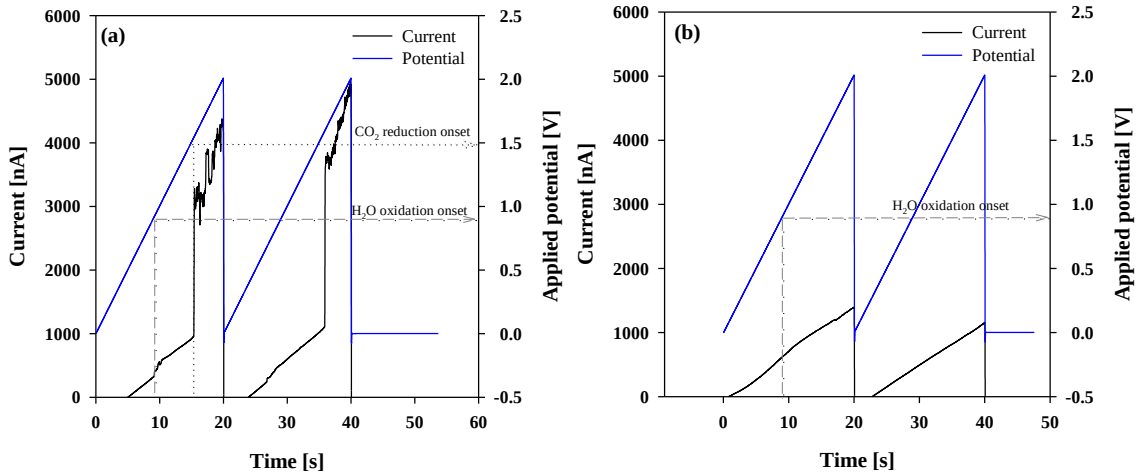

Figure 3-8 Electrochemical experiment of PEC182 when a variable bias was applied to the PEC under no illumination (Co_3O_4 NPs on photoanode, Cu sheet as cathode). The PEC was under continuous purge of water saturated gas at 1 l/min; a) under saturated CO_2; b) under saturated Ar.

Another evidence to support such a conclusion is Cu, which was used as cathode on PEC182, is more active toward CO_2 reduction reaction than H_2 production reaction. A review paper published by Gattrell et al. (*72*) shows in aqueous phase current efficiency of different phases of single crystal Cu toward hydrocarbon production is on average 11.86 times higher than that of H_2 production (this was calculated by diving sum of current efficiencies of CO_2 reduction products, reported in Table 2 of the cited work, to current efficiency of H_2). In PEC182, ratio of measured current before and after second current interruption was ~ 30 (see Figure 3-9 for calculation details). Given that the reaction media for PEC182 was proton deprived at 98% CO_2 and 2% H_2O, it is reasonable that current efficiency of CO_2 reduction relative to H_2 production

be higher than that of aqueous phase reactions. Therefore, this experiment can be counted toward proving that the manufactured PEC is capable of reducing CO_2 to some product, although the only definitive evidence might be detection of formation of some products (solid, liquid, or gas) in the reactor chamber or on the cathode surface. This is discussed in section 3.5.

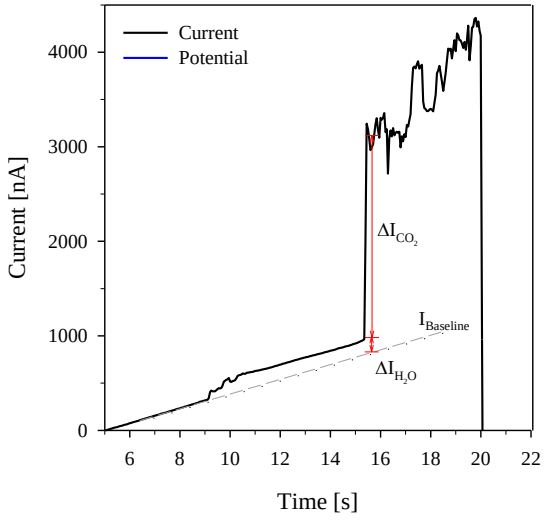

Figure 3-9 Method used for calculation of relative current of CO_2 reduction reaction to H_2O splitting reaction ($\frac{\Delta I_{CO_2}}{\Delta I_{H_2O}} \cong 30$).

3.4 Assisted photoelectrochemical experimentation of assembled PECs

As shown in Table 3-1, PEC182 had a V_{OC} of 0.95 V. Since this V_{OC} is relatively low we tried to repeat the photoelectrochemical test, outlined in section 3.2, but this time with applied bias voltage (to increase available driving force for simultaneous CO_2 reduction and H_2O splitting reaction) and observe the effect of applied bias on generated photocurrent. The hypothesis for this experiment is if the generated photocurrent is truly related to CO_2 reduction reaction, noticeably higher photocurrent should be generated by increasing V_{OC} of PEC182, simply because more driving force for occurrence of CO_2 reduction reaction is available. In this

way, PEC182 can be assisted to drive the desirable CO_2 reduction reactions. The result of the experiment was in agreement with the outlined hypothesis. As shown in Figure 3-10a, in case of applying +1 V bias generated photocurrent was almost doubled relative to unassisted PEC182, on average, throughout six cycles of dark and light tests. If the detected photocurrent for +1 V bias case and no bias case were subtracted by 1,250 nA and −470 nA, respectively, contribution of initial dark electrocurrent from detected photocurrent can be eliminated, as shown in Figure 3-10b (the selected bassline values correspond to the measured current at t = 0 s of experiment when PEC182 was in dark). In this case, applied bias causes photocurrent to increase by 54% in the first cycle and ~ 0% on the fifth cycle.

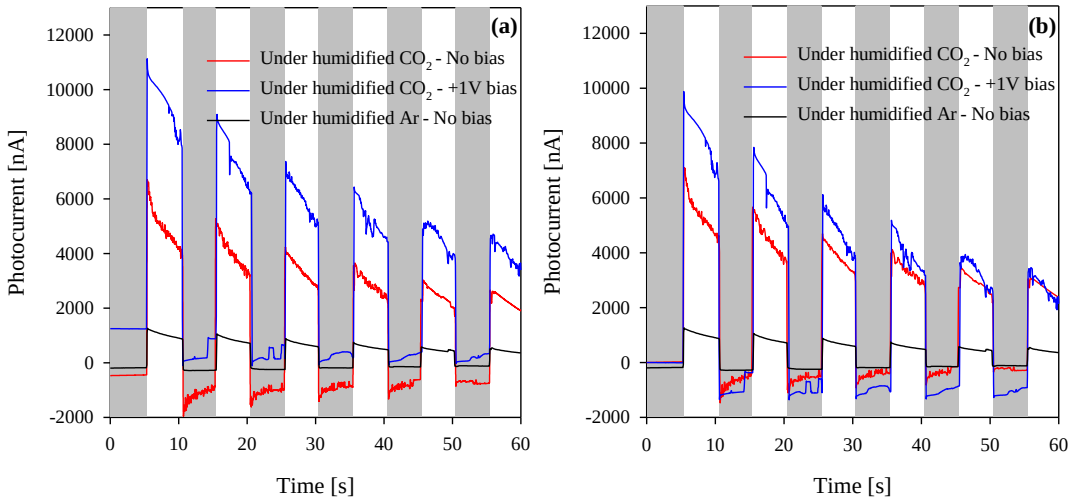

Figure 3-10 Assisted photoelectrochemical experimentation of PEC182 (Co_3O_4 NPs on photoanode, Cu sheet as cathode). Gray areas are related to durations at which no light is being illuminated on the PEC. a) Generated photocurrent without baseline correction; b) generated photocurrent with baseline correction.

3.5 Observation of solid carbon formation

As mentioned in section 3.3, the definitive evidence of successful operation of the proposed PEC is observation of formation of CO_2 reduction reaction product in gas, liquid, or solid phase on the PEC cathode or in reactor atmosphere. At this stage, it is not possible to detect gaseous or liquid products due to low level of generated photocurrent. The maximum photocurrent

generated among all of the tested PECs in this thesis were ~ 10 μA. If we assume all of this photocurrent is resulted from formation of the least difficult to form product of CO_2 reduction reaction (which is CO according to $CO_2 + 2e^- + 2H^+ \rightarrow CO + H_2O$), then 10 μA corresponds to 6.241 x 10^{12} $\frac{e^-}{s}$ which further corresponds to formation of ~ 0.05 $\frac{\text{nmol CO}}{s}$. Given the reactor is under 1 $\frac{L}{s}$ continuous purge of CO_2 (or 0.041 $\frac{\text{mol CO}_2}{s}$), concentration of CO in gas phase would be 0.0013 ppm. This low concentration is far below detection limit of typical gas chromatographer or mass spectrometer. Therefore, we need to look somewhere else for a sign of CO_2 reduction products.

As mentioned in Chapter 2, the goal of this device is to convert CO_2 from gas phase to solid carbon. Conversion of CO to solid carbon is thermodynamically favorable because CO_2 to CO reaction occurs at −0.11 V_{she} (PH = 7) while CO to solid carbon reaction takes place at +0.52 V_{she} (the overall CO_2 to solid carbon reaction takes place at +0.63 V, relative to *she*). Therefore, if our hypothesis is correct we should search the cathode surface for any sign of deposited C. Interestingly, by exploring Cu cathode of PEC182 we observed formation of some black spots on the surface of the Cu cathode. During photoelectrochemical test of PEC182 in the reactor, the surface of Cu cathode has changed color in numerous spots. A digital photograph of PEC182 with the black spots are shown in Image 3-2.

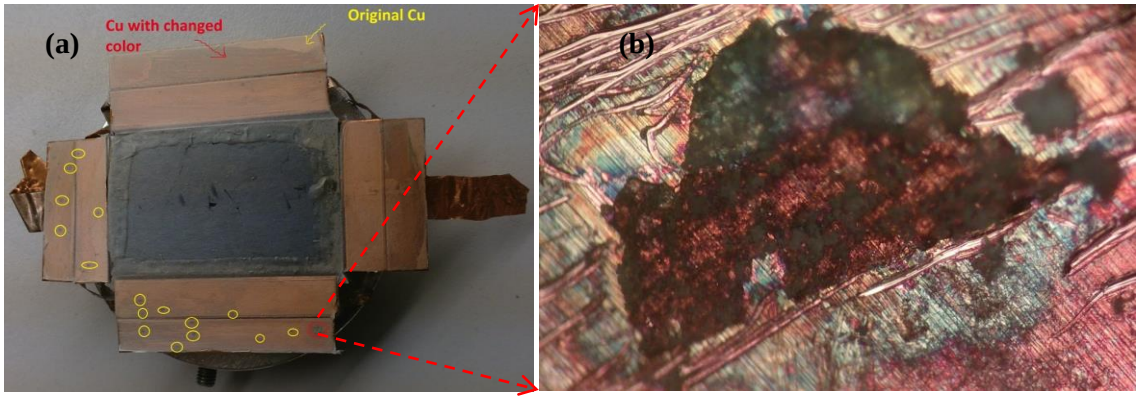

Image 3-2 Digital photograph of PEC182 after photoelectrochemical test under humidified CO_2. a) digital photograph of PEC182 showing formed dark spots; b) Digital micrograph of one of the spots (marked by red circle in the left image) under optical microscope.

Visual observation showed that the dark spots and areas with changed color are under the Nafion® mat. In addition, further analysis showed that the dark area is fully attached to the Cu electrode (it could not be removed by tilting or rising with acetone or ethanol). The block spots were further analyzed using optical microscope and scanning electron microscope (SEM). Specifically, the spot which is marked by a red circle in Image 3-2a is ~ 1 mm in width and 2 mm in height, transparent in visible light (Image 3-2b) but not transparent under SEM (Image 3-3a), had layered structure (inferred from inspecting the edges by SEM, Image 3-3b), and is less conductive than Cu but still conductive (charge accumulation on the surface of the spot as observed in Image 3-3a-b was related to residuals of Nafion® mat on the analyzed spot). Energy-dispersive X-ray spectroscopy (EDS) analysis on the spots showed that the spots mainly consists of C atoms. Full characterization of these spots using optical microscopy, Scanning Electron Microscopy (SEM), Energy Dispersive Spectroscopy (EDS), X-ray Photoelectron Spectroscopy (XPS), Infrared spectroscopy, Raman spectroscopy, Atomic Force Microscopy (AFM), Laser profilometry, UV-Vis spectroscopy, and Time of Flight-Secondary Mass Spectroscopy (ToF-SIMS) is subject of Chapter 5.

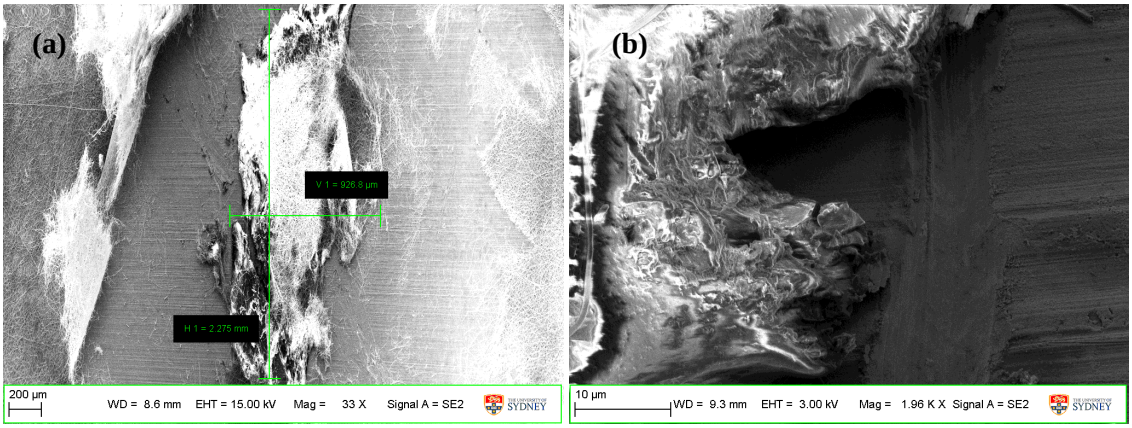

Image 3-3 SEM micrograph of one of the dark spots on the cathode of PEC182. a) showing the whole of one of the spots (marked by red circle in the Image 3-2a) and dimension; b) showing the edge of one of the spots.

3.6 Summary

In this chapter we examine six assembled PECs with different specifications under a variety of conditions including dry and humidified Ar and CO_2 gases, through assisted and unassisted photoelectrochemical and electrochemical tests. Numerous evidences on occurrence of simultaneous H_2O oxidation and CO_2 reduction reactions were found and discussed. The most definitive evidence for successful operation of the PECs was observation of CO_2 reduction products in form of solid carbonous material on cathode of PEC182. From the above mentioned evidences and analysis it was concluded that the designed and assembled PECs are functional in terms of converting CO_2 to some other carbonous chemicals, although chemical nature of the formed chemicals were only briefly discussed here. In-depth insight on the nature of CO_2 reduction products were qualitatively and quantitatively discussed in Chapter 5. In the next chapter, the issue of decline in generated photocurrent with time is discussed in detail, and possible solutions are suggested to minimize or eliminate the problem. Total elimination of photocurrent decline issue leads to stable operation of PEC, which is required for further optimization of its design.

Chapter four

The photocurrent decline

It was shown in Chapter 3 that although PECs which could provide enough driving force for drive CO_2 reduction reaction did produce higher photocurrent in humidified CO_2 atmosphere in comparison to humidified Ar atmosphere, the generated photocurrent declined over time very quickly. Decline of generated photocurrent were not limited to capable PECs, rather it took place for all assembled PECs, irrespective of V_{OC} and reactor atmosphere. In this chapter we try to discover the reasons behind such a photocurrent decline.

There is one critical observation which points us toward the cause of observed photocurrent decline. The observation is, when the PECs is kept in dark (no illumination on the PEC surface), the photocurrent recovered. The experimental data related to this observation is shown in Figure 3-1a. As shown in Figure 3-1, the longer PEC115 were kept in dark, the higher the rate of photocurrent recovery to the point that keeping in dark for 120 s lead to complete recovery of generated photocurrent to the starting value. This suggests that the reason behind photocurrent decline is of physical nature rather than chemical nature because when PEC115, and an indicative PEC, was kept in dark there was no driving force for any reverse reaction to take place, especially at room temperature and atmospheric pressure, and consequently eliminate the chemical cause of decline in detected photocurrent. In addition, the recovery time is not affected by the duration that the PECs were under illumination (see Figure 3-1a). This means, catalyst poisoning cannot be involved here because in case of catalyst poisoning one expects the rate of poisoning to be proportional with the reaction time, which is equal to time under illumination. Based on the observed evidences, four major hypotheses were suggested here to explain this behavior, as detailed in section 4.1. Solutions for confirmed hypotheses through experimentation were suggested in section 4.2.

4.1 Hypotheses on photocurrent decline

4.1.1 Hypothesis 1: Product accumulation on catalyst surface

We observed when we illuminated proper PECs, such as PEC115, PEC182, and PEC165, in humidified CO_2 atmosphere, significantly higher photocurrent was detected. When the atmosphere was switched to humidified Ar, the generated photocurrent was noticeably less. In dry atmosphere (Ar or CO_2) no photocurrent was detected. When the Nafion® nanoribbon mat (proton exchange bridge) was cut (Figure 3-1b), no photocurrent was generated in humidified or dry atmospheres. In addition, the intensity of generate photocurrent highly depended on concentration of CO_2 in the atmosphere (Figure 3-6). For example, lower CO_2 concentration lead to lower photocurrent generation. These pieces of observation, along with others discussed in detail in Chapter 3, proved that generated photocurrent was the result of reactions that occurred on the PECs and the overall rate of reaction depended on concentration of CO_2 in reaction atmosphere. If any reaction is happening, formation of a product is inevitable, as shown in Image 3-2. Therefore, one hypothesis toward the cause of observed decline in photocurrent can be accumulation of reaction products on PEC surface. Whatever this (these) product(s) was (were), it did not poison the catalyst because the loss of photocurrent, and consequently decline of reaction rate, was temporary. If the product(s) was (were) not poisoning the catalyst and it was (were) easily removable from PEC by keeping in dark, which practically removed the driving force for any reaction, then the product(s) has (have) to be liquid or gashouse which can simply evaporate and escape from PEC surface, provided enough time for escape exist. This scape requires some time which is being made available by keeping the PECs in dark while continuously purging off reactants (CO_2 and H_2O) from the reactor environment. To verify this

hypothesis, a simple experiment was carried out. In this experiment, we aim to evaluate the correlation between photocurrent decline and extent of reaction.

A PEC with four cathode surface made of pure Cu sheet with no Co_3O_4 NPs on photoanode was selected for this experiment (PEC137, for details on PEC137 refer to Table 3-1). PEC137 and the reactor was kept under continues purge of humidified CO_2 ($T_{bubbler} = 25$ ℃) for one hour at 0.5 l/min before start of the experiment to make sure Nafion® mat is saturated with reactants (CO_2 and H_2O) and concentration of unwanted gases are minimized in the reactor. This high flow rate means the reactor atmosphere was throughly purged 50 times before the start of the experiment. Then, PEC137 was kept under illumination for very short period of time (< 0.5 s) to measure the initial generated photocurrent. Immediately after the short exposer with light, the counter and reference electrode wires of the potentiostat were disconnected from the PEC. This action simply makes an open circuit for PEC137 and breaks electrical connection between the cathode and photoanode. As the result, no flow of electrons from cathode to photoanode can exist and therefore no photoelectrochemical reaction can occur. After 5 s the wires were connected back and the photocurrent was measured. We repeatedly connected and disconnected the wires in ~ 5 s time intervals. If the photocurrent vs. time curve measured under this condition follows the same trend of the previously measured photocurrent vs. time curves, then hypothesis 1 is not valid. The result of this experiment is shown in Figure 4-1.

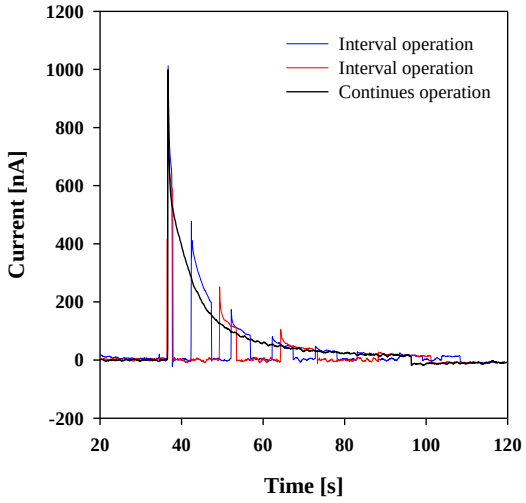

Figure 4-1 Variation of generated photocurrent with time under illumination for continues and interval operation of the PEC137. Experiment was taken under humidified CO_2 atmosphere.

As shown in Figure 4-1, disconnecting the working and counter electrode and as a result disconnecting the electronic connection between photoanode and cathode has minimal effect on the way generated photocurrent declines. Furthermore, comparing the blue line with the red line in Figure 4-1, no obvious change in trend is observable when the time between operation intervals was altered. This is strong evidence that accumulation of products has a minimal role to play on photocurrent decline, if any. Therefore, it was concluded experimental evidences do not support hypothesis 1, and therefore hypothesis 1 is invalid.

4.1.2 Hypothesis 2: Loss of connection between Nafion® mat and photoanode/cathode surface due to thermal expansion

The experiment performed in pervious section clearly showed that drop in generated photocurrent was related to the amount of time PEC137, as an indicative PEC, was under illumination. Therefore, we hypothesis loss in photocurrent is related to incident light, and not occurrence or not-occurrence of any reaction. One possible way that incident light may play a role is through warming the PEC. Incident light is high in energy (1000 W/m^2 or 100 mW/cm^2).

If we assume we used a piece of stainless steel with similar dimensions to that of PEC137, then this amount of incident light is able to increase stainless steel temperature by 17 °C in only one minuet (assumed 3.5 g weight for stainless steel, specific heat of 590 J/kg.K, area of 6 cm^2, and no heat loss using equation (4-1)). Therefore, we need to investigate the effect of warming closely.

$$I_{simulated\ sunlight} \times A_{stainless\ steel} \times t_{incidnece\ time} = m_{stainless\ steel} \times Cp_{stainless\ steel} \times \Delta T_{stainless\ steel} \quad (4\text{-}1)$$

Before proceeding with hypothesizing on the reasons of photocurrent decline based on temperature rise, we designed an experiment in order to measure true temperature rise of the PECs when kept under illumination. In this experiment we measured surface temperature of PEC137 and ambient temperature of the reactor when the PEC was under simulated sunlight using infrared thermometer and k-type thermocouple, respectively. Experiment conduction was similar to that of photoelectrochemical condition outlined in section 3.2 of Chapter 3. Image 4-1 shows a digital photograph of the assembled experiment apparatus. For this experiment the quartz glass window were removed from the reactor to allow measurement of surface temperature of the PEC using IR thermometer. At the same time, V_{OC} of PEC137 was measured continuously to examine any possible correlations between temperature and generated photopotential. The result of this experiment is shown in Figure 4-2.

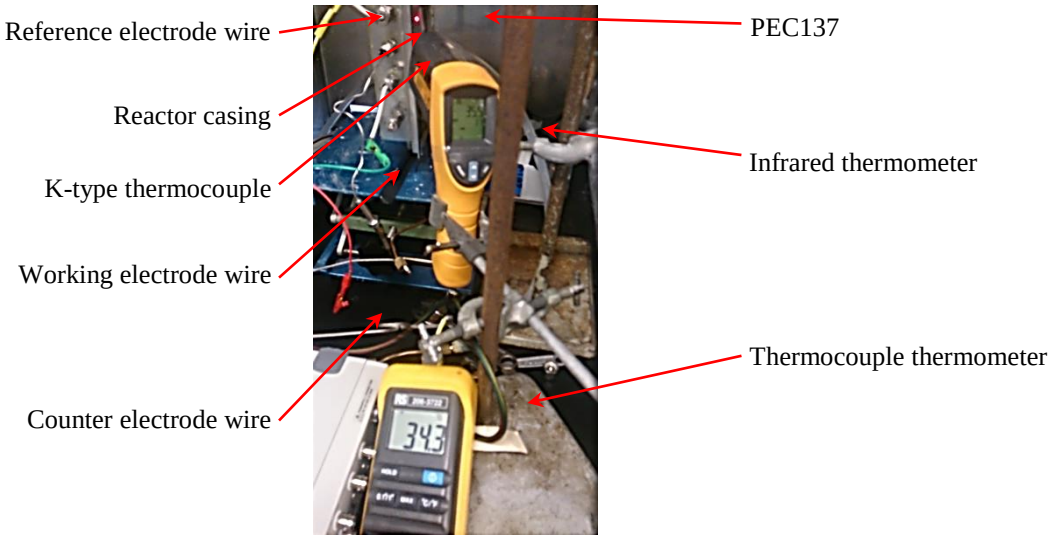

Image 4-1- Digital photograph of simultaneous measurement of ambient temperature of the reactor and surface temperature of PEC137 when the PEC was under illumination of 1 sun simulated sunlight. For measuring reactor ambient temperature, K-type thermocouple was placed directly behind the PEC. Therefore, incident light did not cause direct heating of the thermocouple. The result of this experiment is shown in Figure 4-2. Red spot on the PEC is the laser pointer of the infrared thermometer pointing on the surface of PEC137.

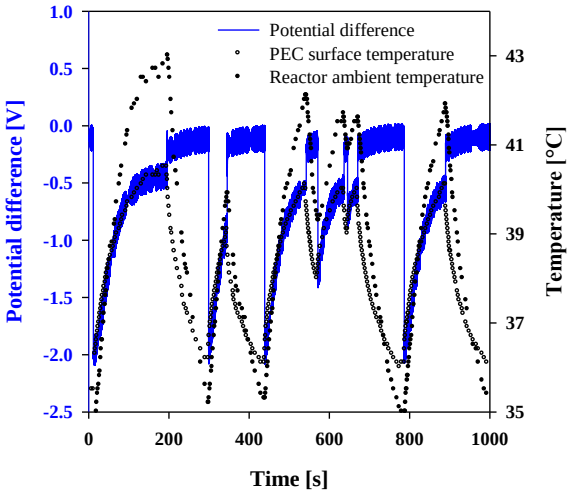

Figure 4-2- Functionality of PEC137 potential difference between PEC137 cathode and photoanode while under 1 sun illumination. The PEC was kept in laboratory atmosphere while performing this test. The experimental setup for this test is shown in Image 4-1.

As shown in Figure 4-2 when PEC137 was under illumination, surface temperature of the PEC raised by over 5 °C during the first 60 s. Raise in the reactor ambient temperature was even higher at ~ 9 °C. This confirmed that the incident light truly causes temperature rise on the PECs and in the reactor environment. Furthermore, the rise in temperature was highly correlated with

produced photopotential by PEC137. When PEC137 was kept in dark, both surface and ambient temperature decreased and PEC137 regenerated to produce high photopotential again. It was determined that PEC137 fully regenerated after 60 s in dark. This resting time is not enough for photoelectrochemical experiments presented in Chapter 3 because in those experiments quartz glass windows does not allow PECs to cool down as fast as what was observed in Figure 4-2. In addition, temperature raise of the PECs under real photoelectrochemical testing condition is higher because due to existence of the quartz window and therefore isolation of reactor environment from the surroundings, heat loss to the environment is lower.

In order to measure potential loss of the PEC under relevant photoelectrochemical condition, PEC137, as an indicative PEC, was place in the reactor that was used for proof-of-concept experiments in Chapter 3. Reactor atmosphere was set to similar conditions by purging the reactor with humidified CO_2 and closing the quartz glass window. While PEC137 was under illumination, operating photopotential and generated photocurrent of the PEC was measured. The results were insightful. Figure 4-3 shows generated photocurrent drops from initial value of ~ 1000 nA to as low as ~ 40 nA within 60 s. At the same time interval generate photopotential dropped from an initial value of ~ 1.4 V to below ~ 0.8 within 60 s.

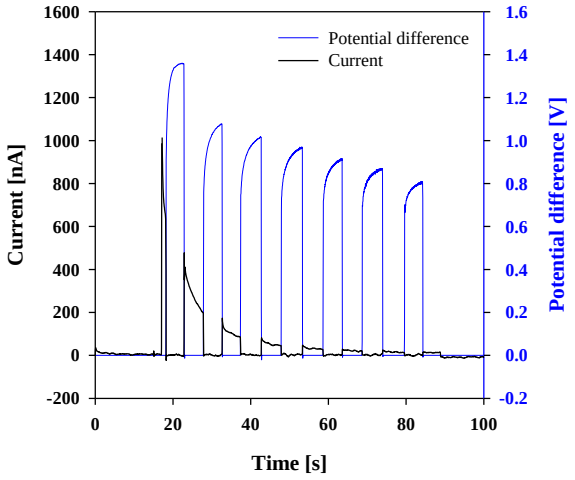

Figure 4-3- Variation of photocurrent and photopotential of PEC137 when under 1 sun illumination while being purged with humidified CO_2 (RH = 97% and bubbler temperature = 27.0 ℃) for 3.5 h at 500 SCCM. The cell was kept in dark for 10 min before this experiment. For measuring photocurrent, counter and reference electrode wires of potentiostat were short-circuited. To measure photopotential counter electrode was disconnected from the PEC.

In a different experiment, only photopotential was measured (see Figure 4-4). Figure 4-4 shows generated photopotential dropped rapidly from ~ 1.7 V to ~ 0.5 V during 110 s under illumination. It is noteworthy that no drop in photopotential was observed when Nafion® coated PVs were tested in laboratory environment for continues illuminations up to 5 minutes.

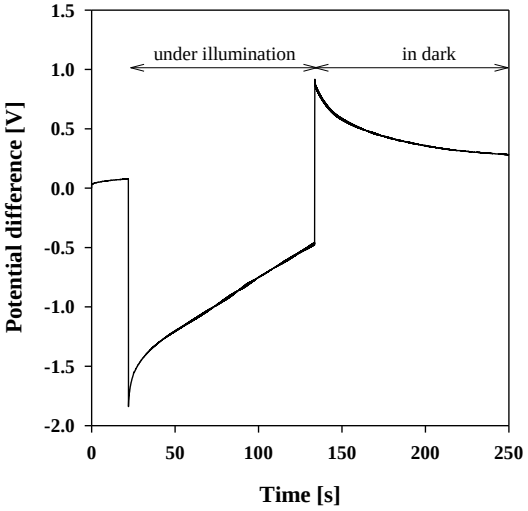

Figure 4-4- Drop of potential difference between PEC137 cathode and photoanode when under 1 sun illumination while being purged with humidified CO_2 (RH = 97% and bubbler temperature = 27.0 ℃) for 3.5 h at 500 SCCM. The cell was kept in dark for 10 min before this experiment.

Based on this observation we proposed hypothesis 2. This hypothesis is based on different thermal expansion rates of different components of the PECs. Hypothesis 2 suggests upon illumination the PECs warm up and as a result all components of the PECs expand, however, at different expansion rates due to difference in thermal properties of the materials used. Since the PECs were assembled at room temperature, expansion at different rates causes the components to lose physical and ohmic connection. This phenomenon may be more drastic at Nafion® mat/photoanode or Nafion® mat/cathode interface, than at interface of Nafion® nanoribbons with each other.

Expansion rate of different components of the PECs are reported in Table 4-1. As shown, Nafion® expands almost 30 times more than steel when exposed to the same temperature raise. This simple calculation suggests hypothesis 2 is theoretically not invalid. In order to test if this hypothesis is true, we designed a new experiment.

Table 4-1- Thermal expansion coefficient of Nafion®, Steel, and SS 304 under 5 °C temperature rise from 35 °C to 40 °C.

Material	Thermal expansion [um/um]	Temperature change [°C]
Nafion® 112	0.035000 (*163*)	from 35-40
Steel	0.001170	from 35-40
SS 304	0.001730	from 35-40

In this experiment, PECs after assembly were thermally treated. The purpose of heat treatment were two things: to enhance mechanical properties of Nafion® nanoribbon mats by welding all individual Nafion® nanoribbons to one single 3D Nafion® structure, and to strengthen physical contact of Nafion®/photoanode and Nafion®/cathode interface. Thermal annealing method were adopted from Ballengee's work (*85*). Successful welding of Nafion® nanoribbon mat was examined using scanning electron microscopy. Initial trials of thermal annealing failed to produce the results reported in Ballengee's work (*85*). Therefore, we tried developing a new procedure by heating Nafion® mat under different atmospheres and at different temperatures for different amount of time. A summary of such attempts and corresponding achieved results are summarized in Table 4-2. All trails on N/G samples (Nafion® mat coated of glass substrate) were failed to produce a well formed 3D welded Nafion® structure. However, we were able to achieve partial (see Image 4-2) and full (Image 4-3) welding for Nafion® mat that were coated on PECs. Therefore, we concluded substrate plays a significant role on thermal annealing performance of Nafion® nanoribbon/nanofiber mat. This point was not addressed in any of Ballengee's work (*85, 148*) nor in relevant literature.

Table 4-2 List of tested experimental conditions for thermal annealing of Nafion® nanoribbon/nanofiber mat. Rows in green are successful trials.

Sample	Duration [min]	T [°C]	Atm.	Sample	Duration [min]	T [°C]	Atm.	Sample	Duration [min]	T [°C]	Atm.
N/G01	10	150	Air	N/G14	20	140	N_2	N/G27	70	150	Vac.
N/G02	20			N/G15		150		N/G28	130	185	Vac.
N/G03	30			N/G16		160		N/G29	430	185	Vac.
N/G04	40			N/G17		170		PEC115	70	150	Vac.
N/G05	50			N/G18		180		PEC137	120	170	Vac.
N/G06	60			N/G19		190					
N/G07	70			N/G20		200					
N/G08	80			N/G21	60	140					
N/G09	90			N/G22		150					
N/G10	100			N/G23		160					
N/G11	110			N/G24		170					
N/G12	120			N/G25		180					
N/G13	130			N/G26		190					

* N/G stands for Nafion® nanofiber on glass substrate, Atm. for Atmosphere, Vac. for Vacuum.

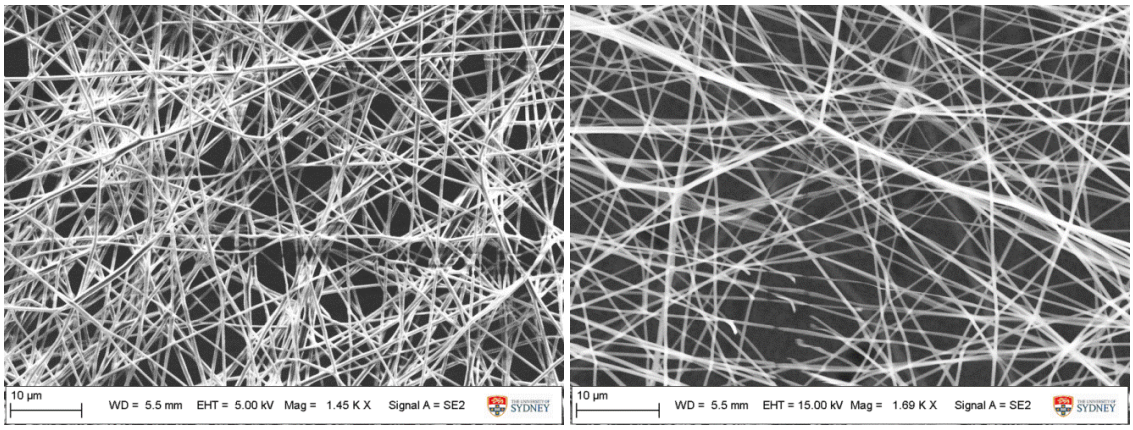

Image 4-2- SEM micrograph of Nafion® nanofiber mat on PEC137. left: before thermal annealing; right: after thermal annealing at 170 ℃ for 2 h under vacuum.

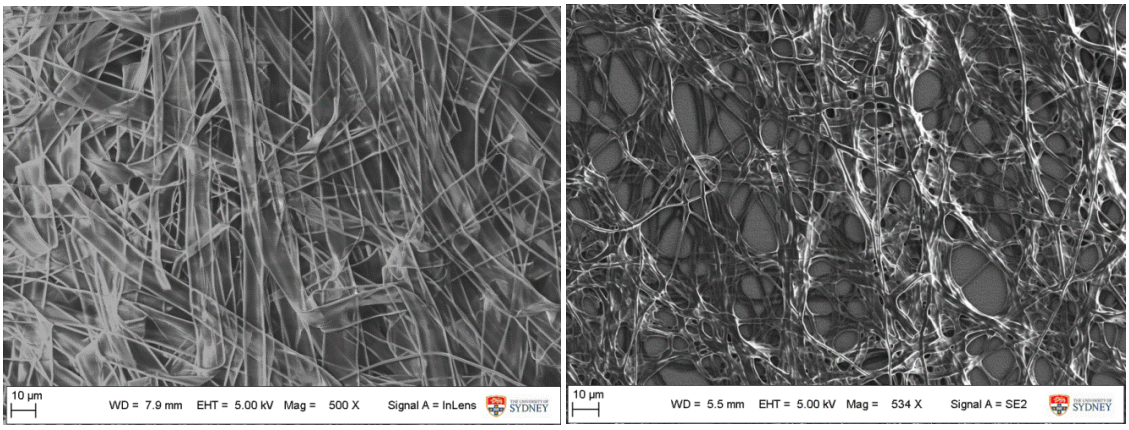

Image 4-3- SEM micrograph of Nafion® nanoribbon mat on PEC115. left: before thermal annealing; right: after thermal annealing at 150 ℃ for 2 h under vacuum.

Thermally annealed PEC137 were tested under similar conditions as outlined in section 3.2 and generated photocurrent was measured. As shown in Figure 4-5, photoelectrochemical testing of thermally annealed PEC137 showed a minor improvement in rate of photocurrent drop. Therefore, although in this section we proved photocurrent drop was related to temperature rise but we failed to significantly improve photocurrent drop by thermal annealing of PECs. It is noteworthy that after thermal annealing, PEC137 had a different appearance. Cu cathode were partially turned red, an indication of partial oxidation of Cu cathode. In addition, Nafion® mat was shrunk after thermal annealing and upon cooling expanded again, resulting in a loose Nafion® mat. Therefore, it is possible to reach to higher degree of improvement in PEC performance by modifying the annealing process. No further experimentation to verify hypothesis 2 was conducted in this thesis.

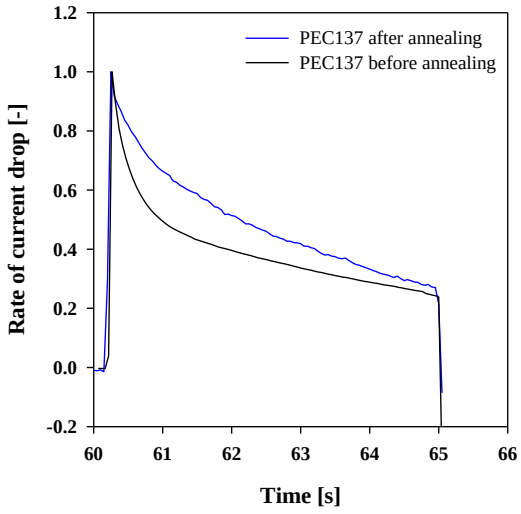

Figure 4-5 Photocurrent drop ratio for PEC137 versus time before and after thermal annealing at 170 ℃ for 2 h under vacuum.

4.1.3 Hypothesis 3: Increase in proton conductivity resistance of Nafion® mat due to rise of temperature

It is well-known that Nafion® proton conductivity changes with temperature and relative humidity. Rieke and Vanderborgh (*164*) reported Nafion® conductivity increased from 25 to ~ 50 °C and then decreased afterwards. Almost a decade later, Sone et al. (*155*) showed proton conductivity of Nafion® decreased from 20 to 45 °C and then increased up to 70 °C, using a more accurate 4-probe AC impedonsymetry. A hypothesis, i.e. hypothesis 3, can be defined based on the variation of proton conductivity of Nafion® at temperature range of 25–45 °C. According to hypothesis 3, the real reason behind decline of generated photocurrent is increase of Nafion® mat resistivity toward proton conduction due to rise of Nafion® mat temperature. In order to verify this hypothesis we must measure functionality of proton resistance of the synthesized Nafion® nanoribbon mat with mat temperature. For this purpose, we coated a piece of glass with Nafion® mat under the same condition as outlined in section 2.3.4 of Chapter 2. Digital photograph of nanofiber coated glass used for this measurement is shown in Image 4-4. The result of proton resistance measurement is shown in Figure 4-6.

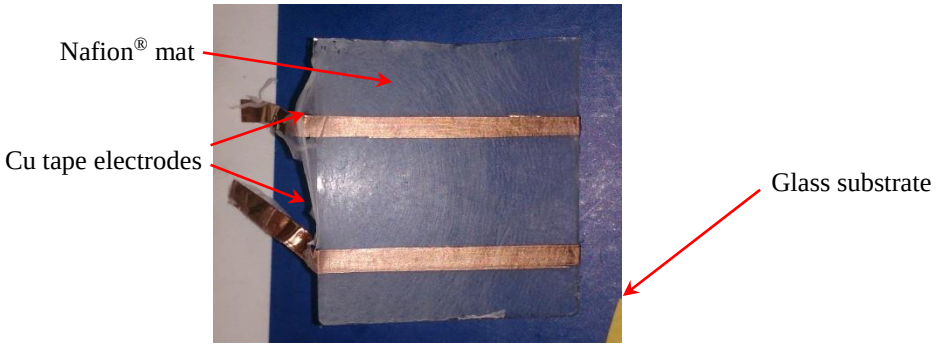

Image 4-4- Digital photograph of Nafion® nanofiber coated glass with Cu tape electrodes (glass length = 20 mm, glass width = 20 mm, Cu tape electrode length = 20 mm, Cu tape electrode width = 2 mm, distance between electrodes = 10 mm). Proton resistance measurement results using this Nafion® nanofiber glass were shown in Figure 4-6.

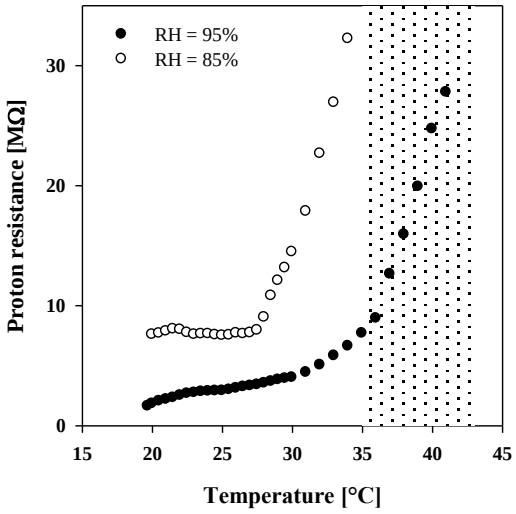

Figure 4-6-Proton resistance measurement versus temperature and relative humidity of Nafion® nanofiber mat. Measurements carried out in humidity chamber where chamber atmosphere temperature was increased gradually (2 ℃/min) while keeping relative humidity constant. Nafion® nanofiber mat was coated on glass substrate where ribbons of copper tape were used as electrodes. Electrodes width were 2 mm and distance between electrodes were 10 mm (Image 4-4). The dotted area shows the region where the assembled PECs operate in current experimental setup. A DC multimeter with a maximum resistance measurement limit of 32 MΩ were used for this experiment.

Figure 4-6 shows proton resistance of the Nafion® mat was increased steadily from 20 to 32 ℃ and then suddenly increased exponentially up to 40 °C when RH = 95%. At RH = 85%, proton resistance remained almost constant in range of 20–27 °C, and then suddenly started to rise drastically. At conditions relevant to the experiments reported in Figure 4-2–Figure 4-4, shown by dotted area in Figure 4-6, proton resistivity of Nafion® mat almost tripled. This shows increase of proton resistivity of Nafion® mat during PEC photoelectrochemical tests can indeed be a major contributing factor to loss of photocurrent in experimented PECs. However, one observations does not fit within this picture. That is almost the same decline in generated photocurrent was observed when the PECs were tested at various temperature ranges (specifically at ~ 23 °C). If decrease in proton conductivity of Nafion® mat due to rise in temperature were the sole major cause of decline in generated photocurrent, then one expects the rate of photocurrent decline to correspond to the measured increase in proton resistance shown in

Figure 4-6. This incompatibility between results suggests the underlying cause for photocurrent decline may not be only one. Based on this observation we propose hypothesis 4 as explained in section 4.1.4.

4.1.4 Hypothesis 4: Increase in proton conductivity resistance of Nafion® mat due humidity loss from Nafion® mat

Hypothesis 4 is proposed based on a totally physical phenomenon. This hypothesis is related to humidity level on surface of the PECs and in atmosphere close to the PECs. According to hypothesis 4, upon illumination, surface temperature of the PECs increases, as experimentally confirmed in section 4.1.2. This temperature rise causes Nafion® mat to dry up and loose humidity, and consequently drastically increases Nafion® mat proton resistivity. At the same time, atmosphere in vicinity of the PECs warms up. This local increase in atmosphere temperature, results in local increase in carrier air temperature and therefore local decrease in relative humidity because, according to psychometric charts of CO_2 and Ar (*165*), at higher temperatures carrier gases can carry more humidity before reaching the saturation point. Decrease in local relative humidity means decrease of local activity of water in gas phase because activity of water in gas phase is directly related to relative humidity ($a_{water} = \frac{f}{f_0} \sim \frac{P}{P_0} = \frac{RH}{100}$ where a_{water} is activity of water, f is fugacity of water in gas, f_0 is saturation fugacity, P is partial pressure of water in gas, P_0 is saturation partial pressure of water, and RH is relative humidity). Consequently, a driving force for evaporation of water from surface of the PECs appeasers upon illumination, a driving force which does not exist before illumination. Thus, according to hypothesis 4, decrease in local relative humidity levels both on surface of the PECs and surrounding atmosphere is the major cause for observed decline in photocurrent.

Although no experiment was designed to prove hypothesis 4, no evidence was also found to disprove it. Therefore, we conclude that the major cause of decline in generated photocurrent is decrease in local activity of water in vicinity of the PECs upon illumination and simultaneous increase of PECs temperature. In next section, we proposed two solutions to coupe with his problem.

4.2 Solutions for photocurrent decline

Based on Hypothesis 3 and 4, we propose two solutions to remove the cause of decline in generated photocurrent of PECs upon illumination. The first solution is to prevent rise of PEC temperature by increasing its weight. The second solution is to conduct photoelectrochemical tests at higher temperatures to eliminate the drying driving force of Nafion® mats on the PECs. These solutions are discussed in detail in sections 4.2.1 and 4.2.2, respectively.

4.2.1 Preventing PECs temperature rise by increasing PECs weight

One way to decrease the extent of temperature rise of the PECs upon illumination is to increase weight of the PECs. Assembled PECs weight between 2–6 g depending on cathode surface area. If we increase their weight by 20 g through installation of thermally conductive material, heat sinks, on the back of the PECs, then theoretically we may be able to limit the amount of temperature rise to < 2 °C. Heat sinks act as additional heat storage mass to absorb the incoming energy from solar simulator through incident light. Actual temperature rise depends on many factors including heat loss and heat gain rates through different mechanisms of heat transfer including conduction, convection, and radiation (the number reported here is only a rough estimation, and is used here only as an indication to understand the temperature change trends. Equation (4-1) was used for temperature rise estimations.). Therefore, installation of heat

sinks to the PECs should result in noticeable improvement in photocurrent decline rate. Image 4-5 shows digital photograph of PEC113, as an example, after installation of heat sinks. Stainless steel bolts were used as heat sinks with a total weight of ~ 20 g.

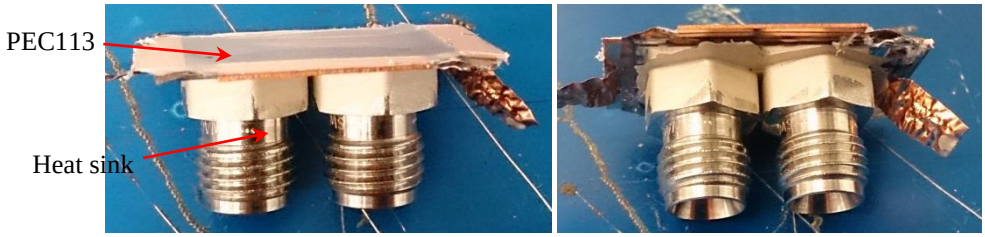

Image 4-5- Digital photograph of PEC113 after installation of heat sinks. Heat sinks were attached to PEC113 using silver conductive paste in this instance.

Performance of PEC113 after and before installation of heat sinks is shown in Figure 4-7. As shown in Figure 4-7, after installation of heat sinks generated photocurrent were significantly stabilized. Photocurrent of PEC113 with heat sinks after 6 times of interval illumination declined less than PEC113 after 2 intervals. In addition, after 110 s of illumination PEC113 with heat sink was still generating higher photocurrent than PEC113 without heat sink at 5^{th} illumination cycle. Although this level of stabilization is not enough for real-life application of the proposed PEC, this experiment shows photocurrent can be stabilized significantly if the PECs were kept isotherm.

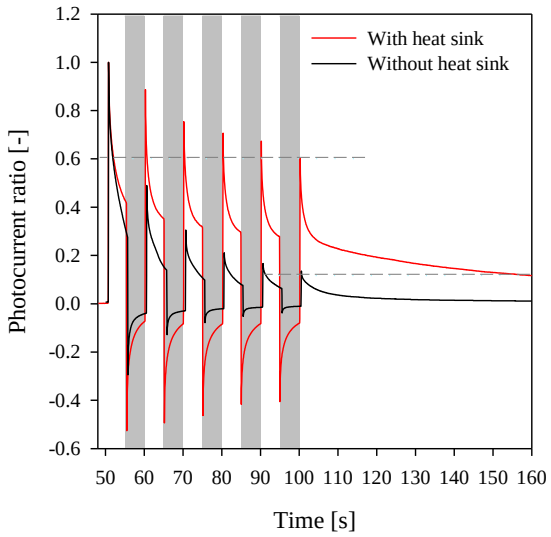

Figure 4-7- Photoelectrochemical test of PEC113 before and after installation of heat sinks. 1 sun simulate sunlight were used as source of light. The reactor was under continuous purge using humidified CO_2 (RH = 96% and bubbler temperature = 27.0 ℃) at 500 SCCM. The PEC was kept in dark for 10 min before this experiment. Gray areas indicate durations at which no light is being illuminated on the PEC. Gray horizontal dashed lines are to facilitated evaluation of effect of heat sinks on photocurrent decline rate.

4.2.2 Conducting photoelectrochemical reaction at higher temperature

Another solution which may be useful in stabilizing photocurrent is to increase reaction temperature. Increasing reaction temperature may benefit PECs operation in two ways. First, it shifts Nafion® mat operating temperature to a temperature range at which, according to literature (*166*), proton conductivity of Nafion® increases with increase of temperature. Therefore, contribution of temperature on loss of proton conductivity of Nafion® mat, as outlined in Hypothesis 3, can be eliminated. Second, at higher temperatures more humidity is available to be swallowed by Nafion® mat and incident light has less driving force to evaporate absorbed water from the PECs, as outlined in Hypothesis 4. However, three major risks may also be involved in raising reaction temperature. First, catalysts used for cathode an photoanode part may not be stable at higher temperatures. Specifically, Cu_2O NRs are less stable at higher temperatures than at room temperature. Cu may also turn to Cu_2O and CuO or $Cu(OH)_2$ at surface at higher

temperatures and under humidity. Therefore, catalyst used may not be able to act as good at high temperatures in comparison to room temperature. Second, product of CO_2 reduction reaction may be different at higher temperatures. Specifically, conversion of CO_2 to CO (an intermediate produce of CO_2 conversion to solid carbon, as discussed in section 5.2) is more favorable at lower temperatures (*38*). Third, a-Si PV loses efficiency at higher temperatures due to higher rate of electron/hole recombination and increased chance of developing microfractures (*167*). Therefore, conducting CO_2 reduction reaction at higher temperature may lead to loss of generated photovoltage and therefore loss of photocurrent through different mechanisms. Thus, although increasing the reaction temperature might be an attractive solution for photocurrent decline problem, it has to be carried out with care.

4.3 **Summary**

In this chapter various possible reasons of decline in generated photocurrent of the PECs were analyzed through hypothesizing and experimenting. It was experimentally confirmed that rise in PEC temperature was the major underlying cause of photocurrent decline although the exact mechanism is subject to debate and further experimentations and verifications. It was found that increasing weight of the PECs by installing a heat sink drastically stabilized generated photocurrent. However, further improvements might be achievable through modifying PEC design or photoelectrochemical testing conditions.

Chapter five

Characterization of CO_2 reduction product

As reported in Chapter 3 section 3.5, after a number of light ON/OFF cycling tests using PEC182 under humidified CO_2 atmosphere, color of copper cathode was changed and blackish deposited materials were formed on multiple locations under Nafion® nanoribbon mat (Figure 5-1A). The dark spots, hereafter referred to as "deposited material", were characterized using optical microscope and Scanning Electron Microscopy in section 5.1.1, Atomic Force Microscopy in section 5.1.2, Energy Dispersive Spectroscopy in section 5.1.3, X-ray Photoelectron Spectroscopy in section 5.1.4, Infrared and Raman spectroscopy in section 5.1.5, Time of Flight-Secondary Mass Spectroscopy in section 5.1.6, and UV-Visible spectroscopy in section 5.1.7. Based on the observed evidences and detected properties of the deposited material, a mechanism of CO_2 reduction on PEC182 is also suggested in section 5.2.

5.1 Characterization of the deposited material

5.1.1 Optical Microscopy and Scanning Electron Microscopy (SEM)

In order to gain an insight on morphology of the deposited material we first used Optical Microscopy and Scanning Electron Microscopy. Figure 5-1A shows a number of deposited materials that was formed on PEC182. For consistency sake, we chose the biggest deposited material in size and focused our characterization effort on that spot. This spot is highlighted by a red circle in Figure 5-1A. Figure 5-1B is the deposited material under optical microscope. The deposited material on this spot was ~ 2 × 1 mm in dimension and it was formed under the Nafion® mat, as expected. Therefore, in order to characterize the deposited material we had to peel off Nafion® mat using tweezers. Figure 5-1B shows the deposited material is semi-transparent to yellow light. It was found that under lower wavelength light, the deposited material has lower transparency (see section 5.1.7). This indicates possible semi-conductive properties of the deposited material, which may have played a role in further reduction of CO_2.

This is discussed further in section 5.1.7. However, it was inferred thickness also plays an important role because in thicker areas deposited material appeared non-transparent (Figure 5-1B and D). Surface morphology may also have played a role because morphology of surface may affect light penetration and reflection from the deposited material. Furthermore, the deposited material is highly conductive (inferred from absence of charge accumulation under SEM at low and high electron gun voltages shown in Figure 5-2A), highly porous in many spots (see Figure 5-2C, pore diameter ~ 0.05–1 μm), has multiple layers (see Figure 5-1D and Figure 5-2C–D, layer thickness ~ 30 nm), and consists of nanorods (Figure 5-1C and Figure 5-2E–G, diameter ~ 50 nm, height ~ 400 nm), sheets (Figure 5-2B–D), and nanoparticles (Figure 5-2H–J, diameter 10–50 nm) morphologies. Layered morphology indicates the deposited material was formed layer by layer. Therefore, it should have self-assembly properties along with catalytic activity for CO_2 reduction, therefore allowing continuation of growth of deposited material rather than blockage of reaction sites (the deposited material is ~ 20 μm thick, see section 5.1.2). A variety of analytical techniques were used to in a search for other evidences of self-assembly properties of the deposited material throughout this chapter. Catalytic activity for CO_2 reduction was previously reported for graphenic materials (*168, 169*) through nanoconfinment mechanism (*170-172*). Analysis of deposited material using EDS (section 5.1.3) showed the deposited material consists of 80–84 at% carbon and 3–5 at% oxygen (similar results were obtained using XPS, see section 5.1.4.3). High levels of carbon were also detected in areas were no visible sign of deposition was observed through EDS mapping (18 at% vs. 8 at% for as received copper sheet, see section 5.1.3). Uniform distribution of atomic composition of carbon and oxygen were confirmed through EDS mapping (see Figure 5-5 and Figure 5-6 in section 5.1.3).

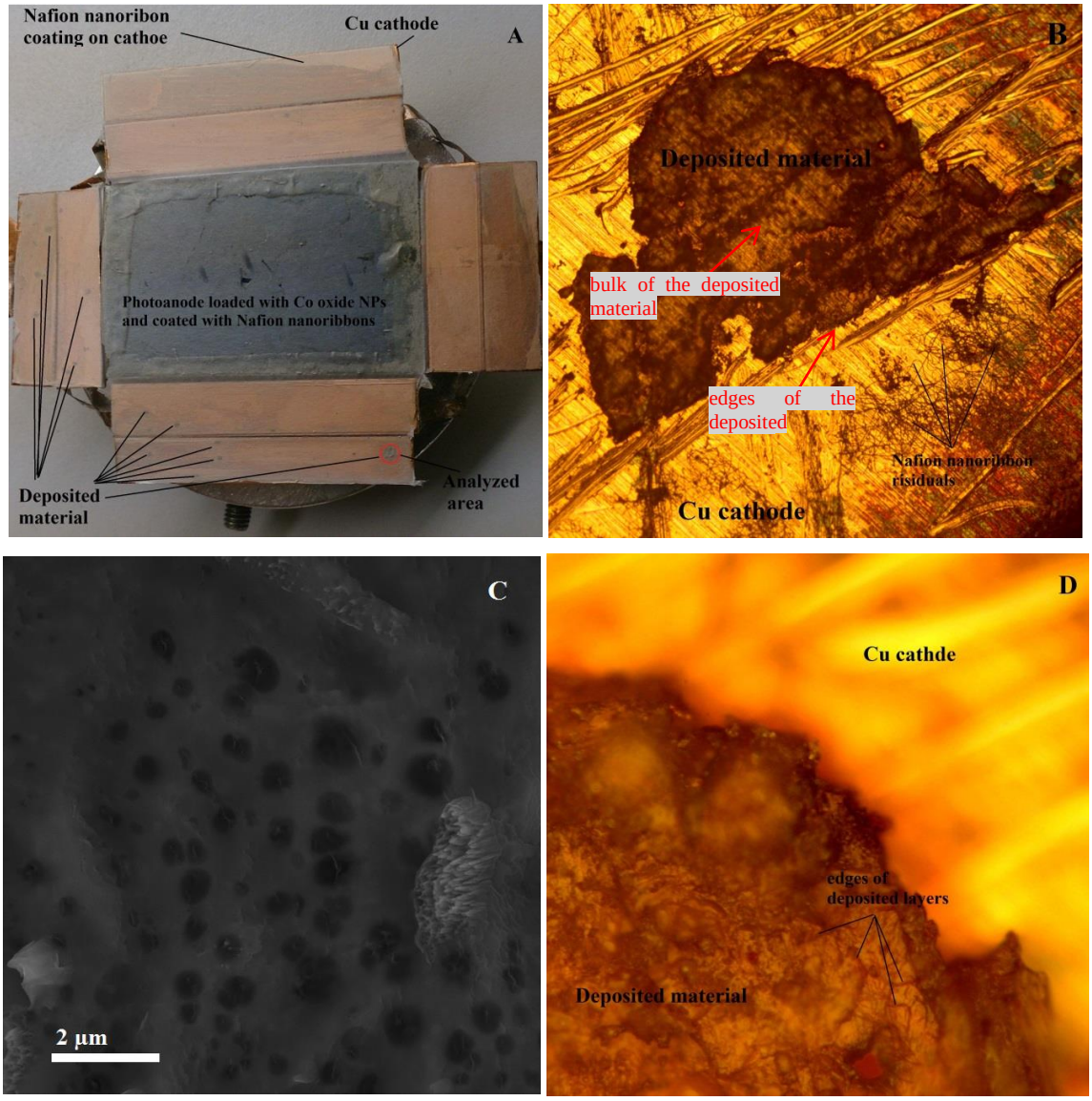

Figure 5-1 (A) Digital photograph of the PEC with copper sheet as cathode catalyst in side-by-side configuration after reaction under humidified CO_2 environment under solar simulator at 1 sun intensity. Color of copper cathode was changed and CO_2 reduction product were deposited on cathode forming deposited materials. The spot highlighted with a red circle was used for detail analysis because it was the biggest bulk of deposited material. (photoanode area = 5.5 cm^2, cathode area = 10 cm^2). (B) Optical microscope image of the deposited material. (C) SEM image of the deposited material using secondary electron detector at 10 kV showing the deposited material has porous structure. In addition, special formations resembling carbon nanorods were also observed (see Figure 5-2). (D) Edges of the deposited material under optical microspore. Edges of different layers of the deposited material is observable in this image. The yellow color is reflection of light from copper cathode substrate. Observation of dimmed yellow color is a sign of semi-transparency of the deposited material at yellow wavelength.

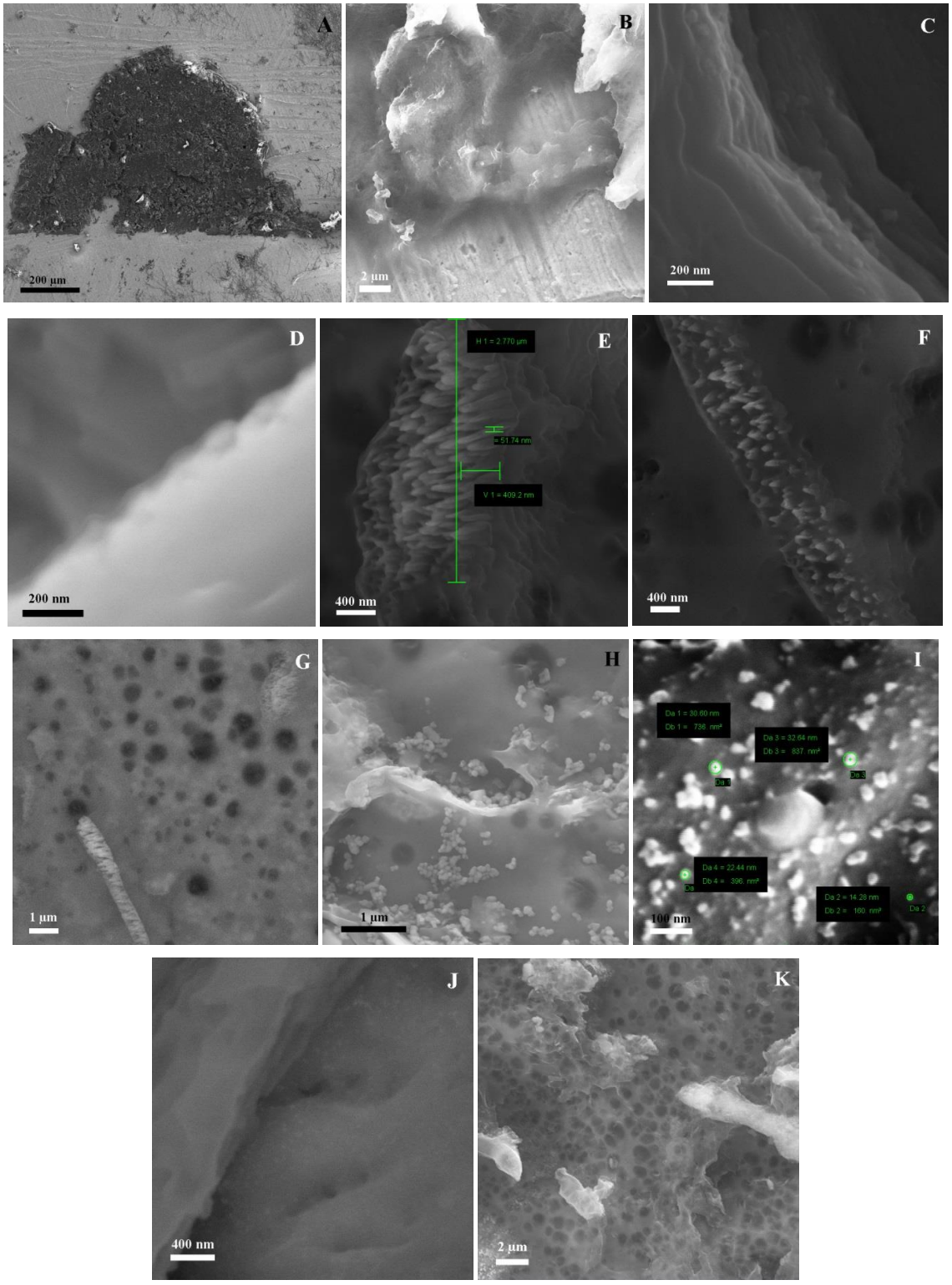

Figure 5-2 SEM micrograph of the deposited material at various locations and using various detectors. (A) The analyzed deposited material using secondary electron (SE) detector at electron gun voltage of 20 kV. Bright area, showing high charge accumulation, are residuals of Nafion® nanoribbon mat, confirmed by EDS analysis

shown in Figure 5-5 (B) Graphenic morphology can be seen in this micrograph. The deposited material is extremely thin at the edges. (C) Micrograph providing evidence of layered structure of the deposited material at high magnification using SE detector. Some carbon nanoparticles are observable in this micrograph. (D) High magnification micrograph from edges of the deposited material revealing individual layers of carbon. (E) Micrograph of nanorods formation and the dimensions using SE detector. (F) Micrograph showing early stages of nanorods formation on the deposited material. (G) Micrograph of carbon nanorods using back scattered (BSE) detector revealing extreme similarity in elemental composition of the rods and bulk of deposited material. (H) Micrograph of carbon nanoparticles formation using SE detector. Formation of sphere carbon nanoparticles were observed during synthesis of carbon aerogels (*173*) (I) Micrograph of carbon nanoparticles and the dimensions using InLense detector providing topography information. (J) Micrograph of carbon nanoparticles using back scattered (BSE) detector revealing extreme similarity in elemental composition of the rods and bulk of deposited material. (K) Micrograph of porous structure of the deposited material using SE detector.

5.1.2 Morphology examination using Atomic Force Microscopy (AFM) and Laser profilometry

To confirm porous structure that was observed under SEM is not an artifact, we used atomic force microscopy to derive topology information from the deposited material. Using high resolution AFM, height profile of a small area of the deposited material (5 × 3 μm) were measured, as shown in Figure 5-3. Using this technique we were able to confirm existence of pores with the same dimension range of what was observed under SEM. Pores with diameter range of 0.2 μm up to 0.8 μm was observable in the scanned area. We were not able to scan a bigger area due to extreme non-uniformity of the deposited material. Tip of AFM frequently hit the material, disturbing measurement process. As shown, in the small analyzed area height of the deposited material was varied from +400 nm to −400 nm with sharp gradient in some locations (showing the deposited material had a minimum thickness of 800 nm). Therefore, we were not able to measure the thickness of the deposited material using this technique. In order to get an estimation of the thickness of the deposited material we used Laser profilometry,

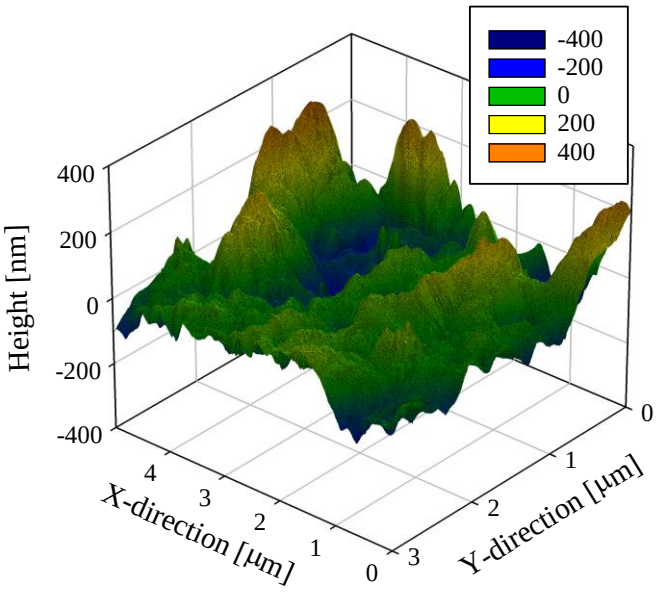

Figure 5-3 Height profile of the deposited material, measured using Atomic Force Microscopy (AFM) at scan resolution of 200 points per µm (4.85 nm per point), showing high roughness of surface of the deposited material. The high roughness effects IR absorbance intensity by affecting pathlength of IR through the sample.

Laser profilometry uses a beam of visible light to detected the distance between the sample and the detector through interface pattern analysis (*174*). Using this technique height profile of the whole deposited material was measured. According to those measurements, the deposited material had an average thickness of ~ 20 µm (see Figure 5-4). Because the deposited material was transparent to visible light in some spots (as seen in Figure 5-1B), profilometer were not able to provide a good measurement of height throughout the sample.

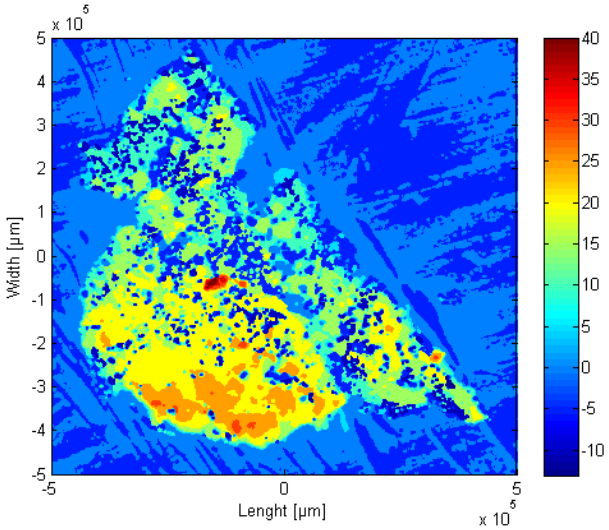

Figure 5-4 Height profile of the deposited material, measured using white light laser profilometry. Color scale in µm.

5.1.3 Energy Dispersive X-ray Spectroscopy (EDS)

We used EDS to determine elemental composition of the deposited material in various spots. Using EDS mapping, we measured elemental composition of the deposited material. As shown in Figure 5-5, carbon (shown by blue color) is dominantly exists almost uniformly throughout the deposited material while, as expected, copper (shown by orange color) is dominant were deposited material does not exist. In addition, carbon deposits also exist in areas surrounding the deposited material in from of islands. Residuals of Nafion® mat is identifiable by high fluorine content, shown by green color (atomic ratio of F:C in Nafion® is 2:1, see Scheme 2-7). Oxygen is also fairly uniformly distributed throughout the deposited material and in some spots on surface of copper cathode. Individual elements are shown in Figure 5-6 for better visibility.

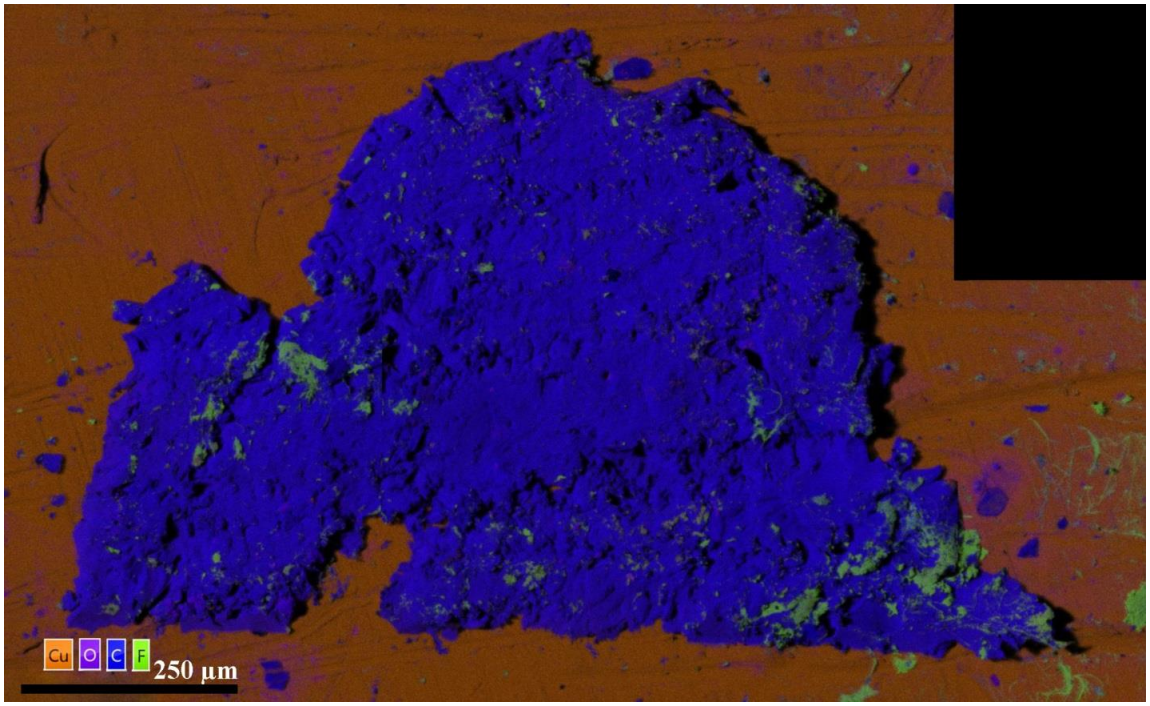

Figure 5-5 Elemental composition of the deposited material and surrounding areas using Energy dispersive x-ray spectroscopy (EDS) mapping showing uniform distribution of carbon and oxygen throughout the deposited material. Dominance of carbon is visible in this image. Residuals of Nafion® nanoribbon mat were observed, indicated by fluorine element, shown with green color. Nafion® mat were physically peeled off before spectroscopy. Individual elements are shown in Figure 5-6. This is a TruMap, meaning the intensity of each color is representative of atomic abundance of the corresponding element.

EDS mapping were also performed on the whole area of one of the eight cathodes of PEC182 to see if carbon was deposited in other spots which were not visible by naked eye (PEC182 was consisted of four 30 × 5 mm copper sheets and four 20 × 5 mm copper sheets as cathode, as shown in Figure 5-1A). The resulted map is shown in Figure 5-7.

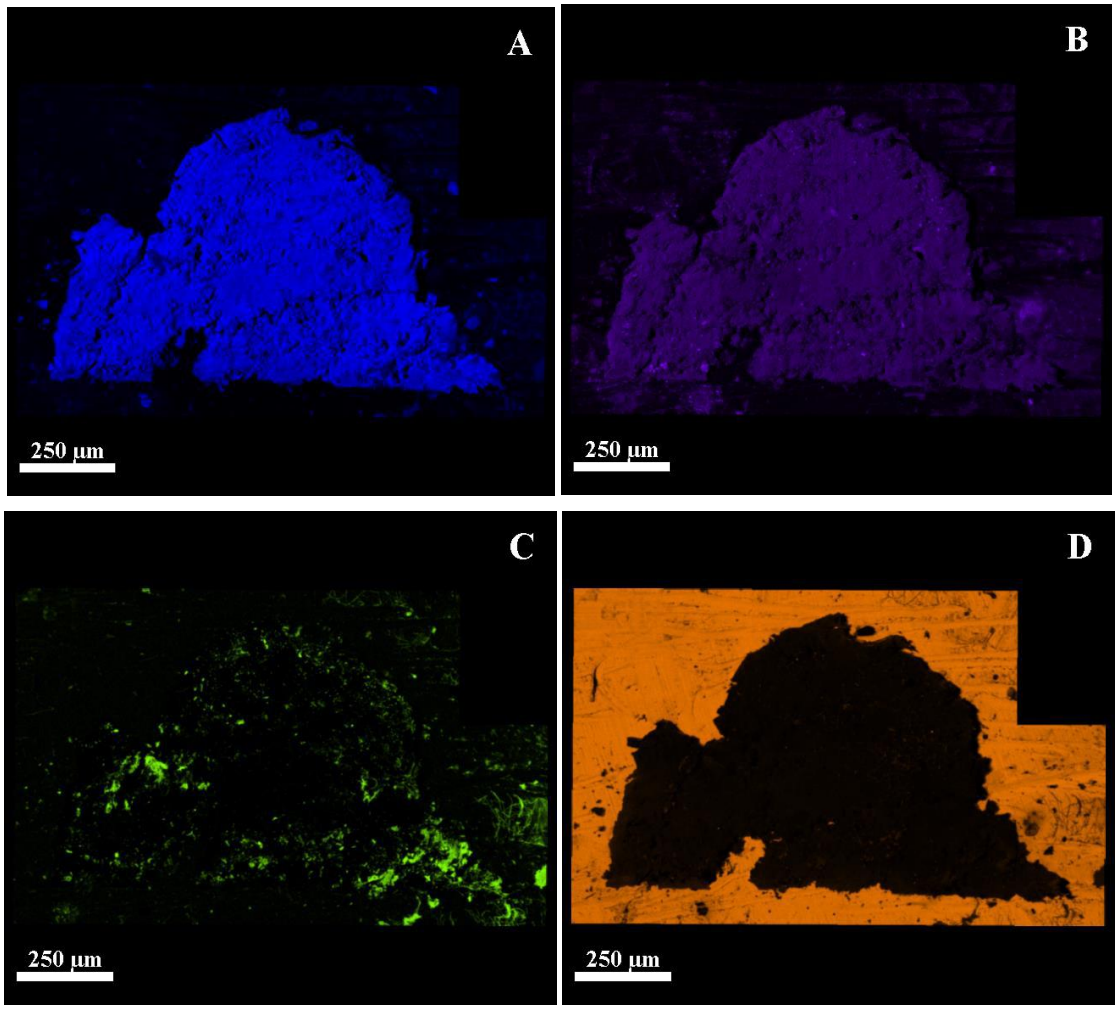

Figure 5-6 Distribution of different elements on the deposited material and surrounding area using Energy dispersive x-ray spectroscopy (EDS) showing the deposited material was mainly consist of carbon (C) and oxygen (O). Fluorine (F) signals are sourced from Nafion® mat residuals on the surface of deposited material and copper cathode. The overlay image is shown in Figure 5-5.

In this figure, carbon is shown by bright green color. Blue color corresponds to flouring which is related to Nafion® mat. As highlighted by red markers, islands of carbon were formed in various sizes throughout the inspected cathode. Furthermore, fair amount of carbon were also detected in areas were Nafion® mat was not removed successfully (residuals of Nafion® mat were not visible by naked eye). This shows probably some portion of deposited carbon on cathode were lost during Nafion® mat removal process.

Figure 5-7 High resolution EDS map of one of PEC182 cathodes (30 × 5 mm). Orang, blue, purple, and bright green corresponds to Cu, F, oxygen and carbon elements, respectively. For better visibility, areas with high amount of carbon are marked by red markers. Only some of the areas where intense carbon signal were detected are marked. This is a TruMap, meaning the intensity of each color is representative of atomic abundance of the corresponding element. Nafion® mat was peeled off from the cathode, then the cathode was lightly raised with acetone and ethanol to remove residuals of Nafion® from cathode surface. The remained residues of Nafion®, shown with blue color on right side of the image, were not visible with naked eye.

In order to gain quantitative understanding of the amount of deposited carbon area mapping (LayerMap), line scanning (QuantLine), and dot scanning (Point&ID) were used. For all of the EDS analysis Aztec software, OXFORD Instruments, were used. LayerMap of a small portion of the deposited material is shown in Figure 5-8A. As shown in this figure, over 71 wt% carbon, 6.6 wt% oxygen was detected on the deposited material. Cu, and sulfur were also detected in this spot. EDS technique is generally known to be a surface technique. However, by manipulating electron gun power one may change the penetration depth of X-ray signal to limit analysis on surface of the sample or collect information form the bulk as well as the surface of the sample. For this analysis, 20 kV electron gun voltage was used to collect elemental data from the bulk of the sample as well. It was confirmed that this voltage was enough by detecting copper signal from the surface of the deposited material. Copper was the substrate of the deposited material. Detecting copper on the deposited material means the gun power is high enough to excite X-ray from the substrate as well as the deposited material. Sulfur may be detected due to contamination of the sample, however not effort was made to determine source of sulfur signal, because it was not detected in all deposited material, as confirmed by XPS in section 5.1.4.

While investigating PEC182 cathode under SEM using secondary electron detector we noticed the cathode was relatively dark and blur in some areas. We used QuantLine line scanning to confirm if these areas were associated with early stages of formation of the

deposited material. As shown in Figure 5-8B, copper wt% drastically decreases in the mentioned area followed by increase in carbon wt%. It is shown in Figure 5-8C that as received copper sheets, which was used as raw material of PEC182 cathode, has an average of 9.3 wt% carbon. However, it was found during QuantLine line scanning that in many area carbon wt% was significantly higher than 9.3 wt%. Spots at which carbon content was over 20 wt% on PEC182 cathode is shown with red dots in Figure 5-8B. In some spots, carbon content were as high at 40 wt% (78 at%). This high level on carbon was not observed on as received copper sheet during through examination. As can be seen these areas do correspond to dark and blurry areas. Therefore, from evidences shown in Figure 5-8 and Figure 5-7, it was concluded these small islands of carbon are in fact early stages of formation of the bigger carbonous spots.

Although EDS is a very strong tool for elemental analysis, it does not provide insight into chemical state of the detected elements. For that purpose we used X-ray Photoelectron Spectroscopy in section 5.1.4 and carried out a through examination of the deposited material.

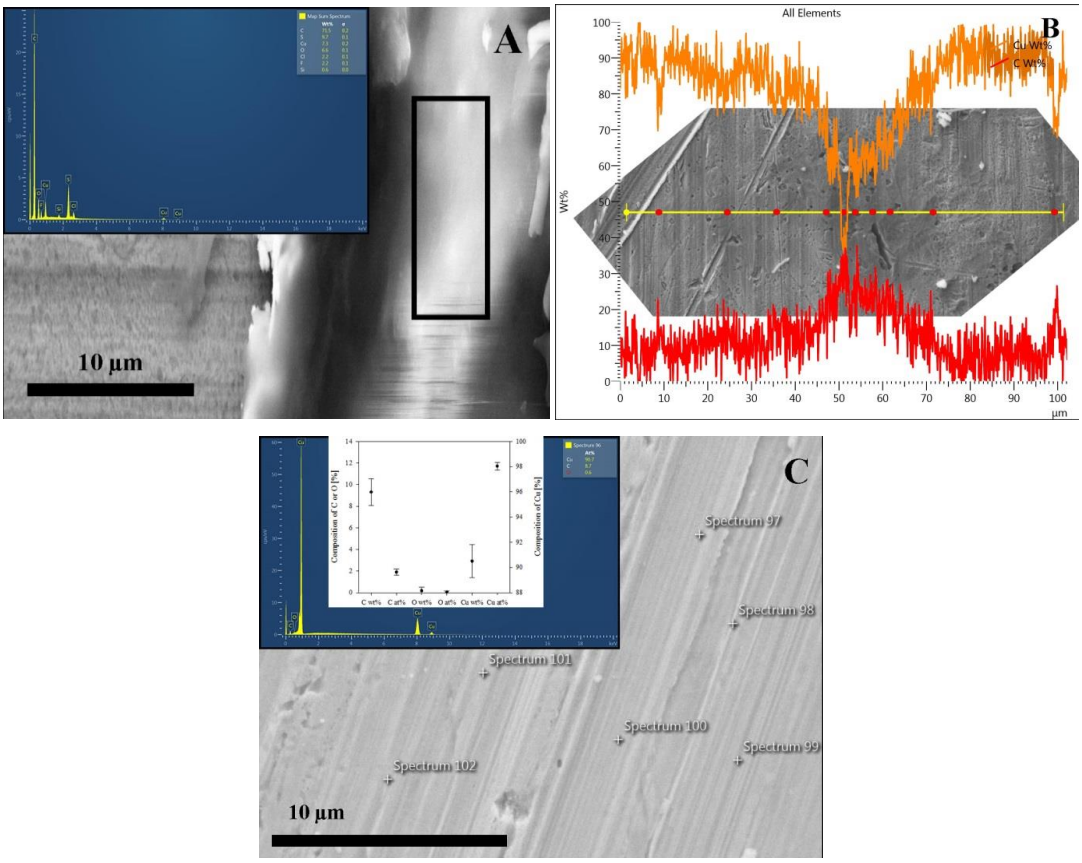

Figure 5-8 (A) EDS spectra of deposited material on PEC-Cu (B) Overlay of EDS spectra and SEM micrograph of the PEC-Cu copper cathode showing early stages of formation of deposited material on copper cathode. The darker area on copper cathode was accompanied by increase of carbon x-ray signal intensity. Red dots show spots at which concentration of carbon on copper cathode exceeds 20 wt% (57 at%). (C) EDS spectra of as received copper sheet showing an average of 9.3 wt% (1.2 at%) already exists on copper (data were averaged over 105 analyzed points). No dark area was observed on as received copper sheet using SEM.

5.1.4 X-ray Photoelectron Spectroscopy (XPS)

To determine chemical nature of the deposited material that was formed on PEC182, X-Ray Photoelectron Spectroscopy (XPS) was used. In XPS analysis, the sample of interest is bombarded by high energy X-ray beam at different energy levels to shoot-off electrons from the sample. Then, a detractor counts the number of electrons that were successfully detached form sample surface and the energy at which the electrons were detached. This data is used to quantify elemental analysis of the sample (by atom percent) and the nature of chemical bonds that hold elements together at any specific energy level. Sweeping from a wide range of energy

level (0 – 1352 eV), a spectrum is produced. By comparing this spectrum with reported spectrums in literature or available XPS databases, one may be able to determine the chemical composition of the sample along with its elemental analysis.

5.1.4.1 XPS spectrum of the deposited material at surface

Here we used XPS on different areas of copper cathode in an attempt to determine the chemical nature of the deposited material that was formed on PEC182. Two spots were specifically analyzed: the deposited material (denoted as "DS-O") and an area on copper cathode where no deposits were formed (denoted as "CuC-O"). Both areas were analyzed after physically peeling off Nafion® mat from the surface of the cathode. As shown previously in Figure 5-5, Figure 5-6C, and Figure 5-7, full detachment of Nafion® mat was not achieved by peeling off method. Therefore, we expect to detect high intensity signals from Nafion® residuals on both DS-O and CuC-O. In order to minimise the Nafion® residual, DS-O area were rinsed using acetone and the resulted sample were denoted as "DS-R". Acetone was chosen for this process due to two reasons: first, it was observed during electrospinning process that Nafion® can be washed away from electrospinning target using acetone; and secondly, acetone evaporates easier and quicker than alcohol base solvents, therefore, less residual of the rinsing agent from rinsing process may remain on the sample. Rinsing time was 1 min and the sample were left to dry at room temperature for a minimum of 2 days before XPS analysis. For comparison purpose, a piece of as received copper sheet was rinsed with acetone using the same procedure (denoted as "Cu-R") and a piece of Nafion® mat after electrospinning using copper target (denoted as "Nafion®-M") were also analyzed with XPS. The conditions at which XPS analysis were performed are shown in Table 5-1. The results related to this analysis are presented and discussed here in detail. Digital micrographs of the analyzed spots for DS-O and CuC-O are shown in Image 5-1.

Table 5-1- XPS analysis condition for each sample.

	DS-O	CuC-O	DS-R	Cu-R	Nafion®-M
Number of scans [-]	30	30	30	10	10
Duration of scan [s]	241.4	241.4	301.4	200.4	80.5
Window size [um]	400	400	200	200	400

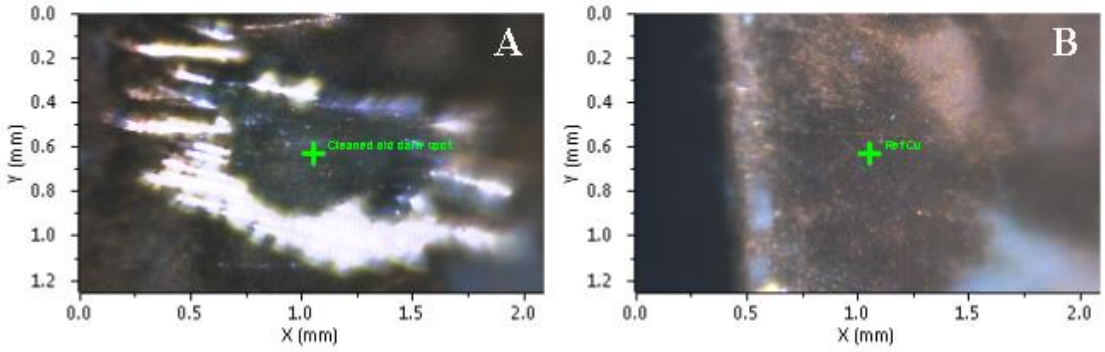

Image 5-1 Optical micrograph of analyzed spots using XPS. (A) analyzed spot on the deposited material (DS-O); (B) analyzed spot adjacent to the deposited material (CuC-O). Residuals of Nafion® nanoribbon mat can be seen in the image.

Table 5-2 summarizes atomic composition of each of the five samples. As shown, carbon, fluorine, oxygen, and copper were the major elements that exist on the surface of the samples. All other elements, including sulfur, nitrogen, and chlorine, form between 1.52 – 2.75 at% of surface atomic composition and hence are not discussed here. The first observation that is made through analyzing data presented in Table 5-2 is low atomic percentage of copper even in Cu-R sample. This shows the low penetration depth of X-ray in XPS analysis (to be exact, ability of excited electrons to escape from the sample is the determining factor rather than penetration depth of X-ray). In addition, XPS analysis of sample Nafion®-M also shows traces of copper atoms. Copper element was detected on Nafion®-M probably because copper were used as the target collector during electrospinning process. This shows the sensitivity of XPS analysis. Therefore, the results of XPS analysis should be treated with care. Thus, detection of high levels of fluorine in all samples, except Cu-R which did not have any contact with Nafion® solution or Nafion® mat, is of no surprise and is been related to low ability of excited electrons to escape from the sample. However, still some useful information can be drawn from this analysis to find

out chemical nature of the deposited material by exploring XPS spectra for each element on each sample. The change in shape of the spectra and peak intensities may lead us to some insights on chemical states and nature of chemical bonds of different elements on each sample.

Table 5-2-Atomic percentage of major elements on surface of samples analyzed using XPS.

Element	Sample				
	DS-O	CuC-O	DS-R	Cu-R	Nafion®-M
C	52.69	33.09	55.34	65.05	30.19
F	22.63	49.36	18.42	0	59.63
O	19.89	12.45	20.26	26.07	7.7
Cu	2.86	3.58	3.23	7.14	0.73
Total	98.07	98.48	97.25	98.26	98.25

As shown in Figure 5-9a, the overall XPS spectrum for DS-O is largely similar to that of CuC-O in terms of the location of the peaks. However, the signal intensities and shapes for some elements were different. These differences will be discussed in detail later. XPS spectrums and the relevant deconvoluted spectrums for the major elements are depicted in Figure 5-9b–d in thick and thin lines, respectively. The deconvoluted spectrum were denoted by a–f to facilitate the discussion. The exact location of the peaks for each element is shown in Table 5-3 for the five analyzed samples.

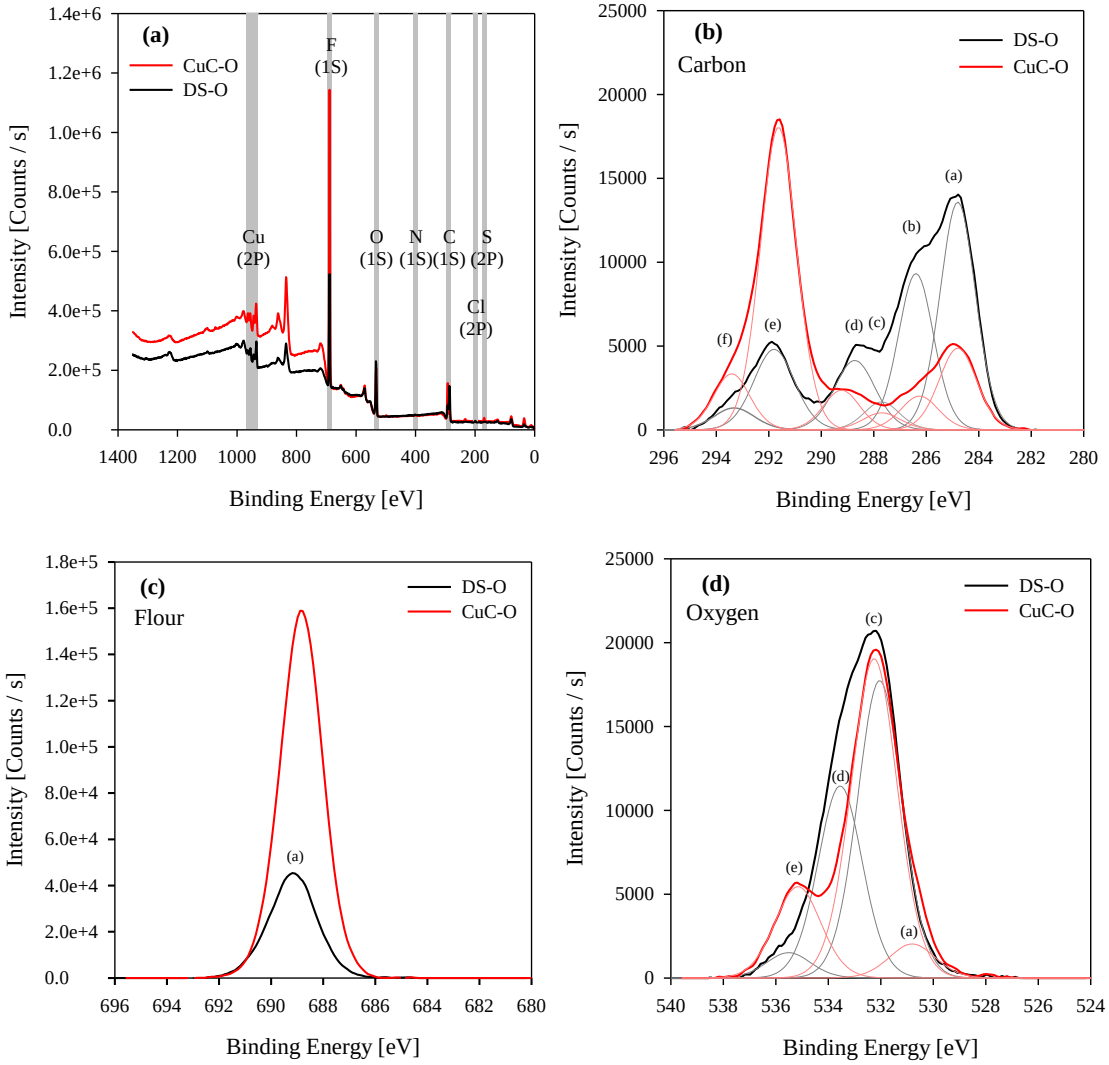

Figure 5-9- XPS spectra for the deposited material on PEC182 and copper reference before cleaning with Acetone. The signals were corrected by removing the baseline signals.

Table 5-3- Deconvoluted peak locations on binding energy scale for the major analyzed elements.

Element	Peak ID	Peak type	Peak location [eV]				
			DS-O	CuC-O	DS-R	Cu-R	Nafion®-M
C	a	1s	284.78	284.78	284.78	284.78	284.78
	b		286.38	286.28	286.28	286.28	286.38
	c		287.68	287.68	287.68	287.68	-
	d		288.78	289.28	288.88	288.78	288.58
	e		291.78	291.68	291.58	-	291.18
	f		293.38	293.38	-	-	292.88
F	a	1s	689.18	688.88	688.68	-	688.28

Table 5 3 (continue) Deconvoluted peak locations on binding energy scale for the major analyzed elements.

Element	Peak ID	Peak type	Peak location [eV]				
			DS-O	CuC-O	DS-R	Cu-R	Nafion®-M
O	a	1s	-	530.88	-	530.28	-
	b		-	-	531.68	531.68	-
	c		532.08	532.28	-	-	531.98
	d		533.58	-	533.18	533.38	-
	e		535.48	535.18	534.78	-	534.68

5.1.4.2 XPS spectrum of pure deposited material at surface

To gain an accurate understanding of chemical structure of the deposited material on DS-O sample, the first step is to try to remove contribution of Nafion® mat and the contaminations that existed on copper cathode from the overall spectrum for each element (contamination on copper may come from different sources ranging from copper sheet manufacturing process, PEC manufacturing and assembly process, lab environment, and etc.). From EDS analysis it was shown that the major element of the deposited material on DS-O is carbon. Therefore, we start the analysis by comparing spectrum for carbon element between DS-O and CuC-O. For carbon atoms, shape of the XPS spectrum for the samples, DS-O and CuC-O were significantly different (Figure 5-9b). This shows a possible difference in chemical state of carbon atoms in the two samples. This is expected, because the major source of carbon atoms in the two samples are presumably different; one is the result of CO_2 reduction reaction during photoelectrochemical tests and the other one is from Nafion® structure and contaminations on surface of Cu. However, the deconvolution of carbon spectrum showed peaks at the same locations. Therefore, the reason that the spectrums for the two samples are different is largely due to different intensity of the deconvoluted peaks. However, this does not necessarily mean that the overall chemical state of carbon atoms in each sample is a combination of similar chemical states of carbon atoms, because different states of carbon atoms may produce XPS peaks at similar binding energies. This will be discussed later.

As shown in Figure 5-9b, the major difference between the overall spectrum of carbon for DS-O and CuC-O is the highest intensive peak for DS-O, peak (a), is located on lower binding energy levels whereas the reverse is true for CuC-O. One the other hand, the ratio of peak (e) for CuC-O and DS-O ($\frac{I^C{}_{e,CuC-O}}{I^C{}_{e,DS-O}} = 3.75$ from Figure 5-9b) was similar to the ratio of peak (a) for flour ($\frac{I^F{}_{a,CuC-O}}{I^F{}_{a,DS-O}} = 3.50$ from Figure 5-9c). This strongly suggests peak (e) for carbon was originated form Nafion® mat residues. This suggestion is further supported by comparing XPS spectrums for carbon for Nafion®-M, Cu-R, and DS-O as in Figure 5-10. As shown in Figure 5-10 and Table 5-3, Nafion®-M had five peaks of carbon among which peak (e) was significantly more intense. On the other hand, Cu-R did not have peak (e) and there was no deposited material on CuC-O to cause peak (e). Therefore, it is concluded that peak (e) was originated from Nafion® residues that remained on deposited material on DS-O sample after physical pealing.

As shown in Figure 5-10, the spectrum for Nafion®-M overlaps the spectrum from CuC-O with a good precision for peaks (e) and (f). Therefore, it is concluded that peak (e) shares the same origin as peak (f) for carbon element. Thus, in order to determine chemical state of carbon in DS-O, peaks (a)–(d) for carbon element should be analyzed further in detail. However, a portion of peaks (a)–(d) for carbon element are coming from contaminations on copper surface and a portion are coming from residuals of Nafion® mat on DS-O. An accurate analysis on these peaks requires extraction of contributing intensities from sources other than the deposited material. This enables us to identify the most important peaks that are purely from the deposited material and therefore determine relative abundance of different states of carbon in the deposited material and further gain insight into the CO_2 reduction reactions that took place using PEC182.

This can be done by re-convoluting a hypothetical XPS spectrum in which the interaction of non-deposited materials is reduced to minimum.

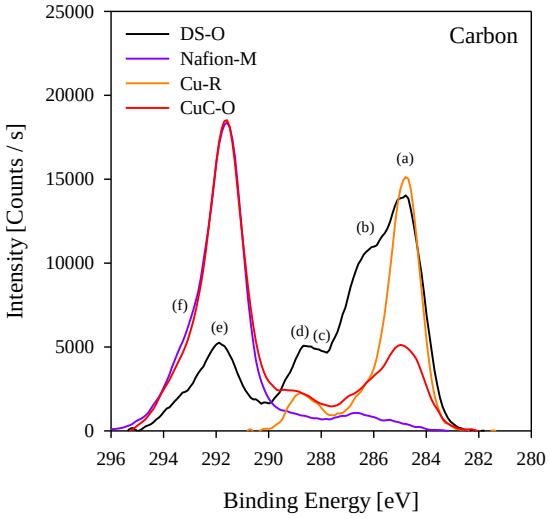

Figure 5-10- XPS spectrum of DS-O, CuC-O, Cu-R, and Nafion®-M samples. Binding energy range corresponding to carbon is shown in this figure.

In order to re-convolute the hypothetical XPS spectrums a procedure is suggested here which is based on the fact that in an XPS spectrum, the ratio of peak intensities between different elements of a particular chemical or material is constant if XPS measurements are carried out under identical condition (*175*). For example, if the ratio between ${I^F}_{a,Nafion-M}$ and ${I^C}_{e,Nafion-M}$ in Nafion®-M sample is x, this ratio remains the same if any arbitrary amount of Nafion®-M is mixed with a sample which does not have XPS peaks (a) and (e) for elements fluorine and carbon, respectively. That is true in the absence of interfering or overlapping peaks: the ratio of intensity of any two arbitrary peaks for a given material is constant. This is formulated in Eq. (5-1). This concept can be used to calculate relative abundance of different materials in the material of interest. Using this fundamental feature of XPS the following procedure is proposed.

$$No\ signal\ interferece\ or\ overlap\ \rightarrow \frac{{I^F}_{a,Nafion-M}}{{I^C}_{e,Nafion-M}} = x = const. \quad \textbf{(5-1)}$$

The proposed procedure involves two steps. First, sufficient number of reference elements and corresponding reference XPS spectrums should be determined. These reference elements should not have interfering or overlapping XPS spectrum with the material of interest (the material of interest in our experiment is the deposited material). Second, a set of coefficients, conceptually similar to x, should be determined or calculated. The criteria for a suitable set of coefficients is that by when those coefficients are used to re-convolute a hypothetical XPS spectrum (using an equation similar to Eq. (5-3)), the difference between the calculated hypothetical XPS spectrum and XPS spectrum of the material of interest is minimum. These coefficients may be determined through trial-and-error or through optimization. Here, we used an optimization method based on a stochastic global search algorithm (vide infra). This procedure is used as follows.

As mentioned, the material of interest in this experiment is the deposited material on sample DS-O. Here we chose fluorine and copper as the reference elements because these elements are not expected to appear in CO_2 reduction reaction product and therefore not expected to be in chemical structure of the deposited material. We used Nafion®-M as the sample from which reference XPS spectrum for fluorine can be obtained. For Cu, we used CuC-O and Cu-R samples as the sources of XPS spectrums. The reason we chose these two reference samples for copper is we noted XPS spectrums of copper is different between these two samples indicating different chemical states of Cu. These differences were found to be related to oxidation states of copper in forms of Cu_2O and CuO (*176*). This was further confirmed by observing different colors of copper in the vicinity of the deposited dark material on sample DS-O (shown in Image 3-2b). In addition, by considering spectrums of copper from these two reference samples, the highest resemblance between the copper spectrum of DS-O and CuC-O and Cu-R was found. It should be noted that in order to avoid double counting for carbon and

oxygen the contribution of XPS spectrum of carbon and oxygen from Nafion® mat was deducted from the spectrum of carbon and oxygen for CuC-O reference sample (such a correction was not required for Cu-R sample because Cu-R sample had no XPS spectrum for element fluorine, which is an indication for presence of Nafion®, as shown in Table 5-3).

The optimization problem to find the required set of coefficients that were describe in the proposed procedure can be formulated as shown in Eq. (5-2). The re-convoluted XPS spectrum can be calculated using optimized coefficients (i.e. $x_{reference\ sample}$) using Eq. (5-3). Here we used Genetic Algorithm (GA) as the governing mathematical optimization algorithm (*177*). We used a population size of 200 individuals and a constraint dependent mutation method through optimization toolbox (*optimtool*) of MATLAB program. The results of several instances of such an optimization are shown in Table 5-4. As shown in Table 5-4, all three trials of GA were converged to very similar solutions. In addition, the value for objective function (which is the difference between the re-convoluted hypothetical XPS spectrum and the real XPS spectrum for DS-O) is very close to 0, i.e. the best possible fit. Therefore, we concluded that the converged solutions are global or near-global optimal values for $x_{reference\ sample}$ and result of the instance 2 was selected and used for the rest of analysis due to the lower Obj. Therefore, the optimal coefficients are $x_{Nafion-M} = 0.2799$, $x_{CuC-O} = 0.3844$, and $x_{Cu-R} = 0.3357$.

$$\begin{aligned}\min Obj = &\left| x_{Nafion-M}\int_{680}^{696} XPS^{F}{}_{Nafion-M} + x_{CuC-O}\int_{680}^{696} XPS^{F}{}_{CuC-O} \right.\\ &\left. + x_{Cu-R}\int_{680}^{696} XPS^{F}{}_{Cu-R} - \int_{680}^{696} XPS^{F}{}_{DS-O} \right|\\ &+ \left| x_{Nafion-M}\int_{930}^{950} XPS^{Cu}{}_{Nafion-M} + x_{CuC-O}\int_{930}^{950} XPS^{Cu}{}_{CuC-O} \right.\\ &\left. + x_{Cu-R}\int_{930}^{950} XPS^{Cu}{}_{Cu-R} - \int_{930}^{950} XPS^{Cu}{}_{DS-O} \right|\end{aligned} \quad \textbf{(5-2)}$$

$$subject\ to: \begin{cases} x_{Nafion-M} + x_{CuC-O} + x_{Cu-R} = 1 \\ 0 \le x_{Nafion-M} \le 1 \\ 0 \le x_{CuC-O} \le 1 \\ 0 \le x_{Cu-R} \le 1 \end{cases}$$

$$XPS_{Re-convoluted} = x_{Nafion-M}XPS_{Nafion-M} + x_{CuC-O}XPS_{CuC-O} + x_{Cu-R}XPS_{Cu-R} \quad \textbf{(5-3)}$$

$$XPS_{Deposited\ material} = XPS_{DS-O} - XPS_{Re-convoluted} \quad \textbf{(5-4)}$$

Table 5-4- The optimal coefficients values for Nafion®-M, CuC-O, and Cu-R samples. GA was used as the governing optimization algorithm.

Instance	$x_{Nafion-M}$	x_{CuC-O}	x_{Cu-R}	Obj
1	0.2801	0.3847	0.3352	0.0055
2	0.2799	0.3844	0.3357	0.0005
3	0.2800	0.3845	0.3355	0.0013

Goodness of fit can also be visually examined with the reference elements as shown in Figure 5-11a and b. For fluorine, as shown in Figure 5-11a, the re-convoluted curve (the blue solid line) is very similar to the original XPS spectrum of DS-O sample (the black solid line). Interestingly, the optimal value for $x_{Nafion-M}$ at 0.2799 is very close to $\frac{I^F{}_{a,DS-O}}{I^F{}_{a,CuC-O}} = 0.2857$ (or $\frac{I^F{}_{a,CuC-O}}{I^F{}_{a,DS-O}} = 3.50$) which was reporter earlier. For copper, the visual comparison of the re-convoluted spectrum with original DS-O spectrum leads to the same conclusion although there are minor differences at peak (a) and (b) between DS-O spectrum and the re-convoluted spectrum. Therefore, a reasonable match between the re-convoluted spectrums and the DS-O spectrums is reached with respect to reference elements. Using the optimal coefficients and Eq. (5-4) the spectrum for deposited material on DS-O for elements carbon and oxygen was calculated as shown in Figure 5-11c and d by gray area. The spectrum for the deposited material was further deconvoluted to gain quantitative information on chemical state of carbon and oxygen, as shown in Figure 5-12.

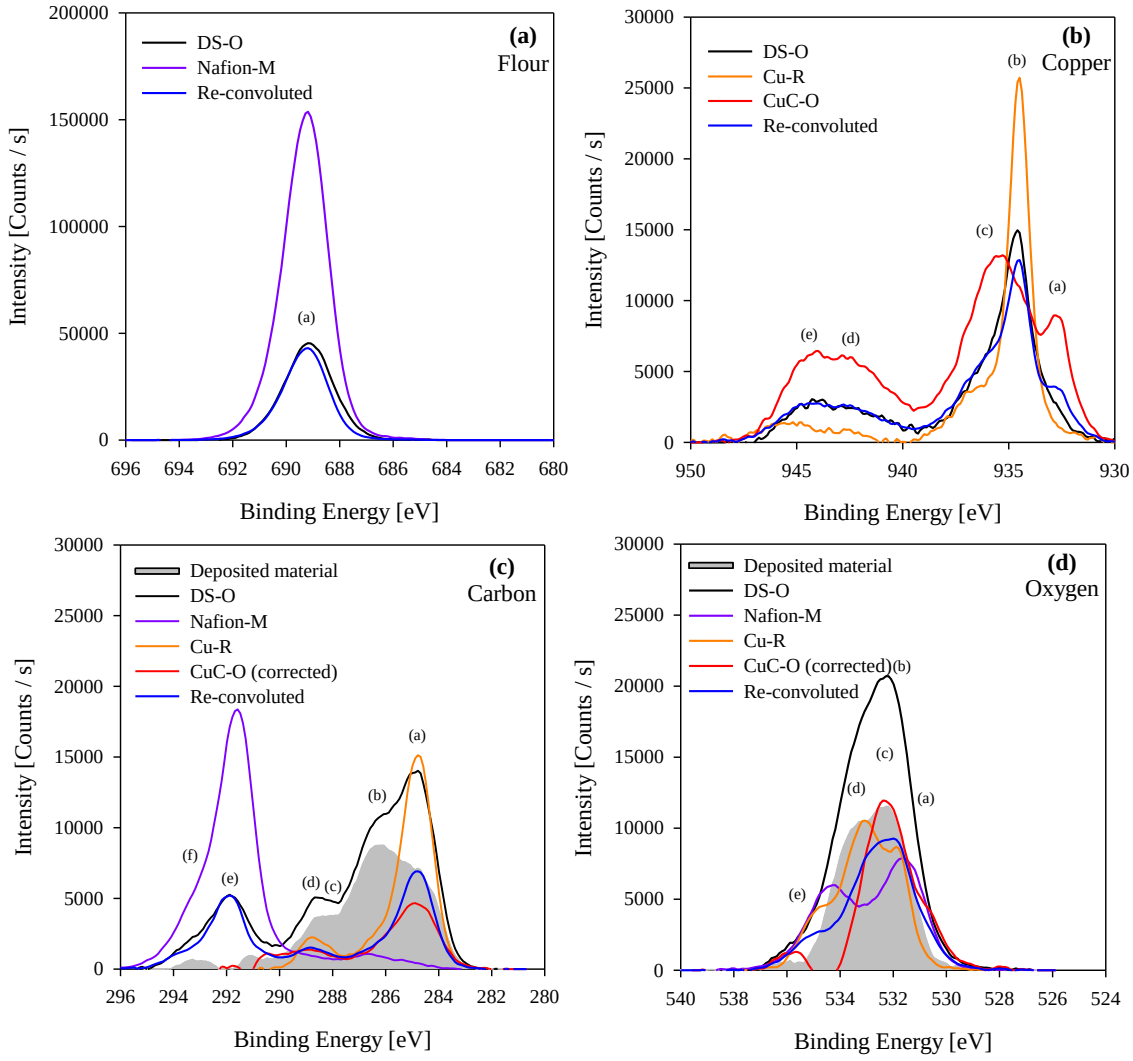

Figure 5-11- Re-convoluted XPS spectrum for carbon, copper, fluorine, and oxygen. Gray areas shown in (c) and (d) are related to pure deposited material on the surface at analyzed sample DS-O.

According to the results of performed deconvolution, the deposited material, on surface, consists of 50.47 at% carbon and 49.53 at% oxygen. However, some part of oxygen atoms in the re-convoluted XPS spectrum are not related to the deposited material because they have too high or too low binding energy to be correlated to carbon atoms. Those are deconvoluted at 531.9 and 536.15 eV corresponding to that of Cu−O and F−O bonds, respectively. For carbon, there are some spectra at > 290 eV which correspond to C−F bonds. If we exclude these contributions from that of deposited material then we reach to elemental composition of 56.58 at% carbon and

43.42 at% oxygen at the surface of the deposited material. Furthermore, In addition, higher portion of carbon that exists on the deposited material are sp^2 carbon in comparison to sp^3 carbon (sp^2: sp^3 = 1.69). This is particularly important if the deposited material has self-growing properties, because sp^2 carbon is specifically active in CO_2 reduction reaction (*178*). In addition, it is clear from this analysis that the surface of the deposited material is partially oxidized or a wide range of functional groups exists on the surface. These functional groups may be contaminations or the nature of the deposited material, however since the overall elemental composition of the surface through this analysis does not match that of EDS, it can be concluded these composition are only valid at the surface of the deposited material. This suggests for gaining a better understanding of chemical structure of the deposited material, we should perform depth analysis of the deposited material. This is discussed in section 5.1.4.3.

The other conclusion that was derived from this analysis is the proposed method for XPS spectrum analysis is effective because although the re-convoluted spectra is hypothetical (i.e. it is the result of calculations), we managed to reach to a consistent deconvolution of carbon and oxygen. For example, as shown in Figure 5-12a, 31.22 at% of carbon atoms are associated with a combination of C−O−C, C−O, and C−OH functional groups. Deconvolution of oxygen also suggests 32.43 at% of oxygen atoms are associated with C−O bonds. Clearly these two different sources of information agree with each other very well. The same is true for C=O bonds from carbon and oxygen perspective. More importantly, the same conclusion on the difference of DS-O surface and bulk was also derived from results of XPS depth profile measurements, Raman spectroscopy, and IR spectroscopy, as discussed later in this chapter.

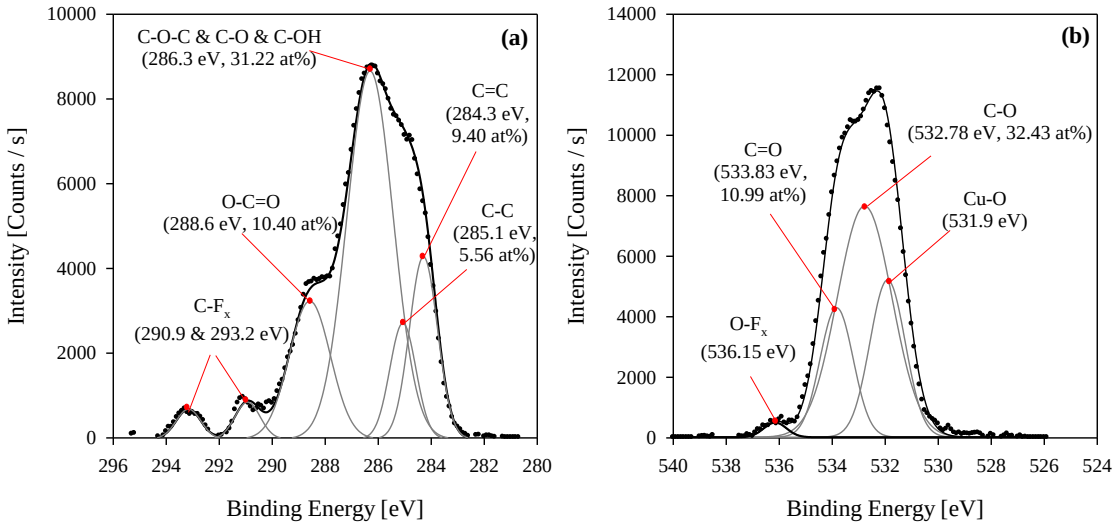

Figure 5-12- Deconvolution of XPS spectra of the pure deposited material on surface of DS-O. a) carbon; b) oxygen. Gaussian model was used for deconvolution curve fitting using Origin software. NIST Standard Database 20 Version 4.1 (*179*), was used for XPS peak assignments.

5.1.4.3 XPS spectrum of the deposited material at bulk

In order to gain insight on chemical structure of the bulk of the deposit material, we carried out XPS depth profiling using etching technique. For these measurements, Ar ion beam was used to remove thin layers from the surface of the deposited material on DS-O sample. Then XPS spectrum of the deposited material was collected. This process was repeated sequentially to reach a depth at which elemental composition of the deposited material did not change with depth. The depth profile results of DS-O are shown in Figure 5-13. For comparison, the same technique was used for CuC-O sample. The depth profile results of CuC-O are shown in Figure 5-14.

As shown in Figure 5-13a carbon element in DS-O, intensity of XPS peak increased drastically. In addition, shape of the peak was changed. At z = 0 nm, XPS spectra of carbon had multiple peaks, however, at z = 300 nm spectra of carbon shows a single intense peak at ~ 285 eV. Fluorine peak, Figure 5-13b, drastically decreased in the first 75 nm from the surface. The same happened for oxygen and copper (see Figure 5-13c and d, respectively). This clearly shows

elemental composition and chemical structure of the deposited material is significantly different in bulk from that of surface. This is in agreement with analysis performed in section 0, confirming the final conclusion of section 0.

A different trend in elemental composition variation with depth was observed for Cu-C. Figure 5-14a shows for carbon, intensity of XPS spectra significantly declined in the first 60 nm. Similar to DS-O, intensity of fluorine, Figure 5-14b, declined in the first 50 nm from the surface. Oxygen in Cu-C, Figure 5-14c, showed a totally different behavior than in DS-O. At first, peak intensity at ~ 533.5 eV increases while peak intensity at 535.5 eV decreases. After z = 75 nm the reverse took place. Signal intensity at ~ 533.5 eV decreased. Simultaneously, peak intensity at ~ 535.5 eV increased significantly. All oxygen peaks started to decrease at z ≈ 300 nm. Copper peak intensity in Cu-C showed an inverse trend in comparison to DS-O. Copper spectra continuously increased until reaching a maximum at z ≈ 220 nm. This experiment showed in order to gain reliable information about the bulk of the deposited material, etching up to 300 nm is unavoidable, as was the case for Cu-C reference sample.

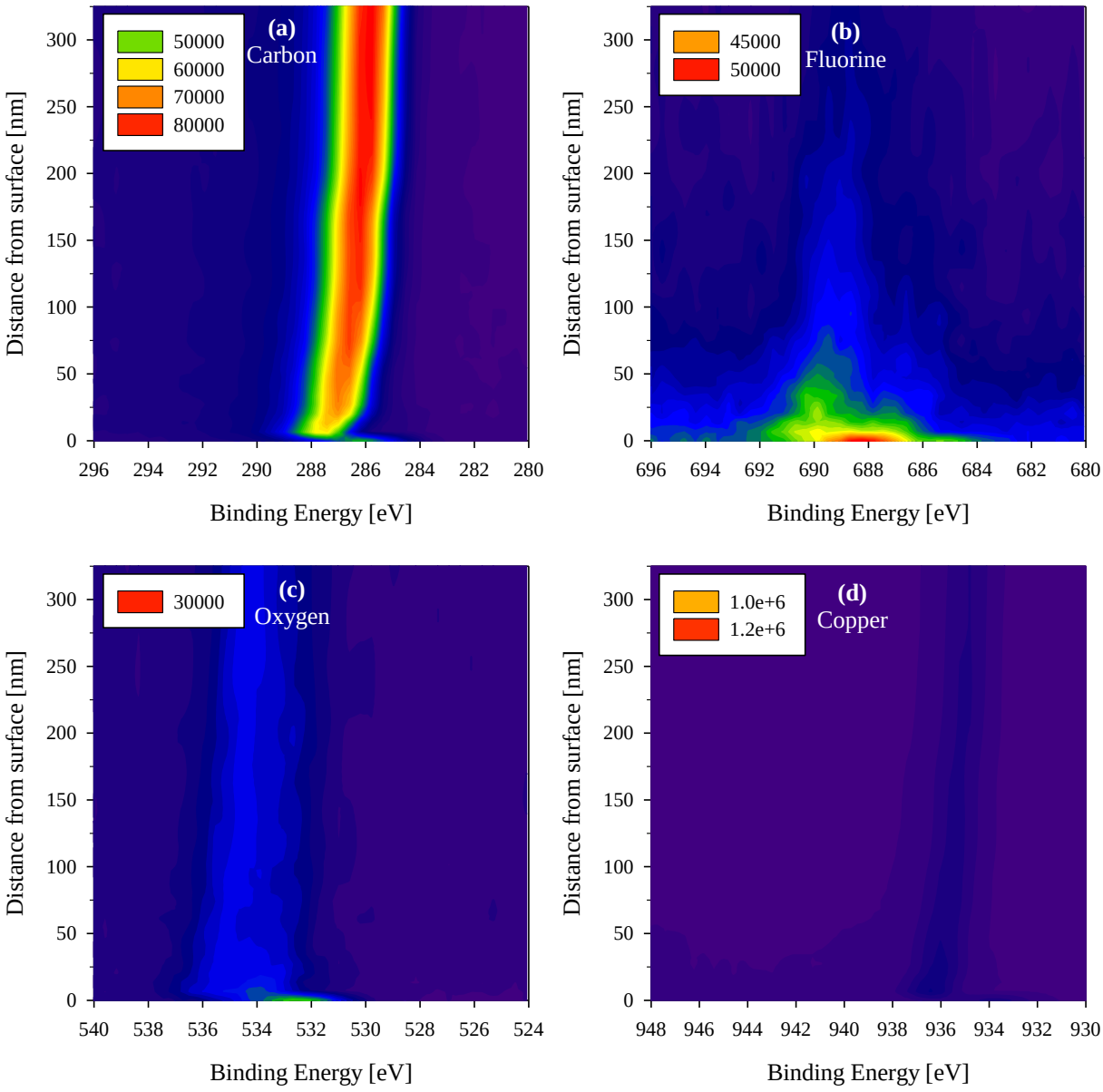

Figure 5-13- XPS Depth profile spectra of DS-O. Color gradient shows XPS signal intensity. Etching process was controlled by etching time. Ar ion beam at 3 keV were used for etching. An area of 1 × 1 mm were etched for this experiment. Reference etching rate were 0.91 nm/s for Ta_2O_5. We assumed the same etching rate is valid for our sample and calculated etched depth using the same value having known etching time. The observed shifts in spectrums from higher energy to lower energy was related to instrument drag.

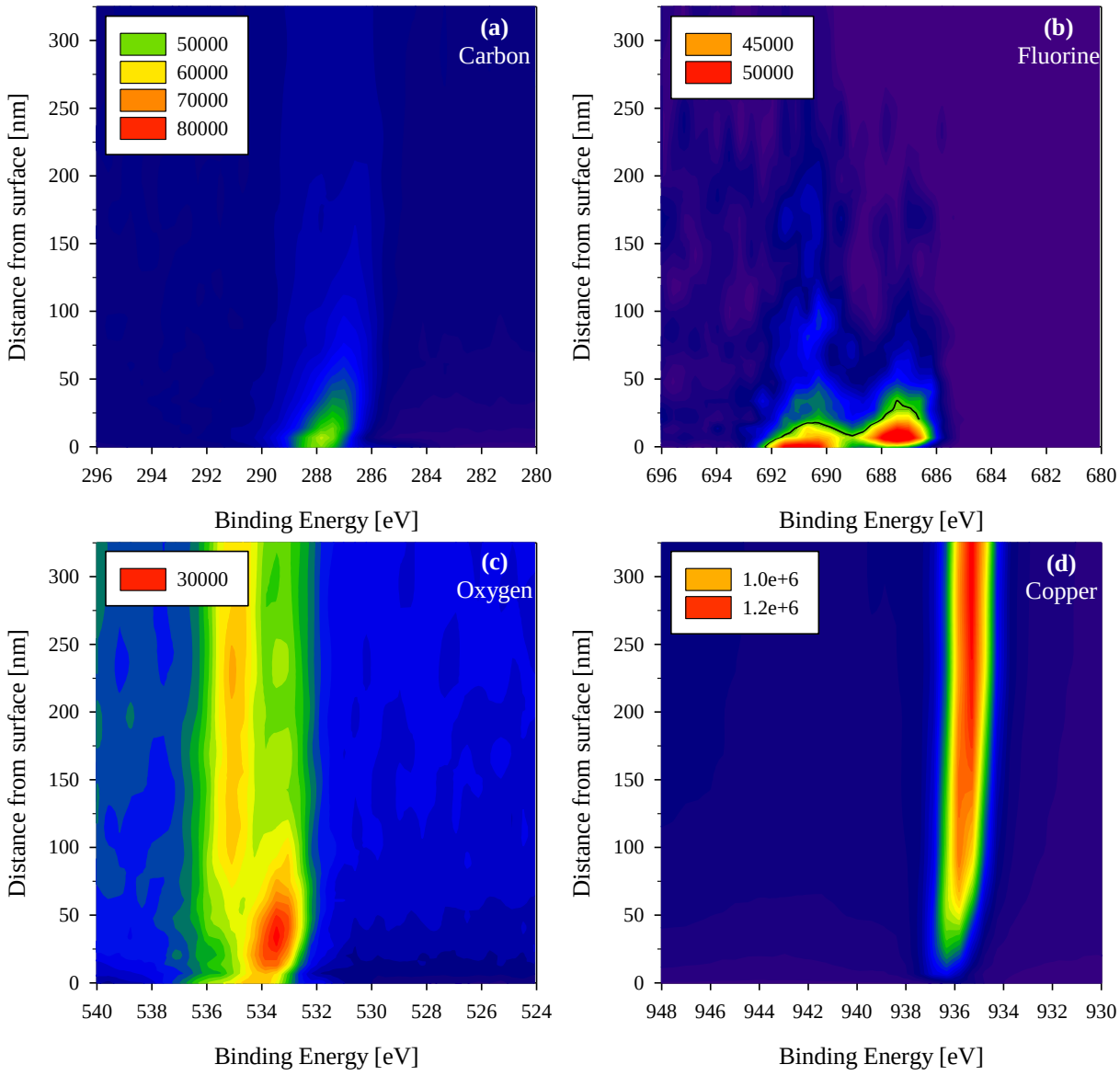

Figure 5-14 XPS Depth profile spectra of CuC-O. Color gradient shows XPS signal intensity. Etching process was controlled by etching time. Ar ion beam at 3 keV were used for etching. An area of 1 × 1 mm were etched for this experiment. Reference etching rate were 0.91 nm/s for Ta_2O_5. We assumed the same etching rate is valid for our sample and calculated etched depth using the same value having known etching time. The observed shifts in spectrums from higher energy to lower energy was related to instrument drag.

Variation of atomic composition of the deposited material from surface to bulk can be analyzed by summing up and normalizing of areas under the curve of the above shown XPS spectra at each specific depth. Figure 5-15A and B shows atomic depth profile of the deposited material and a spot adjacent to the deposited material (as the reference), where no visible sign of

deposited material were observed under XPS microscope (Image 5-3), respectively. For the deposited material, atomic composition of carbon increased from ~ 52 at% at surface to ~ 88 at% at 300 nm from the surface. No other element showed the same trend, indicating carbon is the major consisting element of the deposited material. However, for the reference sample (Cu-C), atomic composition of carbon decreased from ~ 60 at% at surface, reaching ~8 at% at 300 nm from the surface, which is equal to carbon contamination of as received copper sheet (Figure 5-8C). Composition of fluorine followed the same trend for Cu-C, decreasing from ~25.5 at% to < 1 at%. Composition of copper, however, increased up to 85 at% as expected (Figure 5-15B), matching elemental composition derived from EDS analysis (Figure 5-8C).

Deconvolution of XPS spectra of carbon at z = 325 nm for DS-O shows 61.54 at% and 31.78 at% of carbon atoms have sp^2 and sp^3 hybridization , respectively (sp^2:sp^3 = 1.93). In addition, C:O ratio of DS-O at z = 325 nm were equal to 31.5. This sp^2:sp^3, C:O ratio, and shape of C1s and O1s XPS spectra correspond very closely to that of synthesized reduced graphene oxide (*180*), graphite (*181*), amorphous carbon (*182*), slightly hydrogenated amorphous carbon (a-C:H) (*183*), and copper doped carbon aerogel (*173*). Furthermore, deconvolution of oxygen at z = 325 were compatible with that of carbon. This shows small portion of carbon atoms are bounded to oxygen atoms in different forms. This may mean that CO_2 were converted to a form of defected graphenic material. This hypothesis can be further investigated using other analytical methods as discussed in the next sections.

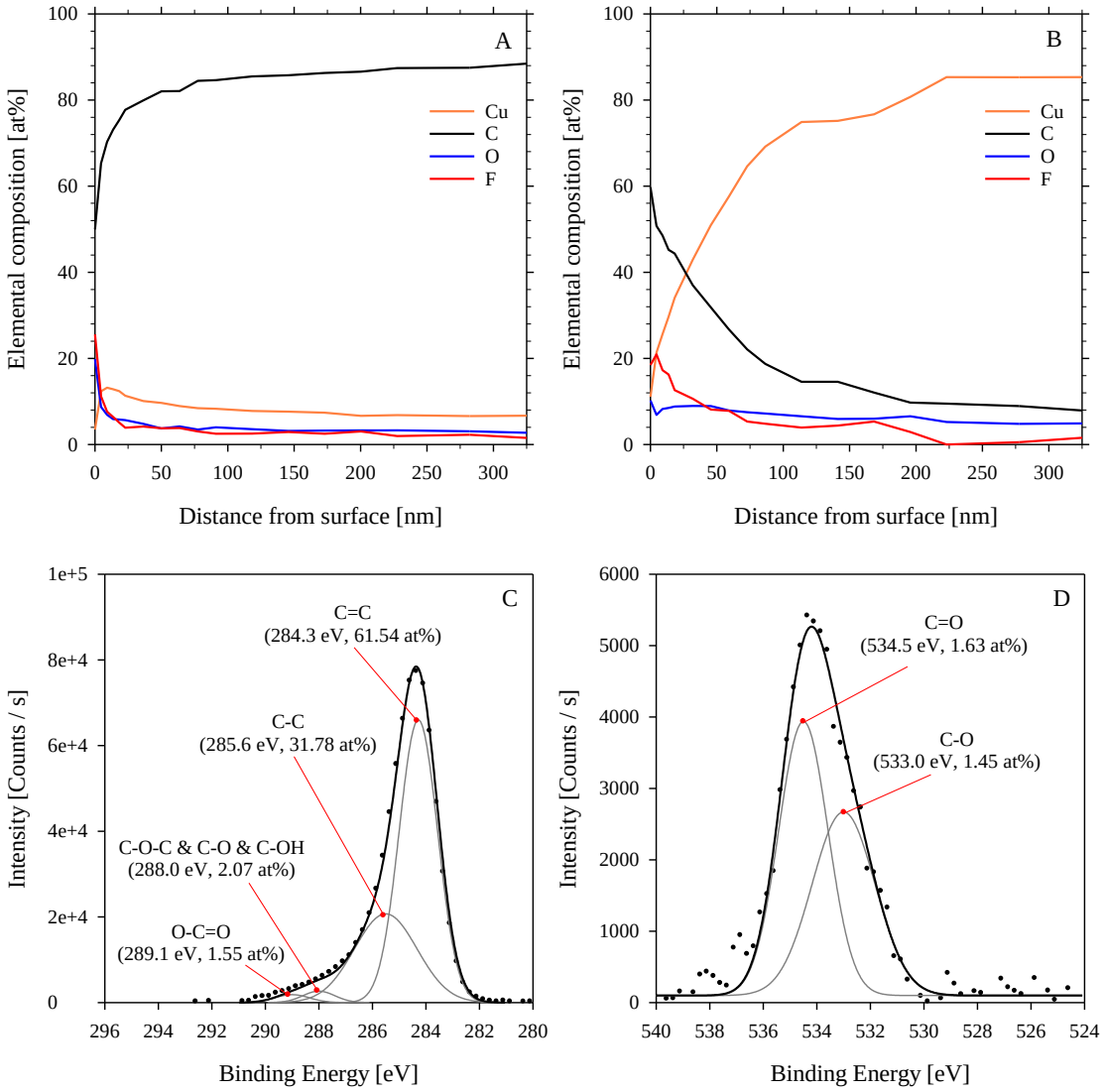

Figure 5-15 Depth profile and XPS spectrum of the deposited material (DS-O) and reference Cu cathode (Cu-C). (A) depth profile of elemental composition of the deposited material. Depth profile was obtained through ion beam etching of the surface of the deposited material. (B) depth profile of elemental composition of copper substrate adjacent to the deposited material. Depth profile was obtained through Ar ion beam etching of the copper cathode. (C) XPS spectra and deconvolution for element carbon at 300 nm distance of surface of the deposited material. (D) XPS spectra and deconvolution for element oxygen at 300 nm distance of the surface of the deposited material. Values shown in brackets are atomic percentage of the respective element at each chemical state. Hydrogen content of the deposited material is not included in the calculations. NIST Standard Database 20 Version 4.1 (*179*), was used for XPS peak assignments.

5.1.5 Infrared and Raman spectroscopy

Although EDS and XPS are strong analytical tools, but they cannot show existence of hydrogen atoms and determine type of functional groups that exist on a sample. Therefore, we

used Infrared (IR) and Raman spectroscopy for this purpose. The results are shown in Figure 5-16. IR and Raman peaks were identified through extensive search of literature and available databases. These peaks are annotated by letters in Figure 5-16. Exact locations of the peaks are listed in Table 5-5.

Figure 5-16A shows strong Raman peaks for sp^2 carbon in comparison to that of sp^3 carbon. This partially confirms the deconvoluted XPS results discussed in sections 0 and 5.1.4.3. Strong peaks of aromatic carbon was also observed (peaks d, e, i). High similarity between Raman spectra of hydrogenated amorphous carbon and the deposited material were observed (single solid black line in Figure 5-16A is related to hydrogenated amorphous carbon adopted from ref. (*180*)). Traces of hydrogen can be found in many functional groups on the deposited material (peaks g–h and m–q in Figure 5-16A and peaks a–b, h–I, and s–v in Figure 5-16B). Importantly, peaks (l) and (r) correspond to traces of CO_2 and CO on the deposited material in Figure 5-16A. Figure 5-16B also shows strong IR peaks of CO_2 (peaks q and r) and week IR peak of CO (peak w). Strong peaks of CO_2 indicates relatively high amounts of CO_2 gas exits on the deposited material, probably trapped in the pores that were observed in SEM micrographs (Figure 5-1C). This suggests the porous structure was formed at the time of CO_2 reduction, which lead to trapping of a portion of CO_2 gas in the pores (vide infra).

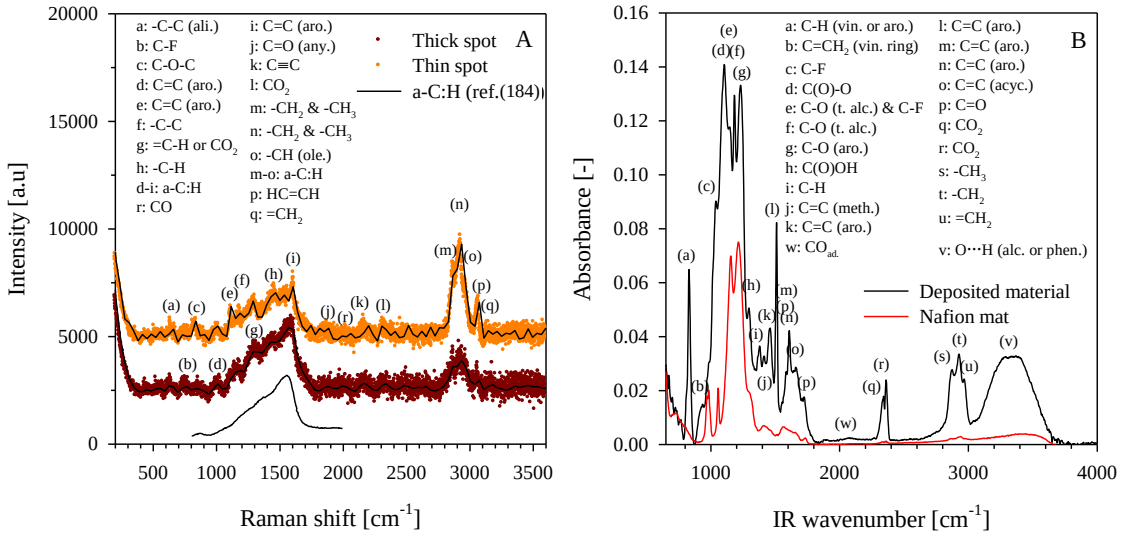

Figure 5-16 (A) Raman spectra of the deposited material on a thinner area and thicker area. Spectra for the thin spot (orange line) were shifted upward by 5000 a.u. to facilitate visibility. Solid black line on orange and brown data are smoothened data. They are presented to facilitate peak detection. Peaks d–i and m–o may also be associated with amorphous carbon (*184*) and hydrogenated amorphous carbon (*185-187*). Traces of CO was observed in Raman spectra at peak r (*188*) B) IR spectra of deposited material. Traces of CO was observed in IR spectra at peak w (*189*). Abbreviations: ali. = aliphatic, aro. = aromatic, any. = anhydride, ole. = olephin, vin. = vinyl, alc. = alcohol, phen. = phenol, acyc. = acyclic, meth. = methylene, t. alc. = tertiary alcohol, ad. = adsorbed. Characterization peaks were extracted from ref. (*190*) except IR peaks s, t, and u which were extracted from (*191*) and IR peak w which were extracted from (*189*). Peaks for Nafion® nanoribbon mat were detected at 979.4, 1055.35, 1153.62, 1218.38, 1410.45, and 1566.78. For exact values of detected Raman and IR peaks refer to Table 5-5. For IR spectroscopy, IR background signal of the air was removed from the sample spectra. Therefore, the sample spectrum does not include signal of air. There was no purging of the sample chamber but the optics was purged with N_2.

Table 5-5. List of identified peaks for IR and Raman spectroscopy as annotated in Figure 5-16.

IR peaks				Raman peaks			
letter	wavelength [cm^{-1}]	letter	wavelength [cm^{-1}]	letter	wavelength [cm^{-1}]	letter	wavelength [cm^{-1}]
a	828	m	1580	a	634.0	m	2871.3
b	933	n	1610	b	751.9	n	2930.2
c	1030	o	1660	c	834.7	o	2966.5
d	1106	p	1720	d	1012.6	p	3077.5
e	1150	q	2333	e	1118.0	q	3148.9
f	1184	r	2357	f	1183.7	r	2029.2
g	1234	s	2868	g	1301.6		
h	1292	t	2919	h	1460.3		
i	1376	u	2961	i	1608.7		
j	1411	v	3085-3649	j	1874.0		
k	1454	w	2077	k	2162.9		
l	1512			l	2317.1		

Through IR mapping, we were able to identify areas of the deposited material at which a positive CO_2 peak was observed. These areas are shown by semitransparent red boxes in Figure 5-17. As shown in Figure 5-17, positive CO_2 peaks were more distributed on the deposited material, rather than surrounding Cu only area. Comparing this map with EDS map for fluorine (see Figure 5-6C) confirms positive CO_2 peak were also observed in areas were residuals of Nafion® did exit. This suggests positive CO_2 peak was observed in areas where some sort of porosity existed (i.e. on the deposited material or on residual of Nafion® mat). Observance of weak CO peaks in both Raman and IR spectra suggests CO was a byproduct and/or intermediate product of CO_2 reduction reaction. A close-up of the CO peak in IR spectra confirms this peak is not a misidentified noise (see Figure 5-18).

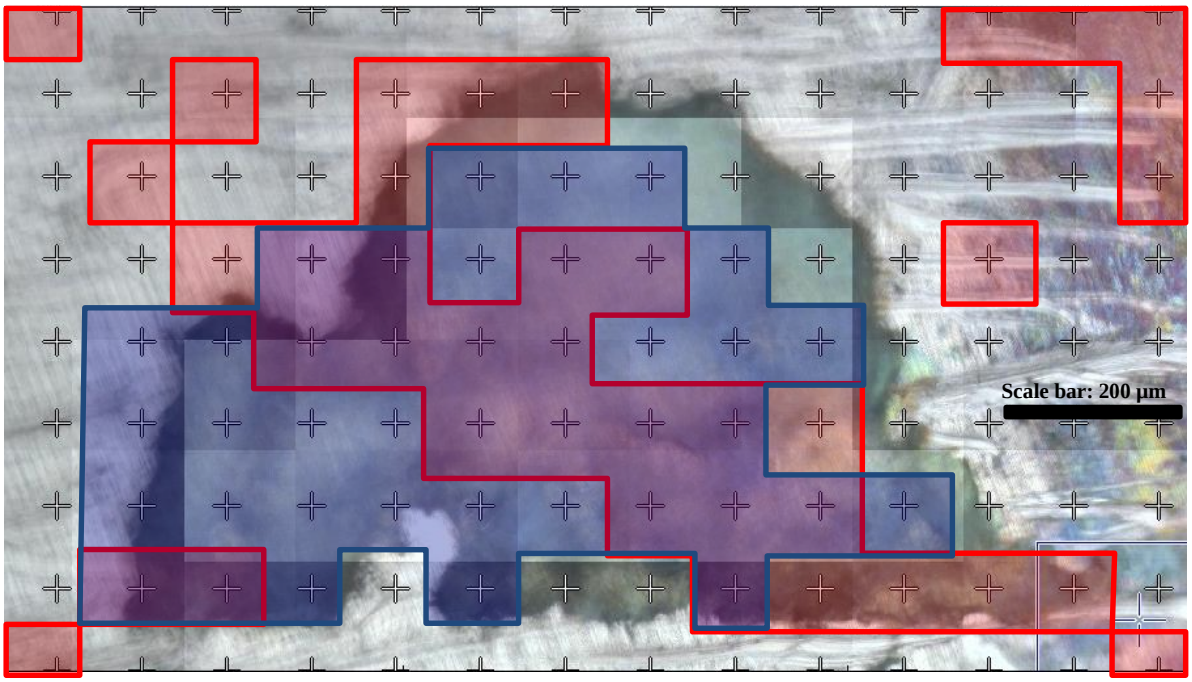

Figure 5-17 Map of area under the curve of IR CO_2 peak for IR wavelengths of 2389–2275 cm^{-1}. The locations at which area under the IR curve for the specified wavelength range was positive are marked by red markers (background was subtracted from the spectra in that range). Crosses show approximate position of the center of the IR prism detector. Prism detector diameter was 100 µm. Areas shown with blue markers are areas at which IR peaks similar to that of presented in Figure 5-16B was observed.

Through IR and EDS mapping, it was confirmed that chemical and elemental composition of the deposited material were relatively uniform throughout the deposited material, although

intensities of different IR peaks slightly varied (Figure 5-6 and Figure 5-19, respectively). Variation of IR peak intensities may be related to non-flat surface of the deposited material, which was observed under SEM and optical microscope and further confirmed by Atomic Force Microscopy (Figure 5-3). It is well-known that the intensity of IR peak depends on factors such as the angle of incidence, the refractive index of surface, surface roughness, and IR absorption (*192*). In case of a non-uniform surface, effective IR incidence angle (the angle between incident IR and a line perpendicular to local surface) cannot be kept constant throughout IR spectroscopy. The same concept is true for Raman spectroscopy.

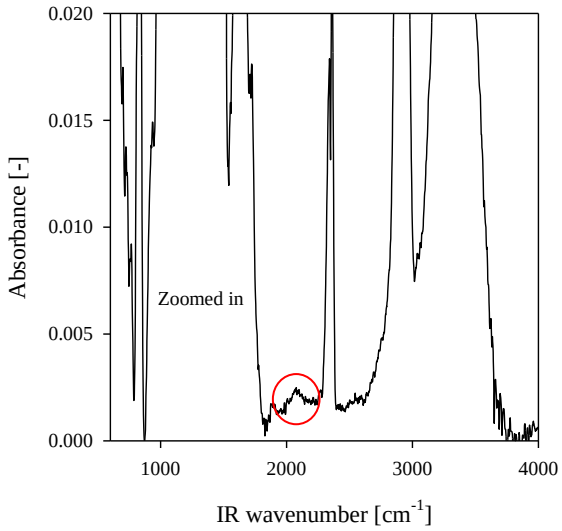

Figure 5-18 Close-up of IR peak (w) at 2077 cm^{-1} as annotated in Figure 5-16B. This figure shows peak (w), shown with the red circle, is not a misidentified noise because the same peak was observed in Raman spectra (peak r in Figure 5-16A) and the intensity of peak (w) were higher in other repeats of IR spectra as shown in Figure 5-19.

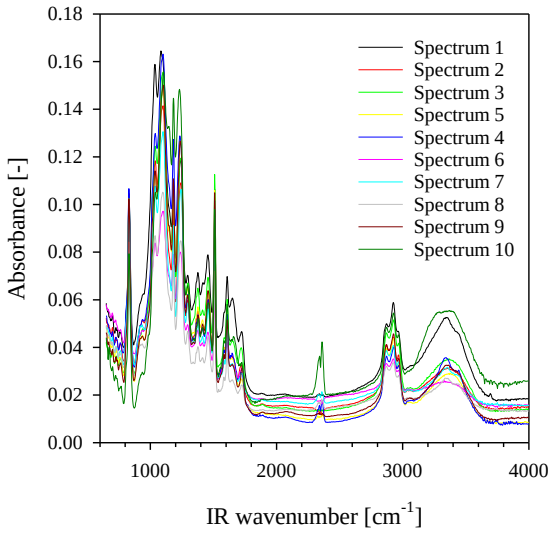

Figure 5-19 Infrared spectrum of the deposited mateiral in multiple spots showing variation of signals intensity on the deposited material. The shape of the spetrum were relaively similar, indicating relative chemical unifrmity of the deposited material.

When we were analyzing the deposited material under SEM, we noticed at some spots the deposited material greatly resembled appearance of graphene sheets, particularly at the edges (see Figure 5-2B at the edges). Therefore, we took Raman spectra of the deposited material at the edges to see if the detected Raman spectrum is greatly differ from what was shown in Figure 5-16A. In fact, the collected Raman spectra at the edges of the deposited material resembled that of graphite and graphene. Figure 5-20 shows were clear D and G bands (at 1375.62 and 1589.94 cm^{-1}, respectively) existed in Raman spectra of the deposited material at the edges. Using these spectra it is possible to clearly determine if the deposited material is graphitic or graphenic at the edges. King et al. (*193*) developed a methodology based on which clear distinction between graphite, graphene, reduced graphene oxide, and graphene oxide can be made only using Raman spectra of the sample. Following the same peak fitting methodogy using Lorentzian model, apparent G band peak ($G_{app.}$) and D peak were located at D = 1375.62 cm^{-1} and $G_{app.}$ = 1589.94 cm^{-1}. G band is related to relative motion of sp^2 carbon atoms (bond stretching) and D band is related to breathing of sp^2 carbon atoms in aromatic ring when under photonic excitation (*182*). D band is related to defects that exists in a graphenic material (*194*). If we consider $G_{app.}$ is

actually a convolution of G band and D' band peaks then we can fit G = 1573.68 cm^{-1} and D' = 1610.04 cm^{-1} with very high goodness of fit (R^2 = 0.9998, see Figure 5-21). Therefore, the difference between D' and $G_{app.}$ peaks location is 20.1 cm^{-1} (D'- $G_{app.}$ = 20.1). According to King et al. (*193*) this difference corresponds to C:O ratio of ~ 310, and is categorized as graphene. Therefore, the deposited material is graphene, at least at the edges.

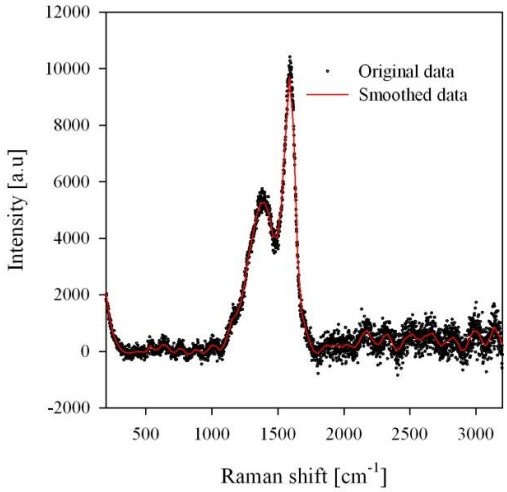

Figure 5-20 Raman spectra of the edge of the deposited material. This shows D and G_{app} band at 1375.62 and 1589.94 cm^{-1}. Green laser (514 nm) at 50% intensity was used for all Raman spectrometry analysis.

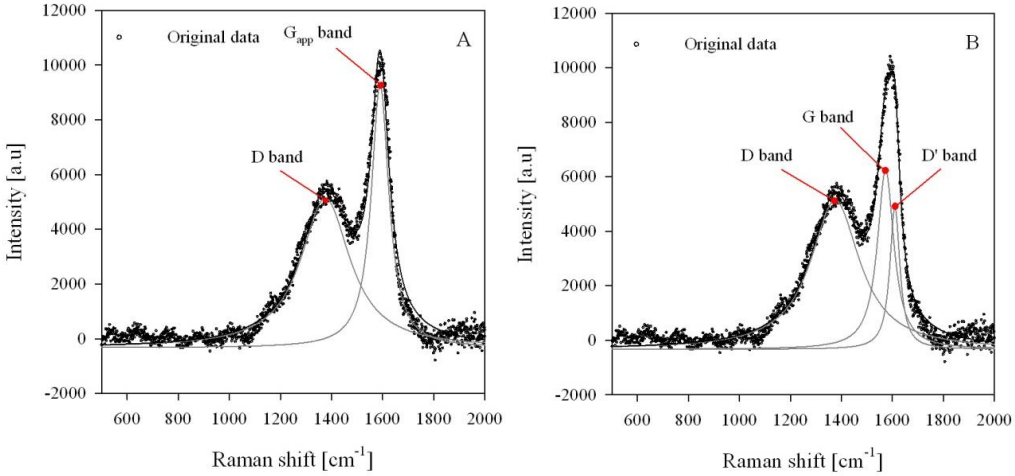

Figure 5-21 Deconvolution of Raman spectra of the edge of the deposited material. A) deconvoluted Raman spectra for D and G_{app} bands at 1375.62 and 1589.94 cm^{-1}; B) deconvoluted Raman spectra for D, G, and D' bands at 1375.62, 1573.68, and 1610.04 cm^{-1}, respectively. Deconvolution methodology was adapted from ref. (*193*).

Since the deposited material at the edges is characterized as graphene, in-plane crystallite size of the deposited material at the edges can be calculated by the following formula (*195*):

$$L_a[nm] = (2.4E-10)\lambda^4 \frac{I_{G_{app.}}}{I_D} \quad (5\text{-}5)$$

where λ is wavelength used for Raman measurements and $I_{G_{app.}}$ and I_D are integrated intensities (i.e. area under the curve) of the $G_{app.}$ and D bands in Raman spectrum. According to equation (5-5), $L_a = 10.3\ nm$ at $\frac{I_{G_{app.}}}{I_D} = 0.63$ which is in similar range of what was achieved for boron doped graphene by Panchakarla et al. (*196*).

Despite in-plane crystallite size analysis, appearance of D band in Raman spectrum indicates increase rate of order for amorphous carbon (*182*). Therefore, it is concluded that the deposited material is more ordered at the edges than away from edges. In addition, D band is correlated with sp^3 carbon defects. From XPS analyses of the bulk of the deposited material, we saw ~ 34% of carbon atoms were sp^3 carbons. Interestingly, $\frac{I_{G_{app.}}}{I_D + I_{G_{app.}}} \times 100 = 38\%$, which is in good agreement with XPS results of the bulk of the deposited material. This suggests the Raman spectra shown in Figure 5-21 may be the same as Raman spectra of the bulk of the deposited material.

D band in Raman spectra shown in Figure 5-21 may also be related to C-H bonds, as shown in Figure 5-16A. This is a known feature of hydrogen tad amorphous carbon (*197*). Hydrogenated amorphous carbon (a-C:H) films may have different levels of hydrogen, associated with strength of D band. a-C:H films may have H content of 40–50%. They are known as polymer-like a-C:H (PLCH) and they can have band gaps in range of 2–4 eV. Most of the sp^3 bonds are hydrogen terminated. a-C:H films with intermediate H content (20–40 at%), having a lower overall sp^3 content, are known as diamond-like a-C:H (DLCH). They have more

C-C sp^3 bonds compared to PLCH. Their band gap is between 1 and 2 eV. The next category is ta-C:H (hydrogenated tetrahedral amorphous carbon). They have high C-C sp^3 (~ 70 at%) content but fixed H content (~ 25 at%), with a band gap of ~ 2.3 eV. The last category is graphite-like a-C:H (GLCH) with high sp^2 content and sp^2 clustering and lower H content (< 20 at%) (*197*). Raman spectroscopy is a good method to determine the type of amorphous carbon. In addition, properties like band gap and density of the amorphous carbon can be correlated to the measured D and G bands. Presence of hydrogen in amorphous carbon may be responsible for semiconducting behavior of hydrogenated amorphous carbon because a good correlation between H content and band gap of a-C:H was observed (*197*). In Figure 5-16A relatively high level of noise was observed. This level of noise might be related to photoluminescence background (PL) which may be a sign of relatively high hydrogen content of the deposited material (*198*). In addition, peaks m–o in Figure 5-16A, corresponding to hydrogen terminal on carbon atoms, are relatively intense. Therefore, it is anticipated that the deposited material has semiconducting properties and therefore a measurable band gap. This is investigated further using ultraviolet-visible spectroscopy in section 5.1.7.

5.1.6 Time-of-Flight Secondary Ion Mass Spectrometry (ToF-SIMS)

If the deposited material is a graphenic material, then it should have a high molecular weight and should consist of clusters of carbon molecules. Time-of-Flight Secondary Ion Mass Spectrometry (ToF-SIMS) is a very relevant instrument to analysis the deposited material from molecular weight perspective. Electron ionization is the most appropriate technique for relatively small (molecular weight < 600) neutral organic molecules which can easily be promoted to the gas phase without decomposition (*199*). Molecular weight of the deposited material were measured using ToF-SIMS, deploying Bi gun at negative and positive polarities as shown in Figure 5-22. The analyzed area on PEC182 cathode are shown in Image 5-2. Using different

polarities allows detection of different fragments of the analyzed samples because some materials are easier to ionize using either of negatively or positively charged ionization source. As shown in Figure 5-22, using negative polarity we were able to ionize and detect heavier fragments easier. Using Bi3 gun and negative polarity, fragments of up to 1400 Da were detected. In addition, since the analyzed sample in Figure 5-22 was etched with Cs prior to analysis, effect of positive Cs charges on analysis when positive polarity were used was evident (high signal intensity at m/z = 132 were observed). However, irrespective of polarization mode (positive or negative), for m/z > 50 significantly lower mass spectrometer signal intensity was detected.

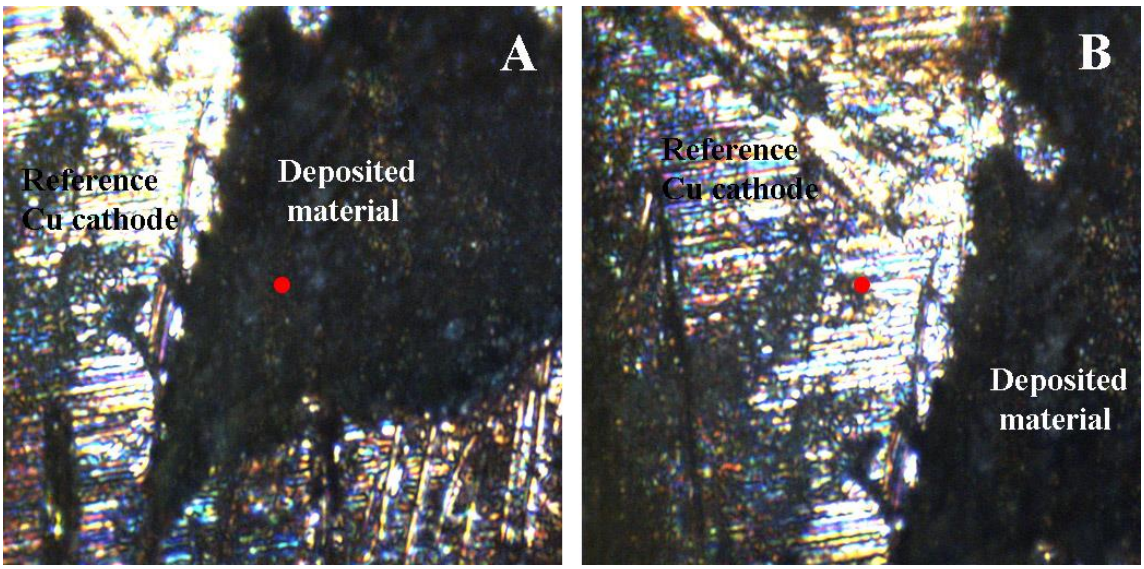

Image 5-2 Digital photograph of the sample used for ToF-SIMS analysis. The analyzed spots are shown with the red circles. The corresponding mass spectrometer spectra are shown in Figure 5-23.

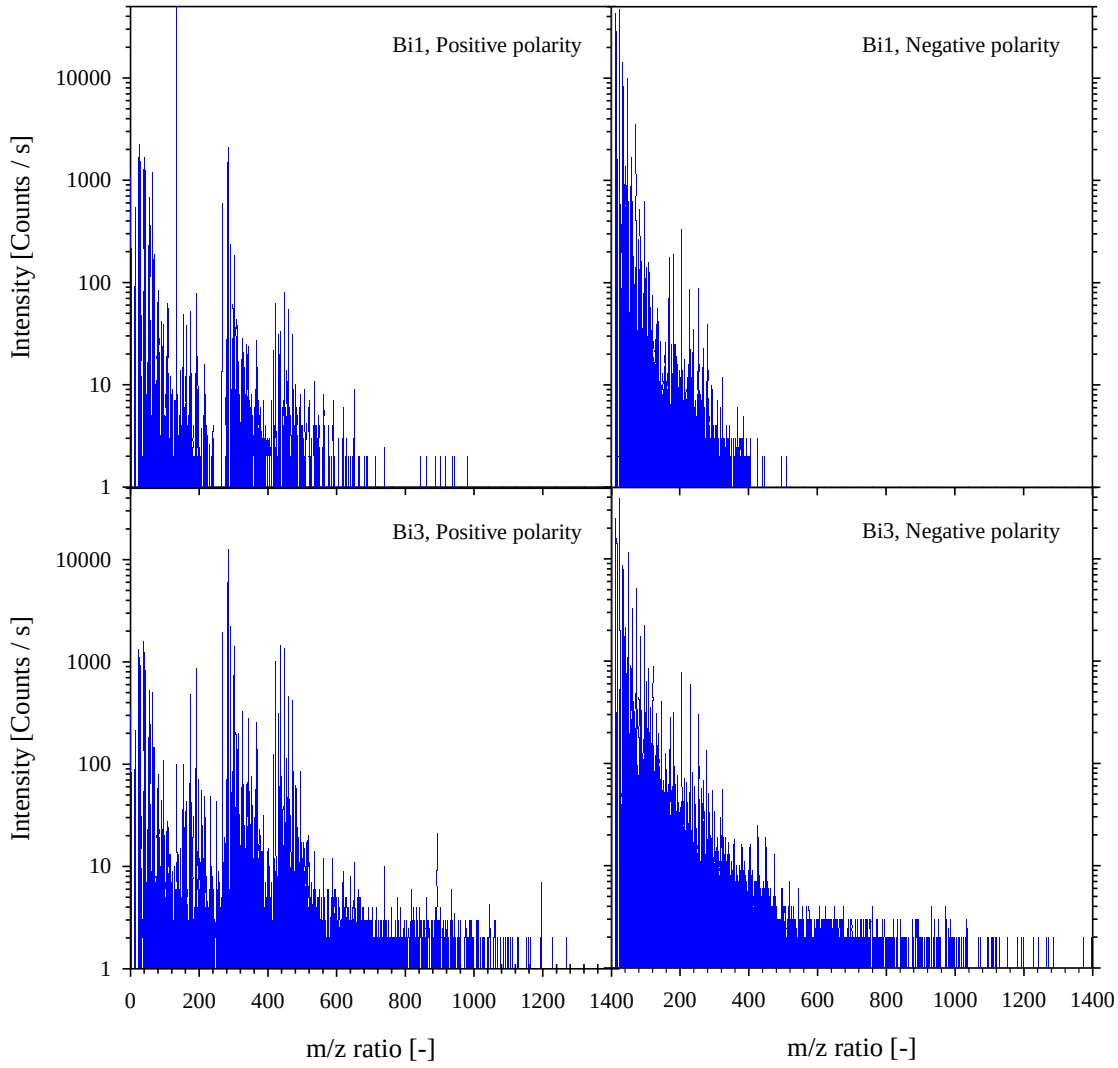

Figure 5-22 ToF-SIMS data of the deposited material using Bi1 and Bi3 gun at 30kV potential. Analyzed area on the deposited material were etched for 100 s using Cs ion beam at 1 kV potential before analysis.

Signal intensities of the deposited material were compared with that of reference copper cathode in Figure 5-23a and m/z ratios at which ratio of single intensity of the deposited material were higher than that of reference copper cathode were marked with red circles ($\frac{I_{\text{deposited material}}}{I_{\text{reference copper cathode}}} > 1$). This is a reliable method to determine if the detected signal is sourced from the deposited material or from surface contaminations such as Nafion® residuals. As expected, the majority of the red circles correspond to m/z ratios of clusters of carbon or

hydrogenated carbon. Figure 5-23b shows the results of the same analysis before etching the analyzed area using Cs ion beam.

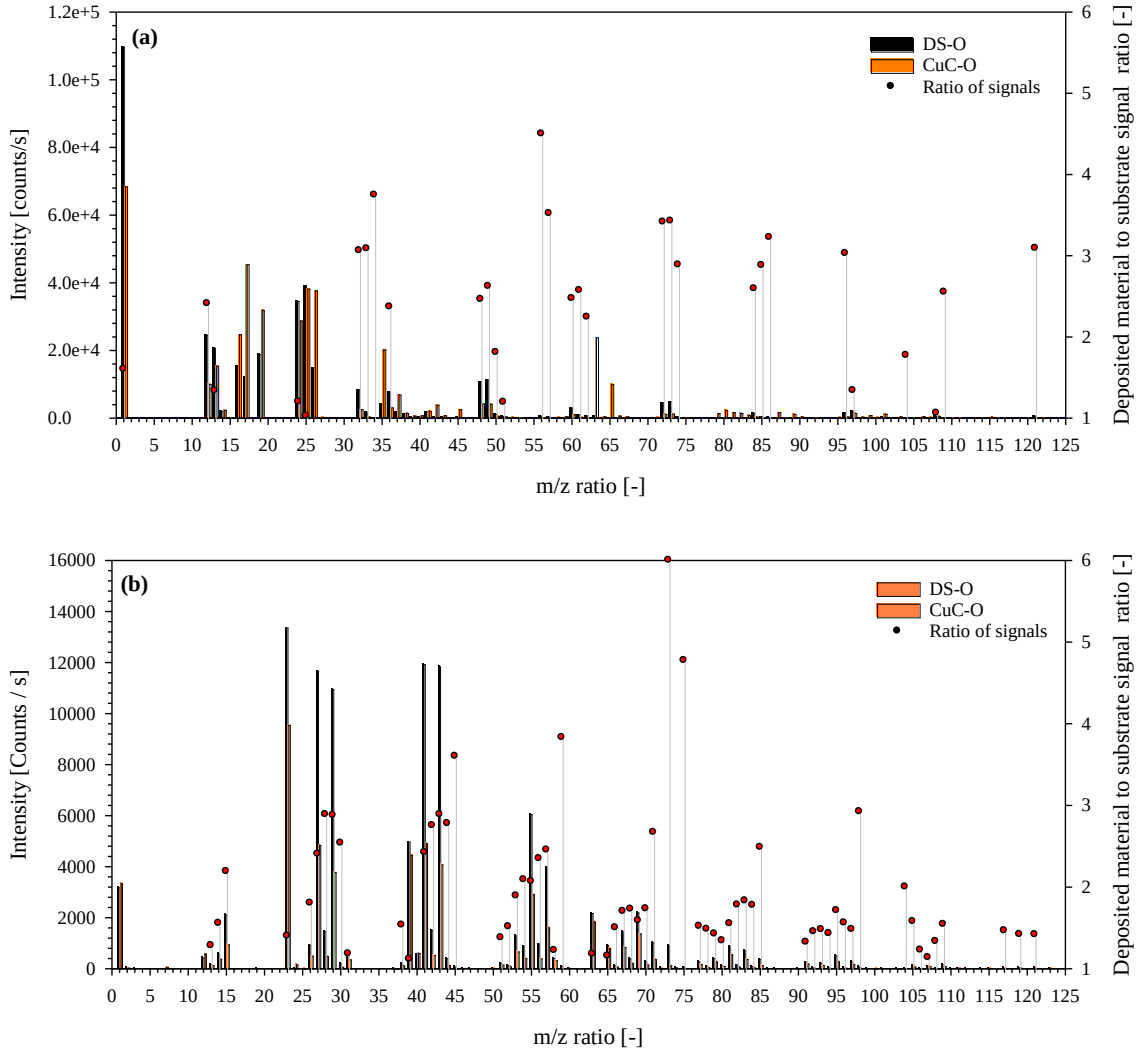

Figure 5-23 ToF-SIMS spectra of the deposited material vs. reference copper cathode. a) Bi3 at 30 kV were used as ionization gun (negative polarization). Samples were etched for 100 s using Cs ion beam at 1 kV potential before analysis. b) non-etched Bi1 Positive. Corresponding molecules for each specific m/z ratio were extracted from MassBank public mass spectral database (*200-202*)

In addition, comparing the MS spectra derived from the deposited material with a number of long chain hydrocarbons shows a meaningful resemblance. Figure 5-24 shows although the larger hydrocarbon had high molecular weights, but ToF-SIMS was not able to ionize the whole molecule without fragmentation of the large hydrocarbon molecule. For all four reference

materials the highest MS intensity were detected at m/z ~ 40, similar to DS-O, except OCCC(C)CCO which was the lightest molecule among others at MW = 118 with higher number of oxygen molecules and a branched structure.

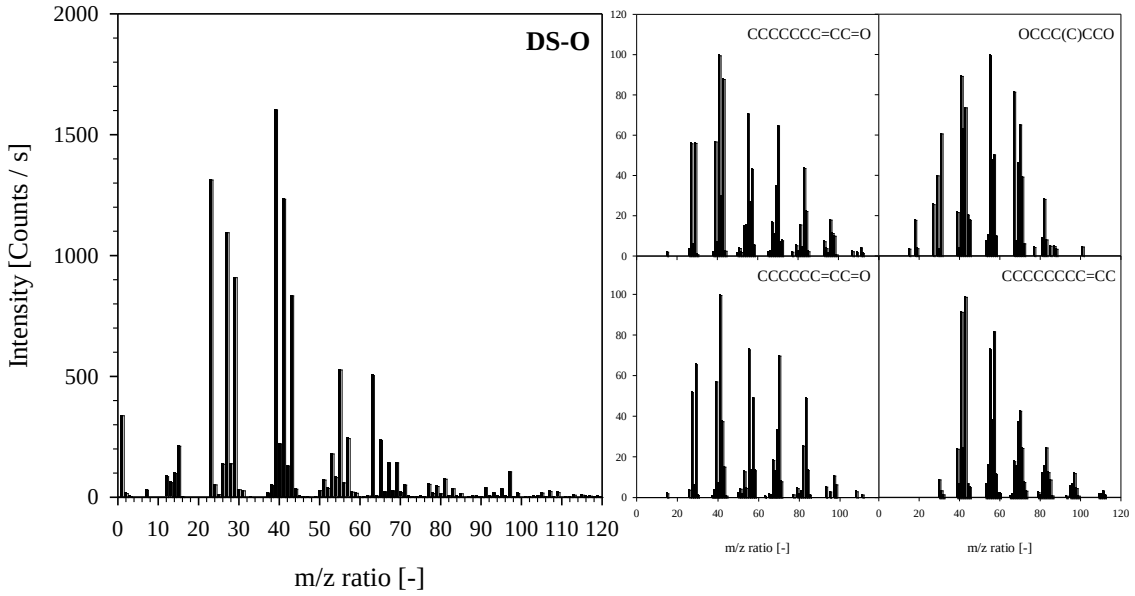

Figure 5-24 ToF-SIMS analysis of the deposited material using Bi3 at 30kV with positive polarity. The sample was etched with Cs at 1kV for 100 s prior to analysis. Sample of ToF-SIMS of a variety of large hydrocarbons are also presented on right when the same ionization polarity was used. Spectrums were extracted from MassBank public mass spectral database (*200-202*).

5.1.7 Ultraviolet-Visible (UV-Vis) spectroscopy

It is reported in literature that graphenic material may also have semiconducting properties. In addition, evidences were observed in section 5.1.5 that predicts semiconducting properties for the deposited material. Furthermore, relatively high thickness and relatively big size of the deposited material (2000 × 1000 × 20 µm) suggests the deposited material should have catalytic activity toward CO_2 reduction. Presumably, this catalytic activity allowed CO_2 to continually grow on the deposited material. High portion of sp^2 carbon may be partially responsible for this. However, potential semiconducting properties of the deposited material with correct band gap may also contribute toward self-catalytic activity of the deposited material.

The semiconducting behavior of the deposited material was initially proved through a simple experiment. In this experiment, the deposited material were placed under optical microscope and looked at under different colors of light. If the deposited material had semiconducting properties, then it should show different levels of transparency under different colors of light, which subsequently correspond to different light wavelength and excitation energies. One of the key properties on semiconducting materials is variable light absorption properties due to their electronic structure. For example, different wavelengths of electromagnetic wave have different wavelength. When the energy of electromagnetic wave exceeds that of required to excite electrons in a material, then the material absorbs that energy and therefore does not allow the electromagnetic wave to pass through the material and therefore the material becomes opaque respective to that specific wavelength. This is the fundamental of UV-Vis. analysis, which is essentially a way to measure opacity of a material when the material is subjected to a range of electromagnetic waves with different wavelengths. The results of such a test are shown in Image 5-3. Here, possibility to see the Cu substrate was treated as a criterion of transparency. As shown in Image 5-3, when the deposited material was under red light, the lateral groves of the Cu substrate were clearly visible. When blue light was used instead, a very small portion of the lateral grooves were visible under optical microscope. This observation, provided an initial proof for semiconducting behavior of the deposited material, and therefore lead us to measure its band gap.

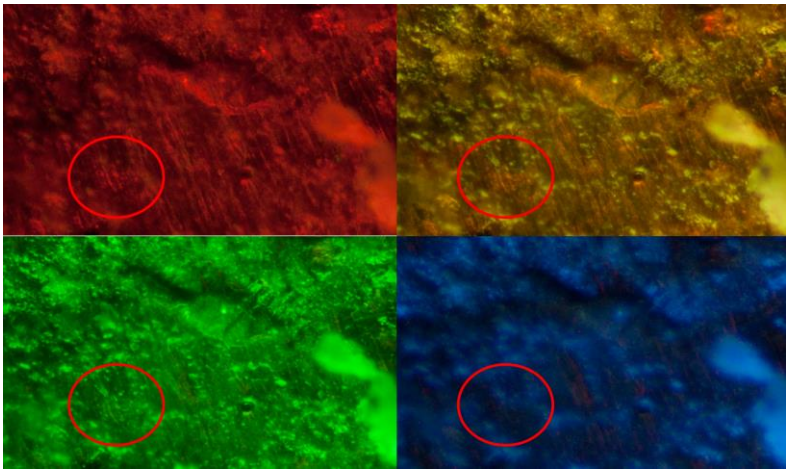

Image 5-3 Digital micrograph of the deposited material under optical microscope using various light colors as light source.

Band gap of the deposited material were measured using a hand held Ultraviolet-Visible spectrometer. The results confirm the initial observation under optical microscope. Figure 5-25 shows the deposited material has two band-gaps. One at 2.02 eV, which corresponds to a wavelength of 614 nm (between orange and red light), and one at 2.52 eV, which corresponds to a wavelength of 491 nm (between blue and green light).

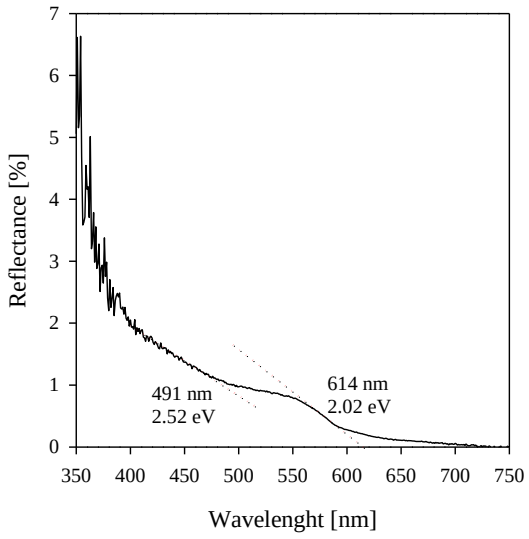

Figure 5-25 Band gap measurement of the deposited material using UV-Vis. spectroscopy.

The reason behind observation of two band gaps on the deposited material is not clear. However, based on the observed evidences, two distinct hypotheses can be made. First hypothesis is that the band gap at 2.02 eV may not be related to the deposited material. The reason is this band gap is very similar to that of Cu_2O. In addition, oxygen was observed during EDS analysis in vicinity of the deposited material (see Figure 5-6B) and through XPS analysis. Therefore, the lower band gap may only be related to Cu substrate and, possibly, partial oxidization of copper during CO_2 reduction reaction (copper may react with H_2O, CO_2, or residuals of O_2 that remained in the reactor from purging process, to produce CuO or Cu_2O). Second hypothesis is that the deposited material may have consisted of two distinct phases of graphenic material and consequently has two separated band gaps. One evidence that supports this hypothesis is observation of two different types of Raman spectra for different parts of the deposited material (at the edge and away from edge of the deposited material, see Figure 5-16A and Figure 5-20). This may be a consequence of different levels of graphenization on the deposited material. DFT studies show number of aromatic rings may also affect the band gap of graphenic materials (*203*). For large number of aromatic units (N = 37), a band gap of ~ 2.05 eV was predicted. For lower number of aromatic units predicted band gap was larger (for N = 1, band gap = ~ 7.4 eV). In addition, defects highly affect band gap of graphenic materials. Pure graphene does not have an energy gap in its electronic structure (*204*). Panchakarla et al. (*196*) reported doping monolayer graphene with boron lead to a band gap opening of ~ 0.9 eV. Shen et al. (*205*) reported band gap of reduced graphene oxide was tunable from 2 to 0.02 eV depending on reduction level. Zhou et al. (*204*) reported for thin layers of graphene, substrate may induce a band gap. In addition, number of layers may also affect the measured band gap. Therefore, it is possible that CO_2 was converted to different types of graphenic material at different locations or different depths, during photoelectrochemical test of PEC182.

Using Raman spectra of the deposited material and using a correlation for band gap measurement of different a-C:H we can estimate band gap of the deposited material and compare the estimated value with measured value. The correlation used here is shown in Eq. (5-6) below (*197*):

$$band\ gap\ [eV] = 7.12 - 0.0666\ FWHM_G + 0.000186\ {FWHM_G}^2 \quad (5\text{-}6)$$

where $FWHM_G$ is full-width at half maximum of the $G_{app.}$ peak.

Based on Eq. (5-6) and using deconvolution data shown in Figure 5-21A, band gap of the deposited material at edges were estimated to be 2.85 eV ± 0.53 eV. If we use the spectrum that was shown in Figure 5-16A, which is more compatible with type of Raman spectra used to derive Eq. (5-6), estimated band gap is ~ 2.0 eV, which is similar to the first measured band gap shown in Figure 5-25 at 2.02 eV.

Furthermore, according to Casiraghi et al. (*197*), the correlation between hydrogen content of a-C:H follows Eq. (5-7), which can be rearranged, as shown in (5-8), to estimate hydrogen content of a-C:H based on the band gap.

$$band\ gap\ [eV] = -0.9 + 0.09 \times \mathrm{H}[at\%] \quad (5\text{-}7)$$

$$\mathrm{H}[at\%] = \frac{band\ gap\ [eV] + 0.9}{0.09} \quad (5\text{-}8)$$

Using Eq. (5-8), at measured band gaps of 2.02 and 2.52 eV, hydrogen content is 32.22 and 37.78 at%. Interestingly, this is consistent with 31.78 at% of sp^3 carbon that was measured from XPS analysis of the deposited material at 300 nm from the surface. This strongly suggests a significant portion of sp^3 carbon atoms of the deposited material are hydrogen terminated. According to Casiraghi et al. (*197*), at hydrogen content of > 20 at%, a fair level of PL should appear in Raman spectra in form of noise. This is also compatible with the measured Raman spectra at the places far from the edges of the deposited material (see Figure 5-16A). Therefore, we suggest the multiple band gaps measured are genuinely related to the deposited material and

correspond to multiple phases of hydrogenated amorphous carbon and defected graphenic material on the deposited material.

5.1.8 Conclusion

Overall, from the characterization results presented in sections 5.1.1–5.1.7, it is concluded the product of CO_2 reduction reaction were majorly a form of hydrogenated amorphous carbon with different oxygen and hydrogen containing functional group defects, which provided the deposit material with semiconducting properties, and high sp^2 carbon content, which provided the deposited material catalytic properties and graphenic appearance. These specific features, semiconducting properties and high sp^2 carbon content, provided the deposited material with self-growing properties, which lead to continuation of growth of the deposited material through continues conversion of gaseous CO_2 to a graphenic material first on Cu cathode and then of the deposited material itself.

5.2 Mechanism

Based on the observed evidences we suggest a mechanism for CO_2 reduction using the proposed PECs, as shown in Scheme 5-1, by dividing the mechanism to molecular scale and macro scale. For the main pathway on molecular scale, CO_2 is absorbed on Cu, forming $CuCO_2$ complex, leading to bending of C=O bonds from 180° to 125–135°, due to affinity of copper toward oxygen (*206*). This lead to loosening of C=O bonds. CO_2 then loses one oxygen molecule forming adsorbed CO on surface of copper (also confirmed experimentally (*101*, *207*)), in presence of H^+ which is made available from water splitting reaction on photoanode surface and delivered to copper reaction sites through Nafion® nanoribbon mat. That is why adsorbed CO peaks were observed both in Raman and IR spectroscopy (Figure 5-16).There may be various pathways for further reduction of $CO_{ad.}$ (*208*), however, because the reduction media in

the described device is deprived of protons (in contrast to abundance of H^+ in aqueous phase CO_2 reduction), we propose the most likely pathway is further reduction of CO to solid carbon through cross-coupling of $CO_{ad.}$ species, forming H_2O and O_2 as byproducts. (Using density functional theory (DFT), cross-coupling of carbonous species was confirmed as a feasible explanation for polymerization of aromatic structures during graphene synthesis (*209*).). In addition, when the PEC is illuminated, copper surface is electron rich due to conversion of light to electron/hole pairs in a-Si, providing relatively strong negative charge to copper surface. This electric charge may further disturb charge density distribution of absorbed CO molecules (providing slight positive charge further way of copper surface) and providing more driving force of oxygen end of CO to react with available protons or O on neighbor CO_{ad} molecule, forming H_2O and O_2 gas, and initiating cross-coupling and polymerization of carbon atoms. This provides a pathway for electrons distribution and charge polarity relaxation. Furthermore, due to conductivity and therefore negative charge distribution and abundance of electrons on surface of the newly formed solid carbon, deposited material acts as a catalyst for further adsorption and conversion of CO_2, similar to what is described for polycyclic aromatic structures (*178*). Therefore, solid carbon islands grow. DFT studies support this conclusion by showing CO_2 molecules have high physisorption tendency on carbonous materials with rich hexagonal sp^2 carbon content (*178*).

Conversion of CO to solid carbon is also thermodynamically favorable because CO_2 to CO reaction occurs at -0.11 V_{she} while CO to solid carbon reaction takes place at +0.52 V_{she} (the overall CO_2 to solid carbon reaction takes place at +0.63 V, relative to *she*). This leads to formation of islands of solid carbon as confirmed by SEM and EDS (Figure 5-8B). However, as confirmed by Raman and IR spectroscopy Figure 5-16, in some locations in presence of strong electric potential difference CO may react with available protons or already formed solid carbon

to form carboxyl, ketone, alcohol, ester, and other organic functional groups, forming defects and broken chains similar to that of reduced graphene oxide (*210*).

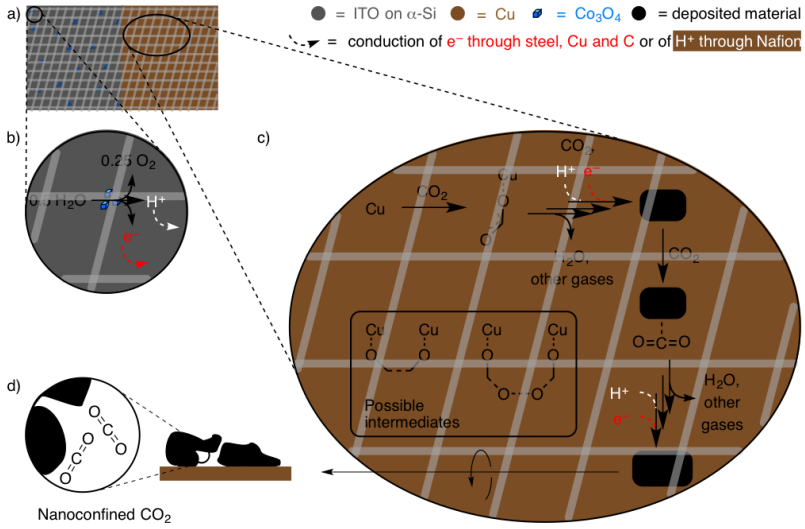

Scheme 5-1 Proposed mechanism of CO_2 reduction to solid carbon on copper surface of the proposed PECs.

On macro scale, carbon islands were formed on multiple spots. The islands merge or bridge in cases where they were close enough (such as in Figure 5-8B), forming cavities which were observed as pores in SEM micrographs (Figure 5-1C and Figure 5-2F, K, H, G). Since the reaction media is rich in CO_2 gas, some portion of CO_2 were trapped in the pores, giving rise to strong CO_2 peaks in IR spectra (Figure 5-16B peaks q and r). Formation of pores and curved surface further enhances CO_2 reduction through nanoconfinment mechanism (*170-172*).

5.3 Summary

In this chapter, we extensively characterized the detected product of CO_2 reduction reaction that was formed on cathode surface of PEC182, using various techniques. Using these analyses we proved that CO_2 can be reduced directly from gas phase, to a form of graphenic material which by itself acts as catalyst of CO_2 reduction. Therefore, the product of CO_2 reduction reaction was a self-growing material, due its semiconducting properties and abundance of sp^2

carbon. In addition, a mechanism for reduction of CO_2 on PEC182 was suggested based on characterization results and published literature.

Chapter six

Conclusion and future work

In this thesis a novel photoelectrochemical cell (PEC) for direct conversion of gaseous CO_2 to solid carbon using earth abundant materials was conceptualized, designed, realized, and tested. It was found that the proposed PEC is able to convert CO_2 to a self-growing graphenic material, which greatly resembled graphene and amorphous hydrogenated carbon, when placed in an environment where gaseous CO_2, gaseous H_2O, and light coexisted. The proposed PEC was extensively experimented under different atmospheres including humidified and dry, Ar and CO_2 using unassisted and assisted photoelectrochemical and electrochemical techniques. The product of CO_2 conversion reaction were extensively characterized using optical microscopy, SEM, EDS, XPS, AFM, ToF-SIMS , IR spectroscopy, Raman spectroscopy, UV-Vis spectroscopy, and Laser profilometry.

During photoelectrochemical tests it was found that generated photocurrent through the proposed PECs declined quickly. This may be one of the major issues that limits application the proposed PECs in real-life applications. It was found that decline in photocurrent was closely related to increase of PECs temperature during operation due to being under illumination. In addition, experimental evidences were provided showing the generated photocurrent can be stabilized if the temperature of the PECs was kept constant. In this thesis, we used heat sinks to prevent the PECs temperature rise. Although use of heat sinks further proved that generated photocurrent can be stabilized using this method, it was not sufficient enough to allow operation of the PECs for extended period of time. We suggest here that thermal sink be replaced with other more efficient thermal stabilization methods such as use of coolants (i.e. flowing water) to achieve higher degree of thermal and consequently photocurrent stabilization.

In this study only two catalysts materials were successfully tested: Cu sheet and Ni NPs on Cu_2O/CuO NRs. Although it was showed that formation of solid carbon occurred on Cu sheet, possible products of CO_2 reduction reaction on Ni NPs on Cu_2O/CuO NRs were not analyzed. In

addition, role of Ni and Cu_2O/CuO NRs was not separately studied. Therefore, we suggest more promising catalysts to be studied. Furthermore, study of possible effects of catalyst type on reaction products and reaction extend is of interest as well.

In this study maximum level of generated photocurrent was ~ 10 µA for PEC182. Although generated photocurrent was significantly increased in comparison to the first conducted proof-of-concept test using PEC115 (generated photocurrent using PEC115 were ~ 0.6–0.9 µA), still higher photocurrents needs to be reached to make real-life application of the proposed PEC feasible. Higher level of photocurrent may be achieved through further improving the PECs assembly procedure to avoid damaging the photoanode of the PECs during assembly steps, and manipulating the PECs configuration to lower proton conductivity resistance. More efficient proton conductive material may also further improve the photocurrent level. Conducting the conversion reaction at higher temperature may also significantly improve detected photocurrent through providing more water vapour to Nafion® and changing crystalline phase of Nafion® to a more proton conductive phase. Use of other more active photocatalysts and electrocatalysts may also help with generated photocurrent. Importance of each one of the above mentioned methods can be evaluated using circuit based modeling techniques in which each of the reaction steps is represented by a hypothetical resistance with a specific resistivity corresponding to that of observed experimentally.

One of the challenges we had to face during assembly of the PECs was low mechanical strength of Nafion® mats. Nafion® mats were easily broke during mounting and unmounting of the PECs in the reactor. In order to avoid breakage of Nafion® mat during assembly and testing of the PECs, one needs to use a mechanically strong support to make sure relative position of cathode and photoanode does not greatly change during PEC handling. In this thesis, this

problem was partially solved by using 1 mm thick plastic supports. However, great improvements are still achievable.

In this thesis, we only manufactured PECs with side-by-side configuration. No study on the effect of change of configuration on PECs performance was carried out. Investigation of other possible configurations may not only provide more insight on mechanism of CO_2 conversion on the PECs, but also may lead to considerable improvement in PECs performance, mainly through reducing proton conduction pathway from photoanode to cathode. Some of the possibly promising configurations are ribbon-like configuration, where thin ribbons of photoanode and cathode are placed side-by-side and then coated with Nafion® mat through electrospinning, and sandwiched configuration, where cathode/Nafion® mat/photoanode assembly is made through pressing. Both of these configurations lead to significant reduction of proton conduction length from photoanode to cathode. Cathode type may be changed to enable realization of different configurations. For example, in sandwiched configuration a mesh type cathode (e.g. Cu mesh) should be used to allow penetration of light and reactants to photoanode and cathode reaction sites. In this way, one of the major barriers of reaching high photocurrent density can be significantly improved. To manufacture a PEC with such a configuration, firstly, water splitting catalyst coated photoanode should be coated with Nafion® nanoribbon mat. Then, pressure can be applied to press cathode mesh on Nafion® coated photoanode surface. Such a configuration is not possible to realize using a-Si PVs due to very high chance of micro fracture development in a-Si PVs due to applied pressure.

In this thesis, we only used a-Si PVs as photoanode material, which deemed to be prone to failure due to low mechanical strength. Other types of photoanode materials may also be studied to manufacture more robust PECs. Specifically, multi-junction flexible semiconductor materials are promising to use in this application.

Light to product efficiency of the developed PECs were not measured in this study because measuring the amount of produced solid carbon were not possible. Such a measurement would be possible if the operation duration of the PECs were extended. In addition, to calculate light to product efficiency, the true photocurrent generation ability of the photoanodes at reaction potential should be known, through measuring PECs I-V curve In order to carry out reliable I-V curve measurement of the assembled PECs, a Cu current collector should be installed on photoanode prior to assembly and be kept on the photoanode to enable investigation of any possible change in I-V curve of the photoanode at any step of assembly procedure.

Although we proved that conversion of CO_2 directly from gas phase to solid carbon is possible using the proposed PECs, no attempt to develop a method to separate solid carbon products were made. One way to coupe with this is to regenerate the PECs after certain operation duration. One may hypothesis the following scenario to coupe with product separation issue. Since the produced solid carbon has self-growing properties, meaning the product of CO_2 conversion is a suitable material for further conversion of gaseous CO_2 to more solid carbon, accumulation of CO_2 product may continue to take place beneath Nafion® mat. Eventually, thickness of the deposited carbon on cathode surface would be high enough to physically disconnect Nafion® mat form photoanode surface. At this point, the PECs fail to operate any further and need to be regenerated. Regeneration of the PECs may be carried out through washing away Nafion® mat from PECs with a proper solvent, e.g. isopropanol, and then disconnecting and cleansing the cathodes using a suitable liquid using sonication. The deposited carbon then may be recovered through filtering and dissolved Nafion and cleansed cathodes may be reused in new PECs.

It was shown in Chapter 3 that photocurrent related to CO_2 reduction reaction was detected for CO_2 concentrations as low as 10 vol%. This potentially means for the proposed PEC to work

in gas phase dilute sources of CO_2 can be used. For example, flue gas of a coal-fired power plant typically consists of 15 vol% CO_2 and 7 vol% H_2O. These concentrations of CO_2 and H_2O in a flue gas already exceeds that of experimented at 10 vol% CO_2 and only ~ 2 vol% H_2O, as shown in Chapter 3. This potentially means if the proposed CO_2 be used for CO_2 conversion no CO_2 capture unit would be required to provide a highly concentrated CO_2 stream. Therefore, the proposed PEC can be used directly in contact with a flue gas stream. This warrants a great potential for the proposed PEC to be explored further. However, one should be mindful of potential risks that other components of a real flue gas such as SO_x and NO_x may impose to operation of the proposed PEC.

Detection of gaseous products like CO and O_2 is required to further validate the concept that complete CO_2 reduction and H_2O oxidation have occurred. In addition, gaseous CO may be a more valuable product than solid carbon. By using a closed reactor, it is possible to detect these gas products by gas chromatography. A closed-reactor experiment can be done and gas samples can be drawn by a syringe to inject to GC.

The carbon deposit on the electrode may deactivate the PEC. A fully carbon-covered electrode may completely lose the activity. Even though it may be regenerated by removing the carbon, economic aspects of this procedure depends of the extent of CO_2 conversion before PEC regeneration. Therefore, one may focus on how to convert CO_2 to gaseous or liquid products rather than carbon. In addition, the lifetime of the PEC is very short, only 100 s even with the help of a heat sink. Demonstration of at least a few hours operation is highly desirable. The short lifetime also prevents the measurement of gaseous products in a continuous operation mode.

PECs operation bottle neck(s) was(were) not identified in this study. PECs operation bottle neck(s) may be either of or a combination of CO_2 reduction catalyst activity, water splitting catalyst activity, photoanode light to current efficiency, photoanode V_{OC}, Nafion® mat proton

conductivity, proton conductivity pathway length and/or other unknown factors. It is important to systematically investigate the operation bottle neck(s) of the PECs in order to reach significant improvements in operation efficiency.

Apart from using the proposed PEC for achieving negative emissions and combating climate change, the proposed PEC can also be used in two additional distinctive applications: Solar energy storage and terraforming of Mars. The major challenge of deploying renewable energies, especially solar energy, as the future of energy economy and the major long-term tactic to decarbonize the economy, is inefficient/expensive energy storage (*211*). For example, in a hybrid solar/wind power plant ~ 43% of total capital costs is related to batteries which are used for electricity storage (*212*). The proposed PEC can be used to convert CO_2 to solid carbon when excess sunlight exists. In this way, solar energy can be stored in chemical bonds of solid carbon. The produced solid carbon may then be used to reproduce energy, possibly through direct carbon fuel cells {Cao, 2007 #317}, at times when sufficient amount of solar energy is not accessible (e.g. during night or cloudy days). In this way, a closed loop of CO_2 is made. Therefore, a carbonous fuel, i.e. produced solid carbon, can be used without contributing to climate change.

Another application of the proposed PEC may be in terraforming of Mars. Terraforming is the process of transforming a hostile environment to an environment which is suitable for human life. Mars is the most Earth-like planet; therefore, it is the best candidate for terraforming {Fogg, 1995 #315}. Martian atmosphere consists of 96.0 vol% (±0.7 vol%) CO_2. O_2 is required for permanent settlement of human on Mars. As explained in section 5.2 of Chapter 5, theoretically, O_2 and H_2O are the byproducts of CO_2 reduction reaction. In addition, light is abundant in Mars. Therefore, one may conceptualize using the proposed PEC to convert CO_2 to O_2 in Martian atmosphere, and produce required O_2 for human's life, instead of splitting valuable and limited liquid water resources that exists on mars. In this way, one may balance CO_2 and O_2

concentration in Martian atmosphere to an acceptable level, quicker, through simultaneous decrease in CO_2 concentration and increase in O_2 concentration.

Appendixes

Appendix A. Optimum CaO:Coal Ratio in Enhanced Hydrogen Production

The practice of enhancing hydrogen (H_2) production from coal pyrolysis and gasification by adding CaO has attracted much interest. However, the optimal ratio of CaO:coal has not been determined. We aimed to find this ratio for Australian lignite and bituminous coals by studying their pyrolysis in the temperature range of 600–800 °C using thermogravimetry and mass spectrometry. The effects of pyrolysis temperature on the optimum CaO loading, the effectiveness of CaO addition on coal gasification, and the improvement in direct and indirect H_2 yields are discussed for each type of coal. The highest H_2 yield from pyrolysis at the most recommended gasification temperature of 650 °C was obtained for a CaO-to-coal ratio of nine to one by mass (equivalent to 10 wt% coal in feed). This optimal ratio varied from 5:1 to 19:1 depending on the temperature, heating rate, and coal type.

A.1 Introduction

Hydrogen, H_2, has increasingly been recognized as a future energy carrier (*213, 214*). Its combustion is clean and efficient and does not emit CO_2, the major contributor to anthropogenic climate change. Although H_2 would act as the energy carrier in this scenario, it could be generated from a number of processes (*215*). Among these, the large-scale production of H_2 from coal pyrolysis and gasification is economically competitive (*216*). In addition, the possibility of electricity and H_2 co-production, along with simultaneous CO_2-capture processes like HyPR-RING (*217*), ZECA (*218*), and UFP (*219*), make H_2 production from coal attractive for large-scale deployment.

Unfortunately, the production cost of H_2 from coal is high for two main reasons—the high temperature requirement, and therefore the high energy demand, of the process, and the low H_2 content of coal, which results in a relatively low rate of H_2 production rate per unit of coal mass. Fortunately, an appropriate catalyst can significantly reduce the process temperature, and steam can be injected to gasify coal, dramatically increasing the rate of H_2 production via the water–gas shift reaction (*220*).

Since the 1970s (*221*), a variety of materials have been tested to find a durable, active, and low-cost catalyst for H_2 generation from coal (see Table A 1). Alkaline earth metal oxides stand out as active catalysts, and among these, CaO has been favored for its high catalytic activity and relatively low cost (*150, 222*). Furthermore, CaO reduces tar formation (*223, 224*) and eliminates sulfur components from the gaseous product stream (*225-227*).

Apart from its catalytic roles, CaO also functions as a strong in situ CO_2 separator in enhanced steam-gasification processes. Its exceptional CO_2-uptake capacity has made it the most attractive sorbent in post-combustion carbon capture (PCC) applications (*228*). However, in PCC applications, CaO loses CO_2-uptake ability, which has raised some concerns (*229*). On the other hand, in steam–coal gasification, the carbonation reactivity of CaO (i.e. Eq. A A1) is more stable, possibly because it is hydrated at the gasifier entrance in each cycle, prior to carbonation (*230, 231*).

$$CaO + CO_2 \rightarrow CaCO_3 \qquad \text{(A1)}$$

The benefits of CaO in calcium-promoted coal gasification have attracted many researchers to investigate the key technical parameters (e.g. coal type, gasification temperature and pressure, gasification atmosphere, coal throughput rate, etc.) that affect H_2 yield (*224*, *226, 230-238*). However, the effect of CaO:coal ratio on H_2 yield is not yet fully investigated. Most studies use

CaO:coal ≤ 2 (by mass), though the reaction stoichiometry and the formation of a carbonate layer on CaO particles have led researchers to suggest CaO:coal ratios as high as 80 (*222*).

The aim of this paper is to shed light on the CaO:coal ratios that optimize the H_2 yield from the pyrolysis of two types of coal (bituminous and lignite). We used thermogravimetric analysis–mass spectrometry and considered two heating rates (10 and 50 °C/min, i.e. 0.17 and 0.83 °C/s). CaO:coal ratios ranging from 19:1 to 0:1 were tested, and optimal ratios were defined over the range of recommended gasification/pyrolysis temperatures (600–800 °C) (*222, 231, 236*).

Table A 1 Materials that have been tested as catalysts in coal pyrolysis and gasification.

Tested material	Ref.
KCl, Li_2CO_3, Bi_2O_3, Sb_2O_5, Fe_3O_4, Cr_2O_3, ZrO_2, Pb_3O_4, CuO, Al_2O_3, Cu_2O, PbO_2, CrO_3, NiO•BaO, TiO_2, CoO, MgO, V_2O_5, MnO_2, MoO_3, Ni_2O_3, SrO, $ZnBr_2$, NaCl, ZnO, $NiCl_2$•$6H_2O$, $NiSO_4$•$6H_2O$, $Ca(OH)_2$, Fe, SnO_2	(*221*)
K_2CO_3	(*221, 239*)
$Ba(OH)_2$, $Sr(OH)_2$, $Mg(OH)_2$	(*240*)
Ni	(*221, 241*)
$Ca(NO_3)_2$, $Ca(OAc)_2$, $Ca(OH)_2$, $CaCO_3$, $CaCl_2$, $CaSO_4$	(*242*)
$FeCl_3$	(*243*)
NaOAc, NaOH, Na_2CO_3, KOAc, $Ca(OAc)_2$, Na_2SO_4, $Ni(OAc)_2$, NaCl	(*220*)
CaO•MgO, NiO, Al_2O_3	(*235*)
Fe_2O_3, Fe_3O_4	(*234*)
Ag_2O, BaO, CaO, Cs_2O, K_2O, Li_2O, MgO, Na_2O, Rb_2O, SrO, ZnO	(*150*)

A.2 Materials and methods

A.2.1 Sample preparation

In this study, bituminous coal from the Drayton colliery (NSW, Australia) and lignite from the Yallourn mine (Victoria, Australia) were used. The proximate, ultimate, and ash analyses of the tested coals (shown in Figure A 3) were carried out by SGS Australia using the AS1038 standard. The coals were ground, sieved to <212 μm, and dried for 3 h at 100 °C in a vacuum oven to minimize their H_2O content and, therefore, any hydration reactions between the

humidity in the coal and the CaO with which the coal is mixed. Commercial CaO (Sigma–Aldrich), was also sieved to <212 μm, and was then calcined under flowing argon for one hour at 900 °C to remove $Ca(OH)_2$ and $CaCO_3$ impurities, and finally stored in a desiccator under dynamic vacuum.

CaO:coal samples were prepared by combining the two components, in the desired mass ratios, in sealed glass containers. These were shaken for 5 min using a sieve shaker to mix their contents homogenously, then stored under dynamic vacuum in a desiccator to prevent contact and subsequent reactions of the CaO with the humidity and CO_2 in the air. Samples were labeled as follows: for each sample, a letter indicates the type of coal (B for bituminous coal; L for lignite), and the subscript gives the mass fraction of coal in the sample. For example, sample $B_{33\%}$ was 33 wt% bituminous coal, with the remainder being CaO.

A.2.2 TG-MS studies

For each test, the total mass of coal was 3 mg; thus the total sample weight varied. The aim was to have the same amount of gasifiable solids in each test. Given that the mass spectrometric signals of the evolved gases are not linearly correlated to the gas concentrations at very low concentration levels, and considering that all gases evolving in the system originate from the coal (CaO acts only as an absorbent and catalyst in the reaction system, but does not decompose under the reaction conditions), more accurate quantitative reactivity comparisons can be obtained from the MS using the same amount of coal in each sample. As we were concerned that the thermogravimetric analysis of large samples could be affected by mass- and heat-transfer limits, we tested the pyrolysis of bituminous coal ($B_{100\%}$) samples of varying sizes (ranging from ~5 to ~93 mg). The derivative weight loss curves measured from these samples (Supporting Information, Figure A 1) showed little variation, indicating that the sample size did not impact

the interpretation of the results. This was likely because the TGA used in this study benefitted from IR lamps that heated only the sample area in the furnace, and because the purging flow rate was high enough to quickly remove evolved gases from the pan.

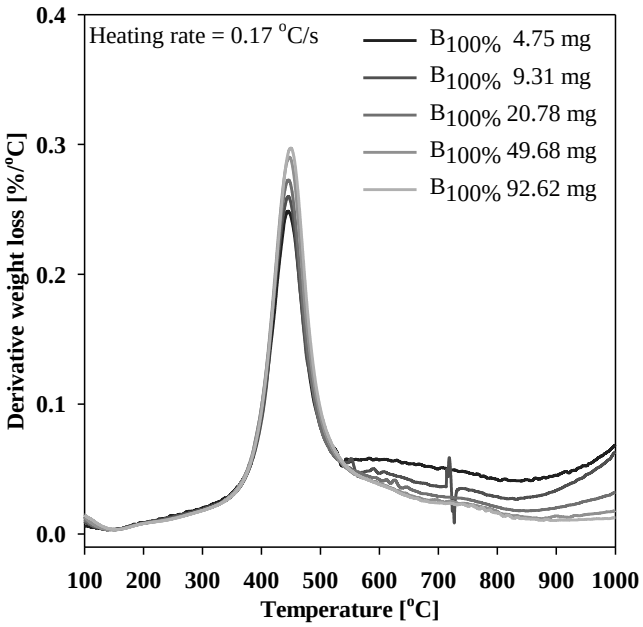

Figure A 1 Effect of analyzed sample mass on the reproducibility of thermogravimetric data during the pyrolysis of bituminous coal.

TG-MS experiments were conducted on a thermogravimetric analyzer (TGA Q5000 IR) that was coupled to a mass spectrometer (Pfeiffer Vacuum/ThermoStar-GSD320 T3) via a heated capillary (200 °C). A mixture of 200 mL/min Argon and 5 mL/min Helium was used as a carrier gas to rapidly renew the atmosphere and convey the evolved gases into the mass spectrometer. Argon was therefore the main carrier gas, and Helium was used as an internal standard. He was chosen as the internal standard because it produced only one signal in the mass spectrometer (m/z = 4), whereas Ar gave multiple peaks (m/z = 18, 20, 36, 38, 39, and 40). In addition, no other species in the reaction system produce signals at m/z = 4, which made signal masking unlikely. A Secondary Electron Multiplier detector, whose output signal was reported as current (in amperes), was used to maximize detection sensitivity. The quick response of the

mass spectrometer to changes in the composition of the evolved gas mixture was verified by decomposing a pure sample of $Ca(OH)_2$ in the TGA and comparing changes in derivative weight loss (from the TGA) and H_2O (from the MS) signals as functions of time (Figure A 2). In each experiment, the TGA furnace was purged for 30 min before the sample was heated, at 0.17 or 0.83 °C/s, to 1000 °C.

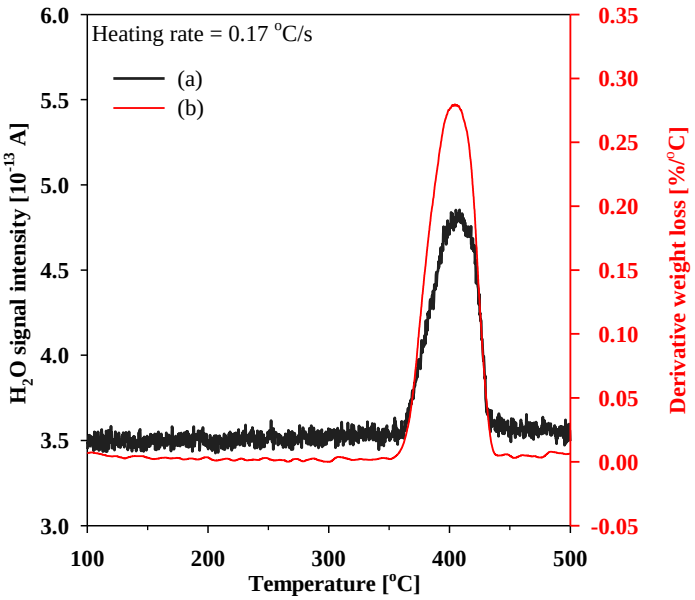

Figure A 2 The thermal decomposition of $Ca(OH)_2$ at 0.17 °C/s in Ar. (a) Signal intensity in the MS for ions with m/z = 18; and (b) Rate of weight loss, measured by TGA.

As low heating rates facilitate the evolution of low-molecular-weight compounds from coal pyrolysis (*244*), the whole m/z range of 1–100 was scanned to identify any changes in ion-fragment signals for each test. Several methods to report ion intensities from TG-MS experiments have been developed (*244-246*); this study used a modified version of the method reported by Arenillas et al. (*246*) Thus, the signal intensity of each fragment was normalized to the He signal intensity using the formula shown in Eq. A2.

$$\bar{I}_i = \frac{I_i}{I_{He,4} \times \Delta m_{sample}} \tag{A2}$$

where $\bar{I}_i$ is the normalized signal intensity, I_i is the signal intensity of gas species *i*, and Δm_{sample} is the weight loss of the sample over the course of the reaction.

All signals that changed in intensity during the course of the experiment were considered for analysis. However, the major signal changes, observed for m/z = 2, 16, 18, 28, and 44 (which corresponded to H_2, CH_4, H_2O, CO, and CO_2, respectively), were treated as the critical signals, and the detection of the corresponding gases is discussed in detail here. As only the signals at m/z = 2 and 28 were treated quantitatively, no attempt was made to mathematically remove any potential contribution of H_2O to the signal at m/z = 16. A comprehensive list of signals displaying changes in intensity is shown in Table A 2.

Table A 2 Detected ion fragment signals and their possible parent ions.

m/z ratio	Possible Ion	m/z ratio	Possible Ion
2	H_2^+	29	CHO^+, $C_2H_5^+$, CH_2NH^+
12	C^+	30	CH_2O^+, $C_2H_6^+$
14	CO_2^+, CH_2^+	32	CH_3OH^+
15	CH_3^+	34	H_2S^+
16	CH_4^+	36	Ar^+
17	NH_3^+	38	Ar^+
18	H_2O^+	39	Ar^+
20	Ar^{2+}	40	Ar^+
27	$C_2H_3^+$, CHN^+	44	CO_2^+,$C_3H_8^+$
28	CO^+, N_2^+		

The derivative weight losses measured from the TGA were modified according to Eq. A3 in order to more accurately compare different samples and testing conditions. Thus, Eq. A3 converts the original derivative weight loss data, which was calculated for the whole sample size, to a derivative weight loss based on the gasifiable fraction of the sample, i.e. the coal content of the sample. The modified derivative weight loss curves were then considered to be reflections of the pyrolytic reactivity of coal at different temperatures, in the presence or absence of CaO. Whereas the relative normalized signal intensities were used to qualitatively compare

reaction pathways for different samples, the cumulative integrals of normalized H_2 and CO signals (Eq. A4 and Eq. A5 for integration over temperature and time, respectively) were used to quantitatively compare the effect of CaO:coal ratio on H_2 and CO production.

$$\overline{w}_{deriv.} = \frac{w_{deriv.}}{r_{coal}} \tag{A3}$$

$$y_{\mathrm{i}}(T) = \int_{T = T_0}^{T} \left(\bar{I}_{\mathrm{i}} - \bar{I}_{\mathrm{i},noise}\right) dT \tag{A4}$$

$$y_{\mathrm{i}}(t) = \int_{t = t_0}^{t} \left(\bar{I}_{\mathrm{i}} - \bar{I}_{\mathrm{i},noise}\right) dt \tag{A5}$$

In Eq. A3, $w_{deriv.}$ is the measured weight loss per unit temperature, r_{coal} is the mass fraction of coal in the sample, and $\overline{w}_{deriv.}$ is the derivative weight loss modified to consider the gasifiable fraction. In Eq. A4, T_0 is the conservative temperature value at which an MS signal begins to rise (occurring at time t_0, Eq. A5), and T is the gasification/pyrolytic temperature of interest (reached at time t, Eq. A5). All temperatures and times are reported in °C and s, respectively. The noise level, $\bar{I}_{\mathrm{i},noise}$, is determined as the average of the signal intensity for species i between the temperatures $T_0 - 200$ and T_0. Eq. A4 is presented here to establish the temperature basis of the calculations; however, values from Eq. A5 (the time-based equivalent of Eq. A4) are reported throughout.

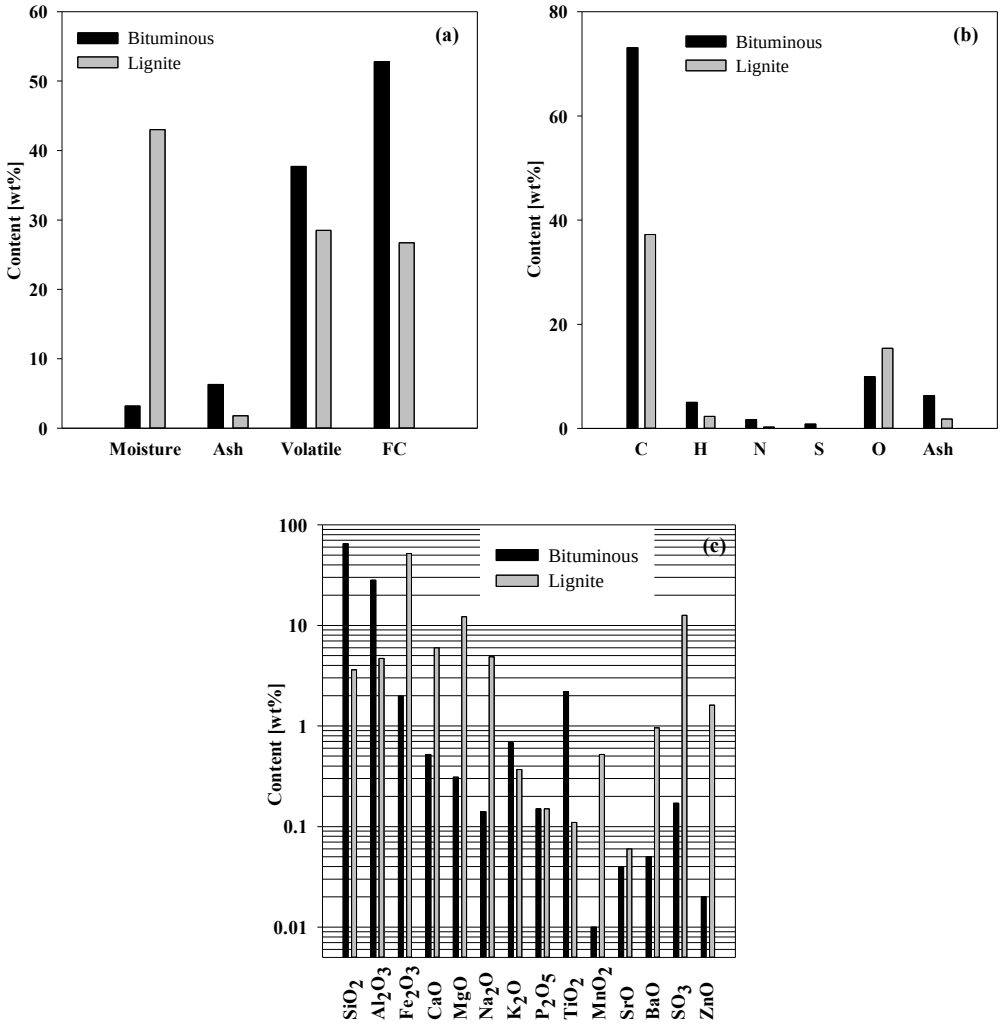

Figure A 3 Results of the (a) proximate; b) ultimate; and c) ash analyses of coal, on the "as-determined" basis. FC: fixed carbon; C: carbon; H: hydrogen, excluding hydrogen in moisture; N: nitrogen; S: sulfur; O: oxygen, which was calculated by difference and excludes the oxygen from moisture.

A.3 Results and Discussion

A.3.1 Effect of CaO addition on the mechanism of coal pyrolysis

The effects of CaO addition on the pyrolysis of two different coals are shown in Figure A 4. As shown in Figure A 4**a** and 2b, the addition of CaO to lignite coal had a huge impact on the amount and distribution of all of the main species evolved (H_2, CO_2, CH_4, CO, and H_2O). When CaO was present, a peak in the signal for H_2O was observed at around 400 °C, and this was

accompanied by rapid weight loss of the sample. This indicated the decomposition of $Ca(OH)_2$, which was formed via the hydration of CaO by moisture released or derived from the lignite. There was a coincident increase in the signal at m/z = 16; however, this was interpreted as an ion fragment from H_2O (i.e. O_2^+) rather than as CH_4 generation. The amount of CO_2 released from lignite at temperatures <500 °C was much lower when CaO was present, evincing the effectiveness of CaO carbonation (see Eq. A 1) during pyrolysis. However, even in the presence of CaO, CO_2 evolution began at 430 °C and reached peak at 650 °C, which is the decomposition temperature of $CaCO_3$ in a CO_2-lean atmosphere (i.e. at low partial pressure of CO_2). The sample also underwent rapid weight loss during this period. While the CO_2 signal reached its maximum, that of CH_4 also increased to a peak at 650 °C. (Here, contributions of O_2^+ (from H_2O, vide supra) to the intensity at m/z = 16 are vitiated by the absence of a signal at m/z = 18.) This was in contrast to the case for pure lignite, where a distinguishable peak in methane production was barely observable.

In the presence of CaO, lignite started to evolve H_2 at around 630 °C, and reached a peak in H_2 generation at 790 °C; whereas no H_2 signal was detected for pure lignite until 730 °C. In that case, the production reached a peak at 830 °C. CO evolution was coincident with that H_2 for both samples. With or without CaO, the high-temperature generation of H_2 and CO was accompanied by an increase in the rate of sample mass loss, indicating a period of significant pyrolysis. This peaked at lower temperature (787 °C) when CaO was present than with pure lignite (827 °C), and the maximum rate of lignite decomposition was 12% higher in the presence of CaO.

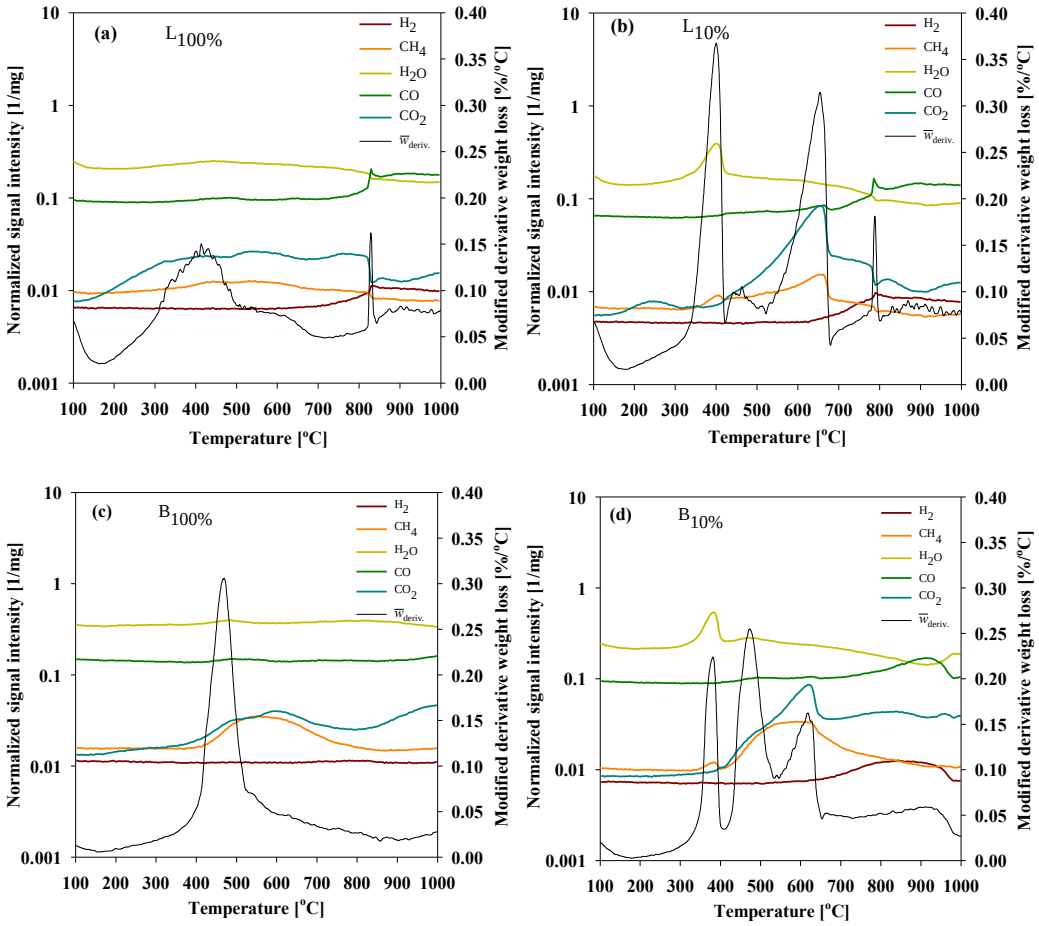

Figure A 4 Thermogravimetric and mass spectrometric observations of coal pyrolysis in the absence and presence of CaO: a) 100% lignite heated at 0.17 °C/s; b) 10% lignite heated at 0.83 °C/s; c) 100% bituminous coal heated at 0.83 °C/s; d) 10% bituminous coal heated at 0.83 °C/s.

The same analysis was performed for bituminous coal (Figure A 4c and 2d). CaO addition had a similar impact on the release of H_2O from bituminous and lignite coals; however, as the bituminous coal contained less moisture (even after being dried using the same procedure), its CaO-enhanced pyrolysis produced a less H_2O upon the decomposition of $Ca(OH)_2$. Maxima in both the rate of weight loss and the detection of the MS signal at m/z = 18 indicated that this occurred at 385 °C for this sample. As was the case for lignite, these were accompanied by a smaller peak in generation of ions with m/z = 16; this was again interpreted as an ion fragment from H_2O (i.e. O_2^+) rather than as CH_4^+. In fact, adding CaO did not significantly impact CH_4 production from bituminous coal. CO_2 production from pure bituminous coal reached a peak at

600 °C, then fell to a minimum at 800 °C before increasing until the end of the experiment at 1000 °C. The addition of CaO increased the rate of CO_2 production at the peak value of 650 °C. This was presumably due to CO_2 release from $CaCO_3$, and was coincident with a maximum in the rate of weight loss. However, bituminous coal pyrolysis in the presence of CaO also showed more sustained CO_2 generation at higher temperatures.

The most interesting effect of CaO addition in the pyrolysis of bituminous coal, however, was noted in the formation of CO and H_2. The pyrolysis of pure bituminous coal yielded no H_2 signal above the baseline, and only a very small CO signal just below 1000 °C. Clearly, the addition of CaO caused a broad peak in H_2 production, just after the decrease in CO_2 generation at 650 °C. Furthermore, CO production peaked at 920 °C, in conjunction with a decrease in the rate of H_2O formation. This suggested that coal was being gasified by H_2O vapor in the system, producing H_2 and CO; this would also account for the broad but evident peak in mass loss that began at 670 °C. As H_2 was only formed from bituminous coal at temperatures above the decomposition point of $CaCO_3$, the role of CaO in the generation of H_2 from bituminous coal was primarily catalytic.

Comparing the two types of coal, in particular with respect to CO and H_2 formation, it was obvious that the addition of CaO had a greater impact on the pyrolytic behavior of bituminous coal. This may have been related to the amount of alkaline earth metal oxides, and particularly CaO, present in the ashes of bituminous and lignite coal. Early studies on the effect of alkaline earth metals oxides in coal ash revealed that the pyrolytic behavior of a coal was more strongly correlated to the concentration of CaO than of other metal oxides in its ash (*247, 248*). In addition, although washing the cations from a coal with HCl(*aq*) drastically diminishes its gasification rate (i.e. rate of carbon conversion during gasification) (*220*), the gasification rate of acid-washed coals could be greatly increased by loading them with Ca^{2+}. This was effective up

to an optimal CaO loading, which gave the maximum reaction rate from gasification, was reached (*249*). As shown in Figure A 3c, lignite coal ash is ~6 wt% CaO, whereas bituminous coal ash is only ~0.5 wt% CaO. Thus, more CaO will be needed to attain to the maximum gasification rate in bituminous than lignite coal. The difference may also be due in part to the different pyrolytic behaviors of the coals. Bituminous coal produces significantly more tar upon pyrolysis than lignite does (*250*); thus, the addition of CaO, a tar-cracking catalyst (*223*), is expected to have a greater impact on the former coal type.

A.3.2 Effect of CaO:coal ratio on coal pyrolytic reactivity

From an industrial point of view, it is important to know how much CaO will optimize coal utilization and H_2 yield. The former quantity is reflected in the modified derivative weight loss curves (see Eq. A3), which were measured at different heating rates. The latter resemble different throughputs in industrial gasifiers: the higher the throughput, the faster the feed must be heated to the gasification temperature. For a given coal type and heating rate, this can be considered from two perspectives. On one hand, the rate of coal consumption can be determined as a function of the amount of CaO added. On the other hand, the temperature at which the coal reactivity is maximized is also important, as it affects the energy requirement of the gasifier; a higher gasification temperature requires more energy.

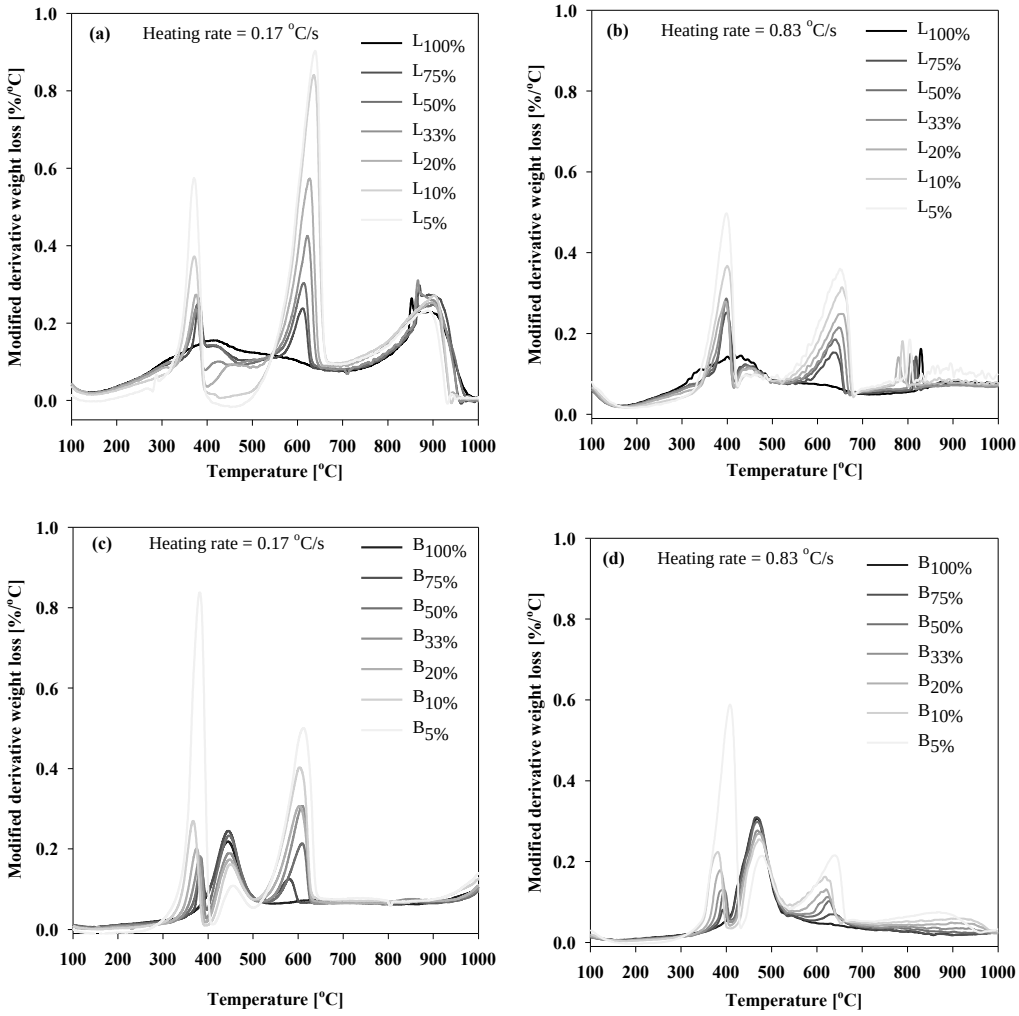

Figure A 5 Modified derivative weight loss curves (Eq. A3) for a) lignite heated at 0.17 °C/s; b) lignite heated at 0.83 °C/s; c) bituminous coal heated at 0.17 °C/s; d) bituminous coal heated at 0.83 °C/s.

As discussed in above, CO and H_2 are produced from coal pyrolysis or gasification at high temperature; therefore, the rate of coal weight loss at high temperature is an indicator of CO/H_2 production. Therefore, the last peak intensity and location on horizontal axis can be discussed as a sign for optimizing the CaO:coal ratio. When lignite was pyrolyzed at 0.17 °C/s (Figure A 5a) in the presence of at least 4:1 CaO:coal, the high-temperature (700–850 °C) weight loss began at lower temperature. However, no significant change in the maximum rate of high-temperature weight loss was observed. The earliest onset of weight loss was observed for $L_{10\%}$, and the highest pyrolysis rate was observed for $L_{33\%}$ at 865 °C. When the same coal was pyrolyzed at

0.83 °C/s (Figure A 5b) the same trends were observed. Thus, $L_{100\%}$ showed the lowest rate of mass loss at all temperatures. The greatest rate of pyrolysis for $L_{100\%}$ occurred at 830 °C, whereas the rate was maximized at lower temperature (776 °C) for $L_{20\%}$. Past this point, adding more CaO did not lower the temperature of maximum weight loss, though the highest reactivity was observed for $L_{5\%}$ at 805 °C.

No clear peak in the rate of weight loss occurred at T > 700 °C during the pyrolysis of bituminous coal at 0.17 °C/s (Figure A 5c), except for a very weak broad peak at 846 °C for $B_{33\%}$. Rather, for this coal and heating rate, the modified derivative weight loss began to increase at 900 °C, with the greatest rate being measured for sample $B_{5\%}$. MS data indicated that this decomposition was related to CO evolution (vide infra). When bituminous coal was heated at 0.83 °C/min (Figure A 5d), higher CaO loadings successively increased the coal reactivity. The above data are summarized in Table A 3.

Table A 3 The CaO:coal ratios that produced the best coal reactivity.

Coal type	Heating rate	Sample showing the greatest	
		Change in *T* of maximum decomposition rate	Decomposition rate
Lignite	0.17 °C/s	$L_{10\%}$	$L_{33\%}$
	0.83 °C/s	$L_{20\%}$	$L_{5\%}$
Bituminous	0.17 °C/s	$B_{33\%}$	$B_{33\%}$
	0.83 °C/s	$B_{5\%}$	$B_{5\%}$

A.3.3 Effect of CaO:coal ratio on H_2 and CO production yield

The impact of the CaO:coal ratio on H_2 production can be more accurately assessed by considering the MS signals. The cumulative H_2 production was calculated, as a function of temperature, using Eq. A4, and is shown in Figure A 6 (the normalized ion intensity signals for H_2 vs. time are shown in Figure A 7). In Figure A 6, the y-axis reflects the total amount of H_2 produced. Thus the figure provides a semi-quantitative assessment of H_2 production, under inert atmosphere, as a function of temperature.

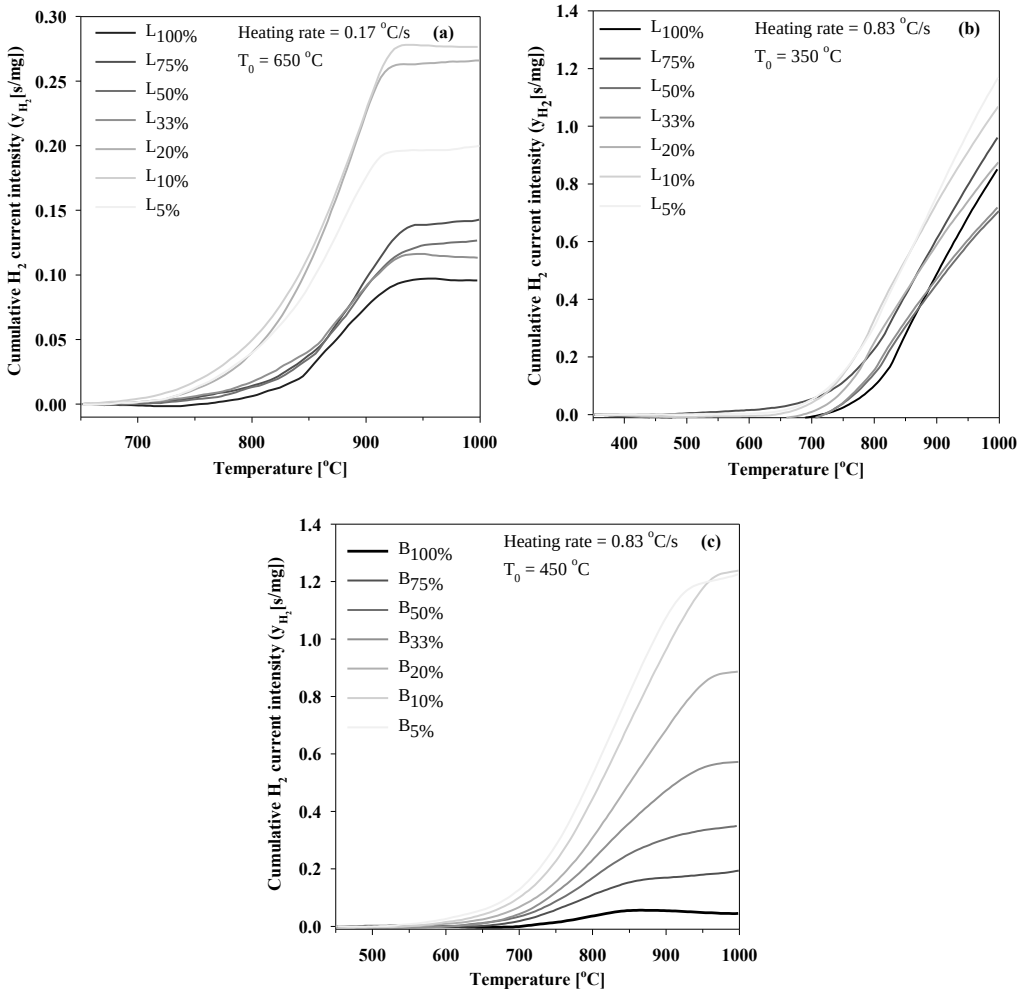

Figure A 6 Cumulative H_2 current intensity (y_{H_2}) vs. pyrolysis temperature for a) lignite heated at 0.17 °C/s; b) lignite heated at 0.83 °C/s; c) bituminous coal heated at 0.17 °C/s; d) bituminous coal heated at 0.83 °C/s.

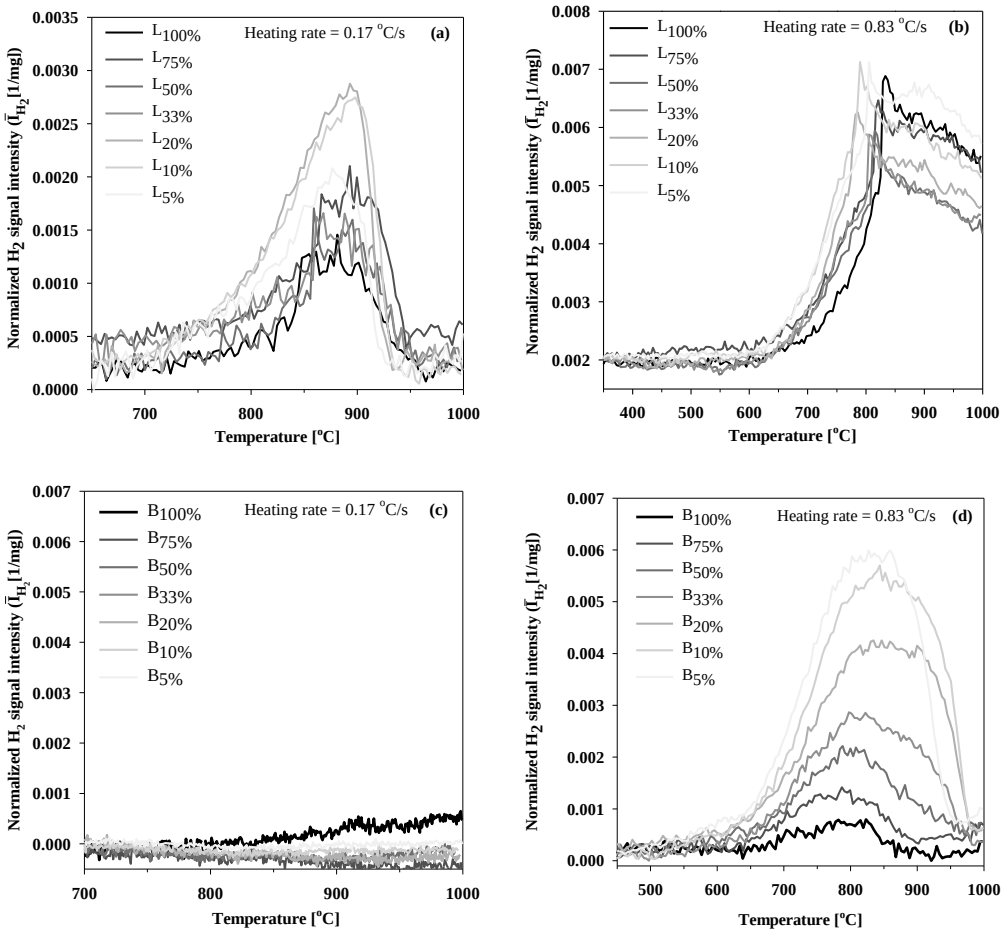

Figure A 7 Normalized H_2 signal intensities vs. pyrolysis temperature for: a) lignite heated at 0.17 °C/s; b) lignite heated at 0.83 °C/s; c) bituminous coal heated at 0.17 °C/s; d) bituminous coal heated at 0.83 °C/s.

Adding CaO to the pyrolysis of lignite at 0.17 °C/s (Figure A 6a) clearly increased H_2 formation at all temperatures. In addition, it decreased the lowest pyrolysis temperature at which hydrogen can be produced; although no H_2 was produced from pure lignite below 745 °C, adding even a small amount of CaO ($L_{75\%}$) shifted the onset of H_2 production to 690 °C. However, some CaO:coal ratios were more effective than others at specific temperatures. For example, below 865 °C, $L_{10\%}$ always produced more H_2 than $L_{20\%}$, but the H_2 production between 865 and 910 °C was nearly equal for these samples. Thus, at pyrolysis temperatures >865 °C there is no point in increasing CaO:coal ratio past 4:1. However, this will not necessarily hold for other coal types and/or heating rates. For example, for lignite pyrolysis at

0.83 °C/s (Figure A 6b), the optimal CaO:coal ratio varied with temperature. Below 700 °C, $L_{75\%}$ produced the most H_2, though $L_{5\%}$ and $L_{10\%}$ were more effective between 700 and 767 °C. Above 900 °C, $L_{5\%}$ produced the most H_2, and $L_{33\%}$ and $L_{50\%}$ actually produced less H_2 than pure lignite. This analysis could not be performed for the pyrolysis of bituminous coal at the lower heating rate (0.17 °C/s), because no H_2 signal was detected for any of these samples at that heating rate. At 0.83 °C/s, on the other hand, H_2 production from bituminous coal (Figure A 6d) increased with the CaO:coal ratio at all temperatures, with $B_{5\%}$ displayed the highest rate of H_2 production. Thus, the optimum CaO:coal ratio depended not only on the coal type, but also on the heating rate and pyrolysis temperature.

The optimum CaO:coal ratios for pyrolysis temperatures between 600 °C and 800 °C are reported in Table A 4, along with the associated improvements in H_2 production over the pyrolysis of pure coal.

Table A 4 Sample compositions that maximize H_2 production from coal pyrolysis at various temperatures (CaO:coal ratios in parentheses).

		Lignite					Bituminous coal				
Pyrolysis temperature (°C)		600	650	700	750	800	600	650	700	750	800
0.17 °C/s	Optimum coal mass ratio (%)	NA[a]	NA[a]	10 (9:1)	10 (9:1)	10 (9:1)	NA[a]	NA[a]	NA[a]	NA[a]	NA[a]
	Improvement (%)	NA[a]	NA[a]	∞[b]	∞[b]	870	NA[a]	NA[a]	NA[a]	NA[a]	NA[a]
0.83 °C/s	Optimum coal mass ratio (%)	NA[a]	20 (5:1)	20 (5:1)	10 (9:1)	10 (9:1)	5 (19:1)	5 (19:1)	5 (19:1)	5 (19:1)	5 (19:1)
	Improvement (%)	NA[a]	∞[b]	∞[b]	580	330	∞[b]	∞[b]	∞[b]	2080	1260

[a] No signal above the noise was detected at m/z = 2.

[b] Infinite due to a lack of detectable signal at m/z = 2 for the case of 100% coal.

The data in Table A 4 show that, for lignite, a CaO:coal ratio between 5:1 and 9:1 produce the most H_2 at pyrolysis temperatures between 600 and 800 °C range. Greater CaO loadings were preferred at higher pyrolysis temperatures, and adding CaO to lignite can increase the rate of H_2 production from its pyrolysis by at least 330% (i.e. threefold). A CaO:coal loading of 19:1

always produced the best H_2 yield from the pyrolysis of bituminous coal, with the minimum improvement in H_2 yield being 1260% (around 12 times higher than pure bituminous). H_2 production from the pyrolysis of either coal was less sensitive to CaO addition at higher pyrolysis temperature, and the addition of CaO had a greater impact (approximately four times greater) on the pyrolysis of bituminous than lignite coal. This was likely because less CaO was initially present in bituminous coal, and because more gasifiable tar was formed during the pyrolysis of bituminous coal.

Although the above discussion is valid for coal pyrolysis under an inert atmosphere, when all H_2 is produced from the coal (i.e. from direct H_2 production). However, coal pyrolysis under an inert atmosphere it not as desirable as the pyrolysis in presence of steam, i.e. steam−coal gasification. In steam gasification, most of H_2 is produced through the water−gas shift reaction, which occurs between the steam and the CO released during coal (i.e. from indirect H_2 production). Consequently, a system in which more CO is available for water−gas shift reaction would yield more H_2 from steam gasification. Thus, under such conditions, the production of CO is much more important than that of H_2. Therefore, the cumulative production of CO in our system was calculated using Eq. A4, and is displayed in Figure A 8 (the normalized ion intensities of CO are shown in Figure A 9).

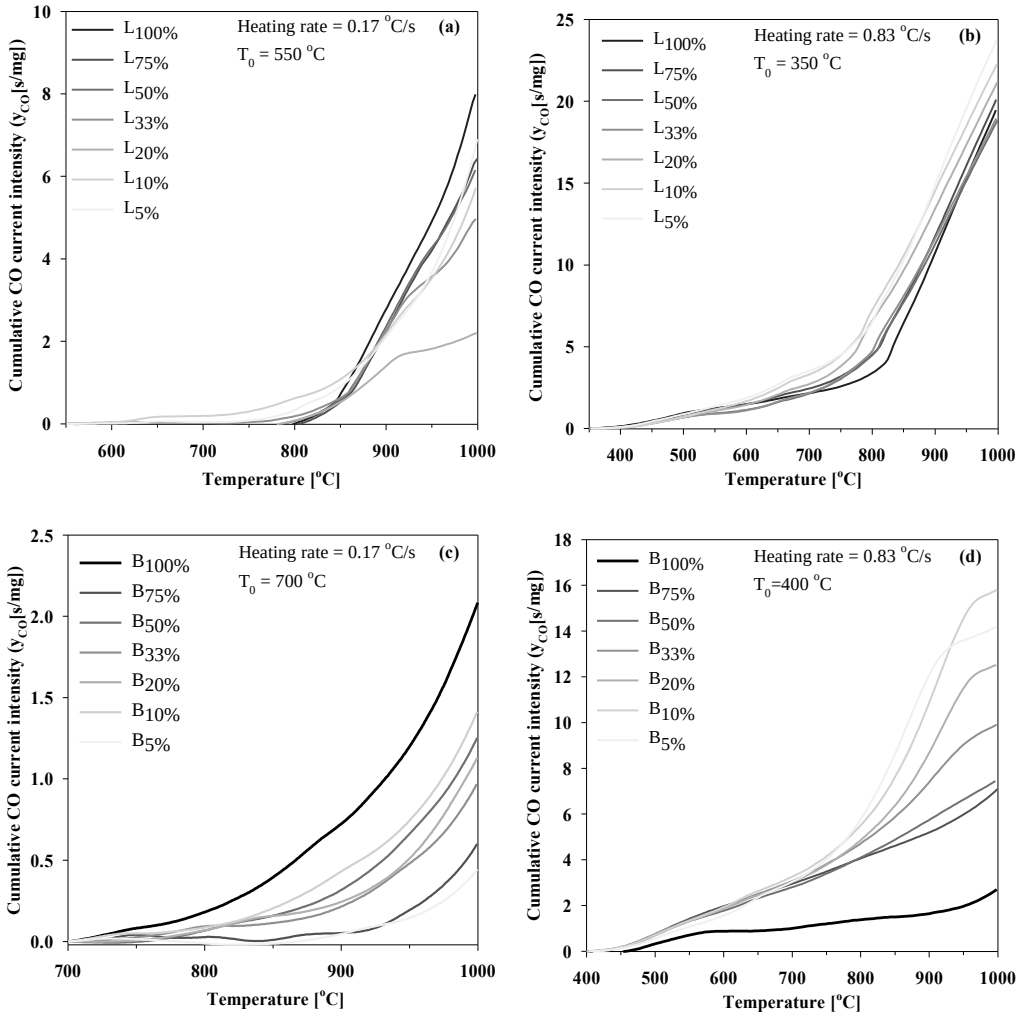

Figure A 8 Cumulative CO production (y_{CO}) vs. pyrolysis temperature for a) lignite heated at 0.17 °C/s; b) lignite heated at 0.83 °C/s; c) bituminous coal heated at 0.17 °C/s; d) bituminous coal heated at 0.83 °C/s.

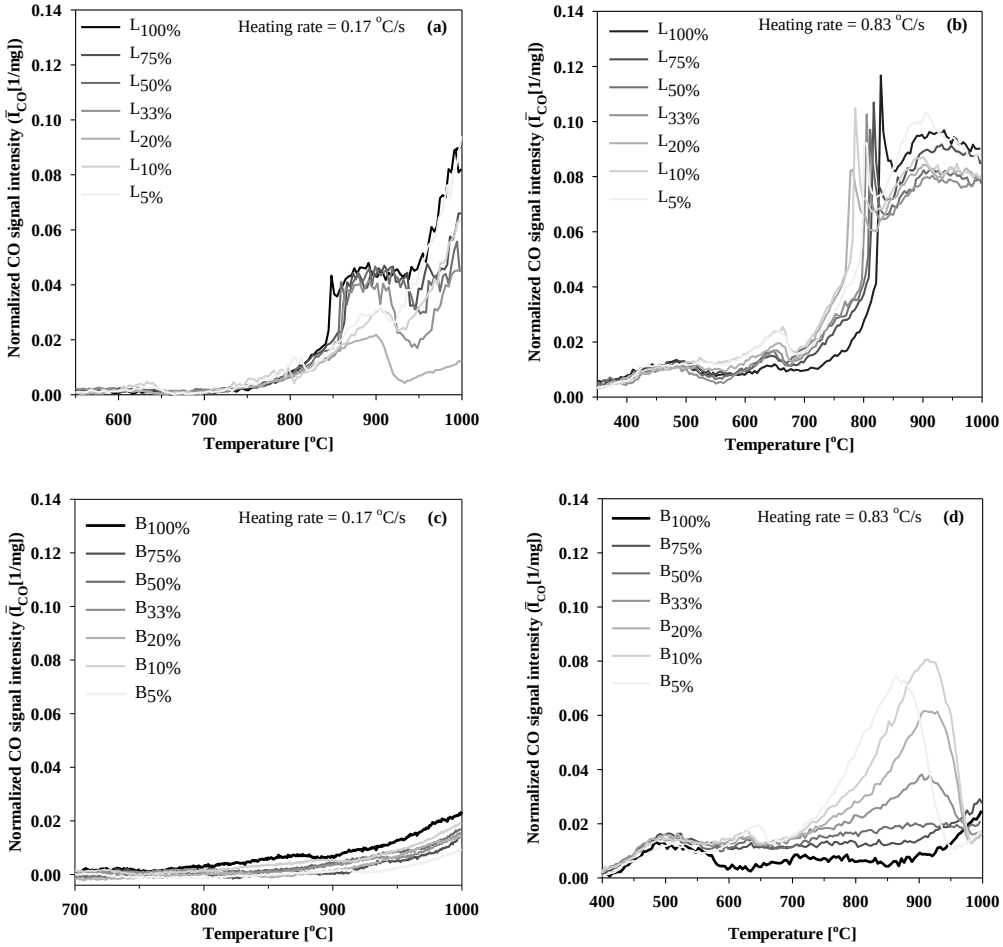

Figure A 9 Normalized CO signal intensities vs. pyrolysis temperature for a) lignite heated at 0.17 °C/s; b) lignite heated at 0.83 °C/s; c) bituminous coal heated at 0.17 °C/s; d) bituminous coal heated at 0.83 °C/s.

Table A 5 Sample compositions that maximize CO production from coal pyrolysis at various temperatures (CaO:coal ratios in parentheses).

		Lignite					Bituminous coal				
Pyrolysis temperature (°C)		600	650	700	750	800	600	650	700	750	800
0.17 °C/s	Optimum coal mass ratio (%)	10 (9:1)	10 (9:1)	10 (9:1)	10 (9:1)	10 (9:1)	100	100	100	100	100
	Improvement (%)	∞[a]	∞[a]	∞[a]	∞[a]	4350	0	0	0	0	0
0.83 °C/s	Optimum coal mass ratio (%)	5 (19:1)	5 (19:1)	5 (19:1)	5 (19:1)	10 (9:1)	20 (5:1)	10 (9:1)	10 (9:1)	10 (9:1)	5 (19:1)
	Improvement (%)	130	150	160	180	220	210	270	300	330	340

[a] Infinite due to a lack of detectable signal at m/z = 28 for the case of 100% coal.

Much like the H_2 yield, the optimal CaO:coal ratio that maximized CO production depended on coal type, heating rate, and gasification temperature (Table A 5).

For lignite coal, CaO:coal ratios of between 9:1 and 19:1 produced the most CO over temperatures from 600 to 800 °C. However, there was a slight difference between CaO:coal ratios of 9:1 and 19:1 when heating at 0.83 °C/s (see Figure A 8b). In that case, a CaO:coal ratio of 9:1 produced the greatest CO yield from lignite pyrolysis at all gasification temperatures between 600 and 800 °C. In addition, adding CaO to lignite increased its CO production in pyrolysis by at least 130% when heating at 0.83 °C/s and at least 4350% when heating at 0.17 °C/s. Therefore, adding CaO to the pyrolysis of lignite coal was far more effective for the lower heating rate.

CaO produced no improvement in CO production from bituminous coal upon heating at 0.17 °C/s. However, this conclusion may not be reliable because the detected MS signals were barely above the noise (illustrated by comparing the y-axis scales of the plots in Figure A 8). On the contrary when bituminous coal was heated at 0.83 °C/s, the minimum improvement in CO yield upon CaO addition was 210%, and the optimum CaO:coal ratio was 9:1 at most temperatures, though the optimum CaO:coal ratio was higher at higher gasification temperatures.

For both types of coal, the effect of CaO addition on CO production increased as with gasification temperature, in contrasting to the effect of CaO on H_2 production. CaO addition again proved more important for bituminous than for lignite coal; in this case, the effect was around twice as large. Furthermore, CaO addition had a greater impact on CO production at lower heating rates.

Finally, we conclude that the CO_2-uptake role of CaO was minor in coal pyrolysis because more of the CO and H_2 was produced at temperatures above the decomposition temperature of CaCO3. Nevertheless, in the steam gasification of coal, a temperature of 650 °C allows the reaction to benefit from the reaction between CO_2 and CaO, which in shifts the equilibrium of the water−gas shift reaction towards the formation of H_2 and CO_2. Moreover, CaO-enhanced

gasification at temperatures above 650 °C leads to serious operational issues (*236*). Thus, practically, providing an optimum CaO:coal ratio for gasification temperatures >650 °C is not useful. Therefore, in indirect H_2 production, a CaO:coal ratio of 9:1 is optimal for both lignite and bituminous coal.

A.4 Conclusion

In this paper the effect of CaO addition on coal pyrolysis mechanism is discussed. Essentially, adding CaO lowered the minimum temperature required for H_2 production and increased the selectivity for H_2. However, increasing the CaO:coal ratio did not necessarily increase the coal reactivity; therefore, an optimum CaO:coal ratio could be defined for each type of coal.

In direct H_2 production from coal (i.e. pyrolysis under an inert atmosphere), adding CaO at the optimal ratio (CaO:coal = 9:1) to lignite at least tripled the H_2 production from its pyrolysis, and 19:1 CaO:coal increased H_2 by an order of magnitude. For both coal types, the impact of CaO addition on H_2 production was lower at higher pyrolysis temperatures. Of interest to indirect H_2 production from coal, such that from the water−gas shift reaction during steam gasification, the optimal ratio of 9:1 CaO:lignite increased CO production by at least 435 and 130% for pyrolysis at 0.17 and 0.83 °C/s, respectively. For bituminous coal, no improvement was observed for the lower heating rate in the temperature range of interest, but at the higher heating rate (0.83 °C/s), adding 9:1 CaO:coal at least doubled CO production.

It should be noted that the optimal ratios determined here were based solely on observed improvements in the production of H_2 and CO. The effect of CaO addition on energy requirements of in a gasifier or on additional capital and operating costs were not considered. In

order to include process and cost factors, a techno-economic model would be required; the data reported here can be used to improve the accuracy of such models.

Appendix B. Solid Particles' Recirculation Distribution in Calcium Looping Post-Combustion Carbon Capture

Post-combustion capture of CO_2 from the flue gas of power plants by calcium looping, in which lime is used to capture CO_2, is currently a promising technology. The decay in CO_2 uptake capacity of natural limestone is an intrinsic disadvantage of this technology, and the design of more stable sorbents has become an important goal. Techno-economic calculations that examine calcium looping must take into account this decay in capacity, and this has to date been accomplished using a formula for the population distribution of particles in the cycling system. However, the formula has some limitations that make it less suited to very stable sorbents, making it difficult to incorporate newer materials in such calculations. We developed a more general formula for the population distribution of solid particles in processes involving recirculations, and compared it with the widely used equation in the calculation of several process metrics. Particular consideration was given to conditions relevant to enhanced or tailored sorbents, for which our modified formula was well suited. In addition, the impacts of calcium looping process configuration on this generalized population distribution of solid particles were studied from mathematical and operational perspectives.

B.1 Introduction

Carbon dioxide has been identified as the main contributor to anthropogenic climate change (*251*). The most important stationary point sources of CO_2 emissions are fossil-fuel-fired heat and power plants where coal provides ~72% of the energy produced, contributing to 41% of global CO_2 emissions (*252*). As a result, finding efficient and economically attractive methods to capture CO_2 from such plants is an active area of research (*228, 253, 254*). One of the most

promising methods of post-combustion CO_2 capture is calcium looping (*228*), in which lime, composed primarily of CaO, is contacted with a CO_2-containing flue gas stream in a carbonator, which is typically a circulating fluidized bed (CFB) working at ~650 °C. The solid is then sent through a calciner, typically a CFB working at ≳ 900 °C, where carbonated CaO (i.e. $CaCO_3$) is decomposed to regenerate the sorbent (Figure B 1a), which is then recirculated to the carbonator. The technology is currently being tested on large scales in Spain (*255*), Germany (*256*), and Taiwan (*102*). The main advantages of the process are high working temperatures, which enable heat integration, steam/power generation, and the availability of the low-cost solid sorbent (derived from natural limestone) (*228*). However, the CO_2-carrying capacity of limestone decays rapidly over multiple recirculations as a result of sintering at elevated temperatures (*257*). Although there have been many efforts to improve the decay behavior of CaO, either by designing more stable sorbents (*258-263*) or by pretreating limestone (*264-268*), an immediately available option to overcome the problem is to continuously replace some of the spent sorbent with a make-up flow of fresh sorbent (F_0), as proposed by Abanades (*269*). The addition of a make-up flow and spent-sorbent purge produces a system that can be constructed in four different configurations (Figure B 1), depending on where these components are located. The rate of sorbent replacement (i.e. the ratio of make-up to circulating sorbent) will affect the capture efficiency and the rate at which circulating solids flow, and consequently the heat requirements of the calciner and material requirements of the process. Therefore, a simple mathematical representation of the process enables one to identify reasonable process parameters at which the intended emission reduction target can be reached. Abanades derived a mathematical relationship between the sorbent replacement rate (F_0/F_R) and the maximum CO_2-capture efficiency (*269*); however, that formula was more useful for systems with high sorbent-replacement rates (*vide infra*). With the advent of higher-performance sorbents and pretreated

sorbents, a revised formula that better suits lower replacement rates is desirable. In this paper, an effort to develop a more general model is presented. Furthermore, some key process performance parameters that have previously been examined (e.g. capture efficiency, solids flow rates, streams costs, etc.) are recalculated using the modified model and compared with the results of Abanades' model.

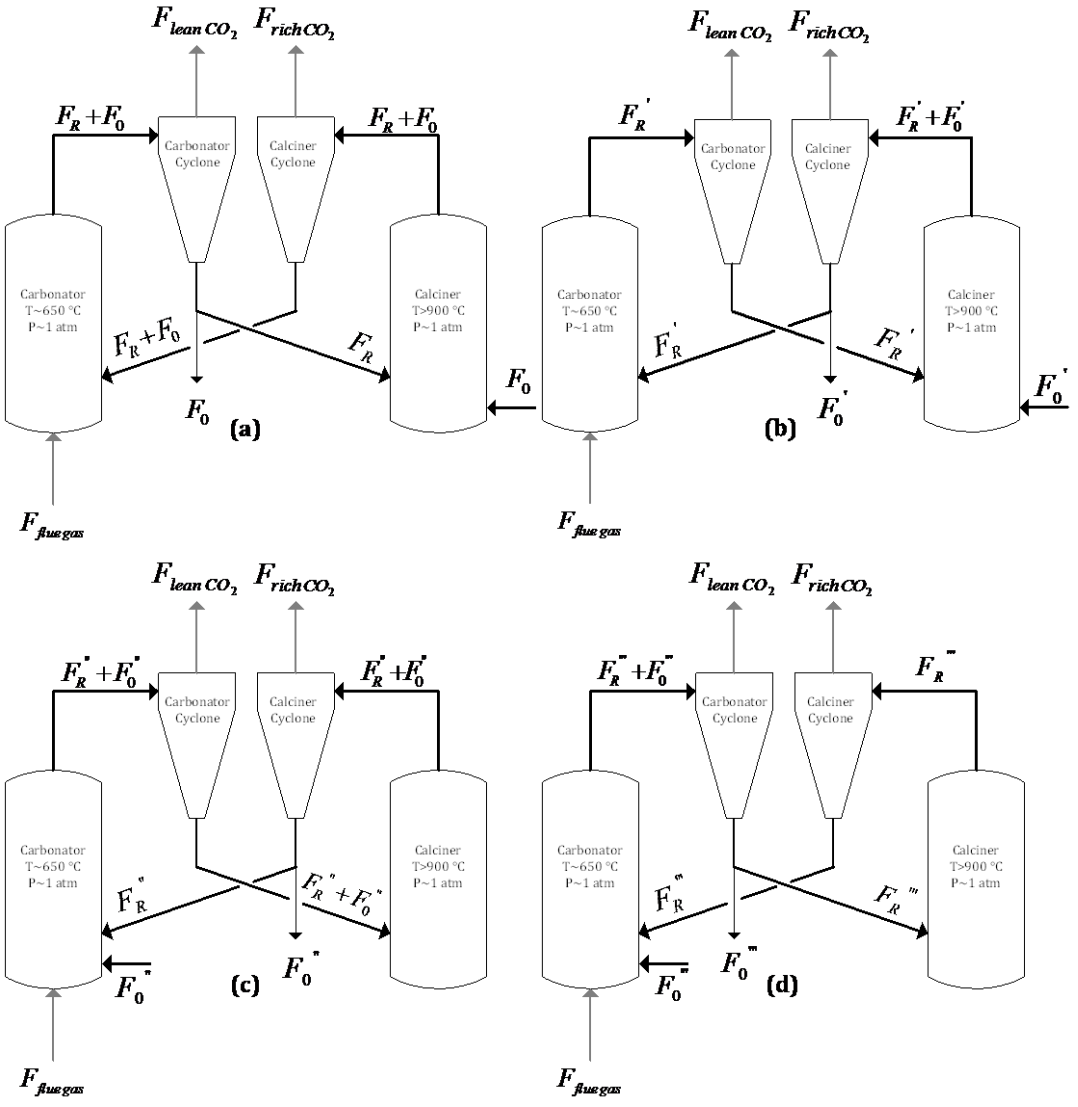

Figure B 1 Schematic of CO_2 capture by calcium looping (F_0 = sorbent make-up stream/spent sorbent purge stream, F_R = sorbent solid circulating stream); a) make-up to calciner, purge from carbonator cyclone; b) make-up to calciner, purge from calciner cyclone; c) make-up to carbonator, purge from calciner cyclone; d) make-up to carbonator, purge from carbonator cyclone.

B.2 Experimental Methods

In order to obtain conversion data under industrially relevant conditions, the sorbent ($CaCO_3$ (Sigma–Aldrich) or CaO/*meso*-$Ca_xAl_yO_z$) was exposed to 50 cycles of calcination (3 min at 900 °C under N_2 atmosphere) and carbonation (3 min at 650 °C in 15% CO_2 in N_2,) in a TGA-Q5000. Heating and cooling rates of 250 °C/min were used.

B.3 Results and discussion

B.3.1 Particles' recirculation distribution

In order to calculate the efficiency of a calcium-looping CO_2-capture process like the one shown in Figure B 1a (the configuration considered by Abanades in (*269*)), we require information about the rate of decay of sorbent reactivity. Abanades et al. have proposed three equations to describe this decay by relating CaO conversion (X_i) to cycle number (i) (equations (B 1) (*269*), (B 2) (*270*), and (B 3) (*229*)); whereas others have developed more complicated models (*257, 271-273*). We exposed commercial $CaCO_3$ to 50 calcination/carbonation cycles (Figure B 2) under industrially relevant conditions. Thus, in contrast to the conditions used to test newer sorbents (typically 10−30 min for carbonation (*267*)), we have used very short carbonation and calcination times (3 min each) and a high heating and cooling rate (250 °C/min) in order to mimic industrial CFB reactors, where particle residence times are 1–5 min (*274*). Under these conditions, the CO_2-capture capacity of the material declined drastically, from ~48 wt% in the first cycle to ~6.8 wt% after 50 cycles. Eq. (B 3) best fit the experimental data (see Table B 1 and Figure B 2), likely because it was derived using a model of the second-order sintering that causes the loss in active surface area of a sorbent over multiple cycles (*229*). Of the power-law models, Eq. (B 1) described the decay in CO_2-capture capacity better than Eq. (B 2).

Having established that Eqs. (B 1) and (B 3) reasonably described the relationship between X_i and i for CO_2 uptake under the conditions studied, we next considered the average carbonation conversion of CaO ($\bar{X}$) and the carbonator capture efficiency ($\eta_{carbonator}$).

$$\boldsymbol{X_i = a^{i+1} + b} \quad \text{(B 1)}$$

$$\boldsymbol{X_i = a^{i}(1 - b) + b} \quad \text{(B 2)}$$

$$\boldsymbol{X_i = \frac{1}{\frac{1}{1-a} + bi} + a} \quad \text{(B 3)}$$

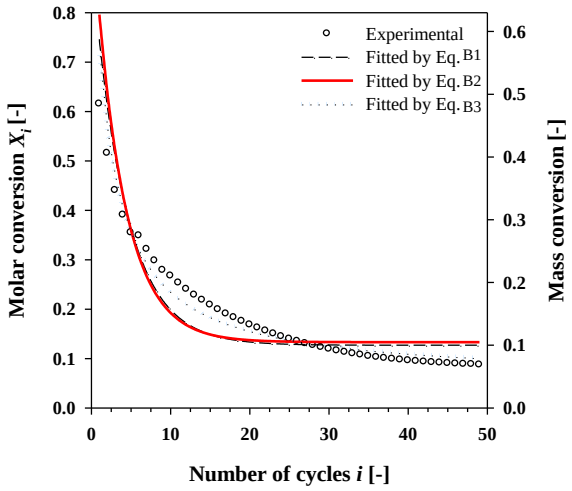

Figure B 2 Carbonation conversion of commercial $CaCO_3$ (Sigma−Aldrich) during 50 cycles of calcination (N_2, 900 °C, 3 min) and carbonation (15% CO_2 in N_2, 650 °C, 3 min) on a TGA-Q5000 using heating/cooling rate of 250 °C/min.

Table B 1 Fitting of the CaO conversion data shown in Figure B 2 to the decay models described by Eqs. (B 1)–(B 3).[a]

Model, Equation	Parameters for the fit X_i vs. i in Figure B 2[a]			
	a	b	R^2	SSE[b]
Power law, (1) (*269*)	0.787	0.127	0.857	0.100
Power law, (2) (*270*)	0.765	0.133	0.803	0.135
Second-order sintering, (3) (*229*)	0.060	0.467	0.961	0.026

[a] Conversion data was obtained by exposing commercial $CaCO_3$ (Sigma−Aldrich) to 50 cycles of calcination (N_2, 900 °C, 3 min) and carbonation (15% CO_2 in N_2, 650 °C, 3 min) in a TGA-Q5000 using heating/cooling rates of 250 °C/min, and is shown in Figure B 2. [b] SSE = sum of squared error = $\sum_{i=1}^{N}(X_i - \overline{X_{calc}})^2$.

Abanades approached the calculation of average carbonation conversion of CaO ($\bar{X}$) and carbonator capture efficiency ($\eta_{carbonator}$) by assuming that the particles in the carbonator and calciner were perfectly mixed and the solids behave as a lump of material when passing through

each step of the recirculation. These assumptions enabled Abanades to derive r_i, the population of particles in the circulating solid stream entering the carbonator that have experienced i **full** carbonation/calcination cycles in the N^{th} cycle (hereafter referred to as the "particles' recirculation distribution"), as shown in Eq. (B 4) (*269*). Here, i corresponds to k in Abanades' (B 4) (*269*). Abanades then combined this with a sorbent decay model (i.e. any of Eqs. (B 1)−(B 3); Abanades' 2002 work used Eq. (B 1)) in Eq. (B 5) to calculate the average CaO conversion in the N^{th} cycle, where N refers to the maximum number of cycles experienced by the portion of sorbents that remain in the recirculation stream.

Here, it is important to consider the physical and computational significance of i and N. In a real steady-state system, there is no distinction between cycles i for streams as a whole, because the recirculation occurs continuously. Cycle number i, on the other hand, can only be defined for single particles, or for groups of particles that have the same cycling experience. In a steady-state system, at any point in the recirculation steam, particles (or groups of particles) with the same cycling experience have cycle numbers from 1 ($i = 1$, for newly injected particles) to infinity ($i = \infty$, for particles which have never been purged from the recirculation stream). Therefore, ideally, the collective reactivity of the solids in the system can be estimated by weighted sum of the reactivity of each particle (or group of particles) from $i = 1$ to $i = \infty$; this is Eq. (B 5) when $N = \infty$. However, summation to infinity is not computationally practical; rather, the calculation must be perform with a finite, but sufficiently large, number N as the upper bound of i. The choice of a finite N is especially important in cases where, due to the mathematical form of X_i, no analytical solution for Eq. (B 5) is available. Thus the calculation of $\bar{X}$, and of quantities that depend upon $\bar{X}$, may require a numerical approximation, and in those cases, N serves as the resolution of the calculation; the more numerical cycles that are calculated, the more closely Eq. (B 5) describes the physical system.

The efficiency in the carbonator, $\eta_{carbonator}$, is the fraction of the CO_2 entering the carbonator that is captured by reaction with CaO, and is defined for the case of Figure B 1a in Eq. (B 6). Here, F_{CO_2} is the molar flow of CO_2 in $F_{flue\ gas}$. Eqs. (B 1) and (B 5) can be substituted into Eq. (B 6), which relates the carbonator efficiency to the average conversion, to give Eq. (B 7), which gives the maximum carbonator efficiency as a function of the empirical reactivity-decay model parameters. In fact, Abanades used a slightly different definition of carbonator efficiency, including the CO_2 in the make-up $CaCO_3$ in the calculation; however, the difference had little impact on calculations of efficiency (*vide infra*). Abanades rearranged this Eq. (B 7) in terms of the make-up ratio F_0/F_R to give Eq. (B 8) (*269*), which relates the computed carbonator efficiency to three process parameters: the make-up ratio F_0/F_R, the ratio F_R/F_{CO_2}, and the number of full cycles *N* (Figure B 6a). The relatively simple form of Eq. (B 1), which was used to describe X_i when the formula for $\bar{X}$ was first developed, enabled Abanades to use geometric series formulation (Eq. (B 9)) to produce Eq. (B 10), an analytical formula for the average conversion ($\bar{X}$) after an infinite number of cycles,(*269*) which would be the case in an actual continuous steady-state system. (Note that, in (*269*), Eq. (B 10) has been printed with an error; the exponent '2' is missing from the numerator. The form given here is correct; derivation is detailed below.). Substituting Eq. (B 10) into Eq. (B 6) gave Eq. (B 11), an analytical formula for carbonator efficiency after an infinite number of cycles in steady-state operation.

$$\boldsymbol{r_i = \frac{F_0 F_R^{i-1}}{(F_0 + F_R)^i}\ i \le N} \tag{B 4}$$

$$\boldsymbol{\bar{X} = \sum_{i=1}^{N} X_i r_i} \tag{B 5}$$

$$\boldsymbol{\eta_{carbonator} = \frac{(F_R + F_0)\bar{X}}{F_{CO_2}}} \tag{B 6}$$

$$\boldsymbol{\eta_{carbonator} = \frac{(F_R + F_0)}{F_{CO_2}} \sum_{i=1}^{N} \left((a^{i+1} + b) \frac{F_0 F_R^{i-1}}{(F_0 + F_R)^i} \right)} \tag{B 7}$$

$$\eta_{carbonator}=\frac{\left(1+{F_0}/{F_R}\right)}{{F_{CO_2}}/{F_R}}\sum_{i=1}^{N}\left((a^{i+1}+b)\frac{{F_0}/{F_R}}{\left({F_0}/{F_R}+1\right)^{i}}\right) \quad \text{(B 8)}$$

$$\sum_{i=1}^{N\to\infty} S^i=\frac{S}{1-S}\ ,|S|<1 \quad \text{(B 9)}$$

$$\bar{X}=\frac{a^2F_0}{F_0+F_R(1-a)}+b \quad \text{(B 10)}$$

$$\eta_{carbonator}=\frac{\left(1+{F_0}/{F_R}\right)}{{F_{CO_2}}/{F_R}}\left[\frac{a^2F_0}{F_0+F_R(1-a)}+b\right] \quad \text{(B 11)}$$

However, the particles' recirculation distribution described by Eq. (B 4) does not take into account the particles that remain in the recirculation stream in the continuous steady-state process, i.e. r_N, the fraction of particles that have circulated N times. Many particles have circulated fewer than N times due to the continuous purge, which removes some particles that have experienced the calcination/carbonation loop a specific number of times, $i < N$, while the continuous make-up adds fresh particles. If the rate of particle replacement (the purge rate, F_0/F_R) is high, so that a large fraction of particles is replaced after each calcination/carbonation cycle, the fraction r_N will be small. On the other hand, if the purge rate is low, as it would be for more stable tailored sorbents, r_N becomes larger; thus this fraction of particles must be considered in order to accurately model such systems. For r_N, the fraction of particles that remain in the cycle in a continuous steady-state process, the generalized form of the distribution equation is given in Eq. (B 27). Derivation of Eq. (B 27) can be demonstrated using the following thought experiment.

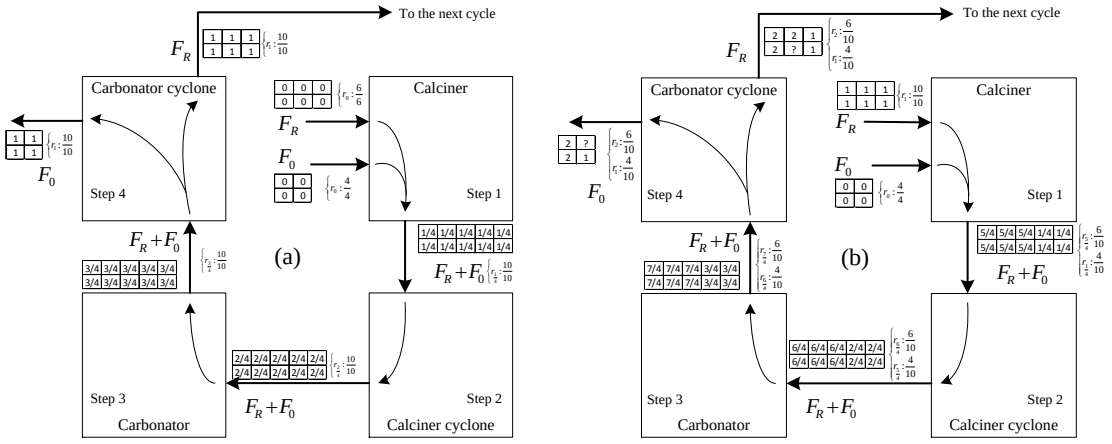

Figure B 3 Schematic diagram of particles circulating in the Ca-looping process. When a portion of solids pass through a step, ¼ is added to its lifetime. The lifetime of the solids is written in the block. A block with a question mark within represents a mixture of various lifetimes. The ratio of circulating solids with specific lifetime after each step is written next to the graphical representation of the recirculation process.

Assume a calcium looping system which consists of 6 blocks of sorbents in the calciner input stream ($F_R = 6$) and four blocks of sorbents in the make-up stream ($F_0 = 4$) as shown in Figure B 3a corresponding to Fig. 1a in the manuscript. For simplicity, the cycle is broken down in to four steps. As a portion of solids pass through a step, ¼ is added to its lifetime. Assume we run exactly two cycles ($N = 2$), with a replacement ratio of 0.4 ($F_0/(F_R + F_0) = 0.4$). We want to calculate the fraction of solids that have been fully recirculated twice (r_2) and the fraction that have been fully recirculated only once (r_1, the portion of fresh particles added between the cycles) at the outlet of the cycle (outlet of step 4). For simplicity, we assume the reactors are perfectly mixed and the solids behave as a lump of material when passing through each step of the recirculation. Perfect mixing means there is no spatial gradient of solids lifetime inside any piece of equipment. Solid lump behavior means that all the solids exit each piece of equipment and enter the next piece of equipment along with any side stream (when applicable); therefore no portion of solids can remain in the equipment (i.e. $r_0 = 0$). $\sum_{i=1}^{2} r_i$ is the sum of the all solid fractions. If $\sum_{i=1}^{2} r_i \neq 1$, then not all fractions of solids have been considered in calculations. As shown in Figure B 3b, at the point that solids are going to experience the next cycle, $r_2 = 0.6$

and $r_1 = 0.4$ giving a total of one ($\sum_{i=1}^{2} r_i = 1.0000$). This is in agreement with the results of Eq. (B 27) in the manuscript. However, Eq. (B 4) gives $\sum_{i=1}^{2} r_i = 0.64$ ($r_2 = 0.24$ and $r_1 = 0.4$) for this simple system, meaning that it fails to include all portions of the particles, because it treats r_N (r_2 in this thought experiment) precisely as it does $r_{i<N}$ (r_1 in this thought experiment). This problem disappears for $N \to \infty$ because in such high number of cycles $r_N \to 0$. Although the situation $N \to \infty$ does most closely approximate a real, continuous system; it cannot always be applied in the computation of sorbent and gas-flow parameters. Our proposed Eq. (B 27) is more general in that it can be used accurately even when it is not mathematically possible to treat the case where $N \to \infty$.

An analytical formula for average sorbent conversion ($\bar{X}$), Eq. **(B 12)**, can be derived from the geometric series (Eq. **(B 13)**) if the sentence *S* in the series can be represented in power law form and is always < 1. Therefore the power law reaction decay model (Eq. **(B 15)**) can benefit from the geometric series equation Eq. **(B 13)**.

$$\bar{X} = \sum_{i=1}^{N\to\infty} X_i r_i \qquad \textbf{(B 12)}$$

$$\sum_{i=1}^{N\to\infty} S^i = \frac{S}{1-S}\,, |S| < 1 \qquad \textbf{(B 13)}$$

$$r_i = \frac{F_0 F_R^{i-1}}{(F_0 + F_R)^i}\; i \le N \qquad \textbf{(B 14)}$$

$$X_i = a^{i+1} + b \qquad \textbf{(B 15)}$$

First, the sum in Eq. **(B 12)** is written using the formulae in Eqs. (B 9) and (B 10) for X_i and r_i, giving Eq. **(B 16)**. Eq. **(B 16)** can be reordered to suit Eq. **(B 13)** by splitting in two parts, as shown in Eq. **(B 17)**. This can be further rearranged, via Eqs. **(B 13)** and **(B 14)**, to give Eq. **(B 20)**.

$$X_i r_i = (a^{i+1} + b)\frac{F_0 F_R^{i-1}}{(F_0 + F_R)^i} \qquad \textbf{(B 16)}$$

$$X_i r_i = a^{i+1} \frac{F_0/F_R}{\left(F_0/F_R + 1\right)^i} + b \frac{F_0/F_R}{\left(F_0/F_R + 1\right)^i} \quad \textbf{(B 17)}$$

$$X_i r_i = a^{F_0/F_R} \left(\frac{a}{F_0/F_R + 1} \right)^i + b^{F_0/F_R} \left(\frac{1}{F_0/F_R + 1} \right)^i \quad \textbf{(B 18)}$$

$$\sum_{i=1}^{N\to\infty} X_i r_i = \sum_{i=1}^{N\to\infty} \left(a^{F_0/F_R} \left(\frac{a}{F_0/F_R + 1} \right)^i + b^{F_0/F_R} \left(\frac{1}{F_0/F_R + 1} \right)^i \right) \quad \textbf{(B 19)}$$

$$\sum_{i=1}^{N\to\infty} X_i r_i = \left(a^{F_0/F_R}\right) \overbrace{\sum_{i=1}^{N\to\infty} \left(\frac{a}{F_0/F_R + 1} \right)^i}^{\varepsilon_1} + \left(b^{F_0/F_R}\right) \overbrace{\sum_{i=1}^{N\to\infty} \left(\frac{1}{F_0/F_R + 1} \right)^i}^{\varepsilon_2} \quad \textbf{(B 20)}$$

Eq. **(B 20)** contains two geometric series, shown by ε_1 and ε_2, and both are always positive values smaller than unity, as shown in Eq. **(B 16)**.

$$S_{\varepsilon_1} = \frac{a}{F_0/F_R + 1} < 1 \;\&\; S_{\varepsilon_2} = \frac{1}{F_0/F_R + 1} < 1 \quad \textbf{(B 21)}$$

Using Eq. **(B 13)**, ε_1 and ε_2 can be simplified to Eq. **(B 22)** and Eq. **(B 23)**.

$$\varepsilon_1 = \frac{S_{\varepsilon_1}}{1 - S_{\varepsilon_1}} = \frac{\frac{a}{F_0/F_R + 1}}{1 - \frac{a}{F_0/F_R + 1}} = \frac{a}{F_0/F_R + 1 - a} \quad \textbf{(B 22)}$$

$$\varepsilon_2 = \frac{S_{\varepsilon_2}}{1 - S_{\varepsilon_2}} = \frac{\frac{1}{F_0/F_R + 1}}{1 - \frac{1}{F_0/F_R + 1}} = \frac{1}{F_0/F_R} \quad \textbf{(B 23)}$$

Substituting Eq. **(B 22)** and Eq. **(B 23)** in Eq. **(B 20)** gives Eq. **(B 24)**, which can be further simplified to give Eq. **(B 25)**.

$$\sum_{i=1}^{N\to\infty} X_i r_i = \left(a^{F_0/F_R}\right) \frac{a}{F_0/F_R + 1 - a} + \left(b^{F_0/F_R}\right) \frac{1}{F_0/F_R} \quad \textbf{(B 24)}$$

$$\sum_{i=1}^{N\to\infty} X_i r_i = \frac{a^2 \; {F_0}/{F_R}}{{F_0}/{F_R} + 1 - a} + b \qquad \textbf{(B 25)}$$

Eq. **(B 25)** can be rearranged to give Eq. **(B 26)**, which is the same as Eq. (B 10).

$$\bar{X} = \sum_{i=1}^{N\to\infty} X_i r_i = \frac{a^2 F_0}{F_0 + F_R(1-a)} + b \qquad \textbf{(B 26)}$$

The distinction between r_i and r_N has immediate consequences for numerical computations (which must be performed when no analytical solution to Eq. (B 5) is available); when r_i is calculated using Eq. (B 4), the sum of fractions of particles is not 1 (i.e. mass is not conserved) unless N is very high ($N > 10^6$), as shown in Figure B 4. When $N \to \infty$, $r_N \to 0$ and therefore the impact of r_N on the $\sum_{i=1}^{N} r_i$ diminishes. The high N required in order for mass to be conserved in Eq. (B 4) can increase computation time by 30–300× (depending on make-up ratio; see Figure B 5) compared to Eq. (B 27). A similar problem arises at low make-up ratios, i.e. when r_N is large; this situation is especially desirable for tailored or enhanced sorbents, which will presumably be more costly, and more stable, than natural limestone. Even for economic sorbents, low make-up ratios are desirable because the make-up flow incurs costs for additional sorbent that must be purchased, handled, and heated to calcination temperature. As make-up ratio decreases, r_N increases to a maximum of unity at zero make-up (i.e. no spent sorbent is removed from the system and no fresh sorbent is added; $F_0 = 0$). This means that, at zero make-up, all of the particles in the recirculation have the same cycling experience, which is equal to number of cycles (N). In this situation, the average sorbent conversion in the carbonator ($\bar{X}$) should equal the residual sorbent conversion (i.e. b in Eqs. (B 1) and (B 2) or a in Eq. (B 3)). However, Eq. (B 4) gives $\bar{X} = 0$ under this condition, irrespective of N, because $F_0 = 0$, and therefore, according to Eq. (B 4), $r_i = 0$ for all values of i from 1 to N.

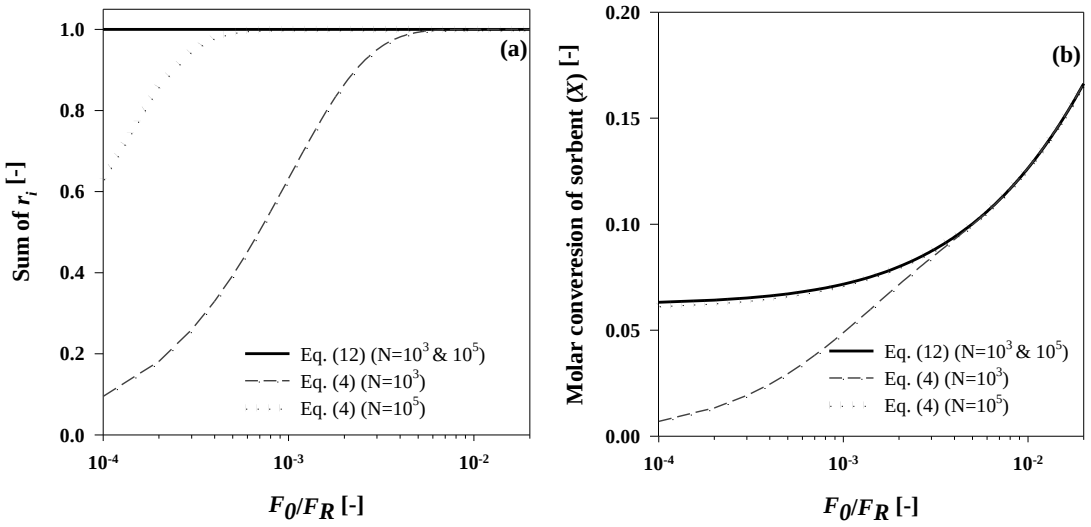

Figure B 4 Effect of total number of recirculations, *N*, on: a) the sum of particles' recirculation distribution ($\sum_{i=1}^{N} r_i$), and b) the calculated average sorbent molar conversion in carbonator ($\sum_{i=1}^{N} X_i r_i$) when *N* = 10^3 and *N* = 10^5. At *N* > 10^6, Eq. (4) accurately presents the particles' recirculation distribution and, as a result, the average molar conversion calculation in the carbonator is reliable.

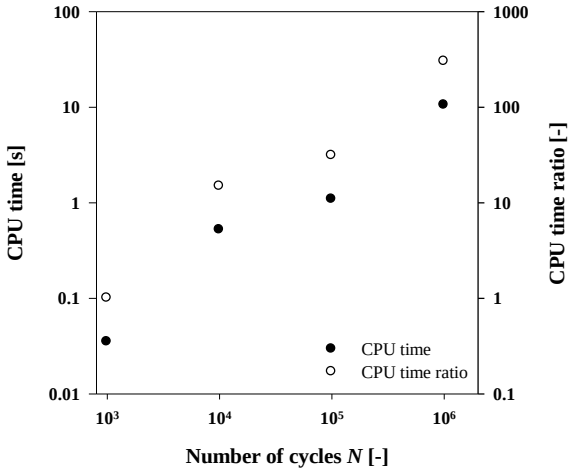

Figure B 5 Effect of the total number of recirculations, *N*, on CPU time. CPU time is measured based on the time it takes for the computer (Intel® Xeon® CPU X5450 @ 3.00 GHz 64-bit, 8.00 GB RAM) to run the MATLAB simulation file for the calcium looping process described in the paper, using Eq. (4). CPU time ratio is the ratio between CPU time for any given *N* and CPU time for $N = 1000$.

$$r_i = \begin{cases} \dfrac{F_0 F_R^{i-1}}{(F_0 + F_R)^i} & i < N \\ \dfrac{F_R^i}{(F_0 + F_R)^i} & i = N \end{cases} \quad \text{(B 27)}$$

Because sorbent conversion affects the computation of a number of other parameters, the difference between Eqs. (B 4) and (B 27) have consequences beyond $\bar{X}$. In order to show how using Eq. (B 27), rather than Eq. (B 4), can impact process design in calcium-looping systems, we used Eq. (B 27) to evaluate a variety of quantities relevant to CO_2 capture by calcium looping, for zero and non-zero make-up flow. The results were then compared to those from Eq. (B 4). We began by substituting the formula for the particles' recirculation distribution into the formulae for average conversion and carbonator efficiency (Eqs. (B 5) and (B 6), respectively) to examine the impacts of gas and solid flow rates on efficiency (*269*); this gave Eq. **(B 28)** for carbonator efficiency. Figure B 6a, which plots carbonator efficiency according to Eqs. (B 8) (*269*), (B 11), and **(B 28)**, reveals the importance of considering the fraction of particles that are not being purged out of the recirculation stream (i.e. r_N) in these calculations, especially at low make-up ratios ($F_0/F_R < 0.01$). Under these conditions, Eq. (B 8) predicts a much lower carbonator efficiency than Eq. **(B 28)** gives. The same is true when comparing Eqs. (B 8) and (B 11). For example, in order to achieve $\eta_{carbonator} = 0.6$, Eq. (B 8) recommends operating with $F_R/F_{CO_2} = 5$ and $\frac{F_0}{F_R} = 0.0022$; whereas, according to Eq. **(B 28)**, $\eta_{carbonator} = 0.6$ cannot be achieved with $F_R/F_{CO_2} = 5$; rather, $F_R/F_{CO_2} = 4$ and $\frac{F_0}{F_R} = 0.0086$ should be used. Practically, this means that less total sorbent needs to be circulated through the system for a given flow of CO_2 (i.e. less sorbent inventory is required), but at a greater sorbent make-up ratio. As expected, Eq. (B 11) yields same values as Eq. **(B 28)**, meaning that the proposed numerical formula (**(B 28)**) is equivalent to the analytical formula obtained using r_i as given in Eq. (B 4) as $i \to \infty$. However, an analytical solution can only be obtained for some forms of X_i.

$$\boldsymbol{\eta_{carbonator}} = \frac{\left(\mathbf{1} + {\boldsymbol{F_0}}/{\boldsymbol{F_R}}\right)}{{\boldsymbol{F_{CO_2}}}/{\boldsymbol{F_R}}} \left[\sum_{i=1}^{N-1} \left((\boldsymbol{a}^{i+1} + \boldsymbol{b}) \frac{{\boldsymbol{F_0}}/{\boldsymbol{F_R}}}{\left({\boldsymbol{F_0}}/{\boldsymbol{F_R}} + \mathbf{1}\right)^{i}} \right) + (\boldsymbol{a}^{N+1} + \boldsymbol{b}) \frac{\mathbf{1}}{\left({\boldsymbol{F_0}}/{\boldsymbol{F_R}} + \mathbf{1}\right)^{N}} \right] \quad \textbf{(B 28)}$$

$$\eta_{capture} = \frac{(F_R + F_0)\bar{X} + F_{CO_2,makeup} + F_{CO_2,calciner}}{F_{CO_2,plant} + F_{CO_2,makeup} + F_{CO_2,calciner}} \quad \textbf{(B 29)}$$

A comparison of Figure B 6a and b shows the importance of using a proper reactivity decay model to describe X_i to fit the sorbent decay behaviour. Figure B 6a shows carbonator efficiency data calculated using the power-law reactivity decay model shown in Eq. (B 1) (*269*); whereas Figure B 6b was created using the second-order sintering model, Eq. (B 3) (*229*). In most cases, a carbonator efficiency ($\eta_{carbonator}$) of ~85% is sufficient to produce a total capture rate ($\eta_{capture}$, Eq. **(B 29)**) of 90%, a common target (*117*, *275*). Figure B 6a offers two sets of operating process parameters that give $\eta_{carbonator} = 0.85$: $F_R/F_{CO_2} = 5$ and $F_0/F_R = 0.016$ or $F_R/F_{CO_2} = 4$ and $F_0/F_R = 0.034$. In contrast, Figure B 6b, which better reflects the actual behaviour of CaO under the industrially relevant conditions used in Figure B 2 and Table B 1.

, gives us $F_R/F_{CO_2} = 5$ and $F_0/F_R = 0.021$ or $F_R/F_{CO_2} = 4$ and $F_0/F_R = 0.036$. Thus, the more accurate calculations indicate that more solids are required to meet the capture rate; these values can strongly affect decision-making regarding capture plant operation and design.

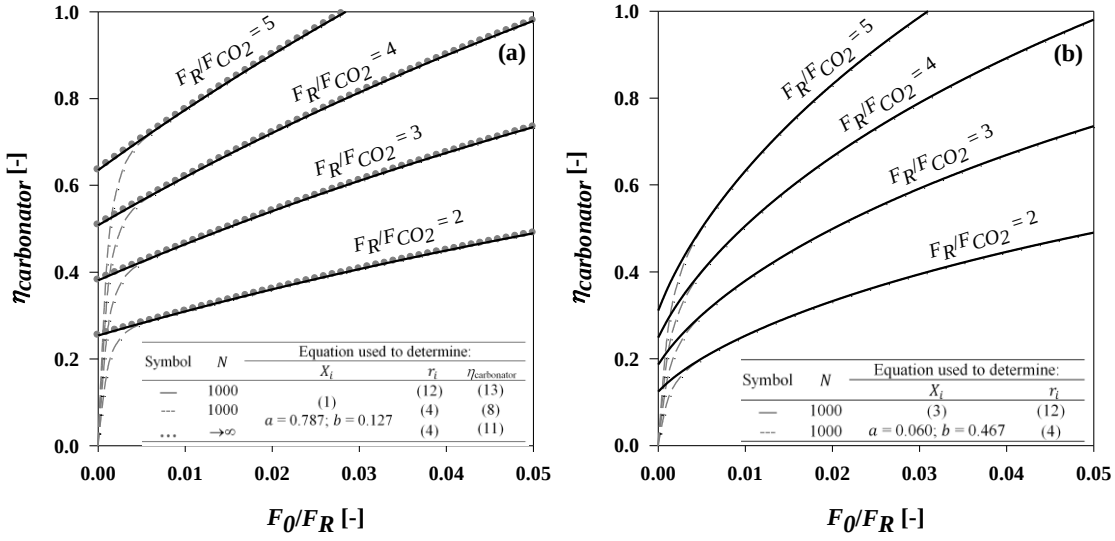

Figure B 6 Maximum CO_2 capture efficiencies in the carbonator, calculated using analytical formula and series numerical calculations: a) using Eq. (B 1) to describe the conversion X_i ($N = 1000$; $a = 0.787$ and $b = 0.127$, Table B 1), and b) using Eq. (B 3) to describe the conversion X_i ($N = 1000$; $a = 0.060$ and $b =$

0.467, Table B 1). Analogous figures produced using Abanades' definition of $\eta_{carbonator}$ are shown as Fig. S3.

The results in Figure B 6, along with the desire for a carbonator efficiency of $\eta_{carbonator} = \sim 0.85$ in order to reach $\eta_{capture} = 0.90$, seem at first to indicate that the difference between the particles' recirculation distributions given in Eqs. (B 4) and (B 27) is moot compared to the difference between Eqs. (B 1) and (B 3) for conversion. That is, when the more accurate Eq. (B 3) is used to describe the carbonation conversion as a function of cycle number, the desired carbonator efficiencies can only be reached for $F_0/F_R > 0.01$, a regime in which Eqs. (B 27) and (B 4) produce identical results. However, the ideal make-up ratio F_0/F_R is expected to be lower for synthetic or pretreated sorbents, because of their durability and cost, and we therefore considered the importance of particles that have been present in the reactor during the entire process, r_N (which distinguishes Eqs. (B 4) and (B 27)) on process decisions involving such sorbents. Romeo et al. (*276*) described the performance of an enhanced sorbent using the parameters α and β (Eqs. (B 30) and (B 31)), to represent the improvements in initial and residual carbonation conversion, respectively, over the reference sorbent. For example, $\alpha = \beta = 0$ corresponds to the reference sorbent, $\beta > 0$ means the residual conversion of the sorbent is better than the reference sorbent, and $\alpha > 0$ means the initial activity of sorbent in the first cycle is better than the reference sorbent. We have adopted this terminology, and taken the commercial CaO performance as measured under industrially relevant conditions (Figure B 2; fit to Eq. (B 3) as per Table B 1) as the reference sorbent. Figure B 7a and b show how including r_N impacts the design targets for the sorbent improvement parameters α and β. For example, when this fraction of particles is not considered (i.e. r_i is given by Eq. (B 4); see Figure B 7a) and the arbitrary process parameters $F_{CaO}/F_{CO_2} = 1.5$ (F_{CaO} = flow of CaO into the carbonator; this is $F_R + F_0$ in Figure B 1a) and $F_0/F_{CaO} = 0.001$ are chosen, the carbonator efficiency $\eta_{carbonator} = 0.85$ (and thus, in most cases, the capture efficiency $\eta_{capture}$ = 0.90, vide supra) cannot be reached

just by improving the residual conversion of sorbent (β). On the contrary, when all of the sorbent is considered (i.e. r_i is given by Eq. (B 27), Figure B 7b), solely improving the residual conversion by ~86 percentage points is sufficient to reach $\eta_{carbonator} = 0.85$. Similarly, if α and β are improved by 10 percentage points each, Eq. (B 4) predicts an improvement in $\eta_{carbonator}$ of 11 percentage points; whereas Eq. (B 27) predicts an improvement of 17.5 percentage points. If limestone is chosen as the reference sorbent as per (*276*), improvements are 12.5 vs. 19.8 percentage points, respectively (see Figure B 8). This clearly refines our understanding of the improvements to sorbent characteristics that are required to reach a target plant performance.

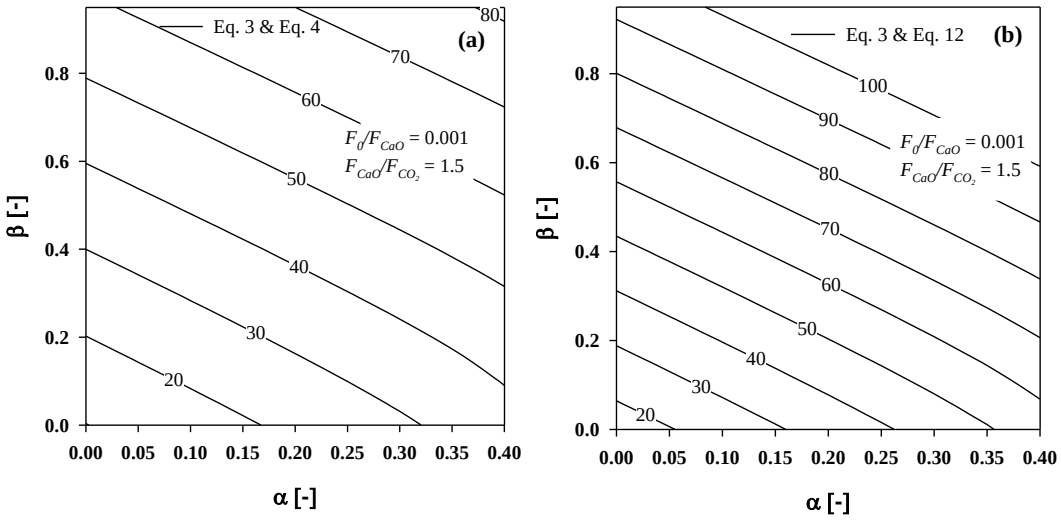

Figure B 7 Isolines of carbonator capture efficiency ($\eta_{carbonator}$) for improved sorbent properties in a calcium looping process, as calculated for $N = 1000$ using a) Eq. (B 4); b) Eq. (B 27). The parameters α and β are the differences in initial and residual conversion, respectively, between a tailored sorbent and commercial CaO (X_i given by Eq. (B 3); $a = 0.006$ and $b = 0.467$).

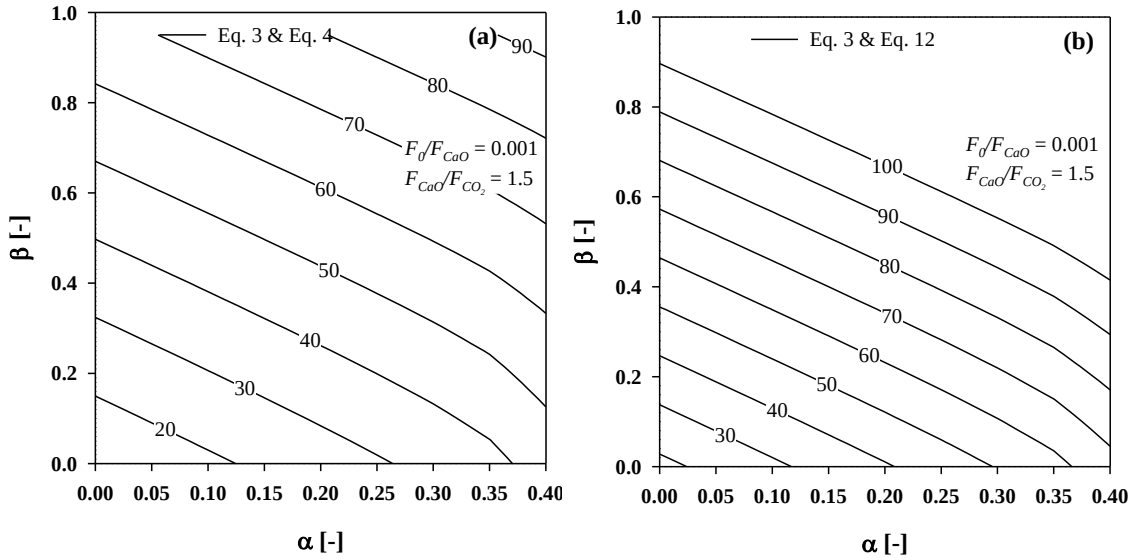

Figure B 8 Effect of different models for particles' recirculation distribution on calculated improvements in carbonator capture efficiency when comparing enhanced sorbents to limestone (Eq. (B 3); a = 0.075, b = 0.52 [2]): a) Using Eq. (B 4); b) Using Eq. (B 27).

$$\boldsymbol{\alpha = \frac{X_0 - X_{0,ref}}{X_{0,ref}}} \tag{B 30}$$

$$\boldsymbol{\beta = 1 - \frac{X_0 - X_r}{X_{0,ref} - X_{r,ref}}} \tag{B 31}$$

Abanades used the definition of $\eta_{carbonator}$ given in Eq. **(B 32)** (cf. Eq. (B 6)) (*269*). This equation can be expanded as in Eqs. **(B 33)–(B 36)**, and computed numerically as in Fig. Figure B 9 (cf. Fig. Figure B 7). Despite the slightly different form of $\eta_{carbonator}$, the fundamental difference that exists between the definitions of r_i in Eqs. (B 4) and (B 27) still produces the differences in $\eta_{carbonator}$.

$$\boldsymbol{\eta_{carbonator} = \frac{(F_R + F_0)\bar{X}}{F_{CO_2} + F_0}} \tag{B 32}$$

$$\boldsymbol{\eta_{carbonator} = \frac{(F_R + F_0)}{F_{CO_2} + F_0} \sum_{i=1}^{N} \left((a^{i+1} + b) \frac{F_0 F_R^{i-1}}{(F_0 + F_R)^i} \right)} \tag{B 33}$$

$$\boldsymbol{\eta_{carbonator} = \frac{\left(1 + {F_0}/{F_R}\right)}{{F_{CO_2}}/{F_R} + {F_0}/{F_R}} \sum_{i=1}^{N} \left((a^{i+1} + b) \frac{{F_0}/{F_R}}{\left({F_0}/{F_R} + 1\right)^i} \right)} \tag{B 34}$$

$$\boldsymbol{\eta_{carbonator} = \frac{\left(1 + {F_0}/{F_R}\right)}{{F_{CO_2}}/{F_R} + {F_0}/{F_R}} \left[\frac{a^2 F_0}{F_0 + F_R(1 - a)} + b \right]} \tag{B 35}$$

$$\eta_{carbonator} = \frac{\left(1 + {F_0}/{F_R}\right)}{{F_{CO_2}}/{F_R} + {F_0}/{F_R}} \left[\sum_{i=1}^{N-1} \left((a^{i+1} + b) \frac{{F_0}/{F_R}}{\left({F_0}/{F_R} + 1\right)^i} \right) + (a^{N+1} + b) \frac{1}{\left({F_0}/{F_R} + 1\right)^N} \right] \quad \textbf{(B 36)}$$

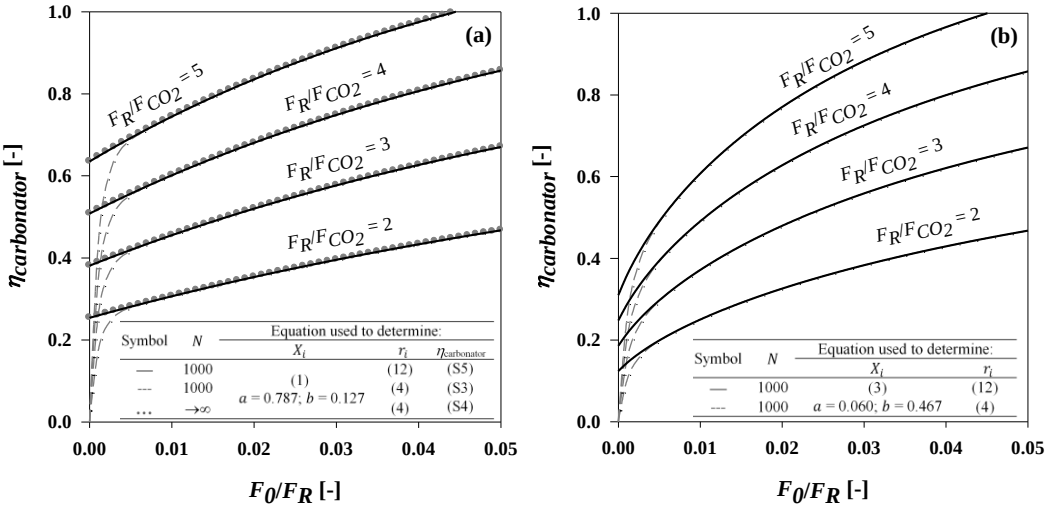

Figure B 9 Maximum CO_2 capture efficiencies in the carbonator, calculated using analytical formula and series numerical calculations when Abanades definition of carbonator efficiency (Eq. (B 32)**) is used (*269*): a) using Eq. (B 1) to describe the conversion X_i ($N = 1000$; $a = 0.787$ and $b = 0.127$, Table B 1), and b) using Eq. (B 3) to describe the conversion X_i ($N = 1000$; $a = 0.060$ and $b = 0.467$, Table B 1).**

B.3.2 Estimation of streams cost and energy penalty

The importance of including r_N when planning a CO_2-capture processes can also be considered in terms of the operating costs of a power plant outfitted with calcium-looping carbon capture. Eq. (B 37) gives the annual stream costs of such a CO_2-capture system, assuming that the calciner is heated via the combustion of coal in O_2. Eq. (B 37) is not intended to include all the variable costs associated with the operation of the plant or to reflect the profitability or change in levelized cost of electricity due to calcium looping. It is only a reflection of how the streams cost is affected by changing the sorbent in calcium looping process. Therefore, the possible incomes associated with calcium looping process are not included (e.g. excess

electricity produced). Here, C_{coal} is the price of the coal fed to the calciner, $C_{sorbent}$ is the price for the sorbent, C_{O_2} is the price for oxygen required for oxy-combustion, and f_c is the capacity factor of the power plant. Figure B 11 shows the impact of make-up ratio on annual stream costs for a 1000-MWe coal-fired power plant operating at 85% capacity (f_c = 0.85) and connected to a calcium-looping CO_2-capture plant operating at a capture rate of 90%.

$$C_{streams} = \left(C_{coal}F_{coal} + C_{sorbent}F_{sorbent} + C_{O_2}F_{O_2}\right) \times f_c \quad \text{(B 37)}$$

Bituminous coal having the composition considered by Arias et al. (*277*) was used in the calculations, and was assigned a cost $C_{coal} = \text{A\$}44/\text{ton}$ (A$ = Australian dollars) (*278*). It is assumed here that O_2 is generated on-site using an air separation unit. Therefore, the price of O_2 is calculated based on the price of electricity and amount of electricity required for O_2 generation (220 kWhe per tonne of O_2 (*279*)). Therefore, O_2 price was estimated here to be $C_{O_2} = \text{A\$}10/\text{ton}$, consistent with an electricity price of A$0.05/kWh (*279, 280*). CaO was assigned a price of A$10/ton (*281*). In order to compare a high-performance sorbent to CaO, we tested a tailored sorbent produced in our laboratory, CaO/meso-$Ca_xAl_yO_z$ (*282*), under the harsh conditions used to evaluate CaO in Table B 1. Under these conditions, CaO/meso-$Ca_xAl_yO_z$ was indeed more stable than commercial CaO, giving $\alpha = -0.135$ and $\beta = 0.507$ (see Figure B 10). This sorbent has only been synthesized on small scales to date, so its bulk cost is not known; thus, estimates of 2, 5, and 10× the cost of CaO (i.e. 20, 50, and 100 A$/ton) were used. As shown in Figure B 11, when Eq. (B 4) was used to describe the particles' recirculation distribution, the operating cost of maintaining a capture rate of 90% increased dramatically at lower sorbent make-up ratios. This increase resulted from a huge decrease in calculated average CaO conversion ($\bar{X}$), which led to a subsequent increase in F_{CaO}/F_{CO_2} ratios, solids circulating flow rate, and finally increased demand for coal to heat the calciner to the required temperature

of 950 °C while maintaining the overall capture rate. However, when Eq. (B 27) was used, the annual stream costs were predicted to be relatively stable at low make-up ratios. This difference would have a significant impact on capital costs, as the case predicted by Eq. (B 4) would require bigger equipment. Moreover, Eqs. (B 4) and (B 27) predicted significantly different optimum operation points from the perspective of streams cost (Figure B 11, Table B 2). For example, for case iv, the optimum make-up ratio is 2.3×10^{-3} when Eq. (B 4) is used, but only 9.6×10^{-6} when Eq. (B 27) is used. For CaO (Figure B 11, i), a low quality sorbent, the equations show virtually the same optimum ratio of 2.0%.

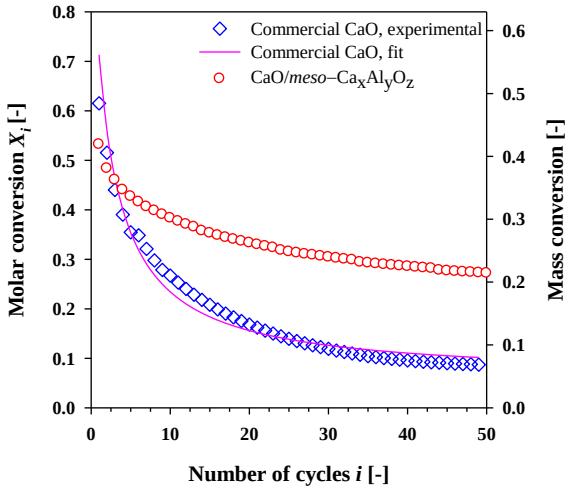

Figure B 10 CO_2 uptake by commercial CaO and by CaO/*meso*-$Ca_xAl_yO_z$ [3] over 50 cycles of carbonation (15% CO_2 in N_2, 650 °C, 3 min) and calcination (N_2, 900 °C, 3 min) at industrially relevant conditions (d*T*/d*t* = 250 °C/min).

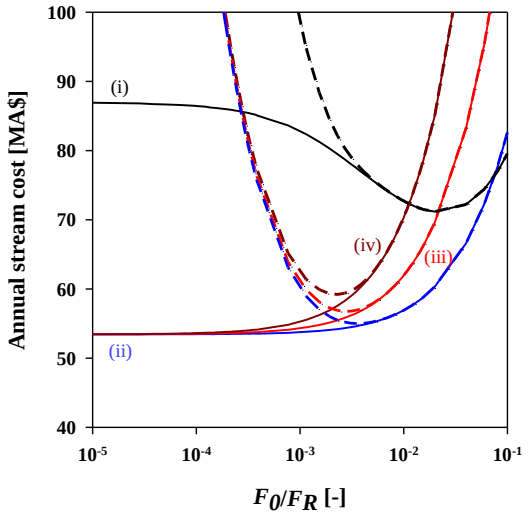

Figure B 11 Annual stream costs, calculated using Eq. (B 37), when different models for r_i are used at $\eta_{capture} = 0.9$ for a 1000-MWe coal fired power plant. Dashed lines show data calculated using Eq. (B 4), whereas solid lines show data calculated using Eq. (B 27) while $a = 0.060$ and $b = 0.467$. (i) CaO at \$10/ton; and (ii–iv) CaO/meso-$Ca_xAl_yO_z$ ($\alpha = -0.135$ and $\beta = 0.507$) at 20, 50, and 100 A\$ /ton, respectively.

Table B 2 Process parameters that minimise the stream costs of a calcium-looping CO_2 capture plant retrofitted to a bituminous-coal-fired power plant operating at an average capacity of 85% ($f_c = 0.85$).

Case	r_i given by Eq.	Stream Costs Minimised for ($\eta_{capture} = 0.9$, $f_c = 0.85$)		
		F_0/F_R [-]	F_{CO2}/F_R [-]	Stream Costs [M$A/a]
(i)	(B 4)	0.02	4.3	71
	(B 27)	0.02	4.3	71
(ii)	(B 4)	3.5×10^{-3}	2.8	55
	(B 27)	2.9×10^{-5}	2.8	53
(iii)	(B 4)	2.7×10^{-3}	2.9	57
	(B 27)	9.6×10^{-6}	2.8	53
(iv)	(B 4)	2.3×10^{-3}	3.0	59
	(B 27)	9.6×10^{-6}	2.8	53

In addition to considering the particles that have been present throughout the calcium looping process for a maximum of N cycles, which produces clear advantages for making predictions in systems employing low make-up ratios F_0/F_R, Eq. (B 27) offers improved flexibility and stability compared to Eq. (B 4). This can be demonstrated by considering the heat required for a power plant modified with calcium looping. Rodriguez et al. (*283*) calculated this quantity as a function of sorbent conversion in the carbonator X_{carb}. $\bar{X}$ is the theoretical maximum value of X_{carb}, i.e. $X_{carb} \leq \bar{X}$. X_{carb} may be lower than $\bar{X}$ if, for example, particle

residence times are insufficient. Here we assumed the residence time in carbonator is long enough to reach the maximum achievable conversion as explained in (*283*) and therefore $X_{carb} = \bar{X}$. We have repeated the calculations using Eq. (B 27), as shown in Figure B 12. Note that we have assumed Rodriguez et al.'s values for *a* and *b* ($a = 0.075$ and $b = 0.52$ (*283*)) here in order to permit a direct comparison. One difference between the results obtained using Eq. (B 4) for the particles' recirculation distribution and those obtained using our updated formula (Eq. (B 27)) is that the former produces data in the region $X_{carb} < 0.075$ (grey region in Figure B 12). In reality, this is not possible when the particle residence time is sufficient, as these values lie below the residual conversion of limestone, X_r (*276*). Eq. (B 27) takes this information into account, and therefore shows no values in this region. More importantly, however, Eq. (B 27) is less sensitive to N, the number of cycles considered in series calculations, than Eq. (B 4) is. For example, the minimum heat requirement for the calcium looping system (i.e. the minimum of the curve in Figure B 12) occurs at $X_{carb} = 0.2376$ for $N = 50$ and at $X_{carb} = 0.2359$ for $N = 10^6$ when the particles' recirculation distribution is described by Eq. (B 27) (X_{carb} decreases by 0.7%). Using Eq. (B 4), on the other hand, gives $X_{carb} = 0.2692$ at $N = 50$ and $X_{carb} = 0.2359$ at $N = 10^6$ (X_{carb} decreases by 12.4%). Thus, calculating over a greater number of cycles was much more important using Eq. (B 4).

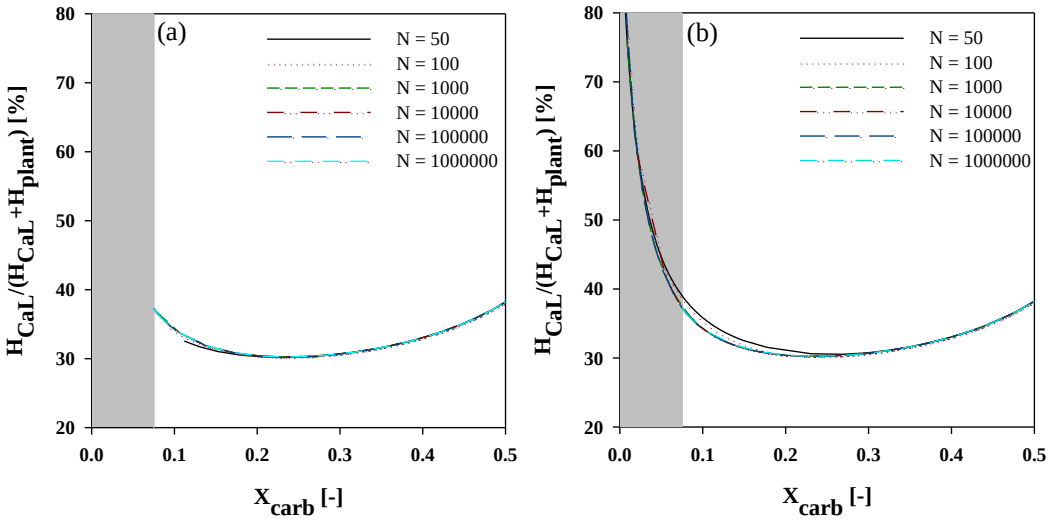

Figure B 12 Effect of total number of cycles (*N*) in predicting heat requirement of the capture plant when different cyclic distribution equations are used (*a* = 0.075 and *b* = 0.52 as defined (*283*); a) Eqs. (B 3) & (B 27), b) Eqs. (B 3) & (B 4). The data presented in this figure correspond only to the dashed line in Figure 5 of (*283*). Here we do not attempt to replicate the solid lines Figure 5 of Rodriguez et al., (*283*) which describe the case where real carbonator efficiency X_{carb} is below maximum carbonation efficiency $\bar{X}$.

The minimum N required to accurately determine $\eta_{carbonator}$ using the particles' recirculation distribution given in Eq. (B 27) is shown in Figure B 13a and b. When the simpler power-law model (Eq. (B 1)) was used for reactivity decay (yielding Eq. **(B 28)** for $\eta_{carbonator}$), $\eta_{carbonator}$ was approximately independent of N for $N \geq 30$ (Figure B 13a); however, when the more complex, but more accurate sintering-based reactivity decay model (Eq. (B 3)) was used (Figure B 13b), $\eta_{carbonator}$ became independent of N only after $N = 100$ for $F_R/F_{CO_2} = 5$, and only after $N = 1000$ for $F_R/F_{CO_2} = 2$. However, when Abanades' particles' recirculation distribution, given in Eq. (B 4), was used, the minimum N required increased significantly (see Figure B 13c and d). When the power-law model (Eq. (B 1)) was used, the minimum N required was 1000 and when the sintering-based reactivity decay model was used, the minimum N required was 10,000. Thus the modified particles' recirculation distribution model presented here (Eq. (B 27)) decreased the minimum N required by around one order of magnitude.

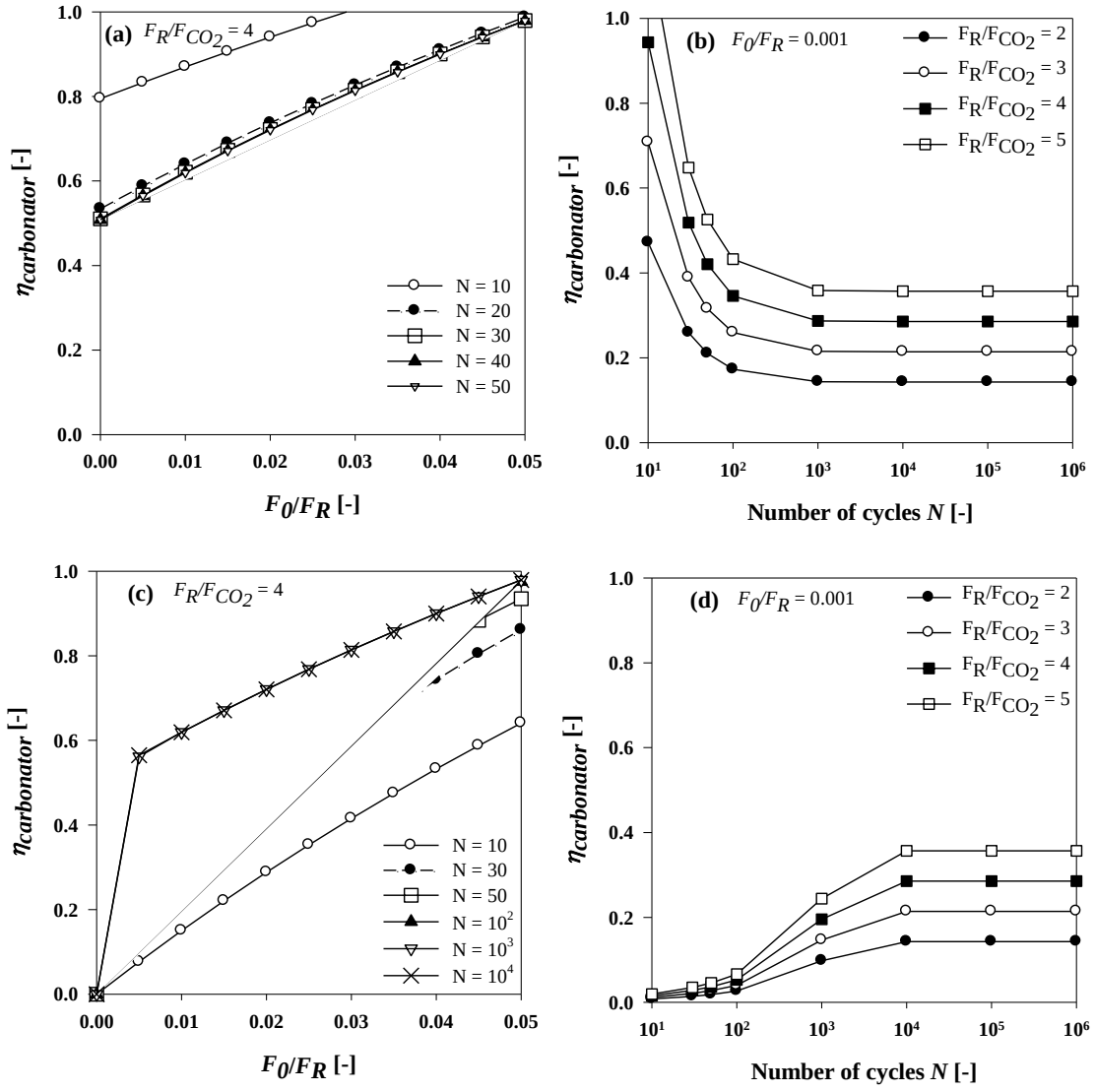

Figure B 13 Effect of total number of cycles (*N*) on carbonator efficiency ($\eta_{carbonator}$) when series calculation is used: a) when Eq. (B 1) and Eq. (B 27) are used for calculating carbonator efficiency ($a = 0.787$ and $b = 0.127$, Table B 1); b) when Eq. (B 3) and Eq. (B 27) are used for calculating carbonator efficiency ($a = 0.060$ and $b = 0.467$, Table B 1); c) when Eq. (B 1) and Eq. (B 4) are used for calculating carbonator efficiency ($a = 0.787$ and $b = 0.127$, Table B 1); d) when Eq. (B 3) and Eq. (B 4) are used for calculating carbonator efficiency ($a = 0.060$ and $b = 0.467$, Table B 1).

Just as the accuracy of the particles' recirculation distribution equation affects $\eta_{carbonator}$, so does the reactivity-decay model. Figure B 14 compares the error in carbonator efficiency as a function of make-up ratio, using Eq. **(B 28)** for $\eta_{carbonator}$ and either Eq. (B 1), (B 2), or (B 3)

for the conversion X_i. The error, $Error_j$ is calculated according to Eq. (B 38), with the experimental decay data derived from Figure B 2. As shown in Figure B 14, the reactivity decay model dramatically impacted $\eta_{carbonator}$ at lower make-up ratios. At higher make-up ratios, the selected reactivity model was not as important. Therefore, when high performance sorbents are to be used, it becomes extremely important to use an accurate reactivity decay model (i.e. Eq. (B 3)) along with a proper particles' recirculation distribution (i.e. Eq. (B 27)) in the analysis and design of the carbonator. Regardless of the reactivity decay model used, the fitting parameters should be derived from experimental data obtained under conditions consistent with the intended industrial process; that is, the residence time, temperature, atmosphere, and pressure etc. in the carbonator and calciner should be the same ones expected in the industrial process.

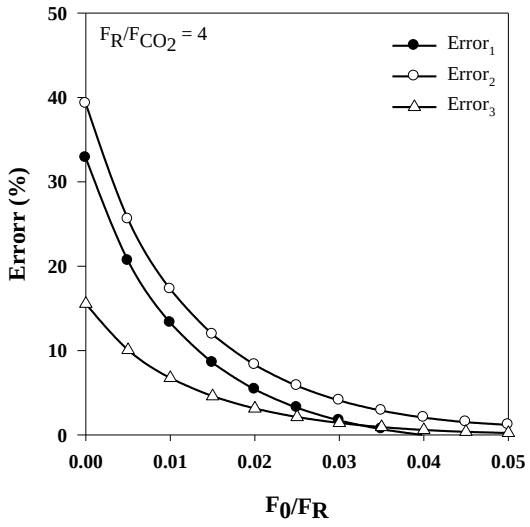

Figure B 14 The error in carbonator efficiency estimation caused by using different reactivity decay models in comparison with using experimental reactive decay data ($N = 50$).

$$\boldsymbol{Error_j}(\%) = \frac{\boldsymbol{\eta_{carbonator,Eq.j} - \eta_{carbonator,Exp.}}}{\boldsymbol{\eta_{carbonator,Exp.}}} \times \mathbf{100} \qquad \text{(B 38)}$$

All in all, the proposed particles' recirculation distribution formula shown in Eq. (B 27) offers high numerical stability due to the relaxed and realistic sensitivity of the model toward operation and cost parameters. The stability of a computational model is very important when it is used in planning a calcium looping process, because a numerically unstable model can

produce confusion in optimization algorithms, which in turn can lead to unreal results or convergence problems. In addition, the modified particles' recirculation distribution proposed in this study (Eq. (B 27)), due to its reduced sensitivity to N, enables the use of more complex, and thus more accurate, reactivity decay models and experimental decay data to describe a sorbent when evaluating carbonator efficiency at different process parameters, and therefore to determine the optimum process parameters (F_0/F_R and F_{CaO}/F_{CO_2}) more accurately.

B.3.3 Variations

Another challenge in the design of calcium looping cycle is the location of solid purge and make-up stream. As shown in Figure B 1, there are two options available for each: purging from carbonator, purging from calciner, make-up into carbonator, and make-up into calciner. This makes a total of four theoretically possible configurations, as shown in Figure B 1a–d. In many cases, the materials used determine the best design. For example, if a sorbent must be calcined before use (which is the case for $CaCO_3$), then the make-up flow must be into the calciner, or the fresh sorbent must cycle through the carbonator once as inactive $CaCO_3$. On the other hand, if the post-combustion carbon capture plant is to be integrated with the cement industry (*284*), the purge should be from the calciner, as purging from the carbonator would yield a mixture of $CaCO_3$ and CaO. In the absence of such factors, the optimum configuration of a calcium looping cycle can be considered in terms of carbonator efficiency and material flows.

Abanades considered a system in which spent sorbent was purged from the carbonator (as in Figure B 1a) and X_i was defined as in Eq. (B 1) (*269*), as well as a system in which spent sorbent was purged from the calciner (as in Figure B 1b) and X_i was defined as in Eq. (B 2) (*285*), and Romeo et al. (*281*) compared the cost of CO_2 capture in these two scenarios. However, the impacts of the purge and make-up locations on r_i have not been examined.

Because it is simpler to investigate the effect of purge location than of make-up location on the cycle, we first compare two calcium-looping configurations that differ only in the location of purge stream (Figure B 1a vs. Figure B 1b). Figure B 1b shows the case in which fresh sorbent is fed into the calciner and the purge exits from the calciner cyclone; in contrast, the purge exits from the carbonator cyclone in Figure B 1a. As branching the stream of cycling solids after the carbonator does not change the particles' recirculation distribution (i.e. branching does not change the quality of streams), Eq. (B 27) still applies for the reactor configuration shown in Figure B 1b. Thus, for a given sorbent and when the make-up sorbent is added to the calciner, the average carbonation conversion $\bar{X}$ will be the same regardless of the location of the purge. However, branching the stream of particles after the carbonator does affect the actual flow rate of solids entering the carbonator as shown in Figure B 1. For a specific target carbonator efficiency, the ratio of CaO to CO_2 entering the carbonator is a constant. Therefore $\frac{F_{CaO}}{F_{CO_2}}$ is:

$$\frac{F_{CaO}}{F_{CO_2}} = \begin{cases} \frac{F_R + F_0}{F_{CO_2}} & purge\ from\ carbonator\ (Fig. B1a) \\ \frac{F_R{}'}{F_{CO_2}} & purge\ from\ calciner\ (Fig. B1b) \end{cases} \quad \text{(B 39)}$$

$$\bar{X} = \sum_{i=0}^{N} X_i r_i \quad \text{(B 40)}$$

As a result, in case of purging from the carbonator as in Figure B 1a, the flow rate of circulating solids to the calciner is slightly less than in the case of purging from the calciner as in Figure B 1b; that is, $F_R{}' > F_R$. Therefore, a slightly smaller calciner and less heating energy are required in this case. However, the size of the carbonator and required make-up flow to maintain operation at a given target capture rate is the same for these two configurations.

$$r_i = \begin{cases} \frac{F_0'' F_R''^{\,i}}{(F_0'' + F_R'')^{i+1}} & i < N \\ \frac{F_R''^{\,i}}{(F_0'' + F_R'')^{i}} & i = N \end{cases} \quad \text{(B 41)}$$

$$\eta_{carbonator} = \frac{(F_R'' + F_0'')\bar{X}}{F_{CO_2}} \quad \text{(B 42)}$$

$$\eta_{carbonator} = \frac{1 + {F_0''}/{F_R''}}{{F_{CO_2}}/{F_R''}} \left[\sum_{i=0}^{N-1} \left((a^{i+1} + b) \frac{{F_0''}/{F_R''}}{\left({F_0''}/{F_R''} + 1\right)^{i+1}} \right) + (a^{N+1} + b) \frac{1}{\left({F_0''}/{F_R''} + 1\right)^{N}} \right] \quad \text{(B 43)}$$

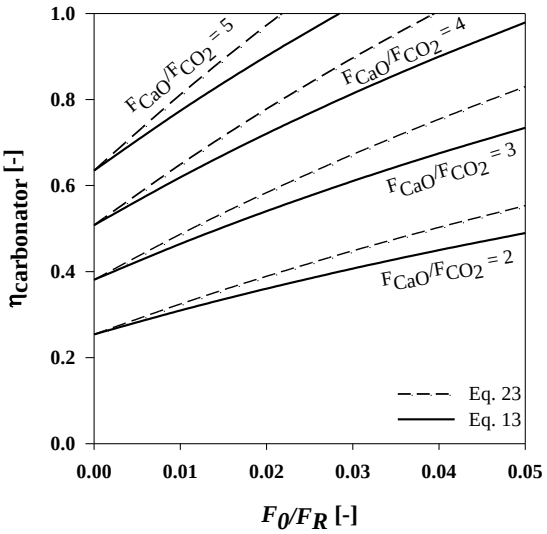

Figure B 15 The effect of change in make-up inlet stream location on carbonator efficiency: make-up into carbonator as in Figure B 1c, as per Eq. (B 43) and make-up into calciner as in Figure B 1a, as per Eq. (B 28) **($\frac{F_0''}{F_R''} = \frac{F_0}{F_R}$; X_i is described by Eq. (B 1), a = 0.787 and b = 0.127 from Table B 1).**

On the other hand, introducing the make-up flow in the carbonator rather than the calciner, as in Figure B 1c, may impact the average conversion because it introduces fresh sorbent at that point, and thus changes the particles' recirculation distribution in the solid flow. Thus fresh materials that have no sintering experience are added, and these can be carbonated if they contain CaO in an available form, such as in the case of synthetic CaO-based sorbents (i.e. *not*

$CaCO_3$-based) or CaO precursors less stable than $CaCO_3$ (e.g. $Ca(OH)_2$). The introduction of fresh sorbent can be treated mathematically by repeating the analysis that was used to derive r_i (vide supra). In this case, the result is a rather different form of the equation, which includes the fraction of solid sorbents that has circulated through the cycle zero times, as in Eq. (B 40). This addition necessitates including the particles with no calcination experience in particles' recirculation distribution formula, as in Eq. (B 41), and should increase the carbonator efficiency. This effect is shown in Figure B 15. In addition, like the case of comparing the effect of purge location, make-up location affects the actual flow-rate of circulating materials when operating at the target capture rate.

As shown in Figure B 15, locating the make-up stream in the carbonator would increase carbonation efficiency because of the very fast decay behavior of CaO. That is, the CO_2-uptake capacity of sorbent that has been calcined at high temperature ($T \geq 900$ °C) even once is significantly lower than that of sorbent that has not been calcined at high temperature. As the result, for $i = 0$, Eq. (B 1) yields $X_0 = a + b = 0.914$. Thus the make-up sorbent entering the carbonator in Figure B 1c, which has no high-temperature calcination experience, behaves as an improved sorbent with $\alpha = 0.225$ would in the case of make-up flow into the calciner as in Figure B 1b. Although the authors believe the mathematical representation presented here is correct, its practical use should be done with care to avoid 'double counting' in sorbent performance. Finally, one should bear in mind that this case is not practical for all types of sorbents: the fresh make-up flow should not require calcination before use. Setting aside material-specific issues, the four calcium-looping configurations shown in Figure B 1a–d can be compared for given values of capture rate and make-up ratio. Table B 3 compares the configurations in terms of material flow rates, energy penalty, and the conversion of sorbents,

for the case in which the total capture rate and make-up ratio are fixed at 90% and 1%, respectively.

Table B 3 Comparison of operating parameters for the four calcium-looping configurations shown in Figure B 1, when the target capture rate is fixed at 90%. [a]

Make-up ratio [-]	Config. as in Figure B 1	F_0 [ton/h]	F_R [ton/h]	Flow of solids into carbonator [ton/h]	Flow of solids into calciner [ton/h]	Total Coal into calciner [ton/h]	Carbonator efficiency, $\eta_{carbonator}$ [-]	Heat requirement ratio[b] [-]	$\frac{F_{CaO}}{F_{CO_2}}$ [-]	$\bar{X}$ [-]
0.01	a	56.43	5643	5699	6246	141.9	0.8461	0.3450	6.223	0.1360
	b	56.41	5641	5641	6244	142.6	0.8458	0.3461	6.221	0.1360
	c	53.16	5316	5369	5920	138.8	0.8473	0.3402	5.863	0.1445
	d	53.18	5318	5371	5922	138.1	0.8476	0.3390	5.865	0.1445
0.05	a	157.31	3146	3304	3756	117.9	0.8553	0.3044	3.470	0.2465
	b	157.06	3141	3141	3750	121.6	0.8539	0.3109	3.464	0.2465
	c	137.45	2749	2886	3359	115.9	0.8560	0.3008	3.032	0.2824
	d	137.67	2753	2891	3364	112.2	0.8574	0.2941	3.036	0.2824

[a] Eq. (B 3) is used as the reactivity decay model with values reported in Table B 1 and $N = 1000$. The results do not change with higher number of N. The reference plant is as described in Section 3.2. [b] $H_{Cal}/(H_{Cal} + H_{Plant})$.

As shown in Table B 3, changing the location of purge and make-up streams affected the efficiency of the capture plant; however, the effect was not large. Configuration d, in which make-up sorbent enters the carbonator and spent sorbent is purged from the calciner (Figure B 1d), was the most efficient method of using a specific sorbent in the capture plant in terms of heat requirement ratio. Similar results were achieved when make-up ratio was set at other values in the range 1–5%. For example, in case of 5% make-up, although heat requirement ratios decrease, the best configuration remains the same (i.e. configuration d in Figure B 1d).

B.3.4 Impurities

Neither the effect of sulfur components nor the presence of ash was included in the analysis presented above. These components have the potential to complicate estimates of the performance of different sorbents in a calcium looping system, irrespective of process parameters (F_0/F_R and F_{CaO}/F_{CO_2}) and the nature of sorbents used. For example, calcium sulfate

is formed when CaO is in contact with flue gas that contains sulfur components, and this occurs over a very wide temperature range (*286, 287*). Calcium sulfate is not easily separable from calcium carbonate and does not decompose at the calcination temperatures appropriate to calcium looping CO_2 capture (decomposition temperature at the partial pressure found in flue gas is 1230 °C) so it builds up in the recirculation stream. Ash may also accumulate, although it may be chemically inert, depending on source of ash (*288*), toward the components of a calcium looping system. However, with proper process engineering design measures (e.g. indirect heating (*285, 289*)) these impurities are manageable. It is worth noting that the proposed modifications are outside of the calcium looping cycle, leaving it mathematically intact. Therefore, the modified particles' recirculation distribution developed here (Eq. (B 27)) would remain valid for assessing the impact of different parameters on the process performance.

B.4 Conclusions

We modified a popular computational model that describes the population of particles in a circulating solid stream that have experienced the cycle i times in N^{th} cycle, in order to take into account particles that remain in the recirculation stream in a steady-state process (i.e. particles for which $i = N$). This formula is general for systems in which particles are being circulated; however, we have applied it to the case of CaO-based sorbents for CO_2 capture. For tailored sorbents that are more stable (and likely more expensive) than limestone, this fraction of particles can be quite significant, and therefore the model developed here leads to techno-economic conclusions that differ from those derived using an earlier model. In particular, we find that higher carbonator efficiencies are achievable with more minor improvements in sorbent performance, and that the stream costs associated with such a sorbent could be lower than those with CaO, despite the (potentially significantly) higher cost of the latter.

References

1. S. A. Arrhenius, On the influence of carbonic acid in the air upon the temperature of the ground. *Philos. Mag.* **41**, (1896).
2. E. L. Friis-christensen, K., Length of the Solar Cycle: An Indicator of Solar Activity Closely Associated with Climate. *Science* **254**, (1991).
3. H. Svensmark, E. Friis-Christensen, Variation of cosmic ray flux and global cloud coverage—a missing link in solar-climate relationships. *Journal of Atmospheric and Solar-Terrestrial Physics* **59**, 1225-1232 (1997).
4. B. Lin, B. A. Wielicki, L. H. Chambers, Y. Hu, K.-M. Xu, The Iris Hypothesis: A Negative or Positive Cloud Feedback? *Journal of Climate* **15**, 3-7 (2002).
5. N. Oreskes, The Scientific Consensus on Climate Change. *Science* **306** (2004).
6. R. K. Pachauri *et al.*, Climate Change 2014: Synthesis Report. Contribution of Working Groups I, II and III to the Fifth Assessment Report of the Intergovernmental Panel on Climate Change. (2014).
7. M. R. Raupach *et al.*, The relationship between peak warming and cumulative CO_2 emissions, and its use to quantify vulnerabilities in the carbon–climate–human system. *Tellus B* **63B**, 19 (2011).
8. T. F. Stocker;, The Closing Door of Climate Targets. *Science* **339**, 3 (2013).
9. IEA, "Energy technology perspectives: Pathways to a clean energy system," (OECD/IEA, 2012).
10. "The global status of CCS," (Global CCS Institute, 2013).
11. M. Meinshausen, What does a 2 °C target mean for greenhouse gas concentrations? A brief analysis based on multi-gas emission pathways and several climate sensitivity uncertainty estimates. *Avoiding dangerous climate change* **270**, (2006).
12. IPCC, "Climate Change 2007: Synthesis Report. Contribution of Working Groups I, II and III to the Fourth Assessment Report of the Intergovernmental Panel on Climate Change," (Geneva, Switzerland, 2007).
13. G. J. O. G. Jos, Janssens-Maenhout; Marilena, Muntean; Jeroen, Peters, A.H.W. , "Trends In Global CO_2 Emissions," (PBL Netherlands Environmental Assesment Agency, 2013).
14. M. den Elzen, M. Meinshausen, D. van Vuuren, Multi-gas emission envelopes to meet greenhouse gas concentration targets: costs versus certainty of limiting temperature increase. *Global Environmental Change* **17**, 260-280 (2007).
15. D. W. Keith, Why Capture CO_2 from the Atmosphere? *Science* **325**, 2 (2009).
16. D. W. Keith, E. Parson, M. G. Morgan, Research on global sun block needed now. *Nature* **463**, 426-427 (2010).
17. S. Barrett, The incredible economics of geoengineering. *Environmental and resource economics* **39**, 45-54 (2008).

18. Z. Khorshidi, M. T. Ho, D. E. Wiley, The impact of biomass quality and quantity on the performance and economics of co-firing plants with and without CO_2 capture. *International Journal of Greenhouse Gas Control* **21**, 191-202 (2014).

19. K. Möllersten, J. Yan, J. R. Moreira, Potential market niches for biomass energy with CO_2 capture and storage—opportunities for energy supply with negative CO_2 emissions. *Biomass and Bioenergy* **25**, 273-285 (2003).

20. J. S. Lehmann, Joseph;, *Biochar for Environmental Management: Science and Technology*. (Earthscan, 2009).

21. R. D. Schuiling, P. Krijgsman, Enhanced Weathering: An Effective and Cheap Tool to Sequester CO_2. *Climatic Change* **74**, 349-354 (2006).

22. S. C. Roy, O. K. Varghese, M. Paulose, C. A. Grimes, Toward Solar Fuels: Photocatalytic Conversion of Carbon Dioxide to Hydrocarbons. *ACS Nano* **4**, 1259-1278 (2010).

23. C. Song, Global challenges and strategies for control, conversion and utilization of CO_2 for sustainable development involving energy, catalysis, adsorption and chemical processing. *Catalysis Today* **115**, 2-32 (2006).

24. N. S. Lewis, D. G. Nocera, Powering the planet: Chemical challenges in solar energy utilization. *Proceedings of the National Academy of Sciences* **103**, 15729-15735 (2006).

25. solargis, Last accessed on: Dec. 9 2015, http://solargis.info/imaps/

26. "Australian PV market since April 2001", Last accessed on: Dec. 9 2015, http://pv-map.apvi.org.au/analyses

27. K. S. Joya, Y. F. Joya, K. Ocakoglu, R. van de Krol, Water-Splitting Catalysis and Solar Fuel Devices: Artificial Leaves on the Move. *Angewandte Chemie International Edition* **52**, 10426-10437 (2013).

28. D. Chen, X. Zhang, A. F. Lee, Synthetic strategies to nanostructured photocatalysts for CO_2 reduction to solar fuels and chemicals. *Journal of Materials Chemistry A*, (2015).

29. P. Lanzafame, G. Centi, S. Perathoner, Catalysis for biomass and CO_2 use through solar energy: opening new scenarios for a sustainable and low-carbon chemical production. *Chemical Society Reviews* **43**, 7562-7580 (2014).

30. S. Das, W. W. Daud, A review on advances in photocatalysts towards CO_2 conversion. *Rsc Advances* **4**, 20856-20893 (2014).

31. W. C. Chueh *et al.*, High-Flux Solar-Driven Thermochemical Dissociation of CO2 and H2O Using Nonstoichiometric Ceria. *Science* **330**, 1797-1801 (2010).

32. B. Kumar *et al.*, Photochemical and photoelectrochemical reduction of CO_2. *Annual review of physical chemistry* **63**, 541-569 (2012).

33. C. Ampelli, R. Passalacqua, C. Genovese, S. Perathoner, G. Centi, A novel photo-electrochemical approach for the chemical recycling of carbon dioxide to fuels. *CHEMICAL ENGINEERING* **25**, (2011).

34. C. Ampelli *et al.*, An Electrochemical Reactor for the CO_2 Reduction in Gas Phase by Using Conductive Polymer Based Electrocatalysts. *CHEMICAL ENGINEERING* **41**, (2014).

35. S. Bensaid, G. Centi, E. Garrone, S. Perathoner, G. Saracco, Towards artificial leaves for solar hydrogen and fuels from carbon dioxide. *ChemSusChem* **5**, 500-521 (2012).

36. J. Schneider, H. Jia, J. T. Muckerman, E. Fujita, Thermodynamics and kinetics of CO_2, CO, and H^+ binding to the metal centre of CO_2 reduction catalysts. *Chemical Society Reviews* **41**, 2036-2051 (2012).

37. Y. Hori *et al.*, "Deactivation of copper electrode" in electrochemical reduction of CO_2. *Electrochimica acta* **50**, 5354-5369 (2005).

38. M. Azuma, K. Hashimoto, M. Hiramoto, M. Watanabe, T. Sakata, Electrochemical Reduction of Carbon Dioxide on Various Metal Electrodes in Low-Temperature Aqueous $KHCO_3$ Media. *Journal of the Electrochemical Society* **137**, 1772-1778 (1990).

39. L. Yang, H. Wang, Recent Advances in Carbon Dioxide Capture, Fixation, and Activation by using N-Heterocyclic Carbenes. *ChemSusChem* **7**, 962-998 (2014).

40. S. Perathoner, G. Centi, D. Su, Turning Perspective in Photoelectrocatalytic Cells for Solar Fuels. *ChemSusChem*, n/a-n/a (2015).

41. C. Ampelli *et al.*, Electrocatalytic conversion of CO_2 to produce solar fuels in electrolyte or electrolyte-less configurations of PEC cells. *Faraday discussions* **183**, 125-145 (2015).

42. C. Genovese, C. Ampelli, S. Perathoner, G. Centi, Electrocatalytic conversion of CO_2 on carbon nanotube-based electrodes for producing solar fuels. *Journal of Catalysis* **308**, 237-249 (2013).

43. D. W. Dewulf, A. J. Bard, The electrochemical reduction of CO_2 to CH_4 and C_2H_4 at Cu/Nafion electrodes (solid polymer electrolyte structures). *Catalysis letters* **1**, 73-79 (1988).

44. R. L. Cook, A. F. Sammells. (Google Patents, 1990).

45. C. Ampelli *et al.*, CO_2 capture and reduction to liquid fuels in a novel electrochemical setup by using metal-doped conjugated microporous polymers. *Journal of Applied Electrochemistry*, 701-713 (2015).

46. C. Ampelli, G. Centi, R. Passalacqua, S. Perathoner, Synthesis of solar fuels by a novel photoelectrocatalytic approach. *Energy & Environmental Science* **3**, 292-301 (2010).

47. G. Centi, S. Perathoner, G. Winè, M. Gangeri, Electrocatalytic conversion of CO_2 to long carbon-chain hydrocarbons. *Green Chemistry* **9**, 671-678 (2007).

48. C. Ampelli, G. Centi, R. Passalacqua, S. Perathoner, Electrolyte-less design of PEC cells for solar fuels: Prospects and open issues in the development of cells and related catalytic electrodes. *Catalysis Today* **259**, 246-258 (2016).

49. A. J. Traynor, R. J. Jensen, Direct solar reduction of CO_2 to fuel: first prototype results. *Industrial & engineering chemistry research* **41**, 1935-1939 (2002).

50. P. G. Loutzenhiser, M. E. Gálvez, I. Hischier, A. Graf, A. Steinfeld, CO_2 splitting in an aerosol flow reactor via the two-step Zn/ZnO solar thermochemical cycle. *Chemical Engineering Science* **65**, 1855-1864 (2010).

51. P. Furler, J. R. Scheffe, A. Steinfeld, Syngas production by simultaneous splitting of H_2O and CO_2 via ceria redox reactions in a high-temperature solar reactor. *Energy & Environmental Science* **5**, 6098-6103 (2012).

52. K. R. Thampi, J. Kiwi, M. Graetzel, Methanation and photo-methanation of carbon dioxide at room temperature and atmospheric pressure. *Nature* **327**, 506-508 (1987).

53. F. Saladin, L. Forss, I. Kamber, Photosynthesis of CH_4 at a TiO_2 surface from gaseous H_2O and CO_2. *J. Chem. Soc., Chem. Commun.*, 533-534 (1995).

54. M. Anpo, H. Yamashita, Y. Ichihashi, Y. Fujii, M. Honda, Photocatalytic reduction of CO_2 with H_2O on titanium oxides anchored within micropores of zeolites: effects of the structure of the active sites and the addition of Pt. *The Journal of Physical Chemistry B* **101**, 2632-2636 (1997).

55. N. Ulagappan, H. Frei, Mechanistic study of CO_2 photoreduction in Ti silicalite molecular sieve by FT-IR spectroscopy. *The Journal of Physical Chemistry A* **104**, 7834-7839 (2000).

56. K. Ikeue, S. Nozaki, M. Ogawa, M. Anpo, Photocatalytic reduction of CO_2 with H_2O on Ti-containing porous silica thin film photocatalysts. *Catalysis letters* **80**, 111-114 (2002).

57. S. S. Tan, L. Zou, E. Hu, Photocatalytic reduction of carbon dioxide into gaseous hydrocarbon using TiO 2 pellets. *Catalysis Today* **115**, 269-273 (2006).

58. X.-H. Xia *et al.*, Preparation of multi-walled carbon nanotube supported TiO_2 and its photocatalytic activity in the reduction of CO_2 with H_2O. *Carbon* **45**, 717-721 (2007).

59. J. C. Wu, T.-H. Wu, T. Chu, H. Huang, D. Tsai, Application of optical-fiber photoreactor for CO_2 photocatalytic reduction. *Topics in Catalysis* **47**, 131-136 (2008).

60. O. K. Varghese, M. Paulose, T. J. LaTempa, C. A. Grimes, High-rate solar photocatalytic conversion of CO_2 and water vapor to hydrocarbon fuels. *Nano letters* **9**, 731-737 (2009).

61. C. Wang, R. L. Thompson, J. Baltrus, C. Matranga, Visible light photoreduction of CO_2 using CdSe/Pt/TiO_2 heterostructured catalysts. *The Journal of Physical Chemistry Letters* **1**, 48-53 (2009).

62. S. Xie, Y. Wang, Q. Zhang, W. Deng, Y. Wang, MgO-and Pt-Promoted TiO2 as an Efficient Photocatalyst for the Preferential Reduction of Carbon Dioxide in the Presence of Water. *ACS Catalysis* **4**, 3644-3653 (2014).

63. S. Ichikawa, Chemical conversion of carbon dioxide by catalytic hydrogenation and room temperature photoelectrocatalysis. *Energy conversion and management* **36**, 613-616 (1995).

64. G. Centi, S. Perathoner, Z. S. Rak, Reduction of greenhouse gas emissions by catalytic processes. *Applied Catalysis B: Environmental* **41**, 143-155 (2003).

65. G. Centi, S. Perathoner, in *Handbook of Climate Change Mitigation*. (Springer, 2012), pp. 1849-1890.

66. C. Genovese *et al.*, Electrocatalytic reduction of CO_2 for the production of fuels: A comparison between liquid and gas phase conditions. *Chemical Engineering Transactions* **43**, 2281-2286 (2015).

67. S. N. Habisreutinger, L. Schmidt-Mende, J. K. Stolarczyk, Photocatalytic reduction of CO_2 on TiO_2 and other semiconductors. *Angewandte Chemie International Edition* **52**, 7372-7408 (2013).

68. T. Sakakura, J.-C. Choi, H. Yasuda, Transformation of carbon dioxide. *Chemical Reviews* **107**, 2365-2387 (2007).

69. G. A. Olah, A. Goeppert, G. S. Prakash, Chemical recycling of carbon dioxide to methanol and dimethyl ether: from greenhouse gas to renewable, environmentally carbon neutral fuels and synthetic hydrocarbons. *The Journal of organic chemistry* **74**, 487-498 (2008).

70. M. Kibria, Z. Mi, Artificial photosynthesis using metal/nonmetal-nitride semiconductors: current status, prospects, and challenges. *Journal of Materials Chemistry A*, (2016).

71. J. Li, N. Wu, Semiconductor-based photocatalysts and photoelectrochemical cells for solar fuel generation: a review. *Catalysis Science & Technology* **5**, 1360-1384 (2015).

72. M. Gattrell, N. Gupta, A. Co, A review of the aqueous electrochemical reduction of CO2 to hydrocarbons at copper. *J. Electroanal. Chem.* **594**, 1-19 (2006).

73. J. Qiao, Y. Liu, F. Hong, J. Zhang, A review of catalysts for the electroreduction of carbon dioxide to produce low-carbon fuels. *Chemical Society Reviews* **43**, 631-675 (2014).

74. T. R. Cook *et al.*, Solar energy supply and storage for the legacy and nonlegacy worlds. *Chemical reviews* **110**, 6474-6502 (2010).

75. C. Ampelli, S. Perathoner, G. Centi, CO_2 utilization: an enabling element to move to a resource-and energy-efficient chemical and fuel production. *Philosophical Transactions of the Royal Society of London A: Mathematical, Physical and Engineering Sciences* **373**, 20140177 (2015).

76. M. Grätzel, Photoelectrochemical cells. *Nature* **414**, 338-344 (2001).

77. D. Tryk, A. Fujishima, K. Honda, Recent topics in photoelectrochemistry: achievements and future prospects. *Electrochimica acta* **45**, 2363-2376 (2000).

78. S. Ichikawa, R. Doi, Hydrogen production from water and conversion of carbon dioxide to useful chemicals by room temperature photoelectrocatalysis. *Catalysis Today* **27**, 271-277 (1996).

79. W. Dai *et al.*, A review on water balance in the membrane electrode assembly of proton exchange membrane fuel cells. *International Journal of Hydrogen Energy* **34**, 9461-9478 (2009).

80. A. West, T. Fuller, Influence of rib spacing in proton-exchange membrane electrode assemblies. *Journal of applied electrochemistry* **26**, 557-565 (1996).

81. V. Mehta, J. S. Cooper, Review and analysis of PEM fuel cell design and manufacturing. *Journal of Power Sources* **114**, 32-53 (2003).

82. C.-Y. Liu, C.-C. Sung, A review of the performance and analysis of proton exchange membrane fuel cell membrane electrode assemblies. *Journal of Power Sources* **220**, 348-353 (2012).

83. Spaceline, Last accessed on: Jan. 06 2016, http://www.spaceline.org/flightchron/gemini5.html

84. P. Basore, Numerical modeling of textured silicon solar cells using PC-1D. *Electron Devices, IEEE Transactions on* **37**, 337-343 (1990).

85. J. B. Ballengee, Vanderbilt University Nashville, Tennessee, USA (2013).

86. D. Giancoli, J. Phillips, in *Physics for Scientists and Engineers with Modern Physics*. (1984), pp. 658.

87. G. Guan, T. Kida, A. Yoshida, Reduction of carbon dioxide with water under concentrated sunlight using photocatalyst combined with Fe-based catalyst. *Applied Catalysis B: Environmental* **41**, 387-396 (2003).

88. E. E. Barton, D. M. Rampulla, A. B. Bocarsly, Selective solar-driven reduction of CO_2 to methanol using a catalyzed p-GaP based photoelectrochemical cell. *Journal of the American Chemical Society* **130**, 6342-6344 (2008).

89. in *Handbook of Photovoltaic Science and Engineering*, A. H. Luque, Steven;, Ed. (John Wiley & Sons, 2011), chap. 12.

90. S. Y. Reece *et al.*, Wireless Solar Water Splitting Using Silicon-Based Semiconductors and Earth-Abundant Catalysts. *Science* **334**, 645-648 (2011).

91. R. E. Rocheleau, E. L. Miller, A. Misra, High-Efficiency Photoelectrochemical Hydrogen Production Using Multijunction Amorphous Silicon Photoelectrodes. *Energy & Fuels* **12**, 3-10 (1998).

92. Y. Yamada *et al.*, One chip photovoltaic water electrolysis device. *International Journal of Hydrogen Energy* **28**, 1167-1169 (2003).

93. M. Jitaru, D. Lowy, M. Toma, B. Toma, L. Oniciu, Electrochemical reduction of carbon dioxide on flat metallic cathodes. *Journal of Applied Electrochemistry* **27**, 875-889 (1997).

94. W. Wang, S. Wang, X. Ma, J. Gong, Recent advances in catalytic hydrogenation of carbon dioxide. *Chemical Society Reviews* **40**, 3703-3727 (2011).

95. Y. Liu, D. Liu, Study of bimetallic Cu–Ni/γ-Al_2O_3 catalysts for carbon dioxide hydrogenation. *International Journal of Hydrogen Energy* **24**, 351-354 (1999).

96. F. Stone, D. Waller, Cu–ZnO and Cu–ZnO/Al2O3 Catalysts for the Reverse Water-Gas Shift Reaction. The Effect of the Cu/Zn Ratio on Precursor Characteristics and on the Activity of the Derived Catalysts. *Topics in Catalysis* **22**, 305-318 (2003).

97. C. W. Li, M. W. Kanan, CO_2 Reduction at Low Overpotential on Cu Electrodes Resulting from the Reduction of Thick Cu_2O Films. *Journal of the American Chemical Society* **134**, 7231-7234 (2012).

98. J. F. d. Brito, A. A. d. Silva, A. J. Cavalheiro, M. V. Boldrin Zanoni, Evaluation of the Parameters Affecting the Photoelectrocatalytic Reduction of CO_2 to CH_3OH at Cu/Cu_2O Electrode. *International Journal Of Electrochemical Science*, 5961-5973 (2014).

99. V. Palanichamy *et al.*, Reduction of CO_2 to Methanol in Photoelectrochemical Cell: CM-n-TiO_2/Cu. *ECS Transactions* **53**, 47-54 (2013).

100. H. Yano, F. Shirai, M. Nakayama, K. Ogura, Efficient electrochemical conversion of CO_2 to CO, C_2H_4 and CH_4 at a three-phase interface on a Cu net electrode in acidic solution. *Journal of Electroanalytical Chemistry* **519**, 93-100 (2002).

101. S. Wasmus, E. Cattaneo, W. Vielstich, Reduction of carbon dioxide to methane and ethene—an on-line MS study with rotating electrodes. *Electrochimica acta* **35**, 771-775 (1990).

102. Q. Li *et al.*, Growth of adlayer graphene on Cu studied by carbon isotope labeling. *Nano letters* **13**, 486-490 (2013).

103. J. KwangáLee, Insights into an autonomously formed oxygen-evacuated Cu_2O electrode for the selective production of C_2H_4 from CO_2. *Physical Chemistry Chemical Physics* **17**, 824-830 (2015).

104. J. Lee, Y. Tak, Electrocatalytic activity of Cu electrode in electroreduction of CO_2. *Electrochimica acta* **46**, 3015-3022 (2001).

105. X. Tao *et al.*, Thermal CVD synthesis of carbon nanotubes filled with single-crystalline Cu nanoneedles at tips. *Diamond and related materials* **15**, 1271-1275 (2006).

106. Y. Yamazaki *et al.*, Synthesis of a closely packed carbon nanotube forest by a multi-step growth method using plasma-based chemical vapor deposition. *Applied physics express* **3**, 055002 (2010).

107. X. Li *et al.*, Large-area synthesis of high-quality and uniform graphene films on copper foils. *Science* **324**, 1312-1314 (2009).

108. S. Bhaviripudi, X. Jia, M. S. Dresselhaus, J. Kong, Role of kinetic factors in chemical vapor deposition synthesis of uniform large area graphene using copper catalyst. *Nano letters* **10**, 4128-4133 (2010).

109. A. Guermoune *et al.*, Chemical vapor deposition synthesis of graphene on copper with methanol, ethanol, and propanol precursors. *Carbon* **49**, 4204-4210 (2011).

110. Y. Hori, in *Modern aspects of electrochemistry*. (Springer, 2008), pp. 89-189.

111. Y. Hori, K. Kikuchi, S. Suzuki, Production of CO and CH 4 in electrochemical reduction of CO 2 at metal electrodes in aqueous hydrogencarbonate solution. *Chemistry Letters* **14**, 1695-1698 (1985).

112. H. Noda *et al.*, Electrochemical reduction of carbon dioxide at various metal electrodes in aqueous potassium hydrogen carbonate solution. *Bulletin of the Chemical Society of Japan* **63**, 2459-2462 (1990).

113. K. Hara, A. Kudo, T. Sakata, Electrochemical reduction of carbon dioxide under high pressure on various electrodes in an aqueous electrolyte. *Journal of Electroanalytical Chemistry* **391**, 141-147 (1995).

114. M. Azuma, K. Hashimoto, M. Hiramoto, M. Watanabe, T. Sakata, Carbon dioxide reduction at low temperature on various metal electrodes. *Journal of electroanalytical chemistry and interfacial electrochemistry* **260**, 441-445 (1989).

115. J. F. de Brito, A. R. Araujo, K. Rajeshwar, M. V. B. Zanoni, Photoelectrochemical reduction of CO_2 on Cu/Cu_2O films: Product distribution and pH effects. *Chemical Engineering Journal* **264**, 302-309 (2015).

116. K. Rajeshwar, N. R. de Tacconi, G. Ghadimkhani, W. Chanmanee, C. Janáky, Tailoring Copper Oxide Semiconductor Nanorod Arrays for Photoelectrochemical Reduction of Carbon Dioxide to Methanol. *ChemPhysChem* **14**, 2251-2259 (2013).

117. G. Ghadimkhani, N. R. de Tacconi, W. Chanmanee, C. Janaky, K. Rajeshwar, Efficient solar photoelectrosynthesis of methanol from carbon dioxide using hybrid CuO-Cu_2O semiconductor nanorod arrays. *Chemical Communications* **49**, 1297-1299 (2013).

118. M. Jitaru, Electrochemical carbon dioxide reduction-fundamental and applied topics. *Journal of the University of chemical Technology and Metallurgy* **42**, 333-344 (2007).

119. B. A. Rosen *et al.*, Ionic liquid–mediated selective conversion of CO_2 to CO at low overpotentials. *Science* **334**, 643-644 (2011).

120. X.-W. Liu, W.-W. Li, H.-Q. Yu, Cathodic catalysts in bioelectrochemical systems for energy recovery from wastewater. *Chemical Society Reviews* **43**, 7718-7745 (2014).

121. T. Inoue, A. Fujishima, S. Konishi, K. Honda, Photoelectrocatalytic reduction of carbon dioxide in aqueous suspensions of semiconductor powders. *Nature* **277**, 637-638 (1979).

122. N. L. Allinger, Conformational analysis. 130. MM2. A hydrocarbon force field utilizing V1 and V2 torsional terms. *Journal of the American Chemical Society* **99**, 8127-8134 (1977).

123. C. R. Corbeil, N. Moitessier, Theory and application of medium to high throughput prediction method techniques for asymmetric catalyst design. *Journal of Molecular Catalysis A: Chemical* **324**, 146-155 (2010).

124. L. Zhao, J. Gao, C. Xu, Methods and applications of molecular simulation in catalyst research. *Petroleum science and technology* **24**, 1395-1415 (2006).

125. G. A. Somorjai, Y. Li, *Introduction to surface chemistry and catalysis*. (John Wiley & Sons, 2010).

126. P. Du, R. Eisenberg, Catalysts made of earth-abundant elements (Co, Ni, Fe) for water splitting: recent progress and future challenges. *Energy & Environmental Science* **5**, 6012-6021 (2012).

127. Q. Yin *et al.*, A fast soluble carbon-free molecular water oxidation catalyst based on abundant metals. *Science* **328**, 342-345 (2010).

128. M. W. Kanan, Y. Surendranath, D. G. Nocera, Cobalt–phosphate oxygen-evolving compound. *Chemical Society Reviews* **38**, 109-114 (2009).

129. M. W. Kanan *et al.*, Structure and valency of a cobalt− phosphate water oxidation catalyst determined by in situ X-ray spectroscopy. *Journal of the American Chemical Society* **132**, 13692-13701 (2010).

130. D. A. Lutterman, Y. Surendranath, D. G. Nocera, A self-healing oxygen-evolving catalyst. *Journal of the American Chemical Society* **131**, 3838-3839 (2009).

131. Y. Surendranath, M. Dinca, D. G. Nocera, Electrolyte-dependent electrosynthesis and activity of cobalt-based water oxidation catalysts. *Journal of the American Chemical Society* **131**, 2615-2620 (2009).

132. M. D. Symes, Y. Surendranath, D. A. Lutterman, D. G. Nocera, Bidirectional and unidirectional PCET in a molecular model of a cobalt-based oxygen-evolving catalyst. *Journal of the American Chemical Society* **133**, 5174-5177 (2011).

133. A. Gasparotto *et al.*, F-doped Co_3O_4 photocatalysts for sustainable H_2 generation from water/ethanol. *Journal of the American Chemical Society* **133**, 19362-19365 (2011).

134. M. W. Kanan, D. G. Nocera, In situ formation of an oxygen-evolving catalyst in neutral water containing phosphate and Co^{2+}. *Science* **321**, 1072-1075 (2008).

135. A. J. Esswein, M. J. McMurdo, P. N. Ross, A. T. Bell, T. D. Tilley, Size-dependent activity of Co_3O_4 nanoparticle anodes for alkaline water electrolysis. *The Journal of Physical Chemistry C* **113**, 15068-15072 (2009).

136. F. Jiao, H. Frei, Nanostructured Cobalt Oxide Clusters in Mesoporous Silica as Efficient Oxygen-Evolving Catalysts. *Angewandte Chemie International Edition* **48**, 1841-1844 (2009).

137. Y. Liang *et al.*, Co_3O_4 nanocrystals on graphene as a synergistic catalyst for oxygen reduction reaction. *Nature Materials* **10**, 780-786 (2011).

138. C.-S. Cheng, M. Serizawa, H. Sakata, T. Hirayama, Electrical conductivity of Co3O4 films prepared by chemical vapour deposition. *Mater. Chem. Phys.* **53**, 225-230 (1998).

139. X. Wang *et al.*, One-Dimensional Arrays of Co3O4 Nanoparticles: Synthesis, Characterization, and Optical and Electrochemical Properties. *The Journal of Physical Chemistry B* **108**, 16401-16404 (2004).

140. M. A. Hickner, H. Ghassemi, Y. S. Kim, B. R. Einsla, J. E. McGrath, Alternative polymer systems for proton exchange membranes (PEMs). *Chemical reviews* **104**, 4587-4612 (2004).

141. M. F. H. S. and, W. H. Meyer, Anhydrous Proton-Conducting Polymers. *Annual Review of Materials Research* **33**, 233-261 (2003).

142. H. Iwahara, Proton conducting ceramics and their applications. *Solid State Ionics* **86**, 9-15 (1996).

143. K. Kreuer, Proton-conducting oxides. *Annual Review of Materials Research* **33**, 333-359 (2003).

144. G. Inzelt, M. Pineri, J. W. Schultze, M. A. Vorotyntsev, Electron and proton conducting polymers: recent developments and prospects. *Electrochimica Acta* **45**, 2403-2421 (2000).

145. P. J. Choi, Nikhil H.; Datta, Ravindra;, Thermodynamics and Proton Transport in Nafion II. Proton Diffusion Mechanisms and Conductivity. *Journal of Electrochemical Society* **152**, 7 (2005).

146. H. Chen, J. D. Snyder, Y. A. Elabd, Electrospinning and Solution Properties of Nafion and Poly(acrylic acid). *Macromolecules* **41**, 128-135 (2007).

147. B. Dong, L. Gwee, D. Salas-de la Cruz, K. I. Winey, Y. A. Elabd, Super Proton Conductive High-Purity Nafion Nanofibers. *Nano Letters* **10**, 3785-3790 (2010).

148. J. B. Ballengee , P. N. Pintauro, Morphological Control of Electrospun Nafion Nanofiber Mats. *Journal of Electrochemical Society* **158**, 4 (2011).

149. M. Köntges, I. Kunze, S. Kajari-Schröder, X. Breitenmoser, B. Bjørneklett, in *25th European Photovoltaic Solar Energy Conference, Valencia, Spain*. (2010).

150. B. Feng, H. An, E. Tan, Screening of CO_2 Adsorbing Materials for Zero Emission Power Generation Systems. *Energy & Fuels* **21**, 426-434 (2007).

151. W. Yue, W. Zhou, Porous crystals of cubic metal oxides templated by cage-containing mesoporous silica. *Journal of Materials Chemistry* **17**, 4947-4952 (2007).

152. P. Scherrer, Bestimmung der Grösse und der inneren Struktur von Kolloidteilchen mittels Röntgenstrahlen. *Nachrichten von der Gesellschaft der Wissenschaften zu Göttingen, mathematisch-physikalische Klasse* **1918**, 98-100 (1918).

153. U. Holzwarth, N. Gibson, The Scherrer equation versus the 'Debye-Scherrer equation'. *Nat Nano* **6**, 534-534 (2011).

154. J. B. Ballengee, Vanderbilt University, (2013).

155. Y. Sone, P. Ekdunge, D. Simonsson, Proton Conductivity of Nafion 117 as Measured by a Four-Electrode AC Impedance Method. *Journal of the Electrochemical Society* **143**, 1254-1259 (1996).

156. P. Choi, N. H. Jalani, R. Datta, Thermodynamics and proton transport in Nafion II. Proton diffusion mechanisms and conductivity. *Journal of the Electrochemical Society* **152**, E123-E130 (2005).

157. P. Choi, N. H. Jalani, R. Datta, Thermodynamics and proton transport in nafion i. membrane swelling, sorption, and ion-exchange equilibrium. *Journal of The Electrochemical Society* **152**, E84-E89 (2005).

158. T. Awatani, H. Midorikawa, N. Kojima, J. Ye, C. Marcott, Morphology of water transport channels and hydrophobic clusters in nafion from high spatial resolution afm-ir spectroscopy and imaging. *Electrochemistry Communications* **30**, 5-8 (2013).

159. K. Schmidt-Rohr, Q. Chen, Parallel cylindrical water nanochannels in Nafion fuel-cell membranes. *Nature materials* **7**, 75-83 (2008).

160. T. Mabuchi, T. Tokumasu, Molecular Dynamics Study of Proton Transport in Modeled Water Cluster Structure of Polymer Electrolyte Membrane. *ECS Transactions* **69**, 723-729 (2015).

161. Z. Qi, A. Kaufman, Low Pt loading high performance cathodes for PEM fuel cells. *Journal of Power Sources* **113**, 37-43 (2003).

162. A. L. Buck, New Equations for Computing Vapor Pressure and Enhancement Factor. *Journal of Applied Meteorology* **20**, 1527-1532 (1981).

163. J. J. Sargianis, (2010).

164. P. C. Rieke, N. E. Vanderborgh, Temperature dependence of water content and proton conductivity in polyperfluorosulfonic acid membranes. *Journal of membrane Science* **32**, 313-328 (1987).

165. D. Shallcross, *Handbook of Psychrometric Charts: Humidity diagrams for engineers*. (Springer Science & Business Media, 2012).

166. J. Choi *et al.*, High Conductivity Perfluorosulfonic Acid Nanofiber Composite Fuel-Cell Membranes. *ChemSusChem* **3**, 1245-1248 (2010).

167. E. Skoplaki, J. Palyvos, On the temperature dependence of photovoltaic module electrical performance: A review of efficiency/power correlations. *Solar energy* **83**, 614-624 (2009).

168. H.-C. Hsu *et al.*, Graphene oxide as a promising photocatalyst for CO_2 to methanol conversion. *Nanoscale* **5**, 262-268 (2013).

169. Y. Zhang *et al.*, Preparation of graphene from Taixi anthracite and its photocatalyst performance for CO_2 conversion. *Proceedings of the Institution of Mechanical Engineers, Part N: Journal of Nanoengineering and Nanosystems*, 1740349913489278 (2013).

170. J. Cheng *et al.*, Photoelectrocatalytic Reduction of CO_2 into Chemicals Using Pt-Modified Reduced Graphene Oxide Combined with Pt-Modified TiO_2 Nanotubes. *Environmental science & technology* **48**, 7076-7084 (2014).

171. N. Tanchoux, S. Pariente, P. Trens, F. Fajula, Confinement and curvature effects as a tool for selectivity orientation in heterogeneous catalysis: Isomerisation of n-hexene over MCM-41-type catalysts. *Journal of Molecular Catalysis A: Chemical* **305**, 8-15 (2009).

172. S. Pariente, P. Trens, F. Fajula, F. Di Renzo, N. Tanchoux, Heterogeneous catalysis and confinement effects: the isomerization of 1-hexene on MCM-41 materials. *Applied Catalysis A: General* **307**, 51-57 (2006).

173. R. Fu *et al.*, XPS study of copper-doped carbon aerogels. *Langmuir* **18**, 10100-10104 (2002).

174. zygo, "Optical Profiler Basics", Last accessed on: 15 Jan. 2016, http://www.zygo.com/?/met/profilers/opticalprofilersabout.htm

175. M. Seah, The quantitative analysis of surfaces by XPS: a review. *Surf. Interface Anal.* **2**, 222-239 (1980).

176. S. Poulston, P. Parlett, P. Stone, M. Bowker, Surface oxidation and reduction of CuO and Cu2O studied using XPS and XAES. *Surf. Interface Anal.* **24**, 811-820 (1996).

177. C. R. Houck, J. Joines, M. G. Kay, A genetic algorithm for function optimization: a Matlab implementation. *NCSU-IE TR* **95**, (1995).

178. D. Umadevi, G. N. Sastry, Molecular and Ionic Interaction with Graphene Nanoflakes: A Computational Investigation of CO_2, H_2O, Li, Mg, Li^+, and Mg^{2+} Interaction with Polycyclic Aromatic Hydrocarbons. *The Journal of Physical Chemistry C* **115**, 9656-9667 (2011).

179. A. V. Naumkin, A. Kraut-Vass, S. W. Gaarenstroom, C. J. Powell. (National Institute of Standards and Technology, Gaithersburg, 2012).

180. D. Yang *et al.*, Chemical analysis of graphene oxide films after heat and chemical treatments by X-ray photoelectron and Micro-Raman spectroscopy. *Carbon* **47**, 145-152 (2009).

181. B. Marchon, J. Carrazza, H. Heinemann, G. Somorjai, TPD and XPS studies of O_2, CO_2, and H_2O adsorption on clean polycrystalline graphite. *Carbon* **26**, 507-514 (1988).

182. A. C. Ferrari, J. Robertson, Interpretation of Raman spectra of disordered and amorphous carbon. *Physical review B* **61**, 14095 (2000).

183. T. Leung *et al.*, Determination of the sp^3/sp^2 ratio of aC: H by XPS and XAES. *Journal of non-crystalline solids* **254**, 156-160 (1999).

184. L. Wang, R. Zhang, U. Jansson, N. Nedfors, A near-wearless and extremely long lifetime amorphous carbon film under high vacuum. *Scientific Reports* **5**, 11119 (2015).

185. J. Filik, P. May, S. Pearce, R. Wild, K. Hallam, XPS and laser Raman analysis of hydrogenated amorphous carbon films. *Diamond and related Materials* **12**, 974-978 (2003).

186. M. Weiler *et al.*, Preparation and properties of highly tetrahedral hydrogenated amorphous carbon. *Physical Review B* **53**, 1594 (1996).

187. M. Ramsteiner, J. Wagner, Resonant Raman scattering of hydrogenated amorphous carbon: Evidence for π-bonded carbon clusters. *Applied physics letters* **51**, 1355-1357 (1987).

188. I. Oda, H. Ogasawara, M. Ito, Carbon monoxide adsorption on copper and silver electrodes during carbon dioxide electroreduction studied by infrared reflection absorption spectroscopy and surface-enhanced Raman spectroscopy. *Langmuir* **12**, 1094-1097 (1996).

189. Y. Hori, O. Koga, H. Yamazaki, T. Matsuo, Infrared spectroscopy of adsorbed CO and intermediate species in electrochemical reduction of CO_2 to hydrocarbons on a Cu electrode. *Electrochimica acta* **40**, 2617-2622 (1995).

190. D. Lin-Vien, N. B. Colthup, W. G. Fateley, J. G. Grasselli, *The handbook of infrared and Raman characteristic frequencies of organic molecules*. (Elsevier, 1991).

191. S. Liu, S. Gangopadhyay, G. Sreenivas, S. Ang, H. Naseem, Infrared studies of hydrogenated amorphous carbon (aC: H) and its alloys (aC: H, N, F). *Physical Review B* **55**, 13020 (1997).

192. B. Stuart, *Infrared spectroscopy*. (Wiley Online Library, 2005).

193. A. A. King *et al.*, A New Raman Metric for the Characterisation of Graphene oxide and its Derivatives. *Scientific Reports* **6**, 19491 (2016).

194. M. Dresselhaus, P. Eklund, Phonons in carbon nanotubes. *Advances in Physics* **49**, 705-814 (2000).

195. L. Cancado *et al.*, General equation for the determination of the crystallite size La of nanographite by Raman spectroscopy. *Applied Physics Letters* **88**, 163106-163106 (2006).

196. L. Panchakarla *et al.*, Synthesis, structure, and properties of boron-and nitrogen-doped graphene. *Advanced Materials* **21**, 4726-4730 (2009).

197. C. Casiraghi, F. Piazza, A. Ferrari, D. Grambole, J. Robertson, Bonding in hydrogenated diamond-like carbon by Raman spectroscopy. *Diamond and Related Materials* **14**, 1098-1102 (2005).

198. J. Robertson, Recombination and photoluminescence mechanism in hydrogenated amorphous carbon. *Physical Review B* **53**, 16302 (1996).

199. "Mass Spectrometry Introduction", Last accessed on: 18 Jan. 2016, http://www.chem.pitt.edu/facilities/mass-spectrometry/introduction

200. H. Horai *et al.*, MassBank: a public repository for sharing mass spectral data for life sciences. *Journal of mass spectrometry* **45**, 703-714 (2010).

201. T. Nishioka, paper presented at the 19th International Mass Spectrometry Conference, Kyoto, Japan, Sep. 20, 2012.

202. H. Horai, M. Arita, T. Nishioka, paper presented at the The 1st International Conference on BioMedical Engineering and Inofrmatics, Sanya, China, May 27-30, 2008.

203. G. Eda *et al.*, Blue photoluminescence from chemically derived graphene oxide. *Advanced Materials* **22**, 505 (2010).

204. S. Zhou *et al.*, Substrate-induced bandgap opening in epitaxial graphene. *Nature materials* **6**, 770-775 (2007).

205. Y. Shen *et al.*, Evolution of the band-gap and optical properties of graphene oxide with controllable reduction level. *Carbon* **62**, 157-164 (2013).

206. R. Caballol, E. Sanchez Marcos, J. C. Barthelat, Theoretical study of the different coordination modes of copper-carbon dioxide complex. *Journal of Physical Chemistry* **91**, 1328-1333 (1987).

207. J. Kim, D. Summers, K. Frese, Reduction of CO_2 and CO to methane on Cu foil electrodes. *Journal of electroanalytical chemistry and interfacial electrochemistry* **245**, 223-244 (1988).

208. X. Nie, W. Luo, M. J. Janik, A. Asthagiri, Reaction mechanisms of CO_2 electrochemical reduction on Cu (111) determined with density functional theory. *Journal of Catalysis* **312**, 108-122 (2014).

209. J. Cai *et al.*, Atomically precise bottom-up fabrication of graphene nanoribbons. *Nature* **466**, 470-473 (2010).

210. A. Bagri *et al.*, Structural evolution during the reduction of chemically derived graphene oxide. *Nature chemistry* **2**, 581-587 (2010).

211. J. P. Barton, D. G. Infield, Energy storage and its use with intermittent renewable energy. *Energy Conversion, IEEE Transactions on* **19**, 441-448 (2004).

212. H. Yang, Z. Wei, L. Chengzhi, Optimal design and techno-economic analysis of a hybrid solar–wind power generation system. *Applied Energy* **86**, 163-169 (2009).

213. J. O. Bockris, The origin of ideas on a Hydrogen Economy and its solution to the decay of the environment. *International Journal of Hydrogen Energy* **27**, 731-740 (2002).

214. B. Johnston, M. C. Mayo, A. Khare, Hydrogen: the energy source for the 21st century. *Technovation* **25**, 569-585 (2005).

215. J. D. Holladay, J. Hu, D. L. King, Y. Wang, An overview of hydrogen production technologies. *Catalysis Today* **139**, 244-260 (2009).

216. G. J. Stiegel, M. Ramezan, Hydrogen from coal gasification: An economical pathway to a sustainable energy future. *International Journal of Coal Geology* **65**, 173-190 (2006).

217. S.-Y. Lin, Y. Suzuki, H. Hatano, M. Harada, Developing an innovative method, HyPr-RING, to produce hydrogen from hydrocarbons. *Energy Conversion and Management* **43**, 1283-1290 (2002).

218. L. Gao, N. Paterson, D. Dugwell, R. Kandiyoti, Zero-Emission Carbon Concept (ZECA): Equipment Commissioning and Extents of the Reaction with Hydrogen and Steam. *Energy & Fuels* **22**, 463-470 (2007).

219. G. Rizeq *et al.*, "Fuel-Flexible Gasification-Combustion Technology for Production of H_2 and Sequestration-Ready CO_2," *Quarterly Technical Progress Report No. 9* (General Electric Energy and Environmental Research Corporation, 2003).

220. D. P. Ye, J. B. Agnew, D. K. Zhang, Gasification of a South Australian low-rank coal with carbon dioxide and steam: Kinetics and reactivity studies. *Fuel* **77**, 1209-1219 (1998).

221. P. Haynes W, J. Gasior S, J. Forney A, in *Coal Gasification*. (AMERICAN CHEMICAL SOCIETY, 1974), vol. 131, chap. 11, pp. 179-202.

222. J. Corella, J. M. Toledo, G. Molina, Steam Gasification of Coal at Low−Medium (600−800 °C) Temperature with Simultaneous CO_2 Capture in Fluidized Bed at Atmospheric Pressure: The Effect of Inorganic Species. 1. Literature Review and Comments. *Industrial & Engineering Chemistry Research* **45**, 6137-6146 (2006).

223. C.-Z. Li, Some recent advances in the understanding of the pyrolysis and gasification behaviour of Victorian brown coal. *Fuel* **86**, 1664-1683 (2007).

224. J. Corella, J. M. Toledo, G. Molina, Steam Gasification of Coal at Low−Medium (600−800 °C) Temperature with Simultaneous CO_2 Capture in a Bubbling Fluidized Bed at Atmospheric Pressure. 2. Results and Recommendations for Scaling Up. *Industrial & Engineering Chemistry Research* **47**, 1798-1811 (2008).

225. A.-G. Collot, Matching gasification technologies to coal properties. *International Journal of Coal Geology* **65**, 191-212 (2006).

226. C. C. Dean, J. Blamey, N. H. Florin, M. J. Al-Jeboori, P. S. Fennell, The calcium looping cycle for CO_2 capture from power generation, cement manufacture and hydrogen production. *Chemical Engineering Research and Design* **89**, 836-855 (2011).

227. L. Liu, H. Liu, M. Cui, Y. Hu, J. Wang, Calcium-promoted catalytic activity of potassium carbonate for steam gasification of coal char: Transformations of sulfur. *Fuel*, (2012).

228. M. Zhao, A. I. Minett, A. T. Harris, A review of techno-economic models for the retrofitting of conventional pulverised-coal power plants for post-combustion capture (PCC) of CO_2. *Energy & Environmental Science* **6**, 25-40 (2013).

229. G. S. Grasa, J. C. Abanades, CO_2 Capture Capacity of CaO in Long Series of Carbonation/Calcination Cycles. *Industrial & Engineering Chemistry Research* **45**, 8846-8851 (2006).

230. H. An *et al.*, Coal gasification with in situ CO2 capture by the synthetic CaO sorbent in a 1 kWth dual fluidised-bed reactor. *International Journal of Hydrogen Energy* **37**, 14195-14204 (2012).

231. S. Lin, M. Harada, Y. Suzuki, H. Hatano, Continuous experiment regarding hydrogen production by Coal/CaO reaction with steam (II) solid formation. *Fuel* **85**, 1143-1150 (2006).

232. X. Wang, Hydrogen Production by Coal Gasification Coupled with in Situ CO_2 Capture. *Energy and Power Engineering* **4**, 210-217 (2012).

233. E. J. Anthony, Solid Looping Cycles: A New Technology for Coal Conversion. *Industrial & Engineering Chemistry Research* **47**, 1747-1754 (2008).

234. J. S. Dennis, S. A. Scott, A. N. Hayhurst, In situ gasification of coal using steam with chemical looping: a technique for isolating CO_2 from burning a solid fuel. *Journal of the Energy Institute* **79**, 187-190 (2006).

235. K. B. Yi, D. P. Harrison, Low-Pressure Sorption-Enhanced Hydrogen Production. *Industrial & Engineering Chemistry Research* **44**, 1665-1669 (2005).

236. S. Lin, M. Harada, Y. Suzuki, H. Hatano, Continuous experiment regarding hydrogen production by coal/CaO reaction with steam (I) gas products. *Fuel* **83**, 869-874 (2004).

237. S. Lin, M. Harada, Y. Suzuki, H. Hatano, Hydrogen production from coal by separating carbon dioxide during gasification. *Fuel* **81**, 2079-2085 (2002).

238. S. Lin, Y. Wang, Y. Suzuki, Effect of Coal Rank on Steam Gasification of Coal/CaO Mixtures. *Energy & Fuels* **21**, 2763-2768 (2007).

239. J. E. Gallagher, C. A. Euker, Catalytic coal gasification for SNG manufacture. *International Journal of Energy Research* **4**, 137-147 (1980).

240. R. J. Lang, R. C. Neavel, Behaviour of calcium as a steam gasification catalyst. *Fuel* **61**, 620-626 (1982).

241. A. Tomita, Y. Watanabe, T. Takarada, Y. Ohtsuka, Y. Tamai, Nickel-catalysed gasification of brown coal in a fluidized bed reactor at atmospheric pressure. *Fuel* **64**, 795-800 (1985).

242. Y. Ohtsuka, A. Tomita, Calcium catalysed steam gasification of Yallourn brown coal. *Fuel* **65**, 1653-1657 (1986).

243. Y. Ohtsuka, K. Asami, Highly active catalysts from inexpensive raw materials for coal gasification. *Catalysis Today* **39**, 111-125 (1997).

244. E. Jakab, F. Till, G. Várhegyi, Thermogravimetric-mass spectrometric study on the low temperature oxidation of coals. *Fuel Processing Technology* **28**, 221-238 (1991).

245. N. H. Florin, A. T. Harris, Mechanistic study of enhanced H_2 synthesis in biomass gasifiers with in-situ CO_2 capture using CaO. *AIChE Journal* **54**, 1096-1109 (2008).

246. A. Arenillas, F. Rubiera, J. J. Pis, Simultaneous thermogravimetric–mass spectrometric study on the pyrolysis behaviour of different rank coals. *Journal of Analytical and Applied Pyrolysis* **50**, 31-46 (1999).

247. R. G. Jenkins, S. P. Nandi, P. L. Walker Jr, Reactivity of heat-treated coals in air at 500 °C. *Fuel* **52**, 288-293 (1973).

248. E. Hippo, P. L. Walker Jr, Reactivity of heat-treated coals in carbon dioxide at 900 °C. *Fuel* **54**, 245-248 (1975).

249. T. D. Hengel, P. L. Walker Jr, Catalysis of lignite char gasification by exchangeable calcium and magnesium. *Fuel* **63**, 1214-1220 (1984).

250. E. M. Suuberg, D. Lee, J. W. Larsen, Temperature dependence of crosslinking processes in pyrolysing coals. *Fuel* **64**, 1668-1671 (1985).

251. N. Oreskes, The Scientific Consensus on Climate Change. *Science* **306** 1686 (2004).

252. IEA, "CO_2 emission from fuel combustion (highlights)," (International Energy Agency, 2012).

253. J. C. M. Pires, F. G. Martins, M. C. M. Alvim-Ferraz, M. Simões, Recent developments on carbon capture and storage: An overview. *Chemical Engineering Research and Design* **89**, 1446-1460 (2011).

254. M.-O. Schach, R. d. Schneider, H. Schramm, J.-U. Repke, Techno-Economic Analysis of Postcombustion Processes for the Capture of Carbon Dioxide from Power Plant Flue Gas. *Industrial & Engineering Chemistry Research* **49**, 2363-2370 (2010).

255. B. Arias *et al.*, Demonstration of steady state CO_2 capture in a 1.7 MWth calcium looping pilot. *International Journal of Greenhouse Gas Control* **18**, 237-245 (2013).

256. J. Ströhle, M. Junk, J. Kremer, A. Galloy, B. Epple, Carbonate looping experiments in a 1 MWth pilot plant and model validation. *Fuel* **127**, 13-22 (2014).

257. P. Sun, J. R. Grace, C. J. Lim, E. J. Anthony, The effect of CaO sintering on cyclic CO_2 capture in energy systems. *AIChE Journal* **53**, 2432-2442 (2007).

258. P.-H. Chang, T.-J. Lee, Y.-P. Chang, S.-Y. Chen, CO_2 Sorbents with Scaffold-like Ca-Al Layered Double Hydroxides as Precursors for CO_2 Capture at High Temperatures. *ChemSusChem* **6**, 1076-1083 (2013).

259. A. Coenen, T. L. Church, A. T. Harris, Biological versus Synthetic Polymers as Templates for Calcium Oxide for CO_2 Capture. *Energy & Fuels* **26**, 162-168 (2011).

260. B. Feng, W. Liu, X. Li, H. An, Overcoming the Problem of Loss-in-Capacity of Calcium Oxide in CO_2 Capture. *Energy & Fuels* **20**, 2417-2420 (2006).

261. F.-Q. Liu, W.-H. Li, B.-C. Liu, R.-X. Liu, Synthesis, Characterization, and High Temperature CO_2 capture of New CaO based Hollow Sphere Sorbents. *Journal of Materials Chemistry A*, (2013).

262. W. Liu *et al.*, Synthesis of Sintering-Resistant Sorbents for CO_2 Capture. *Environmental Science & Technology* **44**, 3093-3097 (2010).

263. Z. Yang, M. Zhao, N. H. Florin, A. T. Harris, Synthesis and Characterization of CaO Nanopods for High Temperature CO_2 Capture. *Industrial & Engineering Chemistry Research* **48**, 10765-10770 (2009).

264. A. M. Kierzkowska, R. Pacciani, C. R. Müller, CaO-Based CO_2 Sorbents: From Fundamentals to the Development of New, Highly Effective Materials. *ChemSusChem* **6**, 1130-1148 (2013).

265. V. Manovic, E. J. Anthony, Thermal Activation of CaO-Based Sorbent and Self-Reactivation during CO_2 Capture Looping Cycles. *Environmental Science & Technology* **42**, 4170-4174 (2008).

266. V. Manovic, E. J. Anthony, D. Loncarevic, looping cycles with CaO-based sorbent pretreated in at high temperature. *Chemical Engineering Science* **64**, 3236-3245 (2009).

267. J. M. Valverde, Ca-based synthetic materials with enhanced CO_2 capture efficiency. *Journal of Materials Chemistry A* **1**, 447-468 (2013).

268. A. Wang *et al.*, Design and Operation of a Fluidized Bed Hydrator for Steam Reactivation of Calcium Sorbent. *Industrial & Engineering Chemistry Research* **52**, 2793-2802 (2013).

269. J. C. Abanades, The maximum capture efficiency of CO_2 using a carbonation/calcination cycle of $CaO/CaCO_3$. *Chemical Engineering Journal* **90**, 303-306 (2002).

270. J. C. Abanades, D. Alvarez, Conversion Limits in the Reaction of CO_2 with Lime. *Energy & Fuels* **17**, 308-315 (2003).

271. P. Sun, C. J. Lim, J. R. Grace, Cyclic CO_2 capture by limestone-derived sorbent during prolonged calcination/carbonation cycling. *AIChE Journal* **54**, 1668-1677 (2008).

272. J. Wang, E. J. Anthony, On the Decay Behavior of the CO_2 Absorption Capacity of CaO-Based Sorbents. *Industrial & Engineering Chemistry Research* **44**, 627-629 (2004).

273. L. Zhen-shan, C. Ning-sheng, E. Croiset, Process analysis of CO_2 capture from flue gas using carbonation/calcination cycles. *AIChE Journal* **54**, 1912-1925 (2008).

274. A. Charitos *et al.*, Experimental Validation of the Calcium Looping CO_2 Capture Process with Two Circulating Fluidized Bed Carbonator Reactors. *Industrial & Engineering Chemistry Research* **50**, 9685-9695 (2011).

275. A. MacKenzie, D. L. Granatstein, E. J. Anthony, J. C. Abanades, Economics of CO_2 Capture Using the Calcium Cycle with a Pressurized Fluidized Bed Combustor. *Energy & Fuels* **21**, 920-926 (2007).

276. L. M. Romeo, Y. Lara, P. Lisbona, A. Martínez, Economical assessment of competitive enhanced limestones for CO_2 capture cycles in power plants. *Fuel Processing Technology* **90**, 803-811 (2009).

277. B. Arias, G. S. Grasa, M. Alonso, J. C. Abanades, Post-combustion calcium looping process with a highly stable sorbent activity by recarbonation. *Energy & Environmental Science* **5**, 7353-7359 (2012).

278. "Fuel cost projections : Updated natural gas and coal outlook for AEMO modelling," (ACIL Tasman, 2012).

279. B. Metz, O. Davidson, H. Coninck, M. Loos, L. Meyer, "IPCC Special Report on Carbon Dioxide Capture and Storage," (IPCC, UK, 2005).

280. W. R. Wilcox "Oxygen costs", Last accessed on: 8 July 2014, http://people.clarkson.edu/~wwilcox/Design/oxycost.htm

281. L. M. Romeo, Y. Lara, P. Lisbona, J. M. Escosa, Optimizing make-up flow in a CO_2 capture system using CaO. *Chemical Engineering Journal* **147**, 252-258 (2009).

282. N. J. Amos *et al.*, Design and synthesis of stable supported-CaO sorbents for CO_2 capture. *Journal of Materials Chemistry A* **2**, 4332-4339 (2014).

283. N. Rodriguez, M. Alonso, G. Grasa, J. C. Abanades, Heat requirements in a calciner of $CaCO_3$ integrated in a CO_2 capture system using CaO. *Chemical Engineering Journal* **138**, 148-154 (2008).

284. C. C. Dean, D. Dugwell, P. S. Fennell, Investigation into potential synergy between power generation, cement manufacture and CO_2 abatement using the calcium looping cycle. *Energy & Environmental Science* **4**, 2050-2053 (2011).

285. J. C. Abanades, E. J. Anthony, J. Wang, J. E. Oakey, Fluidized Bed Combustion Systems Integrating CO_2 Capture with CaO. *Environmental Science & Technology* **39**, 2861-2866 (2005).

286. H. Tsuchiai, T. Ishizuka, T. Ueno, H. Hattori, H. Kita, Highly Active Absorbent for SO_2 Removal Prepared from Coal Fly Ash. *Industrial & Engineering Chemistry Research* **34**, 1404-1411 (1995).

287. R. H. Borgwardt, Kinetics of the reaction of sulfur dioxide with calcined limestone. *Environmental Science & Technology* **4**, 59-63 (1970).

288. R. W. Hughes, A. Macchi, D. Y. Lu, E. J. Anthony, Changes in Limestone Sorbent Morphology during CaO-$CaCO_3$ Looping at Pilot Scale. *Chemical Engineering & Technology* **32**, 425-434 (2009).

289. M. Junk, M. Reitz, J. Ströhle, B. Epple, Thermodynamic Evaluation and Cold Flow Model Testing of an Indirectly Heated Carbonate Looping Process. *Chemical Engineering & Technology* **36**, 1479-1487 (2013).